



Chang Yung-Fa Foundation, International Convention Center,
 Taipei, Taiwan
 December 15-17, 2022

Hosted by



Supported by



Biomedical Imaging and Sensing Conference 2022, edited by Yuan Luo, Toyohiko Yatagai,
 Osamu Matoba, Yasuhiro Awatsuji, Proc. of SPIE Vol. BISC22, BISC2200
 © 2023 SPIE · 0277-786X · doi: 10.1117/12.2683715

National Science and Technology Council

As the Convener of the Biomedical Engineering Program of National Science and Technology Council (NSTC), it is my great pleasure to welcome you to 2022 GCBME/TSBME/BISC, which is the joint meeting of the 5th Global Conference on Biomedical Engineering (GCBME), Annual Meeting of Taiwanese Society of Biomedical Engineering (TSBME), and SPIE Biomedical Imaging and Sensing Conference (BISC) during December 15-17, 2022. Thanks to the great efforts of the organizing committee and program committee, we are expecting a very successful event and fruitful interactions among the attendees.

Our aim is to promote scholarly communications between all Biomedical Engineering researchers of academia and industry, including the principal investigators of NSTC Biomedical Engineering Program. The main purpose of NSTC in supporting the 2022 GCBME/TSBME/BISC conference is not only to increase academic research and development but also industrial research for the overall development of the society. We believe this conference will promote biomedical engineering and photonics research. We hope this conference will create an atmosphere for idea exchange among biomedical engineering and photonics researchers regarding our future focus and opportunities. I would like to acknowledge your attendance, for not only showcasing your outstanding achievements, but also providing your precious opinions, and participating in our future planning. I hope all of you enjoy the technical program and social events in 2022 GCBME/TSBME/BISC.



Shan-Hui Hsu

Convener, Biomedical Engineering Program

National Science and Technology Council



台大醫學院
NTUCM

醫療器材與醫學影像研究所
Institute of Medical Device and Imaging

On behalf of the Institute of Medical Device and Imaging of National Taiwan University, it is my great pleasure to welcome you to the joint conference: The 5th Global Conference on Biomedical Engineering (GCBME), the Annual Meeting of Taiwanese Society of Biomedical Engineering (TSBME) and the 7th SPIE Biomedical Imaging and Sensing Conference (BISC). The conference is supported by the Biomedical Engineering Program of the National Science and Technology Council (NSTC) and the Society of Photo-Optical Instrumentation Engineers (SPIE). This is the first year that the SPIE BISC conference is organized together with the GCBME/TSBME conference.

The primary goal of the joint conference is to bring together great minds from around the globe to share the latest advancements in biomedical engineering research. It is my great pleasure to host this joint event. I hope this conference will provide a great opportunity for the attendees to present their research and come up with new ideas.

SPIE BISC is a premier international conference for biomedical imaging and sensing. It is a regular annual event at the Optics and Photonics Congress in Japan. This is the inaugural edition of SPIE BISC in Taiwan, which I hope to continue in the future. I congratulate the BISC organizing committee from Japan for this new avenue, which will open up new directions for the collaborative research between the two countries.

This year, we are also introducing a Precision Medicine Forum, which will feature distinguished panelists from academia and industry to discuss the current challenges and future directions for precision health and biomedical engineering. The primary goal of the Forum is to have dialogue among all the partners to bring research and development from academic research to the development of smart health products for Taiwanese society. I would like to thank all the panelists for giving their valuable time to join the conference.

I do very much hope that we will together make this event very successful and fruitful for all of us.

Sincerely yours,

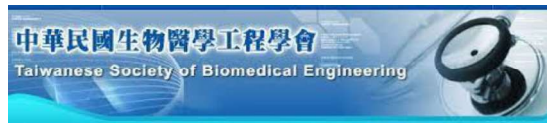
Yuan Luo

Chair, GCBME/TSBME/BISC

Director/Professor, Institute of Medical Device and Imaging

College of Medicine, National Taiwan University

2022.12.15



On behalf of the Taiwanese Biomedical Engineering Society (TSBME), it is my great pleasure to welcome you to 2022 GCBME/TSBME/BISC. The 5th Global Conference on Biomedical Engineering & Annual Meeting on TSBME is the top conference in this research area. The conference is supported by National Science and Technology Council. This year, the Institute of Medical Device and Imaging of National Taiwan University hosts the conference. On behalf of the host organization, we want to thank you for attending the 2022 GCBME/TSBME/BISC.

The aim of the 2022 GCBME/TSBME/BISC is to bring great minds from around the globe to share the latest advancements in biomedical engineering, and photonics research. This year, for the first time, BISC and GCBME/TSBME are organizing a joint conference, which provides the best opportunity for the attendees of different expertise to discuss and exchange knowledge.

The special sessions for the NSTC funded project will be organized. Local and international businesses will display their most recent products at the exhibition. 2022 GCBME/TSBME/BISC: gathering the people from universities, international societies, government, and companies will provide a multi-dimensional perspective. I hope all attendees will enjoy the program of the conference.

Finally, we would like to thank all committee members, the staff, the presiders, and all participants. Your participation will make 2022 GCBME/TSBME/BISC a great success.

Chien-Wen Lai

President, Taiwanese Society of Biomedical Engineering

2022 BISC Conference Chair Welcome Letter

Biomedical Imaging and Sensing Conference

Sponsored by SPIE, International Society for Optics and Photonics

On behalf of the organizing committee and program committee, it is our great pleasure that the 7-th SPIE Biomedical Imaging and Sensing Conference (BISC) in Taiwan is going to open, as a joint conference with the 5th Global Conference on Biomedical Engineering (GCBME), Annual Meeting of Taiwanese Society of Biomedical Engineering (TSBME). BISC is also supported by the Biomedical Engineering Program of the National Science and Technology Council (NSTC). BISC Conferences are held about every two years within the framework of the OPTICS & PHOTONICS International Congress in Yokohama, Japan. This is the first BISC conference outside Japan. I hope fruitful and creative discussions with many Taiwanese colleagues.

In biomedical optics and photonics, optical tools are employed for understanding and treatment of diseases, from the cellular level to macroscopic applications. At the cellular level, highly precise laser applications allow the manipulation, operation or stimulation of cells, even in living organisms or animals. Optical microscopy has been revolutionized by a thorough understanding of the different markers and their switching behavior. marker-free microscopy, like SHG or THG-microscopy is spreading into multiple biological and clinical imaging applications. OCT is continuously broadening its clinical applicability by even higher resolution, higher speed and more compact and the use of Doppler and polarization sensitivity for functional imaging.

In the field of optics and photonics, biomedical imaging and sensing areas are most quickly progressing and expanding. Techniques developed in these areas could bring us great steps in advances of physical, engineering and biological knowledge as well as optics and photonics technology. This Conference aims at covering several aspects from the fundamental studies at cellular level to clinical applications of various optical technologies.

Finally, we hope the 8-th Biomedical Imaging and Sensing Conference contributes to the progress in this field and we hope you enjoy fruitful discussions in the Conference.

Toyohiko Yatagai
BISC Conference Chair
Center for Optical Research and Education,
Utsunomiya University, Japan

Conference Maps

Transportation

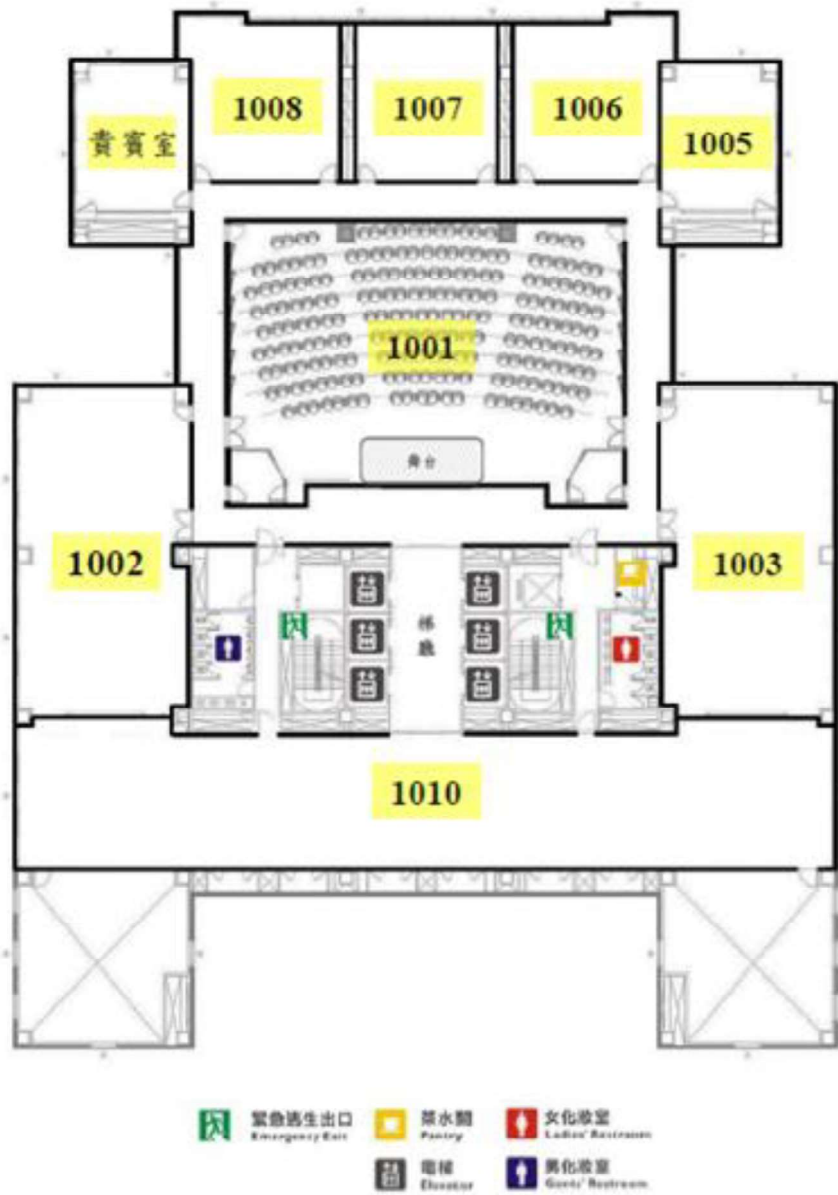
The Chang Yong-Fa Foundation is located on Zhongshan South Road with convenient transportation. It is on the opposite of Ketagalan Boulevard, nearby National Taiwan University Hospital and Liberty Square (Chiang Kai-shek Memorial Hall). It takes a five-minute walk from National Taiwan University Hospital MRT Station and a five-minute car ride from Taipei Main Station to the Chang Yong-Fa Foundation.



There is an underground parking lot for compact car.

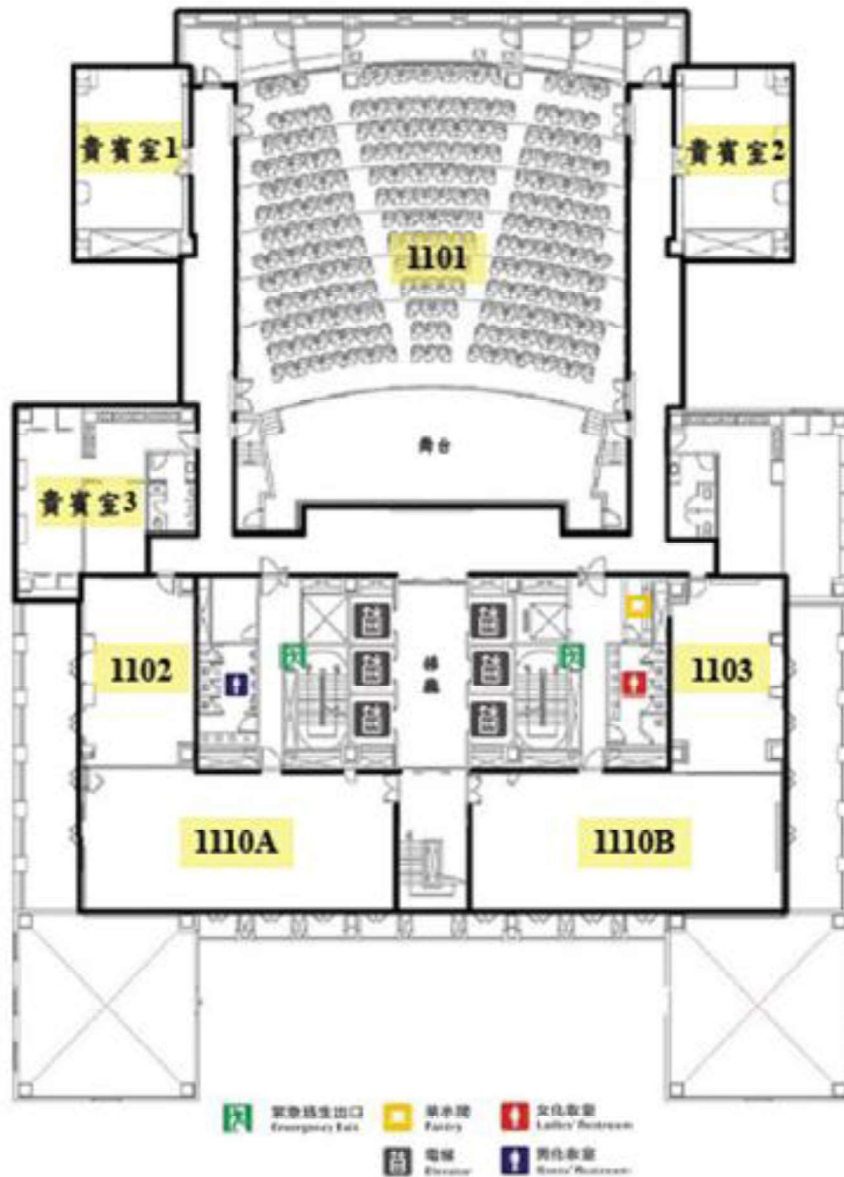
- Zhongshan highway → Jianquo North Road → go down the viaduct → Ran'ai Road → The East Gate (Jingfumen)
- Zhongzheng Bridge → Chongqing South Road → Presidential Office Building → Ketagalan Boulevard → Xinyi Road
- Zhongxiao Road → turn right on Zhongxiao West Road → Zhongshan South Road → Xinyi Road
- Taipei Bridge → Minquan West Road → Zhongshan North Road, Section 2 → Zhongshan South Road → Xinyi Road
- Take the MRT Tamsui Xinyi Line and get off at "National Taiwan University Hospital" station exit 2 (about five-minute walk to the main building)
 - Take the MRT Tamsui Xinyi Line or Songshan Xindian Line and get off at "Chiang Kai-shek Memorial Hall" station exit 5 or exit 6 (about ten-minute walk to the main building)
- Take bus 37, 249, 261, 270, 621, 630, 651, Ren'ai Route, and get off at "Ren'ai Zhongshan Road" station
- Take bus 0 East, 20, 22, 38, 88, 204, 588, 607, 1503 and get off at "National Chiang Kai-shek Memorial Hall" station
- Take bus 15 and 208 and get off at "The East Gate (Jingfumen)"

Location for Plenary talks/ Oral/ Posters Sessions



F10

Location for events on Day 1 morning



F11

GCBME&TSBME&BISC 2022 Committees

Conference Chair



Prof. Yuan Luo

Institute of Medical Device and Imaging, College of Medicine, National Taiwan University

Honorary Chair



Prof. Shan-Chwen Chang

Vice President, National Taiwan University



Prof. Jaw-lin Wang

Department of Biomedical Engineering, National Taiwan University

Secretariat



Institute of Medical Device and Imaging, National Taiwan University

Scientific Committee Chairs



Prof. Pai-Chi Li

Distinguished Professor,
National Taiwan University



Prof. Yen-Hsuan Ni

Dean, College of Medicine,
National Taiwan University

Organizing Committee Chair (Secretary Chair) & Co-Chair



Prof. Hsuan-Ming Huang (Chair)

Institute of Medical Device
and Imaging, College of
Medicine, National Taiwan
University



Prof. Ming-fa Hsieh (Co-Chair)

Chung Yuan Christian
University

International Advisory Committee Chair & Co-Chair



Prof. Toyohiko Yatagai (Chair)

Utsunomiya University
(Japan)



Prof. Jean-Marc Egly (Co-Chair)

French Science Academy

Program Chairs and Co-Chairs (BISC)








Pro. Shi-Wei Chu (Chair)

Department of Physics,
National Taiwan University



Pro. Osamu Matoba (Chair)

Kobe University (Japan)

	Pro. Yoshihisa Aizu (Co-Chair)	Muroran Institute of Technology (Japan)
	Pro. Yasuhiro Awatsuji (Co-Chair)	Kyoto Institute of Technology (Japan)
	Pro. Kung-Bin Sung (Co-Chair)	National Taiwan University (Taiwan)
Program Chairs and Co-Chairs (Assistance Technologies)		
	Pro. Wen-Shiang Chen (Chair)	Department of Physical Medicine and Rehabilitation, National Taiwan University Hospital
	Pro. Wei-Li Hsu (Co-Chair)	School and Graduate Institute of Physical Therapy, National Taiwan University

Program Chairs and Co-Chairs (Biology)



Pro. Sung-Jan Lin (Chair)

Department of Biomedical Engineering, National Taiwan University



Pro. Yu-chun Lin (Co-Chair)

Institute of Medical Device and Imaging, National Taiwan University

Program Chairs and Co-Chairs (Biomechanics)



Pro. Chun-Li Lin (Chair)

Department of Biomedical Engineering, National Yang Ming Chiao Tung University



Pro. Han Chang (Co-Chair)

Institute of Medical Device and Imaging, National Taiwan University

Program Chairs and Co-Chairs (Health Informatics)



Pro. Feipei Lai (Chair)

Graduate Institute of
Biomedical Electronics and
Bioinformatics, National
Taiwan University



Pro. Fu-jen Hsiao (Co-Chair)

Department of Surgery,
National Taiwan University
Hospital

Program Chairs and Co-Chairs (Material Science)



Pro. Shan-Hui Hsu (Chair)

Institute of Polymer Science
and Engineering, National
Taiwan University



Pro. Feng-Huei Lin (Co-Chair)

Department of Biomedical
Engineering, National
Taiwan University

Program Chairs and Co-Chairs (Medical Imaging)



Pro. Wen-Chau Wu

Institute of Medical Device
and Imaging, National
Taiwan University

Program Chairs and Co-Chairs (Medical Electronics)



Pro. Jia-Jin Chen (Chair)

Department of Biomedical
engineering, National
Cheng-Kung University



Pro. Fu-Yu Chen (Co-Chair)

Department of Biomedical
Engineering, Chun Yuan
Christian University

Scientific Committee

Scientific Committee Chair:

Pai-Chi Li National Taiwan University

Yen-Hsuan Ni National Taiwan University

Scientific Committee Members:

Fong-Chin Su National Cheng Kung University

Jia-Yush Yen National Taiwan Technology University

Chung-Ming Chen National Taiwan University

Tung-Wu Lu National Taiwan University

Chih-Han Chang National Cheng Kung University

Yi-You Huang National Taiwan University

Chun-Hsu Yao China Medical University

Kang-ping Lin Chung Yuan Christian University

Tsai-Kun Li National Taiwan University

Organizing Committee

Organizing Committee Chair:

Hsuan-ming Huang National Taiwan University

Organizing Committee Co-Chair:

Ming-fa Hsieh Chung Yuan Christian University

Organizing Committee members:

Shih-ming Lin National Taiwan University

Shih-ming Lin National Taiwan University

Yu-chun Lin National Taiwan University

Han Chang National Taiwan University

Fu-jen Hsiao National Taiwan University Hospital

Kuang-yu Huang National Taiwan University

Hsien-shun Liao National Taiwan University

Yu-hsiu Lee National Taiwan University

Pen-Hsiu Chao National Taiwan University

Chia-chung Wang I-Shou University

Chih-chung Huang National Cheng Kung University

Hsiang-lin Chu	Cathay General Hospital
Chun-kai Chiang	Taiwan Medical Service Coroporation
Ming-lung Yeh	National Cheng Kung University
Shao-liang Chang	Show Chwan Hospital
Po-jen Shih	National Taiwan University
Hsiang-kuang Liang	National Taiwan University
Sai-Wei Yang	National Yang-Ming Chiao Tung University
Liang-Yu Shyu	Chung Yuan Christian University
Shyh-Ming Kuo	I-Shou University
Tzer-Min Lee	National Cheng Kung University
Jiunn-Der Liao	National Cheng Kung University
Chih-Kuang Yeh	National Tsing Hua University
Jaw-Lin Wang	National Taiwan University
Win-Ping Deng	Taipei Medical Unversity
Yuh-Show Tsai	Chung Yuan Christian University

Program Committees

BISC

Chairs:

Shi-Wei Chu	National Taiwan University
Osamu Matoba	Kobe University (Japan)

Co-Chairs:

Yoshihisa Aizu	Muroran Institute of Technology (Japan)
Yasuhiro Awatsuji	Kyoto Institute of Technology (Japan)
Kung-Bin Sung	National Taiwan University (Taiwan)

Members:

Wonshik Choi	Korea University (Republic of Korea)
Katsumasa Fujita	Osaka University (Japan)
Yoshio Hayasaki	Utsunomiya University Center for Optical Research and Education (Japan);
Masaki Hisaka	Osaka Electro-Communication University (Japan)

Wataru Inami	Shizuoka University (Japan)
Ichiro Ishimaru	Kagawa University (Japan)
Toshiaki Iwai	Tokyo University of Agriculture and Technology (Japan)
Dong Li	Chinese Academy of Sciences (China)
Xingde Li	Johns Hopkins University(United States)
Takashi Kakue	Chiba University (Japan)
Myung K. Kim	University of South Florida (United States)
Robert Magnusson	The University of Texas at Arlington (United States)
Yuji Matsuura	Tohoku University (Japan)
Izumi Nishidate	Tokyo University of Agriculture and Technology (Japan)
Goro Nishimura	Hokkaido University (Japan)
Yusuke Ogura	Osaka University (Japan)
Eiji Okada	Keio University (Japan)
Yukitoshi Otani	Utsunomiya University (Japan)
Yong-Keun Park	Korea Advanced Institute of Science and Technology (Republic of Korea)
Xiangyu Quan	Kobe University (Japan)
Manabu Sato	Yamagata University (Japan)
Shunichi Sato	National Defense Medical College (Japan)
Tatsuki Tahara	National Institute of Information and Communications Technology (Japan)
Enrique Tajahuerce	University Jaume I (Spain)
Yosuke Tamada	Utsunomiya University (Japan)
Eriko Watanabe	The University of Electro-Communications (Japan)
Peng Xia	National Institute of Advanced Industrial Science and Technology (Japan)
Yasui Takeshi	The University of Tokushima (Japan)
Sheng-Hao Tseng	National Cheng-Keng University (Taiwan)
Hsiang-Chieh Lee	National Taiwan University (Taiwan)
Shih-Hsuan Chia	National Yang-Ming Chiao Tung University (Taiwan)
Li-An Chu	National Tsing Hua University

Assistance Technologies

Chair:

Wen-Shiang Chen National Taiwan University Hospital

Co-Chair:

Wei-Li Hsu National Taiwan University

Members:

Shih-Ching Chen Taipei Medical University.

Ta-Sen Wei Chunghua Christian Hospital

Wei-Li Hsu National Taiwan University

Jia-Jin Chen National Cheng Kung University

Li-Wei Ko National Yang Ming Chiao Tung University

Hsin-Yi Cheng Chang Gung University

Da-Jie Xu National Taiwan University of Science and Technology

Yu-Hsiu Lee National Taiwan University

Biology

Chair:

Sung-Jan Lin National Taiwan University

Co-Chair:

Yu-chun Lin National Taiwan University

Members:

Wen-Chuan Kuo National Yang-Ming University

Fu-Jen Kao National Yang-Ming University

Ming-Kai Pan National Taiwan University

Chau-Hwang Lee Academia Sinica

T. Tony Yang National Taiwan University

Tsai-Wen Chen National Yang-Ming University

Tzu-Sen Yang Taipei Medical University

Biomechanics

Chair:

Chun-Li Lin National Yang Ming Chiao Tung University

Co-Chair:

Han Chang National Taiwan University

Members:

Ting-Sheng Lin I-Shou University

Heng-Li Huang China Medical University

Ching-Chi Hsu National Taiwan University of Science and Technology

Wei-Li Hsu National Taiwan University

Jui-Ting Hsu China Medical University School of Dentistry

Wei-Chun Hsu National Taiwan University of Science and Technology

Cheng-Yang Liu National Yang Ming Chiao Tung University

Health Informatics

Chair:

Feipei Lai National Taiwan University

Co-Chair:

Fu-jen Hsiao National Taiwan University Hospital

Members:

Jung-Hsien Chiang National Cheng Kung University

Yi-Ju Tseng National Yang Ming Chiao Tung University

Yu-Chuan Li Taipei Medical University

Ruey-Feng Chang National Taiwan University

Yeong-Sung Lin National Taiwan University

Nan-Zhen Xie National Taipei University of Nursing and Health Sciences

Material Science

Chair:

Shan-Hui Hsu National Taiwan University

Co-Chair:

Feng-Huei Lin National Taiwan University

Members:

Pen-Hsiu Chao National Taiwan University

Hsing-Wen Sung National Tsing Hua University

Mei-Chin Chen National Cheng Kung University

Shang-Hsiu Hu National Tsing Hua University

Shu-Zhen Chang I-Shou University

San-Yuan Chen National Yang Ming Chiao Tung University

Hung-Yin Lin National University of Kaohsiung

Ming-Long Yeh National Cheng Kung University

Medical Imaging

Chair:

Wen-Chau Wu National Taiwan University

Members:

Hao-Li Liu National Taiwan University

Tzu-Chao Chuang National Sun Yat-sen University

Shu-Ju Tu Chang Gung University

Chih-Chung Huang National Cheng Kung University

Yi-Ru Lin National Taiwan University of Science and
Technology

Kevin T. Chen National Taiwan University

Chun-Yi Wu National Yang Ming Chiao Tung University

Medical Electronics

Chair:

Jia-Jin Chen National Cheng-Kung University

Co-Chair:

Fu-Yu Chen Chun Yuan Christian University

Members:

Jia-Jung Wang I-Shou University

Chia-Yen Yang Ming Chuan University

Conference Agenda

時間	活動內容			
Thursday, December 15 (Day 1)				
08:00-12:00	Registration (註冊報到) 1101 走廊			
09:30-09:50	Opening Ceremony (開幕典禮) 1101			
09:50-10:00	Tea Break (茶敘)			
10:00-11:40	Forum of Precision Medicine (精準健康論壇/Chinese Version) 1101			
11:40-12:00	Photo Shooting Session (大合照時間) 1101			
12:00-17:00	Registration (註冊報到) 1001 走廊			
12:00-13:00	博鑫醫電公司業務說明會	Poster Session I (海報展 I)		Lunch (午餐)
	1008	1010		B1
13:00-13:45	Plenary Session I (大會特邀講座) 1001			
13:50-15:20	BISC 2022 (光電)	Material Science (材料)	Medical Imaging (影像)	Biomechanics (力學)
	1001	1006	1007	1008
15:20-16:20	Tea Break & Poster Session II (茶敘&海報展 II) 1010			
16:20-17:50	BISC 2022 (光電)	Material Science (材料)	Medical Imaging (影像)	Biomechanics (力學)
	1001	1006	1007	1008

時間	活動內容			
Friday, December 16 (Day 2)				
08:00-17:00	Registration (註冊報到) 1001 走廊			
08:30-10:00	BISC 2022 (光電)	Material Science (材料)	Medical Electronics (醫電)	Health Informatics (醫資)
	1001	1006	1007	1008
10:00-10:20	Tea Break (茶敘)			
10:20-11:50	BISC 2022 (光電)	Material Science (材料)	Medical Electronics (醫電)	Health Informatics (醫資)
	1001	1006	1007	1008
12:00-13:00	TSBME Council Meeting (醫工學會理監事會)		Poster Session III (海報展 III)	Lunch (午餐)
	1007		1010	B1
13:00-13:45	Plenary Session II (大會特邀講座) 1001			
13:50-15:20	BISC 2022 (光電)	Assistive Technologies (輔具)	JMBE best paper Competition (JMBE 最佳論文比賽)	Biology (生物)
	1001	1006	1007	1008
15:20-15:40	Tea Break (茶敘)			
15:40-17:10	BISC 2022 (光電)	Assistive Technologies (輔具)	Medical Imaging (影像)	Biology (生物)
	1001	1006	1007	1008
18:30-20:30	Conference Banquet & Best Student Presentation Awards (Oral/Poster) (大會晚宴 & 學生優秀論文頒獎) B1			

時間	活動內容				
Saturday, December 17 (Day 3)					
08:00-09:00	Registration (註冊報到) 1001 走廊				
08:00-09:30	BISC 2022 (光電)	整合型 計畫演講	Forum of Female Medical Engineers (女性醫學工 程師座談)	Annual Report of Biomedical Engineering Division, NSTC (國科 會醫工學門 成果發表會)	Forum of Clinical Engineering (臨床工程論 壇)
			1001	1005	1006
09:30-09:40	Tea Break (茶敘)				
09:40-11:00	BISC 2022 (光電)	Intracranial Tumor Segmentation (腦瘤分割挑戰 賽)	Forum of Female Medical Engineers (女性醫學工 程師座談)	Annual Report of Biomedical Engineering Division, NSTC (國科 會醫工學門 成果發表會)	Forum of Clinical Engineering (臨床工程論 壇)
			1001	1005	1006
11:00-12:00	NSTC BME Program Yearly Report/Chairman Overview and Discussion & Conference Closing (in Mandarin) (國科會工程處醫工學門報告暨閉幕典禮) 1001				
12:00-12:50	TSBME General Assembly (醫工學會會員大會) 1001				

Conference Highlights

Opening Remarks



**Prof. Shan-Chwen
Chang**
Vice President, NTU



Prof. Shan-Hui Hsu
IPSE, NTU



Prof. Jennifer Barton
Vice President, SPIE



Prof. Osamu Matoba
Kobe University , Japan

Plenary Speakers



Prof. Pai-Chi Li
Vice President, Office of Research & Development, NTU

Abstract: Recent studies on drug screening and disease progression have shown that 3D cell culture systems can better represent the *in vivo* conditions in comparison with 2D monolayer cultures. Studying mechanobiology in 3D cell culture systems also recapitulates cell behaviors in response to various types of mechanical stimuli. An effective tool for measuring the spatiotemporal changes in elastic properties of such 3D cell culture systems without invasively contacting the samples has not been readily available but is undoubtedly needed. We have developed novel optical and acoustic shear wave imaging methods for non-invasive quantification of the matrix stiffness in 3D culture conditions. Such methods require both high sensitivity and adequate spatial resolution. In particular, the complementary physical properties of light and sound are exploited and innovative devices are developed, despite the fact that these two distinctly different physical mechanisms are often separately applied in biomedical problems. Several techniques were developed, and their applications were demonstrated [1-5]. In addition, we will present a simple setup for shear wave elasticity imaging using only one single element transducer with machine learning based image reconstruction. The role of the combined optical and acoustic techniques in *in vitro* research will also be presented.



Prof. Ann-Shyn Chiang
Brain Research Center, National Tsing Hua University

Abstract: A big challenge in mapping brain connectome is visualizing both nanoscale synapses and milliscale long-range neurites in a large volume with densely packed population of neurons. Recent advances in mapping connectomes with serial electron microscopy have allowed 3D reconstruction of synapse-to-synapse connections, but limited within a small volume. Synchrotron x-ray computed tomography (CT) offers the possibility to image large brain volume at isotropic high resolution beyond the depth of focus without physical sectioning [1,2]. However, this requires an effective radiocontrast labelling of target neurons for neuroanatomy validation with the existing knowledge of neuron identity and circuit function [3]. Here, we report an enzyme metallography method to label target neurons expressing specific genes and proteins for x-ray micro-CT of not only the brain but also other tissues in the whole body at subcellular resolution in *Drosophila*. Using a synchrotron-based x-ray micro-CT with much improved resolution and imaging speed—the Accelerated X-ray Observation of Neurons (AXON) system [1], we have imaged and three-dimensionally reconstructed the central nerve system, muscle, and cuticle in the whole *Drosophila* body (Fig. 1, left). Isotropic high-resolution reconstruction allows us to segment boundary of individual neurons and brain neuropils for archiving all the collected data into a common 3D framework (Fig. 1, right). I will discuss potential applications of this new approach for mapping brain connectomes with synchrotron x-ray micro-CT.

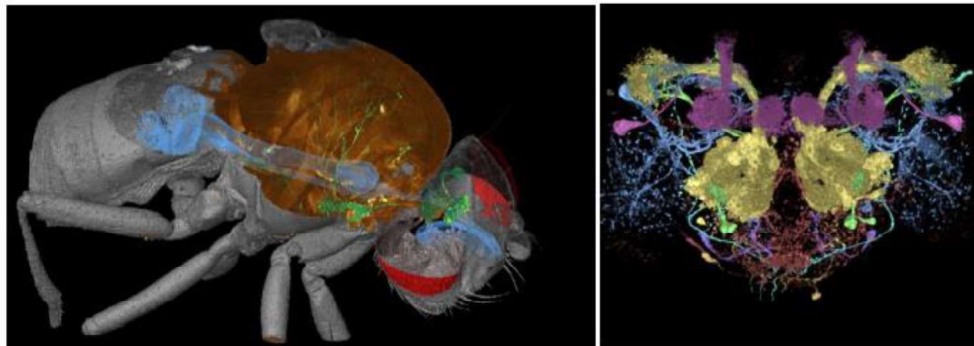


Fig. 1 | Synchrotron X-ray imaging of gene expressions in the whole *Drosophila* body. Tissues were labelled by enzyme metallography followed by osmium counterstaining. Left: lateral view. Green, the nervous system. Blue, the digestive system. Brown, muscle. Red, compound eyes. Grey, cuticle autocontrast. Right: frontal view of olfactory pathways in the brain. Yellow, iACT olfactory projection neurons. Green, mACT olfactory projection neurons. Magenta, the two APL neurons innervating the paired mushroom bodies. The sample fly carries GH146-Gal4>UAS-mCD8::GFP,UAS-GBP::APEX2 transgenes.

Forum Panelists



Prof. Pan-Chyr Yang
Academician, Academia Sinica
Former President, NTU



Prof. Huey-Kang Sytwu
Academician, Academia Sinica Vice
President, NHTU



Prof. Horn-Jiunn Sheen
Institute of Applied Mechanics, NTU
Vice Executive Secretary, BOST, EY



Han-Chang Wu
President, ASUS Cloud



Prof. Chung-Hsiun Wu
President, Development Center
for Biotechnology



Prof. Chien-Wen Lai
President, TSBME Vice Dean,
Changhua Christian Hospital



Prof. Chii-Wann Lin
Vice President & General
Director BDL, ITRI



Dr. Ted Chang
CTO & Vice President, Quanta
Computer Inc.

Invited Speakers

Assistive Technologies



Pro. Li-Wei Ko

Professor
Institute of Electrical and Control Engineering
National Yang Ming Chiao Tung University, Taipei, Taiwan



Pro. Lan-Yuen Guo

Professor
Department of Sports Medicine
Kaohsiung Medical University, Kaohsiung, Taiwan

Biology



Pro. Li-An Chu

Assistant Professor
Department of Biomedical Engineering & Environmental Sciences
National Tsing Hua University, Hsinchu, Taiwan



Dr. Chen-Hui Chen

Associate Research Fellow
Institute of Cellular and Organismic Biology
Academia Sinica, Taipei, Taiwan

Biomechanics



Pro. Wei-Li Hsu

Professor
School and Graduate Institute of Physical Therapy
National Taiwan University, Taipei, Taiwan



Pro. Ying chun Chen

Assistant Professor
Department of Mechanical Engineering
National Taipei University of Technology, Taipei, Taiwan



Pro. Wang, Yu-Tzu

Professor
Department of Mechanical and Electro-Mechanical Engineering
Tamkang University, New Taipei, Taiwan

BISC



Dr. Yen-Hsuan Ni

Dean
College of Medical
National Taiwan University



Pro. Tzi-Dar Chiueh

Dean
Graduate school of Advanced Technology
National Taiwan University



Pro. Shean-Jen Chen

Professor
Institute of Imaging and Biomedical Photonics
National Yang Ming Chiao Tung University, Taipei, Taiwan



Pro. Chi-Kuang Sun

Distinguished Professor
Department of Electrical Engineering
National Taiwan University of Science and Technology, Taipei, Taiwan



Pro. Katsumasa Fujita

Professor
Department of Applied Physics
Osaka University, Osaka, Japan



Pro. Adam T. Eggebrecht

Associate Professor
Mallinckrodt Institute of Radiology
Washington University, St. Louis, State of Missouri, U.S.A.



Pro. Jin-Wu Tsai

Professor
Institute of Brain Science
National Yang Ming Chiao Tung University, Taipei, Taiwan



Dr. YongKeun Park

Principal Investigator
Biomedical Optics Laboratory at KAIST
Korea Advanced Institute of Science and Technology, Republic of
Korea



Dr. Chia-Lung Hsieh

Associate Research Fellow
Institute of Atomic and molecular Sciences
Academia Sinica, Taipei, Taiwan



Pro. Miya Ishihara

Professor
Department of Medical Engineering
National Defense Medical College, Saitama Prefecture, Japan



Pro. Bernhard Baumann

Associate Professor
Center for Medical Physics and Biomedical Engineering
Medical University of Vienna, Vienna, Austria



Pro. Ji-Xin Cheng

Professor
College of Engineering
Boston University College of Engineering, Boston, U.S.A.



Pro. Keisuke Goda

Professor
Department of Chemistry, School of Science
The University of Tokyo, Tokyo, Japan



Dr. Jung-Chi Liao

Research Fellow
Advanced Cell Microscopy Lab
Academia Sinica, Taipei, Taiwan



Pro. En-Te Hwu

Associate Professor
Department of Health Technology
Technical University of Denmark, Copenhagen, Denmark



Pro. Izumi Nishidate

Associate Professor
Division of Advanced Electrical and Electronics Engineering
Tokyo University of Agriculture and Technology, Tokyo, Japan



Pro. Kang-Ping Lin

Professor
Department of Electrical Engineering
Chung yuan Christian University, Taiwan



Pro. Laura Waller

Professor
Electrical Engineering and Computer Science
UC Berkeley, Berkeley, U.S.A.

Health Informatics



Pro. Hsu Fu-Shun

Chief executive officer
Heroic-Faith Medical Science Inc., New Taipei, Taiwan



Pro. Yang Tz Shiang

Deputy Commissioner
Quanta Computer Inc., Taoyuan, Taiwan

Material Science



Pro. Yong. Zhang

R&D Center for Membrane Technology, Department of Chemical
Engineering, Chung Yuan Christian University, Taiwan



Pro. Tse-Ying Liu

Distinguished Professor
Department of Biomedical Engineering
National Yang Ming Chiao Tung University, Taipei, Taiwan



Pro. Jui-Yang Lai

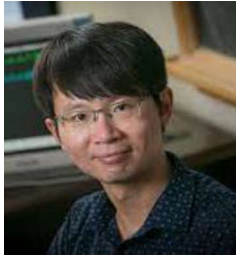
Professor
Chang Gung University, Taiwan

Medical Electronics



Dr. Pei-Yi Lin

Assistant Professor
The Boston Children's Hospital
Division Newborn Medicine, Boston, U.S.A.



Pro. Hua-Tieng Wu

Professor
Duke University, Durham, U.S.A

Medical Imaging



Pro. Wen-Yih Isaac Tseng

Cofounder and Chief Medical Officer
AcroViz Technology, Inc., Taipei, Taiwan



Pro. Che-Chou Shen

Distinguished Professor
Department of Electrical Engineering
National Taiwan University of Science and Technology, Taipei, Taiwan

光電全方位解決方案 Total Solutions !



多波長全自動倒立式顯微鏡系統
Motorized inverted microscopes



半導體雷射光源系統
Diode Laser Systems



超高解析度光譜儀
Extreme Hi-Resolution spectrometers



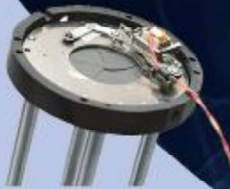
波長可調之均勻光源
Tunable light sources



超高精度線性馬達電控平台
Ultra precision linear motor stages with built-in controllers



小型影像模組
Compact all in one Imaging modules



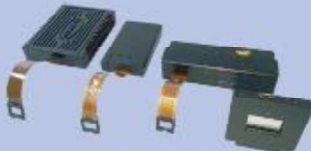
可程式化電控快門系統
Electro-programmable shutter systems



光學隔震裝置
Optical tables



聲光調製器
AO Modulators



空間光調製器
Spatial light modulators



拉曼光譜儀
Raman Spectrometers



液態可變焦透鏡
Liquid focus tunable lens



光功率/能量計
Power / Energy meters



雷射光形分析儀
Laser beam diagnostics



高解析波前分析儀
High resolution wavefront sensors



光束控制器
Fast steering 2D mirrors

Since 1990
ONSET
銓州光電股份有限公司

台北總公司
新北市新店區費橋路235巷129號5樓之2
TEL: (02) 8919-1688

蘇州分公司
蘇州市勞動路28號華亭大廈1702室(215004)
TEL: +86-512-6866-7233

www.onset-eo.com / sales@onset-eo.com



Oral Sessions

Assistive Technologies(輔具) Room 1006

Friday, December 16

Assistive Technologies 13:50-17:10

Chair : Wen-Shiang Chen

*National Taiwan University
Hospital*

Wei-Li Hsu

National Taiwan University

Ta-Sen Wei

Changhua Christian Hospital

Assistive Technologies 13:50 *Invited*

Mobile Brain-controlled Exoskeleton Interfaces (mBExIs) for Post-Stroke Lower Limb Rehabilitation

Li-Wei Ko

Institute of Electrical and Control Engineering, National Yang Ming Chiao Tung University

Assistive Technologies 14:20-14:35

Lip-Reading Recognition System Based on CNN-LSTM Model

Ling-Hsuan Yang, Chia-Yen Yang

Assistive Technologies 14:35-14:50

Development of an Assistant Device of Specific Speech Separation and Enhancement for Hearing Loss Patients Ting-You Liu, Yi-Chun Du

Assistive Technologies 14:50-15:05

Monitoring of Long term Sitting Posture at Work based on Image detection and EMG measurement

Yun-Chi Chuang, Chia-Yen Yang

Assistive Technologies 15:05-15:20

WiFi-Based Human Motion Identification and Quantification for Health Monitoring

Tzu-Yang Weng, Shih-Yuan Chen, Chun-Hsiang Chang, Chi-Lun Lin

Assistive Technologies 15:20-15:40

Coffee Break

Assistive Technologies 15:40 *Invited*

Assistive technologies in dementia care

Lan-Yuen Guo

Department of Sports Medicine, Kaohsiung Medical University

Assistive Technologies 16:10-16:25

Impedimetric Detection of Lactate in Human Sweat via Modified Screen-Printed Carbon Electrodes

Nitish Kumar, Yu-Te Liao, Shu-Ping Lin

Assistive Technologies 16:25-16:40

Tactile Feedback Analysis of Ferrofluids for the Education of the Blind and Visually Impaired

Aaron Raymond See, Aldrin Joshua

C.Tolentino, Renann G. Baldovino

Assistive Technologies 16:40-16:55

An Integrated Wearable and Self Powered Thermoelectric-assisted System for Wound Healing and Tracking Functions

Hsuan-Yu Ho, HuaShan Wu,

ZongHong Lin

Assistive Technologies 16:55-17:10

Barriers of Wearable Medical Device Innovation: A study of Hearing Aids

Chia-Wei Tu, Keng-Chia Kuo, Hsi-An

Shih, Ching-Feng Liu, Peng-Ting

Chen

Biology 13:50-17:10

Chair : Yu-Chun Lin
National Taiwan University
 Ming-Kai Pan
National Taiwan University

Biology 13:50 *Invited*

MOCAT: Combination of long-term tissue preservation and fast-speed organ-level imaging in cellular resolution

Li-An Chu
Institute of Biotechnology, National Tsing Hua University

Biology 14:20-14:35

Rotational Brownian Motion Combined with LAMP for Detection of SARS-CoV-2 On Chip

Dhrubajyoti Das, Cheng-Wen Lin, Han-Sheng Chuang

Biology 14:35-14:50

Microfluidic device for combined anti-cancer drug therapy

Yu-Ting Lin, Kin Fong Lei

Biology 14:50-15:05

Wavy structures control vascular smooth muscle cell phenotype

Chun-Yu Lin, Yu-Yu Hsueh, Pen-hsiu Grace Chao

Biology 15:05-15:20

Cre/LoxP Genetic Recombination Sustains Cartilage Anabolic Factor Expression in Hyaluronan Encapsulated MSCs Alleviates Intervertebral Disc Degeneration

Long Yi Chan, Chin-Yu Lin

Biology 15:20-15:40

Coffee Break

Biology 15:40 *Invited*

In toto imaging of skin and muscle cell dynamics in live zebrafish

Chen-Hui Chen
Institute of Cellular and Organismic Biology, Academia Sinica

Biology 16:10-16:25

Self-assembly mRNA polymeric nanomedicine applied on calvarial bone regeneration through endochondral ossification

Cheng-Hsin Wu, Hsuan Hu, Chin-Yu Lin

Biology 16:25-16:40

Dynamic metrology of biomedical cell

Kai Wu

Biology 16:40-16:55

Single-cell Transcriptomics Reveals Cellular Heterogeneity and Complex Cell-cell Communication Networks in Mouse Cornea

Yueh-Feng Wu, Nai-Wen Chang, Li-An Chu, Hsin-Yu Liu, Hsin-Yuan Tan, Sung Jan Lin

Biology 16:55-17:10

Difficulties in Biomedical Device Innovation from the perspective of innovation barriers

Hsin-Hsiung Huang, Si-Ru Chen, An-Shun Liu, Peng-Ting Chen

Biomechanics 13:50-15:20

Chair : Han Chang
National Taiwan University
Cheng-Yang Liu
National Yang Ming Chiao Tung University

Biomechanics 13:50 *Invited*

Virtual reality skateboarding: A novel virtual reality-based training and its biomechanical characteristics
Wei-Li Hsu
School and Graduate Institute of Physical Therapy, College of Medicine. National Taiwan University

Biomechanics 14:20 *Invited*

Detection and Evaluation of Cartilage at Early Stages Osteoarthritis using UV-VIS-NIR Spectroscopy and its Potential Application
Yingchun Chen
Department of Mechanical Engineering, National Taipei University of Technology

Biomechanics 14:50 *Invited*

The development and biomechanical analysis of mandibular reconstruction plates with a decrease in mandibular segment relapse for different types of Hemifacial microsomia
Yu-Tzu Wang
Department of Mechanical and Electro-Mechanical Engineering, TamKang University

Biomechanics 15:20-16:20

Coffee Break

Biomechanics 16:20-17:50

Chair : Han Chang
National Taiwan University
Ting-Sheng Lin
I-Shou University

Biomechanics 16:20-16:35

Automatic Identification of PainAssociated Imaging Abnormalities from Knee MRI Imaging by Deep Generative Networks
Pin-Hsun Lian, Tzu-I Chuang, Gary Han Chang

Biomechanics 16:35-16:50

Effects of Age on Three-dimensional Kinematics in Toddlers
Tsan-Yang Chen, Ting-Ming Wang, Kuan-Wen Wu, Pei-An Lee, Tung-Wu Lu

Biomechanics 16:50-17:05

Optical forces on human red blood cells induced by a shaped fiber probe with a photonic nanojet
Yu-Kai Hsieh, Wei-Yu Chen, Cheng-Yang Liu

Biomechanics 17:05-17:20

Musculoskeletal Simulation for Muscle Forces during Static Postural Balance in Patients with Degenerative Lumbar Spine Disease
Yi-Ching Tsai, Phunsuk Kantha, Po-Jung Chen, Dar-Ming Lai, Wei-Li Hsu

Biomechanics 17:20-17:35

Elucidate the postural control of dualtask balance assessment in patients with mild traumatic brain injury
Li-Fong Lin, Kai-Yun Chen, Yi-Ju Hung, Ju-Chi Ou, Yung-Hsiao Chiang

Biomechanics 17:35-17:50

Using Extended High Frequency to Explore Effects of Age-related Tympanic-membrane Properties and Negative Middle Ear Pressure on Sound Transmission
You-Cheng Yu, Tang-Chuan Wang, Tzu-Ching Shih

BISC 13:45-16:20

Bioimaging with New Technologies I
Chair : Osamu Matoba
Kobe University, Japan

BISC 13:45-13:50

Opening remark
Osamu Matoba
Kobe University, Japan

BISC 13:50 *Invited*

Temporal focusing-based multiphoton imaging with deep inpainting and prediction
Shean-Jen Chen
Institute of Imaging and Biomedical Photonics, National Yang Ming Chiao Tung University

BISC 14:20 *Invited*

Machine learning-assisted chromatin imaging in live cell nuclei by label-free interference DYNAMICS imaging
Chia-Lung Hsieh
Institute of Atomic and Molecular Sciences, Academia Sinica

BISC 14:50-15:05

Super-resolution imaging for collagen rich tissue
Ya-Han Chuang, Ya-Hui Lin, Yueh-Feng Wu, Sung-Jan Lin, Li-An Chu

BISC 15:05-15:20

Development of high-speed polarization-sensitive optical coherence tomography imaging based on HCG-VCSEL
Chien-Hua Peng, Yu-Cheng Mei, Hung-Kai Chen, Ting-Yen Tsai, Ting-Hao Chen, Chuan-Bor Chueh, Michae C. Y. Huang, Hsiang-Chieh Lee

BISC 15:20-16:20

Coffee Break

BISC 16:20-17:50

Ubiquitous Biology & Physiology
Chair : Sheng-Hao Tseng
National Cheng Kung University, Taiwan

BISC 16:20 *Invited*

Non-contact physiological measurement using camera-based diffuse reflectance spectroscopy
Izumi Nishidate
Tokyo University of Agriculture and Technology

BISC 16:50 *Invited*

Hacking Consumer Electronics for Biomedical Imaging
En-Te Hwu
Technical University of Denmark

BISC 17:20-17:35

Single-Cell Manipulation and Detection Platform Based on Optical Tweezers for investigating the Chemotaxis and Response of Cancer cells to Tyrosine Kinase Inhibitor PD153035
Mamadi M.S Colley, ChengJen Chang, JenChang Yang, Pei-Wen Peng, Tzu-Sen Yang

BISC 17:35-17:50

Rapid detection of SARSCoV-2 nucleocapsid protein antigen by dualcomb biosensing
S. Miyamura, R.Oe, T.Nakahara, S.Okada, S. Taue, Y. Tokizane, T.Minamikawa, T. Yano, K.Otsuka, A.Sakane, T.Sasaki, K.Yasutomo, T.Kajisa, T.Yasui

BISC 08:30-10:20

Bioimaging with New Technologies II
Chair : Shi-Wei Chu
National Taiwan University, Taiwan

BISC 08:30 *Invited*

Mid-Infrared Photothermal Microscopy: Principle, Instrumentation, and Applications
Ji-Xin Cheng
Photonics Center, Boston University

BISC 09:00 *Invited*

Side-illumination Raman microscopy using a Bessel beam for observation of cell spheroids
Katsumasa Fujita
Department of Advanced Physics, Osaka University

BISC 09:30-09:45

Multiple-Plate Continuum for Stimulated Raman Scattering Spectro-Microscopy across the Entire Raman Active Region
Guan-Jie Huang, PeiChen Lai, Kuo-Chuan Chao, Peng Lin, Ji-Xin Cheng, AnnShyn Chiang, Bo-Han Chen, Chih-Hsuan Lu, Shi-Wei Chu, Shang-Da Yang

BISC 09:45-10:00

Super-resolution neuronal imaging in Drosophila, mouse and human
Yi-Ru Luo, Ling-Hui Yen, Ya-Hui Lin, Chi-Wen Liong, ChihMing Wang, Shih-Kuo Chen, Hsueh-Cheng Chiang, Chin-Hsien Lin, Li-An Chu

BISC 10:00-10:20

Coffee Break

BISC 10:20-11:50
Light & Neuroscience
 Chair : Kung-Bin Sung
*National Taiwan University,
 Taiwan*

BISC 10:20 *Keynote*
**Realtime and Noninvasive
 Pathological Diagnosis of Diabetic
 Peripheral Neuropathy by Third-
 harmonic-generation Imaging of
 Free Nerve Ending (TIFNE)**
 Chi-Kuang Sun
*Department of Electrical Engineering,
 National Taiwan University*

BISC 10:50 *Invited*
**Developing optical methods for
 brain mapping at the point-of-care**
 Adam T. Eggebrecht
*Washington University School of
 Medicine*

BISC 11:20-11:35
**High speed automated cell detection
 and quantification in whole mouse
 brain**
 Li-Wen Wang, Ya-Hui Lin, Ching-Han
 Hsu, Li-An Chu

BISC 11:35-11:50
**Single/Multiphoton Light
 Sheet Microscopy for Drosophila
 Whole Brain Functional Imaging**
 Heng Chang, Wei-Kun Chang, Bi-
 Chang Chen, Li-An Chu

BISC 13:50-15:40
Novel Biomolecular Sensing
 Chair : Miya Ishihara
*National Defense Medical
 College, Japan*

BISC 13:50 *Invited*
**Unconventional SERS: metal/plasmon-
 free and wearable/flexible SERS**
 Keisuke Goda
*Department of Chemistry, University
 of Tokyo*

BISC 14:20-14:35
**Using deep learning for bone
 mineral density prediction with near
 infrared light**
 Hsin-Jou Wang, WeiChun Chang,
 Tsai-Hsueh Leu, Yi-Min Wang,
 Gautam Takhellambam, Chia-Wei Sun

BISC 14:35-14:50
**Analysis of lipid molecular properties in
 nonalcoholic fatty liver disease by use
 of Brillouin microspectroscopy**
 Eiji Hase, Takeo Minamikawa, Yu
 Tokizane, Takeshi Yasui

BISC 14:50-15:05
**Single-shot recording of transport of
 intensity equation-based three
 dimensional fluorescent imaging**
 Heng Manoj Kumar Kumar, Naru Yoneda,
 Xiangyu Quan, Osamu Matoba

BISC 15:05-15:20
**Incoherent digital holography system for
 simultaneous imaging of three
 dimensional and polarization information
 without a polarization filter**
 Tatsuki Tahara

BISC 15:20-15:40
Coffee Break

BISC 15:40-17:10
**Large-tissue and High-speed
 Imaging**
 Chair : Hsiang-Chieh Lee
*National Taiwan University,
 Taiwan*

BISC 15:40 *Invited*
**Photoacoustic imaging
 technology to visualize from cells
 to organs in vivo**
 Miya Ishihara
National Defense Medical College

BISC 16:10 *Invited*
**Advancing contrast for optical
 coherence tomography in the eye
 and brain**
 Bernhard Baumann
*Center for Medical Physics and
 Biomedical Engineering, Medical
 University of Vienna*

BISC 16:40-16:55
**Diopter correction
 Spectral Domain Optical
 Coherence Tomography
 Angiography in Ophthalmology**
 Sung-Wen Huang, Jia-Pu Syu,
 Wen-Chuan Kuo

BISC 16:55-17:10
**H&E-compatible Rapid Fresh
 Pathology technique for
 intraoperative tumor assessment
 at a sustained data throughput of
 >700 Mbps**
 Bhaskar Jyoti Borah, Yao-Chen
 Tseng, Chi-Kuang Sun

BISC 08:00-09:40

Label-free Microscopy

Chair : Yasuhiro Awatsuji

*Kyoto Institute of Technology,
japan*BISC 08:00 *Invited***Computational 3D microscopy
with scattering samples**

Laura Waller

*Department of Electrical Engineering
and Computer Sciences, UC Berkley*BISC 08:30 *Invited***Quantitative phase imaging and
artificial intelligence: inference of
molecular-specific information from
label-free imaging**

YongKeun Park

*Korea Advanced Institute of Science
and Technology*

BISC 09:00-09:15

**AI assisted FPGA based Isotropic
Quantitative Differential Phase
Contrast imaging**Yen-Chih Yu, Sunil Vyas, J.Andrew Yeh,
Yuan Luo

BISC 09:15-09:30

**High speed interferometric
scattering confocal microscopy
unveils rapid cell dynamics at the
nanoscale**Yi-Teng Hsiao, TsaiYing Wu, Shi-Wei
Chu, Chia-Lung Hsieh

BISC 09:30-09:40

Coffee Break

BISC 09:40-10:55

Bioimaging with New Technologies III

Chair : Katsumasa Fujita

*Osaka University, japan*BISC 09:40 *Invited***Detection of Neurodegeneration
Using Automated Dendritic Spine
Identification Based on****Convolutional Neural Network**

Jin-Wu Tsai

*Institute of Brain Science, National
Yang Ming Chiao Tung University*BISC 10:10 *Invited***Microscopy-guided subcellular
proteomics**

Jung-Chi Liao

*Institute of Atomic and Molecular
Sciences Academia Sinica. Genome
and Systems Biology Degree
Program, National Taiwan University*

BISC 10:40-10:55

**Volume holographic lenslet
array based confocal imaging**Surag Athippillil Suresh, Sunil Vyas, J.
Andrew Yeh, Yuan Luo

Health Informatics(醫資) Room 1008

Friday, December 16

Health Informatics 08:30-10:50

Chair : Furen Xiao

National Taiwan University

Health Informatics 08:30 *Invited*

**Development An AI-Powered
Respiratory Sound Monitoring and
clinical practice**

Dr. Fu-Shun Hsu

韋信醫療科技執行長

Health Informatics 09:00-09:15

**Evaluating teaching methods via
functional near-infrared
spectroscopy**

Chih-Ting Chang, Wan-Yi Chen, Yu-
Feng Li, Li-Hung Chang, Chia-Wei Sun

Health Informatics 09:15-09:30

**Multimodal Drinking Activity
Identification for Fluid Intake
Monitoring**

Pei-Wei Yu, Chien-Pin Liu, Chia-Yeh
Hsieh, Kai-Chun Liu, Chia-Tai Chan

Health Informatics 09:30-09:45

**Wearable-based Vestibular
Rehabilitation Monitoring System**

Chun-Chi Liu, Kuan-Chung Ting,
Chia-Yeh Hsieh, Kai-Chun Liu, Chia-
Tai Chan

Health Informatics 09:45-10:00

**Utilize embedded sensors in a
3Dprinted, custom-designed
medical gadget to detect
hemodialysis-associated vascular
dysfunction early**

Wei-Ling Chen, Che-Wei Lin, Chung-
Dann Kan

Health Informatics 10:00-10:20

Coffee Break

Health Informatics 10:20-11:50

Chair : Yi-Ju Tseng

National Yang Ming Chiao

Tung University

Health Informatics 10:20 *Invited*

**Quanta QOCA AI-Medical Platform
for Smart Healthcare**

楊子翔博士

廣達電腦副處長

Health Informatics 10:50-11:05

**Pathology image classification of
stroke blood clot origin using
DenseNet**

Chun-Ching Huang, Hung-Wen Chiu

Health Informatics 11:05-11:20

**Feasibility Study of Diagnosis of
Parkinson' s Diseases with Voice
Analysis on Mobile Devices**

Mirna Danisa Tandjung, Zhe-Yuan
Lien, Chao-Min Wu

Health Informatics 11:20-11:35

**Severity Assessment of Patients with
Speech Disorder Using Deep
Learning**

Chieh-Hsin Li, Chien-An Chen, Jia-Jin
Chen

Health Informatics 11:35-11:50

**Personalized Prediction of Cancer
Risk and Treatment Based on the Full
Genome Architecture**Chun-Ching
Kuan-lin Huang

Material Science 13:50-15:20

Chair : Hung-Yin Lin
*National University of
Kaohsiung*
Ming-Long Yeh
*National Cheng Kung
University*

Material Science 13:50-14:05

**Combining Metal Organic
Framework (MOF) Nanocatalysts
and Immunotherapy to Enhance
Cytotoxic T Lymphocytes Infiltration
Ability**

Min-Ren Chiang, Wei-Ting Shen, Pin-
Xuan Huang, Shang-Hsiu Hu

Material Science 14:05-14:20

**Stearic acid modified hydroxyapatite
as a sustained release carrier for
tariquidar to improve brain
penetration of temozolomide**
Cheng-Ping Yu, Yan-Jye Shyong

Material Science 14:20-14:35

**Development of a decellularized
liver matrix-based nanomedicine for
liver regeneration**
Yong-Heng Lin, Yu-Chuan Chiu, Yung-
Te Hou

Material Science 14:35-14:50

**Sebacoyl Dinalbuphine Ester-Loaded
Nanostructured Lipid Carriers in Gel
for Postoperative Pain on Spine
Surgery**
Yi-Lian Li, Cheng-Li Lin, Jui-Chen Tsai,
Yan-Jye Shyong

Material Science 14:50-15:05

**Degradable Biohybrid Hydrogel
Neural Interfaces**
Wan Lou Lei, Tzu-Ya Cheng, Chih-Wei
Peng, Huai-En Lu, Wei-Chen Huang

Material Science 15:05-15:20

**M1 Macrophage Membrane-coated
Porous Magnetic Nanocubes for
Reversing Immune-deficient TME of
Lungmetastatic Colorectal Cancer**
Kang-Li Wang, Cheng-Han Li, Shang-
Hsiu Hu

Material Science 15:20-16:20

Coffee break

Material Science 16:20-17:50

Chair : Hung-Yin Lin
*National University of
Kaohsiung*
Shang-Hsiu Hu
National Tsing Hua University

Material Science 16:20-16:35

**A Structure-Anatomy-Function
Biomimetic Ligament Scaffold using
Interfacial Polyelectrolyte
Complexation Spinning with
Mineralization Gradient**
Yu-Chung Liu, Tzu-Wei Wang

Material Science 16:35-16:50

**Fabless manufacturing neural probe
for in vivo neural recording**
Szu-Ying Li, Yen-Ting Wu, Wie-Yun Li,
YuChun Lo, TaChung Liu, You-Yin
Chen

Material Science 16:50-17:05

**Photo-regulated emissive oxidase-
like nanozyme based sensor for
evaluation of the total antioxidant
capacity from human saliva**
Sanskruiti Swain, Ting-Yi Lin, Hua-En
Chueh, I-Hsuan Chou, Hsing-Ying
Lin, Chen-Han Huang

Material Science 17:05-17:20

**Devising hyperthermia dose of
NIRirradiated Cs_{0.33}WO₃
hyperthermia dose of NIR-irradiated
Cs_{0.33}WO₃ nanoparticles for HepG2
hepatic cancer cells**
Po-Sheng Hu, Hsiu-Jen Chou, Chi-An
Chen, Po-Yi Wu, KaiHsien Hsiao,
YuMin Kuo

Material Science 17:20-17:35

**P-tau Dephosphorylation
Measurement on the Basis of
Biomimetic
Electrochemicalpolymerized Thin
Film Modified EQCM**
Shang-Chi Chien, Jung-Chih Chen

Material Science 17:35-17:50

**Modulation of Schwann cell
behaviors by micro-and
nanopatterned polyurethane
substrates**
Chun-Ting Lin, Lester U.Vinzons,
ShuPing Lin

Material Science 08:30-10:00

Chair : Grace Pen-Hsiu Chao
National Taiwan University
Ming-Fa Hsieh
Chung Yuan Christian University

Material Science 08:30 *Invited*

Study on nanomedicines for tumor cell-targeting radiotherapy
Tse-Ying Liu
Department of Biomedical Engineering, National Yang Ming Chiao Tung University

Material Science 09:00 *Invited*

Bio-inspired Zwitterionic Material System: Molecular Design and Medical Applications
Yung Chang
R&D Center for Membrane Technology, Department of Chemical Engineering, Chung Yuan Christian University

Material Science 09:30 *Invited*

Functional Biomaterial Design for Glaucoma Pharmacotherapy
Jui-Yang Lai
Department of Biomedical Engineering, Chang Gung University

Material Science 10:00-10:20

Coffee break

Material Science 08:30-10:00

Chair : Grace Pen-Hsiu Chao
National Taiwan University
San-Yuan Chen
National Chiao Tung University

Material Science 10:20-10:35

Remdesivir and Dexamethasone loaded Nanostructured Lipid Carrier for pulmonary delivery
Yi-Hsuan Wen, Jui-Chen Tsai, Chian-Wei Chen, Yan-Jye Shyong

Material Science 10:35-10:50

Integrating the microneedles with radiosensitizers to enhance the therapeutic effect of radiotherapy for skin cancers
Min-Hua Chen, Chun-Hung Lee, Hsiang-Kuang Liang, Su-Chin Huang, Jui-Ping Li, Cheng-An J. Lin, Jen-Kun Chen

Material Science 10:50-11:05

Radiolabelled Upconversion nanoformulation for multimodal image guided cancer therapy
Najim Akhtar, Chuan Lin Chen, Surojit Chattopadhyay

Material Science 11:05-11:20

Preparation of polyethyleneimine coated magnetic nanoparticles conjugated with folic acid for hyperthermia application
Yu-Fang Lin, WenTyng Li

Material Science 11:20-11:35

Long-term therapeutic potential of nanoceria in urological chronic pelvic pain syndrome: immunomodulation via SerpinB2 downregulation
Wei-Chih Lien, Pei-Yuan Lee, Feng-Huei Lin, Hui-Min David Wang

Material Science 11:35-11:50

Aminated chitosan-functionalized nano eye-drops for acute glaucoma treatment
Chia-Jung Yang, Jui-Yang Lai

Medical Electronics(醫電) Room 1007

Friday, December 16

Medical Electronics 08:30-11:50

Moderator : Jia-Jin J. Chen

*National Cheng Kung
University*

Fu-Yu Chen

*Chung Yuan Christian
University*

Jia-Jung Wang

I-SHOU University

Chia-Yen Yang

Ming Chuan University

Medical Electronics 08:30 *Invited*

Bedside cerebral physiology monitoring in neonatal neurocritical care

Pei-Yi Lin

Pediatrics at Harvard Medical School

Medical Electronics 09:00-09:15

Quantification of Neonatal Bilirubin and Hemoglobin Concentrations with a Miniaturized DRS Handheld Device

Ying-Yu Chen, Nan-Yu Cheng, Shih-Yu Tzeng, Ming-Chein Fang, Sheng-Hao Tseng

Medical Electronics 09:15-09:30

Prediction of Vascular Access Stenosis from Phonoangiogram Signals Using the VGG16 and VGG19 Models

Jia-Jung Wang, Hangliang Zhang, Thung-Lip Lee

Medical Electronics 09:30-09:45

Ultrasonic Acupuncture Lowers Blood Glucose

Chia-Hsuan Chang, Jung-Chih Chen, Gin-Shin Chen

Medical Electronics 09:45-10:00

Extended-Gate Field-Effect Transistor with an Indium Tin Oxide-Coated Vertically Aligned Silicon Nanowires for the Detection of Cortisol

Yu-Ting Wei, Shu-Ping Lin

Medical Electronics 10:00-10:20

Coffee Break

Medical Electronics 10:20 *Invited*

Turning nonstationary biomedical signals into useful clinical information using modern signal processing

Hau-Tieng Wu

Department of Mathematics, Duke University

Medical Electronics 10:50-11:05

Development of a 6-axis RUS for AVF Stenosis Assessment

Shih-Yang Hung, Cheng-Bin Xu, Yi-Chun Du

Medical Electronics 11:05-11:20

Rapid and sensitive electrochemical biosensor for the detection of TNF- α
Neil Adrian P. Ondevilla, Peng-Wen Liu, Hsien-Chang Chang

Medical Electronics 11:20-11:35

Ultra-sensitive respiration detection mask with low cost SnO₂ sensors
Moumita Deb, Mei-Yu Chen, Po-Yi Chang, Pin-Hsuan Li, Ming-Jen Chan, Ya-Chung Tian, Ping-Hung Yeh, Olivier Soppera, Hsiao-Wen Zan

Medical Electronics 11:35-11:50

Neuroscience Tool: Ultrasensitive Electrochemical Dopamine

Aptasensor on the Multi-Electrode Array

Huai-Hsuan Shao, Ta-Chung Liu, Ting-Wei Kuo, Yu-Chun Lo, Tzu-Hsin Tseng, Min-Chieh Chuang, You-Yin Chen

Medical Imaging(影像) Room 1007

Thursday, December 15

Medical Imaging 13:50-15:20

Chair : Cheng-Wen Ko

*National Sun Yat-sen
University*

Yi-Ping Chao

Chang Gung University

Medical Imaging 13:50 *Invited*

Brain predicted age is an emerging biomarker for brain health

Wen-Yih Issac Tseng

AcroViz Technology

Medical Imaging 14:20-14:35

Oral cavity detection using handheld-probe polarizationsensitive optical coherence tomography

Hui-Ki Lai, Ting Chang, Ting-Yun Deng, Chung-Yu Chang, Wen-Chuan Kuo

Medical Imaging 14:35-14:50

3D Phase-sensitive PatchMatch Searching for Ultrasound Motion Estimation

Li-Fu Lee, Yen-Ting Liu, Po-Syun Chen, Mo-Han Lin, Geng-Shi Jeng

Medical Imaging 14:50-15:05

Pulse-Inversion Shear Wave Elastography (PI-SWE) Estimation of Stiffness Change by High Intensity Focused Ultrasound – Porcine liver

Wei-Cheng Hsiao, Hsien-Jung Chan, Bao-Yu Hsieh

Medical Imaging 15:05-15:20

Phase Aberration Correction Using Point Spread Function Reshaping for Biomedical Ultrasound Imaging

Wei-Hsiang Shen, Meng-Lin Li

Medical Imaging 16:20-17:50

Chair : Chun-Yi Wu

*National Yang Ming Chiao
Tung University*

Meng-Lin Li

National Tsing Hua University

Medical Imaging 16:20-16:35

Mask Guided Generative Adversarial Networks for Osteoarthritis Repair MRI Simulation

Tzu-I Chuang, P-H Liana, G. Changa

Medical Imaging 16:35-16:50

Compensation of out-of-focus blurring for dual-head PET imaging in proton therapy

Ming-Wei Lee, Meei-Ling Jan

Medical Imaging 16:50-17:05

Tunable acoustic lens plus adaptive optics (TAO) for fast volumetric two-photon imaging

Chang-Ling Chung, Tommaso Furieri, Jun-Yi Lin, Ting-Chen Chang, Jye-Chang Lee, Yi-Fan Chen, Ming-Kai Pan, Stefano Bonora, Shi-Wei Chu

Medical Imaging 17:05-17:20

Intratumor Oxygen Measurement in 3D-Multicellular Tumor Spheroids by using Ru(dpp)-based Fluorescent Polymeric Nanosensors

Ashish Kumar, Venkanagouda S.Goudar, Bishal Kumar Nahak, Fan-Gang Tseng

Medical Imaging 17:20-17:35

3D Ultrasound Cardiac Principal Stretch Imaging with LeastSquares-based Regularization

Po-Syun Chen, Lung-Chun Lin, Geng-Shi Jeng

Medical Imaging 17:35-17:50

The Effect of Gender and Age on Jawbone Quality : A Dental CBCT Study

Shiuan-Hui Wang, Jui-Ting Hsu, Lih-Jyh Fuh, Heng-Li Huang

Medical Imaging(影像) Room 1007

Friday, December 16

Medical Imaging 15:40-17:10

Chair : Yi-Ru Lin

*National Taiwan University of
Science and Technology*

Medical Imaging 15:40 *Invited*

**Enhanced Temporal Coherence for
Ultrasound Ultrafast Power Doppler
Imaging: Temporal Multiply-and-
Sum (TMAS) Autocorrelation**

Che-Chou Shen

*Department of Electrical Engineering,
National Taiwan University of Science
and Technology*

Medical Imaging 16:10-16:25

**Nakagami Imaging Combined with
Pulse Inversion Subtraction for
Monitoring of Continuous HIFU
Therapy**

Hsien-Jung Chan, Wei-Cheng Hsiao,
Po-Hsiang Tsui, Bao-Yu Hsieh

Medical Imaging 16:25-16:40

**Target Detection of B-mode Image
through Two-dimensional CFAR
Processing**

Chia-Hsuan Chang, Yuan-Pin Cheng,
Jung-Chih Chen

Medical Imaging 16:40-16:55

**In vivo monitoring of hemoglobin
derivative concentrations and
saturations in rat burn wounds using
diffuse reflectance spectral imaging**

Md Anwar Parvez, Kazuhiro Yashiro,
Izumi Nishidate, Yasuyuki Tsunoi,
Yasue Haruyama, Daizoh Saitoh,
Shunichi Sato

Medical Imaging 16:55-17:10

**Image-domain Material
Decomposition using DIP for Dual
Energy CT**

Hui-Yu Chang, Hsuan-Ming Huang

Interactive 5G Mobile Smart Patient Monitor

BROADSIMS

Beyond Measurement

We Simplify Your Work Flow



| Built-In Features |

- 12-Lead ECG
- Blood Pressure
- SpO2
- Heart Rate



| Add-On Features |



Open
RAW Data



Dashboard



| Solution Features |

- Spot Check
- Continuous Monitoring
- Prediction
- Auto Report



BROADSIMS Inc.
sales@broadSIMS.com



Poster Sessions



Paper ID	Category	Paper Title	Authors
250018	[GCBME] Medical Electronics	Development of Graphene/Polypyrrole Nanocomposite-based SAW Sensors and Its Clinical Applications in Detection of Sub-ppm Ammonia	Shao-Kai Lai Chi-Yen Shen Tien-Tsan Hung Yao-Wei Chuang
250020	[GCBME] Biomechanics	Prediction Traditional Hand Function Assessment through an Innovative Medical Device with Deep Learning	Pu-Chun Mo I-Te Tu Li-Chieh Kuo Hsiu-Yun Hsu Fong-Chin Su
250021	[GCBME] Biomechanics	Dimension Reduction of Time Series Data from Sensorimotor Function through Autoencoder	Pu-Chun Mo I-Te Tu Cheng-Feng Lin Charlie Chen Ma Li-Chieh Kuo Hsiu-Yun Hsu Yih-Kuen Jan Fong-Chin Su
250022	[GCBME] Health Informatics	Investigating the Connection between the Biomarkers in Blood and Hand Sensibility in Hemodialysis Patients	I te TU Yu-Shiuan Cheng Pu-Chun Mo Hsiu-Yun Hsu Li-Chieh Kuo I-Ming Jou Fong-Chin Su
250024	[GCBME] Material Science	Strawberry Extract Facial Mask Function and Biocompatibility Test	劉承祐 徐鼎鈞 林峻誼 吳翎瑄 張軒儒 王明誠
250025	[GCBME] Medical Imaging	Influence of Target Volume to Prediction Accuracy of Tumor Segmentation using U-Net on MRI for Hypopharyngeal Cancer	Shao-Chi Lin Chi-Yi Ho Yu-Chun Lin Shu-Hang Ng
250028	[GCBME] Medical Imaging	Deep Learning Technology and System Development in application to Gynecologic Oncology	Ching-Wei Wang Tai-Kuang Chao Huang-Chun Lien Yung-Ming Jeng

250030	[GCBME] Health Informatics	Interleukin-6 Rapid Diagnostic System for Sequential Monitoring Respiratory Failure in Elderly Pneumonia	Cheng-Han Chen Chao-Min Cheng
250031	[GCBME] Material Science	Molecularly targeted photothermal ablation of epidermal growth factor receptor-expressing cancer cells with a polypyrrole-iron oxide-afatinib nanocomposite	Lekshmi Rethi Chinmaya Mutalik Lekha Rethi Wei Hung Chiang Hsin-Lun Lee Wen Yu Pan Tze-Sen Yang Jeng-Fong Chiou Yin-Ju Chen Er Yuan Chuang Long Sheng Lu
250034	[GCBME] Biomechanics	C-terminus of Hsc70-interacting protein (CHIP) expression enhances survival, anti-senescence and stemness abilities in human Wharton's jelly mesenchymal stem cell	Chun-Hsu Yao Tung-Sheng Chen
250035	[GCBME] Medical Imaging	Decoupling of Brain Connectivity and Heart Rate Variability Underlies Dysautonomia in Familial Amyloid Polyneuropathy	Yuan-Che Min Ming-Chang Chiang
250043	[GCBME] Assistive Technologies	Improving the performance of a deep learning-based speech enhancement system by the scene flow technology: A hearing aid application	You-Ren Lin Bo-Sin Wang Wei-Zhong Zheng Ji-Yan Han Yu-Min Lin Wen-Huei Liao Ying-Hui Lai
250044	[BISC] Photonics & Optoelectronics	Custom-Made Photoacoustic System on Tumor Blood Vessels and Oxygen Saturation Measurement for Small Animals	YU-FONG LIOU Shih-Po Su Huihua Kenny Chiang
250046	[GCBME] Health Informatics	Quantitative Assessment of Physical Changes Based on Acoustic Parameters after Drinking Different Attributes of Beverages	Chuang-Chien Chiu Lun-Chien Lo Yu-Hsien Chen Hsiang Wang Cheng-Ru Yang
250047	[GCBME] Medical Electronics	A Safer Bone-Cement Infusion System for Assisting Osteoporotic Vertebral Compression Fracture Surgeries	Chu Woei Chyn Chen Jhong Yi Hsu Yung Fu Lin Jia Yi

			Tseng Yin Jiun Hwang Shiu Ren Liu An Shun Cheng Shih Hao Tsuei Yu Chuan Chu William
250051	[GCBME] Medical Imaging	Prediction of real-time left ventricular ejection fraction using deep learning algorithm	Madankumar Balasubramani Chih-Wei Sung Mu-Yang Hsieh Edward Pei-Chuan Huang Jiann-Shing Shieh
250056	[GCBME] Health Informatics	Early Warning Score Prediction using Machine Learning Applied in Cardiovascular Intensive Care Unit	Zi-Xuan Yang Ho-Tsung Hsin Jiann-Shing Shieh
250060	[BISC] Photonics & Optoelectronics	Prediction based on machine learning of operation outcome from peripheral arterial occlusive disease	Yung-Chang Chen Pin-Yu Kuo Jen-Kuang Lee Chau-Chung Wu Chia-Wei Sun
250061	[GCBME] Medical Electronics	Cross-domain CNN transfer learning from EEG to heart rate applied to sleep staging	Wen-Chen Huang Chia-Yen Yang
250062	[GCBME] Biomechanics	Mechanical analysis of the porous dental implant with triply periodic minimal surface lattice	Hung-chih Chang Chen-Gyi Yang Yu-Tang Ji Pin-Xin Guo Yu-Chi Chen
250064	[BISC] Photonics & Optoelectronics	Applying Machine learning to extracorporeal membrane oxygenation patients using functional near-infrared spectroscopy	Chang Yi Lee Ting-Wei Chiang Hsiao-Huang Chang Chia-Wei Sun
250065	[GCBME] Biomechanics	ECG classification using continuous wavelet transform and convolutional	Ting-Chi Hou Maysam Abbod Jiann-Shing Shieh
250067	[GCBME] Medical Electronics	Non-invasive continuous arterial blood pressure monitoring via PPG	Najsm Cox Maysam Abbod Jiann-Shing Shieh
250070			許廷鴻

	[BISC] Photonics & Optoelectronics	Analysis of police overwork degree by functional near-infrared spectroscopy: taking the Copenhagen overwork scale as a standard	謝清彥 劉耀鴻 王文瑜 林慶波 孫家偉
250080	[GCBME] Medical Imaging	Automatic Segmentation of Calcified Plaques and Vessel Borders with 2D Spatial Multilayer Machine Vision Classifier	Chia-Hung Lin
250081	[GCBME] Medical Electronics	The Synthesized Conductive/Magnetic Composite Particles for Tumor Magnetic Ablations	Jen-Jie Chieh, Shu-Hsien Liao Ting-Yuan Chen, Wen-Chun Wei
250083	[GCBME] Biomechanics	Remote and local generation of microstreaming vortices by focused ultrasound with vortex lens	Chih-Hsien Li Ching-Hsiang Fan
250085	[GCBME] Biomechanics	Intelligent meal carbohydrate recognition and evaluation based on blood glucose regulation for type 1 diabetic patients	Kai-Chieh Tu Tsung-Chih Lin
250088	[GCBME] Medical Imaging	Dual-Modality Bioluminescence/ Ultrasound 3D 360o Imaging System for Small Animal Tumor Imaging Using Homemade Transducers	Yuan Zhen Yang Shih-Po Su Yun-Chen Lee Huihua Kenny Chiang
250090	[GCBME] Material Science	Design and Development of Atmospheric Plasma Sterilization with Dialysis Machine	Cheng Kuo Tung 李東錦 林慶元 林秉郁 梁能昕 陳祐陞 林宏達 王明誠
250091	[GCBME] Biology	Mechanisms of ultrasound-microbubble cavitation for inducing the permeability of human skin	Ai-Ho Liao Yu-Chen Chen Chih-Hung Wang Shun Cheng Chang Jehng-Kang Wang
250092	[GCBME] Medical Imaging	Micro-bubble composite medical material combined with ultrasound for the development of head and neck diseases and tumor immunotherapy	Ai-Ho Liao Chih-Hung Wang Cheng-Ping Shih Yu-Hsiang Chu Jehng-Kang Wang
250095			

	[GCBME] Material Science	Hepatic Patch for Liver Regeneration after CCl4 Poisoning	Ting Yi Wu Yi Cheng Hsih Yung Te Hou
250096	[BISC] Photonics & Optoelectronics	Biodegradable and implantable polymer optical waveguide plate for guiding lightwaves into biological tissue	Ai-Wei Li Cheng-Yang Liu
250100	[GCBME] Medical Imaging	Monitoring of Pleural Respiratory Signals	Hsiao Tung Hsu Shih Hua Wang Hui Hua Chiang
250102	[GCBME] Health Informatics	Self-attention-based Pre-impact Fall Detection System Using Wearable Sensors	Tin-Han Chi Chien-Pin Liu Chia-Yeh Hsieh Kai-Chun Liu Chia-Tai Chan
250104	[GCBME] Medical Imaging	Portable electrical impedance tomography for lower limb edema	Chang-Lin Hu I-Cheng Cheng Zong-Yan Lin Chien-Ju Li Chii-Wann Lin
250105	[GCBME] Material Science	Design and Testing of Porous Artificial Tooth Roots for 3D Printing Techniques	Feng Min Lai Po Chun Shin Yu Yi Wang Pei Xuan Wu Fu Hsuan Yang Yu Xiu Huang Xin You Ji
250110	[GCBME] Medical Imaging	An Efficient Superimposition Method for Surgical Accuracy Assessment	Yu-Ching Hsiao Jing-Jing Fang
250111	[GCBME] Biomechanics	GAT-based through-the-eyelid tonometry for intraocular pressure monitoring	De-Yi Chiou Chi-Shen Chang Chun-Chuan Lin
250112	[GCBME] Medical Imaging	Lesion delineation framework for vestibular schwannoma, meningioma and brain metastasis for gamma knife radiosurgery using stereotactic magnetic resonance images	Yu-Te Wu Wei-Kai Lee Huai-Che Yang Cheng-Chia Lee Chia-Feng Lu Chih-Chun Wu Wen-Yuh Chung Hsiu-Mei Wu

			Wan-Yuo Guo
250115	[GCBME] Medical Imaging	Integrating Artificial Intelligence Services in Radiology for Diagnostic Assistance	Chin-Lin Lee Woei-Chyn Chu Chung-Yueh Lien Wei-Kai Lee Yu-Te Wu Wan-Yuo Guo
250117	[BISC] Photonics & Optoelectronics	Unsupervised Cross-modality Segmentation and Isotropic Restoration by Pseudo-mask Assisted Deep Generative Network	Meng-yun Wu Ya-ding Liu Da-yu Huang Li-An Chu Gary Han Chang
250119	[GCBME] Medical Imaging	Generative Adversarial Networks for MRI to Different Types of PET Synthesis and Comparison	Jie Ji
250120	[GCBME] Medical Imaging	Development of Surgical Planning and Patient Specific Instrument for High Tibial Osteotomy Surgery	Pei-Rou Chang Wei-Chih Tsemg Jing-Jing Fang
250121	[GCBME] Medical Electronics	Portable Electrochemical Impedance Spectroscopy Device Implementation	Yu-Rong Wang Jung-Chih Chen
250122	[GCBME] Material Science	Enhanced Corrosion Resistance and Promoted Bone Healing Ability of Dicalcium Phosphate Dihydrate Coating on ZK60 Magnesium Alloy	Jie-Yu Chen Guan-Lin Wu Chin-En Yen Ming-Long Yeh
250123	[GCBME] Biomechanics	Construction of a musculoskeletal system for mechanics and EMG analysis	Bo-Sheng Jiang Kuo-Kuang Jen Chia-Wei Lee Shin-Shiue Chen Chi-Kae Wang Shu-Ta Hsieh Ming-Fang Luo Sheng-Yen Hu Yuan Kang Tzong-Rong Ger
250124	[GCBME] Biomechanics	Evaluate the Biomechanical Stability of Different Glenoid Defect Angles for Latarjet Procedure: A Finite Element Analysis	Chun-Kai Chiu Guan-Lin Wu Ming-Long Yeh
250125			Wang-Ching Hung Guan-Lin Wu

	[GCBME] Material Science	To Explore the Application of Temperature-sensitive and Photo-sensitive Hydrogel in Cartilage Tissue Engineering	Yu-Jia Hou Chih-En Ke Ming-Long Yeh
250127	[GCBME] Medical Electronics	Explore the effect of magneto-thermal therapy through the number of MNPs in single cell on melanoma	Ping-Wei Tseng Jou-Hsuan Huang Chi-Hui Wang Tzong-Rong Ger
250128	[GCBME] Material Science	Development of electric heating thin films by using polycaprolactone/polypyrrole composite materials	Xing-Yi Li Wei-Jie Wang Yi-Ting Shu Wu-Zhang Su Tzong-Rong Ger
250129	[GCBME] Medical Electronics	A predicting system for epileptic seizures base on transfer learning from EEG to ECG	Pin Chen Chen Chia-Yen Yang
250131	[GCBME] Medical Imaging	Design and Implementation of the Open-Source DICOM Viewer for Whole Slide Image in Digital Pathology	Shao Yu Chen Chung-Yueh Lien Pau-Choo Chung Chin-Lin Lee
250132	[BISC] Photonics & Optoelectronics	Image Restoration Based on Deep learning in Millisecond-scale Two-photon Fluorescence Volumetric Microscopy	Chien-Sheng Wang
250134	[GCBME] Health Informatics	Deep Learning-based Segmentation of Functional Shoulder Sub-Task for Frozen Shoulder Assessment	En Ping Chu Ting-Yang Lu Chien-Pin Liu Chia-Yeh Hsieh Chih-Ya Chang Kai-Chun Liu Chia-Tai Chan
250135	[GCBME] Material Science	Improve the Material Properties of Biodegradable ZK60 Magnesium Alloy by Different Heat Treatments	Hsin-Te Yu Guan-Lin Wu Ming-Long Yeh
250136	[GCBME] Medical Imaging	CT-based Radiomics Combining the factors of High-grade Patterns for Histopathology Grading Prediction in Lung Adenocarcinoma	Chun-Yu Huang Li-Wei Chen Guan-Lin Huang Shun-Mao Yang Yi-Chang Chen Mong-Wei Lin

			Min-Shu Hsieh Guan-Yu Chen Yeun-Chung Chang Chung-Ming Chen
250137	[GCBME] Biology	Trispecific T-cell Engagers Non-covalently Decorated with PEGylated Nanocarriers for Prolonging Cancer Immunotherapy	Hsin Chen Ho Wei Jie Cheng Hsiu O Ho Chien Ming Hsieh
250138	[GCBME] Medical Imaging	Detection and Morphological Analysis of Adipose Stem Cells in Microscopic Images	Ching-Fen Jiang Chia-Yuan Yuan
250139	[GCBME] Material Science	Surface Modification for Cardiovascular Stents: Preparation and Analysis of PTMC Anti-corrosion Coating for ZK60 Magnesium Alloy	Chi-Fang Li Guan-Lin Wu Ming-Long Yeh
250140	[GCBME] Assistive Technologies	A Scene Analysis-Based Indoor Positioning System	Woei-Chyn Chu Yung-Fu Hsu Chun-Hsiang Laio
250141	[GCBME] Material Science	Developing Multifunctional Biosensing Clusters based on Molecularly Imprinted Polymer	陳駿睿 莊漢聲
250142	[GCBME] Medical Imaging	Using Feature Pyramid Network for Segmentation and Quantification of COVID-19 Infections in Chest Computed Tomography	Ming Chi Wu Adam Huang
250143	[GCBME] Medical Imaging	Ultrasound computed tomography image reconstruction system based on reflection mode	Jheng Ru Chen Po Chi Hu Yu Wei Tsai Sheng Hung Yang Wen Hui Huang Zong Hsin Liu Po Hsiang Tsui
250144	[GCBME] Material Science	Hierarchical SU-8 topographies patterned by nanosphere lens lithography and UV-LED photolithography for modulating PC12 neurite development	Lester Vinzons Cho-Yi Liu Shu-Ping Lin
250147	[GCBME] Medical Electronics	PC Controlled Burst Ultrasound function generator based on an ESP32 module	鄭妃伶 馬亞尼
250148	[GCBME] Material Science	Design and Development of Sterilization Mask Box Using Cold Atmospheric Plasma	趙沁玲, 劉廷涵 彭郁晴, 李冠毅 許家瑋, 陳盈穎

			王明誠, 李東錦 林佩蓉
250149	[GCBME] Biomechanics	The Effect of Virtual Reality Gait Training on Postoperative Lumbar Spinal Stenosis Patients: A Pilot Study	Po Jung Chen Phunsuk Kantha Dar-Ming Lai Wei-Li Hsu
250150	[GCBME] Material Science	Simple and Low-cost Method for Fabricating the Hollow Microneedle Channel Used in Balloon Catheter	Ching-Tzu Wu Guan-Lin Wu Ming-Long Yeh
250151	[GCBME] Biomechanics	Dynamical Information from Normal Mode Analysis Aids Graph Neural Networks in Identification of Protein Functions and Functionally Important Residues When Combined with Protein Contact Maps as Multigraphs	Yenlin Chen Yuan Chiang Wei-Han Hui Shu-Wei Chang
250152	[GCBME] Medical Imaging	Phase-aberrated Point Spread Function Estimation for Biomedical Ultrasound Imaging Using Complex-valued Convolutional Neural Network	YuAn Lin Wei-Hsiang Shen Meng-Lin Li
250153	[GCBME] Biomechanics	Rapid Screening of Diabetic Retinopathy by Enhance Tear Biomarker Fluorescent Signal Using a SAW-based System	Hsuan-An Chen Jae-Sung Kwon Han-Sheng Chuang
250155	[GCBME] Material Science	Membrane-integrated Microfluidic Biosensor for Biomolecule Detection	Hua-En Chueh Chen-Han Huang Klaus Stefan Drese Jonas Kluitmann
250156	[GCBME] Medical Imaging	Intermittent Theta-Burst Stimulation in Central Thalamus Restored Memory Deficits in Mouse Models of Alzheimer's Disease	Yi-Chen Lin Ssu-Ju Li Yu-Chun Lo Tsai-Yu Cho Mu-Hua Wang Ching-Te Chen Sheng-Huang Lin You-Yin Chen
250157	[GCBME] Material Science	Acellular Cartilage Sheets Combined with In-situ Hydrogel for Cartilage Repair	Hao Chuan Chang I Hsuan Lin Guan Lin Wu Ming Long Yeh
250158	[GCBME] Biomechanics	Assessment of the Coordinate Stability between Center of Mass and Center of Pressure during Walking at Different Speeds	Hsuan-Lun Lu Tung-Wu Lu
250161			Wei-Chih Chiu

	[GCBME] Biology	Impedance Analysis of Disk-Shaped Cells Cultured on Microelectrodes	Yu-Han Hung Chun-Min Lo
250166	[GCBME] Material Science	Selectively Cross-linked Hydrogel based Cocktail Drug Delivery Chip for Colon Cancer Drug Screening	Kiran Kaladharan Ouyang Chih-Hsuan Hsin-Yu Yang Fan-Gang Tseng
250167	[GCBME] Material Science	Quantitative in silico assessment of gut microbiota-drug interactions by PBPK modelling	Chien-Ming Hsieh Athika Putri
250168	[GCBME] Material Science	Immobilization of Ag-PTFE by Oxygen Plasma Treatment and UV Light on Silicon Catheter	Xin-Yu Chou Wen-Ching Shih Chung-Yih Wang
250170	[GCBME] Material Science	Tumor acidity-responsive polymeric nanoparticles to promote intracellular delivery of zoledronic acid by PEG detachment and positive charge exposure for enhanced antitumor potency	Ya-Hsuan Chou Nien-Tzu Yeh Yu-Ling Liu Tsai-Ching Hsu Jia Le Yow Bor-Show Tzang Wen-Hsuan Chiang
250171	[GCBME] Material Science	Personalized Bone Plate Fabricated by Selective Laser Melting	Chin-En Yen, Guan-Lin Wu Ching Feng, Ming-Long Yeh
250172	[GCBME] Medical Imaging	An automatic microfluidic system for screening magnetic labeled cell sample	Chia-Ke Tsou Tzong-Rong Ger Chi-Ming Ku Rou-Xuan Huang Huang-Te Li
250173	[GCBME] Medical Electronics	Cell analysis technology of magnetic labeled lung cancer cells	Hsu Chia-Hsiang Chia-ke Tsou Yu-Chi Chiu Huai-Lu Chang Tzong-Rong Ger
250174	[GCBME] Biology	Development of Multi-well Microchip for Rapid Antimicrobial Susceptibility Testing based on Diffusometry	peiwei chen
250178		A Nanocomposite-Based Assistive System for Active Gait Phase Detection	An Li Hou Shin Min Huang

	[GCBME] Assistive Technologies		Po Kang Yang
250180	[GCBME] Assistive Technologies	Investigation of Muscle Fatigue using EMG and Plantar Pressure for the Development of a Digital Foot Pressure Insole for Sarcopenia	Ying-Ying Tsai Yi-Cheng Haung Fu-YU Beverly Chen Tzu-Yao Lin Ching-Cian Wang Mei-Lan Tseng Zi-Ciane Tan
250182	[GCBME] Medical Imaging	Brain-heart interactions under attentional and resting states	Jia-jeng Lee Chun-Chuan Chen Eric Hsiao-Kuang Wu Shih-Ching Yeh
250183	[GCBME] Assistive Technologies	Development and analysis of a passive hip exoskeletal device	Kuo-Kuang Jen Bo-Sheng Jiang Chia-Wei Lee Chi-Ming Ku Chi-Kae Wang Shu-Ta Hsieh Ming-Fang Luo Sheng-Yen Hu Yuan Kang Tzong-Rong Ger
250184	[GCBME] Medical Electronics	Lead-Free Perovskites for Wearable Sensor Application	Shih-Min Huang Po-Kang Yang
250185	[GCBME] Material Science	Design of Biodegradable Soft Scaffold-mimicked Neural Microelectrode Arrays for Drug Releasing and Localized Neural Recording	程姿雅 王馨苙 黃薇蓁
250190	[GCBME] Medical Electronics	A Wireless Gait and Muscle Measurement System for Evaluation of Sarcopenia Disease	Bo Cheng Lin Shing Hong Liu Fu-Yu Beverly Chen
250191	[GCBME] Medical Electronics	Using Weight-Fat Scale for Measurement of Pulse Transit Time	Yan-Rong Wu Shing-Hong Liu
250192	[GCBME] Biomechanics	Anticipatory Postural Adjustments Strategy in Adolescents for Crossing Obstacles of Different Heights	Cheng-Hao Yu Tse-Hua Huang Shiuan-Huei Lu Tung-Wu Lu

250194	[GCBME] Material Science	Impacts of chemical protectors on storage stability of magnetic genosensor	張家鳳 Pravanjan Malla Chi-Hsien Liu
250195	[GCBME] Medical Imaging	Automatic Tooth and Alveolar Bones Segmentations from Cone-Beam CT Images with Deep Learning	Chang Yu Hung Yung Nien Sun Teresa Chanting Sun
250197	[GCBME] Material Science	Development and verification of disinfection equipment using low-temperature plasma technology application and x-ray film cartridge	許家瑋 林造民 李東錦 林慶元 賴家輝 郭婕語 王明誠
250199	[GCBME] Assistive Technologies	Development of clinical shoulder dystocia surgical instruments	李冠毅 許家瑋 呂理政 李欣宜 王品元 江柏昇 王明誠
250200	[GCBME] Assistive Technologies	Sound Localization Training System for Hearing Impaired Children	Te-Chen Shen Shu-Min Yu Pei-Hua Chen Kang-Ping Lin Cheng-Lun Tsai
250209	[GCBME] Assistive Technologies	Designing and Pilot Testing a Novel Transcranial Interfering Electric Field Stimulation (tIEFS) Device for Neural Rehabilitation Application	Chun-Wei George Wu Yu-Ting Li Chih-Wei Peng
250210	[GCBME] Material Science	T Cell Infiltration into Orthotropic Brain Tumors via Rabies Virus Glycoprotein-Mediated Transportation	Shang-Hsiu Hu
250211	[BISC] Photonics & Optoelectronics	Dynamic event measurements by single-shot generalized Hanbury Brown-Twiss intensity interferometry	Naru Yoneda

250212	[GCBME] Medical Electronics	Synchronous pulsed wave modulated biological intravenous red laser Irradiation of Blood integrated with the microscopic clinical hemodialysis blood vessel halogen perovskite imaging system	Jian-Chiun Liou
250214	[GCBME] Medical Imaging	Ultrasound synthetic shear-wave elastography of homogeneous scattering media by using the generative adversarial network	Chun Hao Yu Pei Huan Wu Wei Cheng Hsiao Bao Yu Hsieh Po Hsiang Tsui
250218	[GCBME] Medical Imaging	Tracking-by-detection based compensation system for diaphragm motion	張庭瑋
250219	[GCBME] Medical Electronics	The Effect of Access Region in van der Waals Heterostructures Based Neuromorphic Device on Memory Behavior	Advaita Ghosh Yen-Fu Lin Shu-Ping Lin
250221	[GCBME] Material Science	Tumor site-specific PEG detachment and active tumor homing of therapeutic PEGylated chitosan/folate-decorated polydopamine nanoparticles to augment antitumor efficacy of photothermal/chemo combination therapy	Wen-Hsuan Chiang Ming-Hung Hsieh Tzu-Hao Wang Tsai-Ching Hsu Jia-Le Yow Bor-Show Tzang
250226	[GCBME] Medical Imaging	Assessment of the root-to-crown ratio of a first and second mandibular molar	Ting-Jyun Shen Shiuan-Hui Wang Jui-Ting Hsu Heng-Li Huang
250227	[BISC] Photonics & Optoelectronics	Quantitative Differential Phase Contrast Microscopy with Dual-color Coded Pupil	Ying-Ju Chen Sunil Vyas Tai-Horng Young Yuan Luo
250228	[GCBME] Medical Imaging	Apply Deep Learning to Image Segmentation of Swallow-tail Sign and Evaluate Different Susceptibility Imaging Approaches	Yu-Tzu Kuo Shu-Yi Yeh Hua-Shan Liu
250229	[GCBME] Material Science	Transfection of a CRISPR/dCas9 OCT4 Transcription Activation System Using Magnetic Peptide-imprinted Nanoparticles	Mei-Hwa Lee Cheng-Chih Lin James L. Thomas Chih-Kai Chan

			Jin-An Li Hung-Yin Lin
250231	[GCBME] Health Informatics	Relationship between instrumented Romberg test and dizziness handicap inventory in patients with vestibular disorder	Yu-Ting Sung Kuan-Chung Ting Chia-Yeh Hsieh Kai-Chun Liu Chia-Tai Chan
250232	[GCBME] Medical Electronics	Monitoring of Tumor Hypoxia Dynamics during Treatment with Microbubbles and Gemcitabine by Functional Photoacoustic Imaging	Yuhling Wang Lun-De Liao
250233	[GCBME] Medical Electronics	Key Factor for Medical Device Translational Research: Based on NCKU-SPARK Program	Yu-Pei Huang Chih-Han Chang
250234	[GCBME] Medical Electronics	Development of Barcode Microbeads Based Multiplex Immunoassay for Prognosis of Severe Dengue	Tien-Chun Tsai Tzong-Shiann Ho Ya-Lan Lin
250236	[GCBME] Material Science	The Clinical Trials of 3-Hydroxyanthranilic Acid-imprinted Polymer-based Nanocomposite Sensor	Mei-Hwa Lee James L. Thomas Yu-Chia Chang Yuh-Shyan Tsai Bin-Da Liu Hung-Yin Lin
250239	[BISC] Photonics & Optoelectronics	Data poisoning attack effects on imaging of handwritten digits through scattering media using deep learning	Koki Oishi
250240	[BISC] Photonics & Optoelectronics	Integrated Minimum-Variance and Delay-Multiply-and-Sum Beamformation for Photoacoustic Array Imaging	Chun-Hsien Chiang Meng-Lin Li
250241	[GCBME] Health Informatics	A Web-Based Vestibular Functional Assessment Management System	Yen-Chen Lin Kuan-Chung Ting Chia-Yeh Hsieh Kai-Chun Liu Chia-Tai Chan
250242	[BISC] Photonics & Optoelectronics	Microplastic imaging in marine animals using spectroscopy and polarization	Nobuaki Endo Nathan Hagen Yukitoshi Otani
250243	[GCBME] Medical Imaging	Microvascular Imaging for Mice Brain through 40 MHz High-Frequency Ultrasound Localization Microscopy	Cheng Wei Li Chih Chung Huang

250247	[GCBME] Biomechanics	Predictions of Vertebral Bone Strength by Using CT-Based Finite Element Model	Yen Cheng Po-Liang Lai Hsiang-Ho Chen
250248	[GCBME] Assistive Technologies	Rapid Assessment of Bone Density based on Bilateral Radial X-ray Image Analysis with segmentation by modified Yolov4 method	Yan-Chin Gau Wei-Siang Ciou Yi-Chun Du Ming-Jui Wu
250249	[GCBME] Medical Imaging	Enhancement of Spine Ultrasound Image Contouring Using Plane Wave Angle Compounding	Chun-Tai Chen Bao-Yu Hsieh
250251	[GCBME] Medical Electronics	Real-time impedance measurement of angiogenesis induced by cancer cells	Chun-hao Huang Kin Fong Lei
250253	[BISC] Photonics & Optoelectronics	Optical encoding for fluorescence addressing	Yusuke Ogura Keita Hayashi Suguru Shimomura Takahiro Nishimura Jun Tanida
250254	[GCBME] Material Science	Additive manufacturing of Schwann cell-laden collagen/alginate nerve guidance conduits by freeform reversible embedding regulate neurogenesis towards peripheral nerve regeneration	Ping-Ling Chiu Ming-You Shie Yueh-Sheng Chen Chun-Hsu Yao
250255	[GCBME] Medical Electronics	Precision fast measurements of voltage and current for an electronic load control loop	邵逸夫 馬亞尼
250257	[GCBME] Material Science	Triphenylphosphonium-modified Mitochondria-targeted Gold Nanoparticles for Penetrative Therapeutics at Deep Brain Tumor	Chia-Ko Chen Shang-Hsiu Hu
250260	[GCBME] Material Science	Non-Enzymatic High-Sensitivity Glucose Sensor Fabricated by Ni-Nanowires Decorated Graphene Gated FETs	Sheng Chun Hung Yu-Cheng Lin Chung-Wei Lin Wei-Lun Chen Wen-Hung Chien Chia-Chi Chen Jih-Syuan Huang
250261	[GCBME] Material Science	GelMA microspheres combine with Magnetolectric Organic Metal Frameworks for Nerve Repair in Traumatic Brain Injury	Chun-Yi Liang Yi-Chieh Chan Shang-Hsiu Hu
250262			Yi-Cheng Huang

	[GCBME] Assistive Technologies	Development of a Digital Therapeutic System for the Management of Sarcopenia's Mobility	Ying-Ying Tsai Fu-Yu Beverly Chen
250263	[GCBME] Material Science	An Inhaled Nano-formulation Carrying both FTY720 and Nobiletin Ameliorates LPS-induced Acute Lung Injury in Animal Models	Huei-Han Zhang Ping-Ching Wu Chien-Chung Lin Min-Hsiung Pan
250264	[GCBME] Biology	Delivery of Nitric Oxide with pH-sensitive Nanocarriers for Renal Fibrosis Therapy	Tsung-Ying Lee Yun-Jen Tsai Hung-Hsun Lu Hui-Teng Cheng Hsi-Chien Huang Tsai-Te Lu Chi-How Peng Yunching Chen
250269	[GCBME] Biology	CXCR4-Targeted Nanoparticles Deliver Nitric Oxide and PD-L1 siRNA for Immunotherapy against Glioblastoma	Hsin-Tzu Hsieh Hsi-Chien Huang Chieh-Wei Chung Tsai-Te Lu Yunching Chen
250271	[GCBME] Assistive Technologies	Development of a Weight-shifting Movement Evaluation System under Time or Space Pressure for Patients with Parkinson's Disease	Chia-wei Hou Yu-Ting Hung Sung-Hui Huang Cheng-Ya Huang Yi-Chun Du
250272	[GCBME] Medical Imaging	Application of the Dynamic Radiomics in Gliomas Tumor Grading	Shu-Yi Yeh Yu-Tzu Kuo Hua-Shan Liu
250273	[BISC] Photonics & Optoelectronics	Label-free quantitative refractive index analysis for neuroblastoma cell death with holographic tomography	Chung-Hsuan Huang Yun-Ju Lai Han-Yen Tu Chau-Jern Cheng
250275	[BISC] Photonics & Optoelectronics	Surface modification of ZnO luminescent film by ion-milling for imaging biological specimen with a super-resolution beyond diffraction limit	Kei Hosomi Wataru Inami Yoshimasa Kawata
250276	[BISC] Photonics & Optoelectronics	Multi-plane two-photon imaging from selective excitations	Xiangyu Quan Naru Yoneda Osamu Matoba
250277	[GCBME] Biomechanics		ChihKun Hsiao Yenwei Chiu

		Local thermal effect of power on setting on electro-surgical coagulation: a three dimensional electrothermal coupled finite element study	Yi-Jung Tsai Yuan-Kun Tu Yung-Chuan Chen
250278	[GCBME] Biomechanics	Quantitative Estimation of the Forearm Performance Fatigability in a Screw Driving Model	Yenwei Chiu Hao-Yuan Hsiao Zhi-Yan Wang Wen-Fan Chen Chih-Kun Hsiao Yi-Jung Tsai Yuan-Kun Tu
250279	[GCBME] Medical Imaging	Using multi parametric imaging for predicting pediatric NAFLD by deep learning	Lu Tsung Yung Hsieh Chiao-Shan Tsui Po-Hsiang
250280	[GCBME] Material Science	Fabrication of 3D Biomimetic Skin Tissue for Burn Wound Healing	Si-Ting Wu Kai-Jen Tsai Qi-Hong Hong Feng-Yuan Chien Hsun-Yueh Yang Tsun-Hsuan Wu Ching-Yun Chen
250282	[BISC] Photonics & Optoelectronics	Damage Evaluation Induced by Focused Electron Beam Irradiation onto a Living biological Cell	Asahi Tanaka Wataru Inami Yoshimasa Kawata
250283	[GCBME] Material Science	Lipid-Coated Magnetic Porous Nanocubes to Lung Metastasis for Nanocatalytic Immunotherapy	Pin-Xuan Huang Shang-Hsiu Hu
250285	[GCBME] Assistive Technologies	Face Feature Emergency Bell Based on Artificial Intelligence for Severely Disabled People	Shih-Chan Huang Sheng-Feng Zheng Po-JUI Su Shih-Chung Chen Yeou-Jiunn Chen Chung-Min Wu
250286	[GCBME] Material Science	Comparing Different Shapes of Covalent Organic Frameworks (COFs) Nanoparticles as An Antigen-Capturing Platform for Lung Metastasis Immunotherapy	Pin-Hua Chen Shang-Hsiu Hu
250287	[GCBME] Material Science	The Potential Use of Bone-like Tissues in Surgical Treatment on Empty Nose Syndrome	Jing-ke Chen Zheng-An Yan Chih-Wei Laun Ching-Yun Chen

250290	[GCBME] Medical Electronics	Attention Analysis of EEG Response in Task Recognition with Different Auditory Flash stimuli	Che-Min Hsieh Wen-Hung Chao
250292	[GCBME] Medical Imaging	Deep Learning Enabled Computer-Aided Diagnosis in The Classification of Pancreatic Cystic Lesions based on Confocal Endomicroscopy	Clara Lavita Angelina Tsung-Chun Lee Pradermchai Kongkam Ming-Lun Han Hsiu-Po Wang Hsuan-Ting Chang
250293	[GCBME] Medical Imaging	Feasibility study of a pupil movement assistance system for hearing assessment in infants	Shin-Rui Lee Chen-Sin Huang Pei-Yu Su Yi-Hao Jiang Cheng-Lun Tsai Yu-Chen Hung Fu-Yu Chen
250294	[BISC] Photonics & Optoelectronics	Focused Spot Generation based on Digital Phase Conjugation by Transport of Intensity Equation in Scattering Media	Shiori Matsuda Naru Yoneda Xiangyu Quan Osamu Matoba Wataru Watanabe
250296	[BISC] Photonics & Optoelectronics	Local gene induction by IR-LEGO to trigger stem cell formation in a moss plant	Yuka Yoshida Takumi Tomoi Chizuru Numata Suguru Ohe Joe Sakamoto Yasuhiro Kamei Yosuke Tamada
250298	[GCBME] Medical Electronics	A Facial Skin Colorimetric Image Generation System Based on Pix2Pix Translation Technology	Yu Ting Tu Patrick Po-Han Huang Shu-Chen Chang Chih-Yu Wang
250302	[BISC] Photonics & Optoelectronics	Using adjustable radio frequency MS platform and conjunction-modulation design to improve the synchronization and resolution of the ion trap mass spectrometer for intact protein analysis	Fang Hsu Chen Chun-Yen Cheng Cheng-Han Yang I-Chung Lu Ming-Long Yeh
250303	[GCBME] Material Science	Biomimetic Tissue-engineered Tendon Using Interfacial Polyelectrolyte Complexation Spinning Process	Hao-Xuan Chen Tzu-Wei Wang

250306	[GCBME] Assistive Technologies	Artificial Intelligence Image Assisted Input System for Severely Disabled	Sheng-Feng Zheng Shih-Chan Huang Shih-Chung Chen Chung-Min Wu
250307	[GCBME] Medical Imaging	Ultrasound mastoid imaging by using a clinical convex array system	YU QIAN YIN Yen Heng Lai Po Hsiang Tsui
250311	[BISC] Photonics & Optoelectronics	Quantitative phase imaging with a Fresnel biprism-based digital holographic microscope	Chen-Ming Tsai Yuan Luo
250312	[BISC] Photonics & Optoelectronics	Wavelength coded volume holographic gratings based fluorescence microscopy	Yu-Hsin Chia Sunil Vyas Yi-You Huang Yuan Luo
250313	[BISC] Photonics & Optoelectronics	Differential phase contrast volume holographic incoherent microscopy	Yu-Hsin Chia Sunil Vyas Yi-You Huang Yuan Luo
250314	[GCBME] Material Science	The development of TiO ₂ nanostructure blended PU microfibers for antimicrobial application	Hui-Xuan Huang Shu-Ping Lin Po-Yu Liu
250315	[GCBME] Assistive Technologies	Development of a Smart Watch with Alert for The Hearing Impaired	Wei-lian Ou En-Zhu Lyu Yu-Ting Chu Jia-Yi Tsai Po-Yen Hsiao Yuh-Show Tsai
250318	[BISC] Photonics & Optoelectronics	Development of Optical Coherence Tomography Imaging Engine based on FPGA	Chang-An Shih Ting-Hao Tsai Chuan-Bor Chueh Ting-Hao Chen Hsiang-Chieh Lee
250320	[GCBME] Biomechanics	Impaired Visual-motor integration in School-Aged Children with Unilateral Cerebral Palsy: Application of a Computer-aided Measure of VMI	Wen-Feng Huang Hao-Ling Chen Ren-Yu Chen Tien-Ni Wang Jeng-Yi Shieh
250321	[GCBME] Medical Electronics	Development and Preliminary Evaluation of a Single-Arm Electrocardiogram Device	王家鍾 莊姿涵 蔡丞賢

			Ioannis Manousakas 李統立
250327	[GCBME] Material Science	Immobilization of Tumor-derived Extracellular Vesicles and its Labeling by Gold Nanoparticle	李珊宣 廖品竣 劉冠賢 廖昱翔 林政鞍
250329	[GCBME] Assistive Technologies	Intelligent Physical Exercise Training system design for people with Chronic Obstructive Pulmonary Disease (COPD)	Shih-Ying Chien
250330	[BISC] Photonics & Optoelectronics	3D image analysis of spermatid nuclei to understand the mechanism of the sperm formation in a land plant	Yosuke Tamada Nan Gu
250331	[GCBME] Medical Electronics	Quality Comparison among Single-Arm ECG Signals Recorded at Multiple Locations	陳柏霖 王家鍾 蔡丞賢
250332	[GCBME] Medical Imaging	Unsupervised deep learning-based sinogram outpainting for dual-source, dual-energy computed tomography	Wei-Tse Huang Hsuan-Ming Huang
250333	[BISC] Photonics & Optoelectronics	Classification of fork fringes using VGG 16	Sunil Vyas Yuan Luo
250334	[BISC] Photonics & Optoelectronics	Super-Gaussian Airy beam for light sheet microscopy	Sunil Vyas Yuan Luo
250335	[BISC] Photonics & Optoelectronics	Edge Contrast Enhancement Filters	Sunil Vyas Yuan Luo
250336	[GCBME] Assistive Technologies	An Acupoint Visualization System Based on Image-to-Image Translation Technology	Chun yi Yeh Chang-Yin Lee Shu-Chen Chang Chih-Yu Wang
250340	[BISC] Photonics & Optoelectronics	Development of Multi-view Optical Coherence Tomography (OCT) and Image Registration Algorithm for Tooth Imaging	Heng-Yu Li Tzu-Hsuan Chang Yu-Ren Chou Yin-Lin Wang Hsiang-Chieh Lee
250341			Bayu Tri Murti

	[GCBME] Material Science	A Label-Free Impedimetric Aptasensor Based on Vertically Aligned SnS ₂ Nanostructures for Alzheimer's Biomarker Detection	Chih-Wei Peng Po-Kang Yang
250343	[BISC] Photonics & Optoelectronics	Development of a real-time multifunctional catheter-based optical coherence tomography imaging with multiplexing system	Xiang-Yu Chen Po-Chuan Chen Chuan-Bor Chueh Ting-Yen Tsai Ting-Hao Tsai Cheng-Kuang Lee Hsiang-Chieh Lee
250344	[GCBME] Medical Imaging	The correlation between Hyperspectral Imaging and Neuropathy in Diabetic Foot by using 3D Receptor Operating Characteristic Curve	Hsian-Min Chen Yi-Jing Sheen Chiu-Chin Sung Hsin-Che Wang Yu-Wen Fu
250345	[GCBME] Material Science	A Study of Fish Scale-Chitin Hydroxyapatite Derived Scaffold For Cartilage Regeneration	陳奕璇 唐湘淇 陳翰欣
250346	[GCBME] Medical Imaging	Automatic Classification of Histopathological Images for Lymph Node Metastases with Breast Cancer	Chia-Lin Kao
250347	[GCBME] Medical Imaging	Detection of Histopathological Images for Lung and Colon Cancer	Yi-Wei Chen
250348	[GCBME] Material Science	Electrochemical detection of acetaminophen drug using a glassy carbon electrode modified with a graphene oxide nanosheets	Aravindan Santhan Ravikumar Murugan Kuo-Yuan Hwa
250349	[GCBME] Material Science	A Study of Alginate-Chitosan Nanoparticles Loaded with Moringa leaf powder To Inhibit growth of cancer cells	Xin-Jie Lin Si-Ting Xu
250350	[BISC] Photonics & Optoelectronics	Single Cell Effects of Photobiomodulation on Mitochondrial Membrane Potential and Reactive Oxygen Species Production in Human Adipose Mesenchymal Stem Cells	Le-Thanh-Hang Nguyen Tzu-Sen Yang Li-Chern Pan Mamadi M.S Colley Cheng-Jen Chang
250353			Yong-Ji Chen

	[GCBME] Material Science	Biodegradable Microneedle Mediated Transdermal Stage-Controlled Drug Release and Dual Drug Combination Therapy for Keloid Scar Treatment	Hung-Wei Cheng Wan-Yu Yen Chin-Yi Yeh Jen-Hao Tsai Ching-Jung Chen Jen Tsai Liu San-Yuan Chen Shwu-Jen Chang
250354	[GCBME] Medical Electronics	An automated multi-point laser acupuncture system based on 2-D galva-mirror scanning technology	xinyu wu Kun-Chan Lan Chih-Yu Wang Min-Yu Shen Xiao-Yun Zhang
250356	[GCBME] Medical Electronics	Novel Three-in-one Automatic Coating System for Vascular Stents	Yu-Hsuan Lin Li-Han Lin Hao-Ming Hsiao
250357	[BISC] Photonics & Optoelectronics	Volumetric Imaging of the Ex Vivo Oral Precancerous Lesions with Multi-scale Wide Field- of-View Optical Coherence Microscopy	Chuan-Bor Chueh Po-Hao Tseng Ming-Che Tu Ting-Yen Tsai Ting-Hao Chen Heng-Yu Li Shih-Jung Cheng Hsiang-Chieh Lee
250359	[GCBME] Biomechanics	Investigation of Screw Effect of Anterior Stand- alone Locking cage in Lumbar Interbody Fusion by 3D Finite Element Analysis	Erh-Yi Huang Pao-Hsin Liu
250362	[GCBME] Medical Electronics	Low-intensity pulsed ultrasound stimulation enhances remyelination in lysolecithin-induced model of multiple sclerosis	Zih-Yun Pan Li-Hsin Huang Feng-Yi Yang
250365	[GCBME] Material Science	Surface modification of hydrogel contact lenses underwater for superhydrophilicity with improved biocompatibility	Ting Yi Lin Hua En Chueh I Hsuan Chou Sanskruti Swain Yun Jung Ting Hsing Ying Lin Chen Han Huang
250366	[BISC] Photonics & Optoelectronics	Development of an imaging analysis algorithm for quantitatively assessing skin conditions with optical coherence tomography	Ting-Hao Chen Chau-Yee Ng Cheng-An Huang

			Chau-Hsiang Cheng Yu-Hsuan Lee Meng-Tsan Tsai Cheng-Kuang Lee Hsiang-Chieh Lee
250367	[GCBME] Material Science	Synthesis of functional titanium implants coatings with hierarchical polymers for preventing infection and promoting osseointegration	Yueh-Chen Wu Ting-Yi Lin Hua-En Chueh I-Hsuan Chou Sanskruiti Swain Hsing Ying Lin Chen Han Huang
250368	[GCBME] Material Science	Biocompatible polysaccharide-based anti-bacterial coating for Clear Overlay Appliances	吳芷瑜 Ting-Yi Lin Hua-En Chueh I-Hsuan Chou Sanskruiti Swain Hsing Ying Lin Chen Han Huang
250369	[GCBME] Medical Electronics	Investigation of the Transcranial Ultrasound Stimulation on Neuron Deficits in Intracerebral Hemorrhage Animal Model	Wei Shen Su Chun-Hu Wu Feng-Yi Yang
250370	[GCBME] Material Science	Biodegradable polymeric coating on Magnesium alloy stents enhances corrosion resistance and thromboresistance	謝宜臻 Ting-Yi Lin Hua-En Chueh I-Hsuan Chou Sanskruiti Swain Hsing Ying Lin Chen Han Huang
250373	[BISC] Photonics & Optoelectronics	Three-dimensional optical manipulation using cubic-phase metamaterials	Hung Chuan Hsu Hsin Yu Kuo Sunil Vyas Kuang-Yuh Huang Hsien-Shun Liao Yuan Luo
250375	[GCBME] Medical Electronics	Measurement of Single-Wrist ECG with Two/Three Electrodes at Different Positions	王家鍾 蘇逸軒 相昌霽 蔡丞賢
250376			Clara Lavita Angelina

	[BISC] Photonics & Optoelectronics	Hybrid Vision Transformer based Deep Learning for Pancreatic Cystic Lesion Classification Based on Confocal Endomicroscopy	Yi-Kai Chou Tsung-Chun Lee Pradermchai Kongkam Ming-Lun Han Hsiu-Po Wang Hsuan-Ting Chang
250381	[BISC] Photonics & Optoelectronics	Development of a high-speed catheter-based polarization-sensitive optical coherence tomography system	Meng-Shan Wu Chuan-Bor Chueh Ting-Hao Chen Tai-Ang Wang Ting-Yen Tsai Brett E. Bouma Martin Villiger Hsiang-Chieh Lee
250383	[GCBME] Medical Imaging	EEG Power Spectrum and HRV Changes Correlate Four Types of Breathing during Virtual Reality-based Mindfulness Practice	Yu-ju Chien Hei-Yin Hydra Ng Chun-Hsian Chuang Chih-Mao Huang Changwei W. Wu Yi-Ping Chao
250384	[GCBME] Material Science	Au-decorated magnetic graphene oxide as novel RNA nanocarriers	陳怡君 廖思評 劉繼賢
250385	[BISC] Photonics & Optoelectronics	Artificial intelligence assisted pathology with nonlinear optical microscopy on esophageal cancer	Guan-Yu Zhuo Wei-Hsun Wang Ming-Chi Chen Ming-Xin Lee
250388	[GCBME] Material Science	Biomimetic Composite Cryogels in Dental Alveolar Filling Materials	Jen-Hao Tsai Shwu-Jen Chang Chang-Lin Huange Zhi-Tian Kuo
250389	[GCBME] Medical Imaging	Contrast Enhanced Microcirculation Imaging for Small Animal Skin Flap Transplant Models	Ying-Rue Kao Yu-Chung Shih Fu-Jen Kao
250390	[GCBME] Medical Electronics	Fabrication of finger comb-shaped MoS ₂ composites electrode structure for pH detection using picosecond laser ablation	Mei-En Liu Zhao-Chi Chen Qi-Xuan Wu Tien-Li Chang
250391		Dual-polarization resolved second harmonic generation microscopy for precise tissue imaging	Guan-Yu Zhuo Wei-Hsun Wang

	[BISC] Photonics & Optoelectronics		Ming-Chi Chen
250395	[GCBME] Health Informatics	Hierarchical Clustering analysis of Traffic Accidents Related to Scooters in Tainan, Taiwan	Chenwen Fang Jia-Jin J. Chen Wei-Ru Chen Yang-Kun Ou
250396	[GCBME] Assistive Technologies	Wearable foot pressure sensing system for the track of flatfoot correction improvement and person recognition	Yao-Hsuan Tseng Fu-Cheng Kao Kee-Chin Lim Zong-Hong Lin
250397	[GCBME] Biomechanics	Biomechanical investigations of humeral greater tuberosity fracture with different fixation techniques under various shoulder rehabilitation activities	Ching-Chi Hsu Kao-Shang Shih Hao-Che Hsu Balraj Muthusamy Meng-Hua Lin
250398	[GCBME] Medical Electronics	Estimating Treatment Efficacy of Postural Instability and Gait Disorder in Patients with Parkinson's Disease Using Electroencephalogram	Shin-Yuan Huang Wei-Che Lin Yuan-Pin Lin
250399	[BISC] Photonics & Optoelectronics	Moiré metalens for optical sectioning microscopy	Cheng Hung Chu Yuan Luo Sunil Vyas Hsin Yu Kuo Yu Hsin Chia Mu Ku Chen Yi-You Huang Din Ping Tsai
250400	[GCBME] Assistive Technologies	Preliminary research on wearable walking stability index in walker	Jiun-Hung Lin Chih-Chin Wen Shih-Tsang Tang
250404	[GCBME] Medical Imaging	An Automated Registration Scheme Between Rat Brain MR and Atlas Images for Infarct Evaluation	Ni-Chuan Chung Shin-Joe Yeh Ming-Chang Chiang Sung-Tsang Hsieh Herng-Hua Chang
250405	[BISC] Photonics & Optoelectronics	Perturbation Monte Carlo Applicability for Human Neck Model	Chin-Hsuan Sun Kung-Bin Sung
250406		Machine Learning Prediction Models for Recovery After Colorectal Cancer Surgery Using Wearable	Yu-Hsin Liu Chia Tung Wu

	[GCBME] Health Informatics	Device Data, Air Quality Data and Clinical Evaluation Data	Yi-En Su Feipei Lai Yu-Tso Liao Yun-Jen Chou Shiow-Ching Shun
250407	[GCBME] Material Science	Isolation and Purification of Mouse Cochlear Progenitor Cells	Sheng-Wen Chang Chia-Yu Chang Chia-Ching Chang Hsin-Chien Chen Ching-Yun Chen
250410	[GCBME] Health Informatics	Association analysis between gut microbiota and their metabolites toward vascular calcification in hemodialysis patients	Chun-fan Lung
250411	[GCBME] Material Science	Theranostic Alginate-based Microbubbles: Transformation from Raspberry-like to Core-Shell-like Microbubbles and Their In Vitro Studies	Meng-Yi Bai Tsai-Hsuan Chen Yu-Chi Wang Yu-Ju Lai
250412	[BISC] Photonics & Optoelectronics	Development of surface plasmon resonance-Raman spectroscopy system to detect heparin-induced thrombosis	Chia-Ling Chiang Nan-Fu Chiu Chii-Wann Lin
250419	[BISC] Photonics & Optoelectronics	Design and characterization of flattop beam shapes through volume holographic grating	Surag Suresh Sunil Vyas J. Andrew Yeh Yuan Luo
250421	[GCBME] Medical Imaging	Ultrasound Ultrafast Imaging Using Diverging Waves on Sparse Arrays	Kuang Cheng Hsueh Tzu-Hsien Sang Geng-Shi Jeng
250422	[GCBME] Medical Electronics	Self-Powered Wound Dressing with Antibacterial and Electrical Stimulation Capabilities for Promoting Healing of Infected Wounds	Snigdha Roy Barman Shuen-Wen Chan Zong-Hong Lin
250426	[GCBME] Medical Electronics	Design of Transcranial Electrical Stimulation System with Multiple Programmable Channels	Hao Xheng Lu Chien-An Chen Jia-Jin Chen
250427	[BISC] Photonics & Optoelectronics	Single-shot dual-energy cone-beam CT using an energy-integrating detector	Fang Yu Liang Ming-Wei Lee Meei-Ling Jan
250429	[GCBME] Medical Electronics	Design of Digital Therapeutic Language Rehabilitation System for Aphasic Patients	Yen-Ru Wu Jia-Jin Chen Chien-An Chen

250430	[GCBME] Assistive Technologies	A Development of IoT Based Auto Medication Counting System	Yu-Sheng Lin Ching-Lan Cheng
250431	[BISC] Photonics & Optoelectronics	A novel method for the detection of cell-free Mitochondrial DNA Levels by using an isothermal amplification-assisted Surface Plasmon Resonance biosensor platform of its clinical role	Jian Hong Yang Chii Wann Lin Tzu Heng Wu Ying Ru Chen Hui Yun Lo
250433	[GCBME] Medical Imaging	Hemodynamic Change Monitoring and Lesion Size Prediction Following Stroke by Ultrafast Doppler Imaging	Bao-Yu Hsieh Shih-Ya Huang Yu-Chieh Kao Sung-Yu Chu
250434	[GCBME] Assistive Technologies	Reliability analysis of homemade rehabilitation ring for assessing hand dexterity in stroke patients	Zih-Ming Syu Zhen Dai Shu-Chen Chang Pei-Xuan Lu Xiang-Yi Weng Chih-Yu Wang Chien-Hsiou Liu
250435	[GCBME] Biomechanics	The biomechanical analysis of different thicknesses of vacuum extractors during delivery	Kuo-Chih Su
250438	[GCBME] Health Informatics	Stimulation of SSVEP with dual-frequency 40Hz flicker and detection of visual pathway impairment in Alzheimer's disease	Chun-Hui Huang Chih-Tsung Chang Chii-Wann Lin
250441	[GCBME] Health Informatics	Developing Data Collection and Labeling Software Protocols for Clinical Lung Sound Applications	Dan Jing Chang Fu-Ji Tsai Chii-Wann Lin
250442	[GCBME] Medical Electronics	Electrical Impedimetric Investigation of MCF-7 Breast Cancer Cell Growth on Indium Tin Oxide Coated Vertically Aligned Silicon Nanowires	Hung-Ming Chen Shu-Ping Lin
250444	[GCBME] Medical Imaging	Functional Connectivity Abnormalities in Idiopathic Generalized Epilepsy Patients : An fMRI Study	Yun Chi Hsu Siew Na Lim Yi Ping Chao
250445	[GCBME] Biomechanics	Simulation of occupant kinematics due to inertial force in driving situation	Tsai-Jeon Huang Chun-Yang Lee Zhi-Wei Chen C-Y Shih

250446	[GCBME] Biomechanics	A wearable restraint device to simulate hand strength of elderly	Yun-Hsuan Chiang Tsai-Jeon Huang Yun-Hsin Chang
250447	[GCBME] Health Informatics	Evaluation the Effect of Transcutaneous Auricular Vagus Nerve Stimulation with Pulse Rate Variability	Huang-Chang Chen Chien-An Chen Chun-Wei Wu Fan-Yu Yen Jia-Jin Chen Chao-Chen Lo
250448	[GCBME] Material Science	Preparation and research on soft film powder of roselle and mulberry plant extract	謝詠筑
250450	[BISC] Photonics & Optoelectronics	Optical coherence microscopy (OCM) imaging of the lung carcinoma (CA) cell spheroid	You-Nan Tsai Wei-Tse Huang Yu-Chun Lin Huei-Wen Chen Yuan Luo Hsiang-Chieh Lee
250452	[GCBME] Material Science	Comparision of the Immunogenicity of Decellularized Extracellular Matrix Hydrogels Prepared from the Serums of Various Species in the Decellularization Process	Yi Chin Akrasirakul Sutatta Huynh-Quang-Dieu Nguyen Chen-Yu Kao
250453	[BISC] Photonics & Optoelectronics	Evaluation of Monte Carlo-based Fitting of Diffuse Reflectance Spectroscopy to Quantify Optical Properties of Muscle and Superficial Tissues	Hao-Wei Lee Kung-Bin Sung
250454	[GCBME] Biology	Influence of Mechanical Environment on Corneal Endothelial-stromal Interactions	yuting Jou yuwei Chiang yuchun Lin
250455	[BISC] Photonics & Optoelectronics	VHG-based Airy light-sheet fluorescence microscope	Hung Chuan Hsu Sunil Vyas Kuang-Yuh Huang Hsien-Shun Liao Yuan Luo
250456	[GCBME] Biomechanics	Standing Balance after Combined High Tibial Osteotomy and Layered Chondrocyte Sheet Implantation versus High Tibial Osteotomy alone	Jing-Yu Chen Yuan-Kun Tu Nan-Chun Chen Yi-Jung Tsai
250457			Chen-Ming Tsai

	[BISC] Photonics & Optoelectronics	Optical scanning holography for three-dimensional microscopic imaging	Tzu-Yi Yang Jung-Ping Liu
250458	[BISC] Photonics & Optoelectronics	an immunofluorescence-enhanced photonic crystal biosensor for tear-based diagnosis of diabetic retinopathy	陳俐瑩
250459	[BISC] Photonics & Optoelectronics	U-net Model for Isotropic Differential Phase Contrast Microscopy	An-Cin Li Ying-Ju Chen Sunil Vyas Hsuan-Ming Huang Yuan Luo
250461	[GCBME] Material Science	Developing Monocyte-Targeting Peptide Liposomes for Targeted Drug Delivery	Bill Cheng
250462	[BISC] Photonics & Optoelectronics	Investigate the spatiotemporal dynamics of primary spermatocyte cellularization in <i>C. elegans</i> through light sheet microscopy	Hsiao-Fang Peng Yu-Chun Chen Yuan Luo Jui-ching Wu
250466	[GCBME] Medical Electronics	Analytical Derivation and Experimental Validation of Magnetic Flux for an Electromagnetic Dental Implant Stability Assessment Device	Riza Fanani Min-Chun Pan
250469	[GCBME] Material Science	Polymeric Bead Fabrication for Cell Culture Applications	Gizem Canko Yu-Cheng Liang Hui-Min David Wang Aidan An-Cheng Sun
250470	[GCBME] Biomechanics	Exploring the physical and biological mechanisms of colorectal cancer metastasis and its microenvironment using hydrogel incorporated biomimetic chip	Shao Wei Huang Yi-Hsuan Lin Fan-Gang Tseng
250474	[GCBME] Medical Electronics	A CMOS Biosensor for Sensing Permittivity at Microwave Frequencies	Wei-Liang Hsu Sheng-Hsun Huang Sheng-Yu Peng Chii-Wann Lin
250475	[GCBME] Medical Imaging	Non-invasive imaging of human tendons in vivo using multispectral optoacoustic tomography for anatomical and functional assessment	Ivana Ivankovic Hsiao-Chun Amy Lin Ali Ozbek Ana Orive

			Xose-Luis Deán-Ben Daniel Razansky
250476	[GCBME] Medical Imaging	Non-contacting measurement of skin tension via polarization imaging	Szu-Yu Chen Keng-Yang Li Cheng-Chieh Line
250477	[GCBME] Biology	Property changes of spruce woods with different treatments revealed via two-photon hyperspectral imaging and spectral analysis	Szu-Yu Chen Zhen-Hao Fang Wei-Ting Lai Keng-Yang Li Hwan-Ching Tai
250480	[GCBME] Health Informatics	Research on the commercialization Barriers of AI SaMD	Wei Pin Chen Te-Ai Tang Kuan-Chung Wang Yu-Bin Huang Samuel Wang Angie Aparicio Pi-Ju Tsai Yuan-Hsien Chuang Chao-Chih Hsuehe Peng-Ting Chen
250481	[GCBME] Biology	Barriers of biomedical academic innovations in Taiwan: A case study of Biomedical Commercialization Center	I-Ching Tsai Yi-Jing Lin An-Shun Liu Yu-Tsen Cheng Peng-Ting Chen
250483	[GCBME] Medical Imaging	Ultrasound Motion Estimation Using Modified PWC-Net	Yen-Ting Liu Li-Fu Lee Po-Syun Chen Chih-Wei Liao Geng-Shi Jeng
250484	[GCBME] Material Science	Microwave-hydrothermal synthesis of magnetic biosensor for nucleocapsid gene from coronavirus	Ching-Yi Tai Ssu-Pin Liao Chien-Ho Huang Malla Pravanjan Chi-Hsien Liu
250485	[GCBME] Assistive Technologies	A Predictive Coding Model-Based Sound Therapy on Treating Tinnitus	Chun-Chia Yang Chih-Hsu Huang Chou-Ching Lin
250486		Effect of Hypertension on Alzheimer's Disease: a Fixel-Based Analysis	Jiun-Jie Wang Hsien-Hao Tsao

	[GCBME] Medical Imaging		Yao-Liang Chen Chih-Chien Tsai Yi-Chun Chen
250487	[BISC] Photonics & Optoelectronics	Temporal Focusing Based Deep Learning Computer Generated Holography For Simultaneous Three-Dimensional Micropattern Neuron Stimulation	Liang-Wei Chen Chun-Yu Lin Shang-Yang Lu Feng-Chun Hsu Yvonne Yuling Hu Shean-Jen Chen
250488	[BISC] Photonics & Optoelectronics	Cross-modality image restoration of temporal focusing microscopy via progressive 3D U-Net	Yvonne Hu Chun-Yu Lin Chia-Wei Hsu Yu-Hao Tseng Shean-Jen Chen
250489	[BISC] Photonics & Optoelectronics	An Advanced Volumetric Imaging System Based on Light Field Microscopy with Selective Excitation via Temporal Focusing	Feng-Chun Hsu Chun-Yu Lin Yvonne Yuling Hu Yeu-Kuang Hwu Ann-Shyn Chiang Shean-Jen Chen
250490	[GCBME] Health Informatics	Organizational and user barriers to Telemedicine development	Po-Sen Huang Kuan-Chung Wang Yu-Lin Wang Zheng-Yu Hoe Tsung-Hsun Hsieh Wei-Chih Lien Jian-Yu Lian Peng-Ting Chen
250491	[GCBME] Medical Imaging	High-definition depth-resolved skin images with a portable optical coherence tomography	Meng-Tsan Tsai Chien-Yu Lin Tai-Ang Wang Chau Yee Ng
250492	[BISC] Photonics & Optoelectronics	Biosensing applications of graphene in surface plasmons	Yi-An Wei Pei-Jung Wu Yu-Hua Chen Chan-Shan Yang
250493	[GCBME] Medical Imaging	Pelvic Arteries Segmentation on CT Angiography with Deep Learning	Yu-Tong Cheng Te-Wei Shieh Wen-Jeng Lee Tzung-Dau Wang

250494	[GCBME] Medical Imaging	Using Deep-Learning Approaches to Evaluate the Differentiation Quality of the Human Induced Pluripotent Stem Cell-derived Vessel Organoids	Yi-Ming Wang Ly Meng Che Woei-Chyn Chu Chian-Shiu Chien Chung-Yueh Lien
250495	[GCBME] Medical Imaging	A Physical Paradigm for Metabolic Signals in Hyperpolarized [1-13C]pyruvate: Spectral-Spatial Encoding and Least-Squares Chemical Shift	Ching-Yi Hsieh
250497	[BISC] Photonics & Optoelectronics	High-speed dual-resonance scanning multiphoton microscopy based on deep learning for dynamic volumetric imaging	Chia-Wei Hsu Chun-Yu Lin Yvonne Yuling Hu Shean-Jen Chen
250498	[GCBME] Medical Electronics	Continuous monitoring of exosomes from cancer cell lines by automatic imaging surface plasmon resonance	Jin-Huai Xu Jian-Hong Yang Chii-Wann Lin
250502	[GCBME] Assistive Technologies	An active and passive hand rehabilitation equipment designed with game-interactive function	Jiun-Hung Lin Han-Lin Li Shih-Tsang Tang
250504	[GCBME] Material Science	Development of ACE2 mimicking domain (AMD) recombinant bacterial phage capsid as SARS-CoV-2 entry blocker for COVID-19 prevention and therapy	Hao-Han Pang Nan-Si Li Ying-Pei Hsu Hung-Wei Yang
250505	[GCBME] Assistive Technologies	A Machine Learning Approach for the Temperature Prediction in Ultrasound Diathermy with Implants	Hsiu-Chin Hsu Siang-Rong Lin Hong-Wei Chen Chia-Ching Chou Shu-Wei Chang Chang-Wei Huang
250506	[GCBME] Biomechanics	Dynamic image recognition technology analyzes scuba diving kicking action	Hsin-Chieh Chen, Ming-Hung Lin Yi-You Hou, Syuan-You Lin
250507	[BISC] Photonics & Optoelectronics	In Situ Formation of Au-Glycopolymer Nanoparticles for SERS-Based Biosensing and Single-Cell Immunity	Zi Chun Chia Li-Xing Yang Ting-Yu Cheng Ya-Jyun Chen

			Horng-Long Cheng Fei-Ting Hsu Ying-Jan Wang Tzu-Chi Huang Chih-Chia Huang
250508	[GCBME] Assistive Technologies	Monitoring Respiratory-Swallow Coordination during Feeding: The Influence of Trunk Positions and Food Textures	Wann-Yun Shieh Chin-Man Wang Yan-Ying Ju Yu-Huei Jian Hsin-Yi Cheng

2022 Biomedical Engineering Program Presentation of Department of Engineering and Technologies NSTC

December 17, Saturday

Room 1005

Moderator: Tze-Hao Chang

Time	Speaker	Topic	Affiliation
08:50-09:10	Fan-Gang Tseng	High efficient SACA System for rapid CTCs/CTMs selection/pickup for CRC diagnosis/prognosis and drug screening	Department of Engineering and System Science, National Tsing Hua University
09:10-09:30	Chih-Kuang Yeh	Drug-loaded acoustic droplets with focused ultrasound in theranostics	Department of Biomedical Engineering and Environmental Sciences, National Tsing Hua University

December 17, Saturday

Room 1007

Moderator: Yi-Chen Li, Tzong-Rong Ger, Tze-Hao Chang

Time	Speaker	Topic	Affiliation
08:00-11:00	Yen-Ping Hsu Wan-An Chang Kai-Chun Huang	The experience of proposal writing and submitting for College Student Research Scholarship, NSTC	NSTC Biomedical Engineering Program
11:00-11:15	NSTC Biomedical Engineering Program Convener—Shan-hui Hsu	Opening speech	Institute of Polymer Science and Engineering, National Taiwan University
11:15-11:45	Tze-Hao Chang	The annual business report of NSTC Biomedical Engineering Program	Department of Engineering and Technologies NSTC
11:45-12:00		Q&A	

December 17 (09:40-11:00)
10F Room 1010
NSTC Poster Session
<p>NSTC 110-2221-E-002-008- Investigation of Systemic Antitumor Immunity by Combining Pulsed-Wave Ultrasound Hyperthermia with Anti-PD-L1 Antibody for Cancer Treatment WIN-LI LIN</p>
<p>NSTC 110-2221-E-011-108- Portable Pubillometer(2/2) Yi-Yung Chen</p>
<p>NSTC 110-2628-E-007-003- Rapid diagnostic device development for monitoring the severe cases of the infectious diseases (1/3) Chao-Min Cheng</p>
<p>NSTC 108-2628-E-006-003-MY3 Development of a wearable medical device for arrhythmia and structural heart disease screening using time-frequency spectrogram of wrist artery pulse audiogram (PAG) and artificial intelligence classifier Che-Wei Lin</p>
<p>NSTC 108-2628-E-010-001-MY3 SERS detection of molecules in complex fluids through the integration of plasmonic agarose gels and optofluidic nanomanipulation techniques Yih-Fan Chen</p>
<p>NSTC 108-2221-E-033-017-MY3 Development of an automated microfluidics analysis platform for magnetic labelled bio-sample Tzong-Rong Ger</p>
<p>NSTC 108-2221-E-002-175-MY3 Focused ultrasound neuromodulation for epilepsy treatment: A feasibility study Hao-Li Liu</p>
<p>NSTC 109-2221-E-182-004-MY2 Development of an on-line positron imager for treatment response monitoring in charged-particle therapy (2/3-3/3) MEEI-LING JAN</p>
<p>NSTC 109-2221-E-492-002-MY2 Development of a Biochip System to Accelerate Total Assay Time For Precision Medicine in Clinical Sepsis I-Fang Cheng</p>
<p>NSTC 109-2221-E-009-009-MY2 Development of bacterial detection transistor YUH-SHYONG YANG</p>

<p>NSTC 109-2221-E-003-005-MY2</p> <p>Development of the innovative magnetically-thermal therapy with the high-specificity, rapid treatment, and imaging contrast and the multifunction system of imaging and treatment-II</p> <p>JEN-JIE CHIEH</p>
<p>NSTC 108-2218-E-002-046-MY3</p> <p>Development of a system for quantitatively evaluating the viscoelastic properties of the elbow ulnar collateral ligament for baseball pitchers: toward the goal of quantitative diagnosis and active prevention for ulnar collateral ligament injury</p> <p>Che-Yu Lin</p>
<p>NSTC 109-2222-E-468-001-MY2</p> <p>Evaluating the static and dynamic stability of elastic intramedullary nail in the fixation of tibial diaphyseal fractures</p> <p>Yen-Nien Chen</p>
<p>NSTC 110-2222-E-303-001-</p> <p>Influence of decompression surgery on the kinematics and stability of degenerative lumbar spondylolisthesis: measurement and analysis using 3D fluoroscopy</p> <p>CHUNG-HUA CHU</p>
<p>NSTC 110-2222-E-341-001-</p> <p>Effects of posterior cruciate ligament deficiency and reconstruction on knee biomechanics during level and slope walking using 3D fluoroscopy</p> <p>Yo-Lun Chu</p>
<p>NSTC 110-2628-E-002-004-</p> <p>Using handwriting as a behavioral marker to develop an AI-based early detection system for patient with cognitive decline (1/3)</p> <p>Hao-Ling Chen</p>
<p>NSTC 110-2221-E-182-066-</p> <p>Predictions of Vertebral Bone Strength by Using CT-Based Finite Element Model</p> <p>HSIANG-HO CHEN</p>
<p>NSTC 110-2221-E-039-005-</p> <p>Prediction of structural condition of the bone with orthodontic miniscrew insertion using dental cone-beam computed tomography and its effect on the mechanical stability of the miniscrew</p> <p>Jui-Ting Hsu</p>
<p>NSTC 110-2221-E-182-019-</p> <p>Development of a technology-assisted training device and a muscle quality/function analysis platform with the efficacy evaluation of home exercise on the elderly with Sarcopenia</p> <p>Chih-Hsiu Cheng</p>
<p>NSTC 110-2221-E-166-001-</p> <p>To reevaluate the time-dependent concentration of radioactive I-131 via 9-compartmental biokinetic model and MATLAB program</p> <p>LUNG-KWANG PAN</p>
<p>NSTC 110-2221-E-075A-001-</p>

<p>Biomechanical analysis of different calcaneal slide plate design in medial displacement calcaneal osteotomy(MDCO)</p> <p>Kuo-Chih Su</p>
<p>NSTC 110-2221-E-341-003-</p> <p>Effects of superior capsule reconstruction on the static and dynamic joint stability of the shoulder complex using 3D fluoroscopy</p> <p>Li-Wei Hung</p>
<p>NSTC 108-2628-E-006-002-MY3</p> <p>Development of Rotational Diffusivity based DNA Nanosensors Targeting at Topoisomerase I for Rapid Tuberculosis Diagnosis</p> <p>Han-Sheng Chuang</p>
<p>NSTC 109-2221-E-650-001-MY2</p> <p>To investigate the movement control and rehabilitation program effects in patients after nerve transfer by the multi-joint evaluation system</p> <p>Yi-Jung Tsai</p>
<p>NSTC 109-2222-E-218-001-MY2</p> <p>Spatial Exploration and Environment Recognition (SEER) System for the Visually Impaired and the Blind: Development and Validation</p> <p>SEE AARON RAYMOND ANG</p>
<p>NSTC 110-2221-E-006-041-</p> <p>Development of Innovative Modular 3D-Printed Dynamic Orthoses: Application Programs for Hand Function Facilitation in Patients with Stroke</p> <p>JER-HAO CHANG</p>
<p>NSTC 110-2221-E-152-001-</p> <p>Early warning application program(APP) for smartphone user in head posture control</p> <p>YU-LUEN CHEN</p>
<p>NSTC 110-2221-E-212-007-</p> <p>Development and Regulatory Certification of Assistive Devices for Variable Shuttle Wheelchair with Lightweight Structure</p> <p>Feng-Min Lai</p>
<p>NSTC 110-2221-E-038-011-</p> <p>To investigate the advantages of paired associative nerve stimulation on motor function and cortical excitability in individuals with incomplete spinal cord injury</p> <p>Chien-Hung Lai</p>
<p>NSTC 110-2221-E-715-001-</p> <p>Innovation Development, Motion Analysis, and Effectiveness Evaluation of Intelligent Assist Multi-Axis Cycling Training System for Elderly People</p> <p>Chun-Ting Li</p>
<p>NSTC 110-2221-E-002-077-</p> <p>Biomechanical analysis of the lower extremities and body balance control in adults with developmental dysplasia of the hip during activities: comparing efficacy between Ganz</p>

periacetabular osteotomy and total hip arthroplasty Ting-Ming Wang
NSTC 108-2221-E-009-045-MY3 Development of Ear-EEG and VNS Device for Prediction and Treatment of Migraine Li-Wei Ko
NSTC 108-2221-E-182-016-MY3 A New System to Measure Jaw Opening Force and Speed: Apply in Aging and Stroke, and Correlate to Anterior Tongue Pressure and Swallowing-Respiration Coordination CHIN-MAN WANG
NSTC 109-2221-E-305-001-MY2 Development of a Dynamic, Static Balance Evaluation and AI-based Exercise Prescription System for the Elderly Bor-Shing Lin
NSTC 109-2221-E-195-001-MY2 Biomechanical characteristics and functional analyses of self-expandable nasal stent_Comparison of biomaterials and design features. Chang-Hung Huang
NSTC 109-2222-E-039-001-MY2 Combination of Herbal Extract Loaded Nanocarrier and 3D Bioprinting Technique for Repairing Skin Injury Ming-You Shie
NSTC 109-2222-E-007-003-MY2 Exosome sensing platform development Hsing-Ying Lin
NSTC 110-2222-E-006-004- Development of Barcode Microbeads-based Multiplex Immunoassay for Companion Diagnostics of Severe Dengue Tien-Chun Tsai
NSTC 110-2628-E-005-001- Development of zoledronic acid/IR780-loaded polymeric nanoparticles capable of dually targeting breast cancer cells and tumor-associated macrophages for chemo/photothermal combinatorial cancer therapy (1/3) Wen-Hsuan Chiang
NSTC 110-2221-E-A49A-506- Development and application of polypeptide multilayer nanofilms for proliferation and osteogenic differentiation of human dental pulp stem cells 2/2 Chun-Min Lo
NSTC 110-2221-E-011-027- Norbornene derived block copolymers for reactive oxygen species (hydrogen peroxide) induced hydrogen sulfide gas generation to enhance passive cancer targeting regime Vijayakameswara Rao Neralla

<p>NSTC 110-2221-E-027-012-</p> <p>Investigating of tongue and temporomandibular joint lubrication during chewing process</p> <p>Hsu-Wei Fang</p>
<p>NSTC 110-2221-E-468-003-</p> <p>Development of pigmented human three-dimensional artificial skin by using cell building blocks for the application of large-area injuries</p> <p>Yu-Fang Shen</p>
<p>NSTC 110-2221-E-264-002-</p> <p>Novel Preparation of Carfilzomib-bound Human Serum Albumin (HSA) Nanoparticles to Improve Pharmacokinetic Characteristics and Its Antitumor Efficacy Either alone or Combination with Paclitaxelbound HSA nanoparticles-2</p> <p>Ling Chun Chen</p>
<p>NSTC 110-2221-E-532-001-</p> <p>Evaluation on an Interaction of Furan Derivatives and Bladder Cell Growth by Using Surface Enhanced Raman Scattering and Cellular Imaging</p> <p>Yi-chun Chiu</p>
<p>NSTC 110-2221-E-008-015-</p> <p>Development of Multifunctional Perfluorocarbon Hybrid Hydrogel Assembly for Chronic Wound Healing--- Material Synthesis, in vitro/in vivo Validation, and Mechanism Study</p> <p>Yu-Hsiang Lee</p>
<p>NSTC 108-2221-E-007-038-MY3</p> <p>Bioinspired Self-assembling Peptide Hydrogel with Proteoglycan-assisted Growth Factor Delivery for Therapeutic Angiogenesis</p> <p>TZU-WEI WANG</p>
<p>NSTC 108-2628-E-007-001-MY3</p> <p>Polypeptide Nanocarrier with Programming Dissociation Mechanism for Tumor-associated Stromal Desmoplasia Attenuation</p> <p>TZU-WEI WANG</p>
<p>NSTC 108-2628-E-007-004-MY3</p> <p>Development of smart wound dressings with release of reactive oxygen species activated through temperature difference and pressure regulation</p> <p>Zong-Hong Lin</p>
<p>NSTC 108-2628-E-008-002-MY3</p> <p>The promotion effects of bioreactor for mechanical and electrical stimulations on the reconstruction of muscle tissue</p> <p>Wei-Wen Hu</p>
<p>NSTC 108-2628-E-110-003-MY3</p> <p>Lactate-activated hypoxia-responsive Carrier for viral RNA interference and regulated Tumor-Associated Macrophage for immunotherapy</p> <p>ZI-XIAN LIAO</p>
<p>NSTC 108-2221-E-011-038-MY3</p>

<p>Metallic glasses nanotubes as advanced materials: Development and Application of Drug Delivery Jinn P. Chu</p>
<p>NSTC 108-2221-E-214-010-MY3 Rejuvenation of the reproductive system of older rats through icariin and echinacoside transdermal patches SHYH-MING KUO</p>
<p>NSTC 108-2221-E-038-017-MY3 Smart human platelet pellet incorporated with multifunctional polymeric carrier as a novel therapeutic biomedical platform Er Yuan Chuang</p>
<p>NSTC 108-2628-E-036-001-MY3 Nanoparticle-releasing in situ mucoadhesive hydrogel composite for vaginal delivery (II) Hsi-Chin Wu</p>
<p>NSTC 109-2222-E-038-002-MY2 To create individual risk matrix between long-term drug and cancer Hsuan-Chia Yang</p>
<p>NSTC 110-2222-E-027-002- Using millimeter-wave radar to sense changes in human posture to evaluate rehabilitation effects Chien-Hung Lai</p>
<p>NSTC 110-2222-E-011-014- Developed a high-speed 3D printing rapid prototyping system for lightweight and highly breathable adjustable helmets for infants Chun-Ming Chen</p>
<p>NSTC 110-2221-E-A49-038- Select Independent BOLD Components Using Deep Neural Network and Intrinsic Neural Timescale Jeng-Ren Duann</p>
<p>NSTC 110-2221-E-227-002- Develop open-source software and clinical application for the interoperability of medical imaging and AI results Chung-Yueh Lien</p>
<p>NSTC 110-2628-E-239-001- Development on the sonogram-based referral index of non-alcoholic fatty liver disease (NAFLD) using deep learning techniques for liver diagnosis and diabetes care (1/4) Chia-Yen Lee</p>
<p>NSTC 110-2221-E-035-016- The Development of High-Resolution MUSE IVIM and DKI in Head and Neck – to Discover the Effect of fat on the Parameters of IVIM and DKI, and to Explore the Responses of Parotid, Brain Stem and Hypothalamus under Gustatory Stimulation YI-JUI LIU</p>
<p>NSTC 110-2221-E-038-006- Artificial Intelligence in Detection of Rib Fracture on plain Chest Radiographs</p>

Hung-Wen Chiu
NSTC 110-2628-E-040-001- Hepatic steatosis and fibrosis assessment using ultrasound quantitative index: non-alcoholic fatty liver disease and type 2 diabetes-clinical trials (1/3) Yin-Yin Liao
NSTC 110-2221-E-182-014- The study of the optimal algorithm for acute pancreatitis surgery CHUNG-CHIH LIN
NSTC 110-2221-E-218-005- Optimizing Tidal Volumes for Ventilator-Dependent Patients Tsai-Rong Chang
NSTC 110-2221-E-075-002- Development of intelligent optical imaging system for real-time precise diagnosis of lymphomas and gliomas Sanford PC Hsu
NSTC 108-2221-E-002-081-MY3 Development of Rapid Red Blood Cell Screening System based on Common-path Tomographic Diffractive Microscopy Kung-Bin Sung
NSTC 108-2221-E-011-117-MY3 Calibration of metabolic concentration using water signal: a fast strategy for MRSI Yi-Ru LIN
NSTC 108-2221-E-214-011-MY3 The application of exergame and computerized motor function evaluation on the long term care system NAN-YING YU
NSTC 108-2221-E-040-007-MY3 Investigating the role of intravoxel incoherent motion and diffusion kurtosis in head and neck cancers: a multishot readout-segmented MRI study Ping-Huei Tsai
NSTC 109-2221-E-038-003-MY2 Big data analysis with data mining techniques to develop risk prediction models for intraoperative hypoxemia and postoperative shock Chao-Shun Lin
NSTC 109-2221-E-010-004-MY2 Biomimetic Spatial Memory to Reconstruct Moving Trajectory by Brain Inspired Reinforcement Learning You-Yin Chen
NSTC 109-2221-E-030-002-MY2 Development of patch-based pseudo computed tomography generation frameworks using machine-learning with application to measurement of tibiofemoral and patellofemoral joint kinematics

Cheng-Chung Lin

NSTC 110-2221-E-182-012-MY3

Development of a diverse intelligent movement evaluation and training system- needs assessment for special ed population and assistive device module design

Hsin-Yi Kathy Cheng

Sponsors



國家衛生研究院
生醫工程與奈米醫學研究所

國衛院生醫及奈米所



工業技術研究院
Industrial Technology
Research Institute

工研院生醫與醫材研究所



銓州光電股份有限公司



元利儀器



捷旭有限公司



凱穩電子股份有限公司



JMP Statistical Discovery



TWS台灣智慧雲端服務股份有限公司

Sponsors



博鑫醫電

博鑫醫電



昆禾醫療事業集團



久和醫療



泰華科技



華碩電腦

佑睿企業有限公司
政鎰有限公司
雄鷹有限公司



High-speed interferometric scattering confocal microscopy unveils rapid cell dynamics at the nanoscale

Yi-Teng Hsiao^a, Tsai-Ying Wu^{a,b}, Shi-Wei Chu^b, Chia-Lung Hsieh^{a*}

^aInstitute of Atomic and Molecular Sciences (IAMS), Academia Sinica, Taipei 10617, Taiwan

^bDepartment of Physics, National Taiwan University, Taipei 10617, Taiwan

Abstract

Interferometric scattering (iSCAT) microscopy is a highly sensitive imaging modality that detects backscattering light of a sample through interferometry. Previous studies have demonstrated iSCAT imaging of nano-sized objects, such as very small nanoparticles and single unlabeled biological macromolecules. The iSCAT microscopy is mostly full-field that supports fast image acquisition but with a low axial resolution. The axial resolution of iSCAT can be improved by laser scanning confocal-based iSCAT, but the image acquisition rate is significantly reduced. Here, we demonstrate a high-speed confocal-based iSCAT microscopy with optical sectioning. Using a spinning disk scanning unit, our iSCAT confocal microscopy can reach an image acquisition rate of 1000 frames per second. Using our methods, we successfully capture the rapid movements of single nanoparticles and native vesicles in living biological cells.

Keywords: high-speed, confocal, interferometric scattering microscopy, spinning disk, nanoscopic cell dynamics

I Introduction

Label-free optical microscopy plays a key role in biological studies. The advances on label-free imaging offer the opportunity to characterize the morphology, cooperativity, diffusion, and transport of biological specimens in the native status. For example, the differential interference contrast (DIC) and phase contrast microscopes have become the common methods for cell biologists to examine the cell samples during the culture. Great efforts have been made for quantitative measurements of the molecular mass density and for a higher detection sensitivity, aiming to achieve molecularly specific and functional cell imaging in a label-free manner¹. Among the various microscope techniques, interferometric scattering (iSCAT) microscopy^{2,3,4}, an interference reflection microscope⁵ with a laser illumination, has been recognized as a highly sensitive imaging modality that detects the backscattered light associated with the sample through interferometry. Very small nanoparticles and single biomacromolecules are detected by iSCAT microscopy^{6,7}. The transmission counterpart of iSCAT, referred to as coherent brightfield (COBRI) microscopy, has also been demonstrated as a fast, sensitive technique that is especially suitable for cell imaging^{8,9,10}.

*clh@gate.sinica.edu.tw; phone +886-2-2362-4956

While the iSCAT microscopy provides the excellent imaging sensitivity, the spatial resolution is diffraction-limited where the axial resolution is low due to the full-field configuration. The low axial resolution greatly complicates the visualization of three-dimensional (3D) cell structures. Recently, a confocal-based iSCAT microscope is demonstrated through laser point scanning, where the nanoscopic structures of live cells are resolved with rich details¹¹. However, the method of point scanning significantly reduces the speed of image acquisition, making it unsuitable for monitoring rapid cell dynamics at the nanoscale.

In this work, we demonstrate a high-speed iSCAT confocal microscope, which offers the temporal resolution of a few milliseconds. Notably, we implemented this technique with a commercial spinning disk scanning unit, which allows us to simultaneously measure the iSCAT and fluorescence confocal images. The high-speed 3D cell imaging of iSCAT confocal microscopy reveals nanoscopic diffusion of single nanoparticles in live cells.

II Spinning disk iSCAT confocal microscopy

A confocal-based iSCAT microscopy was constructed by utilizing a Yokogawa spinning disk scanner unit (Fig. 1). The output of a laser diode module at 561 nm wavelength (OBIS 561, Coherent) was coupled into a polarization-maintaining fiber (P3-488PM-FC- 2, Thorlabs) as the light source. To convert the original fluorescence detection into scattering detection, we replaced the dichroic mirror and fluorescence emission filter with a custom-made plate polarization beamsplitter (PBS, Control Optics Taiwan Inc.) and a linear polarizer (LPVISC100, Thorlabs), respectively. In addition, a quarter-wave plate (QWP; WPQ10M-561, Thorlabs) was added in the filter cube of the turret. The combination of the PBS, linear polarizer, and the QWP significantly enhanced the collection efficiency of the backscattered signal and reduced the reflection background of the apparatus. A high numerical aperture (NA), oil-immersion microscope objective (CFI Plan Apochromat Lambda 100X Oil, Nikon) was used. A scientific CMOS camera (Zyla, Andor) served as the detector, which allows us to record high-speed iSCAT videos. We operated the spinning disk at the maximal rotation speed of 10,000 rpm. For Yokogawa scanner unit, a single scan of the specimen is completed every 30-degree rotation, corresponding to a single sample scan time of 0.5 ms. To stabilize the illumination intensity, we set the camera frame time and the exposure time to be the multiples of 0.5 ms.

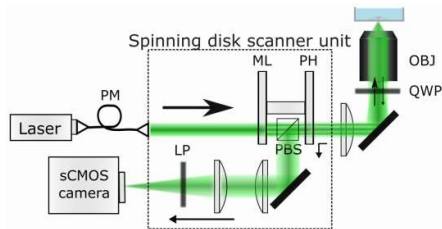


Figure 1. Schematics of spinning disk iSCAT confocal microscopy with spinning disk scanner unit. PM: polarization maintaining fiber; ML: micro lens array; PH: pinhole array; PBS: polarization beamsplitter; QWP: quarter waveplate; LP: linear polarizer, OBJ: microscope objective.

III Nanoscopic dynamics in live cells

We use iSCAT confocal microscopy to observe the biological cells cultured on coverglass (Human bone osteosarcoma epithelial U2OS cell). The high optical sectioning capability of iSCAT resolves the distinct features of the cell at $z = 0 \mu\text{m}$ (basal membrane) and at $z = 0.7 \mu\text{m}$ (at the bottom of the nuclear membrane), shown in Fig. 2. The clear iSCAT contrast variation shows the morphology of the basal membrane and the nuclear membrane. Fluorescence image of the DNA dye (DRAQ5, ab108410, Abcam) indicate the location of the nucleus (Fig. 2).

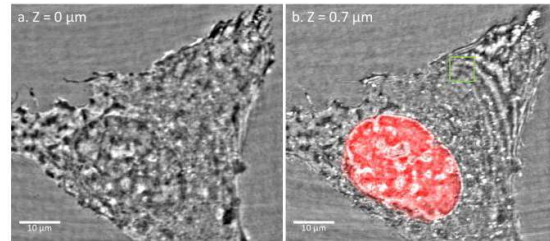


Figure 2. Confocal iSCAT image of a U2OS cell where the focal plane is at the cell-coverglass interface (panel a; $z = 0 \mu\text{m}$) and inside the cell (panel b; $z = 0.7 \mu\text{m}$). Both images are merged with the fluorescence images of DNA dye. A green square is displayed in panel b, indicating the region of single cell vesicles tracking (see Fig. 3).

We observe many native nanoparticles, presumably cell vesicles, moving continuously in the live cells. Taking advantages of the high frame rate and high sensitivity of our iSCAT confocal microscopy, we are able to measure the diffusive motion of the nanoparticles by single-particle tracking. To improve the localization accuracy, the static cellular background is estimated by temporal median filtering and then being removed from the raw image¹². The background removed snapshots of the cell vesicles are shown in Fig. 3a. The iSCAT contrast of the vesicle fluctuates in time, indicating a rapid 3D diffusive motion (Fig. 3b). Using single-particle tracking with home-written MATLAB codes, we obtain the diffusion trajectory of the vesicle at the nanoscale (Fig. 3a).

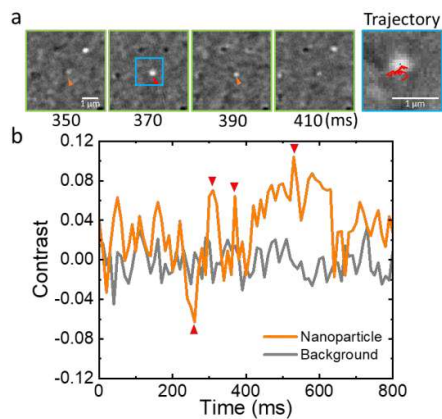


Figure 3. Diffusive motions of biological nanoparticles recorded by high-speed iSCAT confocal microscopy. (a) Snapshots of cell vesicles and a reconstructed diffusion trajectory. (b) The iSCAT contrast of the cell vesicle as a function of time, showing significant variation. The background noise floor is plotted as a reference.

IV Conclusion

We demonstrate a high-speed spinning disk iSCAT confocal microscopy for label-free live cell imaging. Through the spinning disk confocal detection, the optical sectioning and the image acquisition rate are improved significantly. Using our high-speed iSCAT confocal microscopy, many nano-sized particles diffused in live cells were resolved, providing rich dynamic information of the cell sample. Label-free, high-speed iSCAT confocal imaging opens the door to visualize nanoscopic cell dynamics in their most native forms.

References

- [1] Hsiao Y.-T., Tsai C.-N., Cheng C.-Y., and Hsieh C.-L., "Molecularly Specific and Functional Live Cell Imaging by Label-Free Interference Microscopy," *ACS Photonics* 9, 2237–2245 (2022).
- [2] Lindfors K., Kalkbrenner T., Stoller P., and Sandoghdar V. "Detection and Spectroscopy of Gold Nanoparticles Using Supercontinuum White Light Confocal Microscopy." *Phys. Rev. Lett.* 93, 37401 (2004).
- [3] Jaime O.-A. and Philipp K. "Interferometric Scattering Microscopy (iSCAT): New Frontiers in Ultrafast and Ultrasensitive Optical Microscopy," *Physical Chemistry Chemical Physics* 14, 15625-15636 (2012).
- [4] Hsieh C.-L. "Label-Free, Ultrasensitive, Ultrahigh-Speed Scattering-Based Interferometric Imaging," *Optics Communications* 422, 69–74 (2018).
- [5] Curtis A. S. G. "The Mechanism of Adhesion of Cells to Glass: A Study by Interference Reflection Microscopy," *Journal of Cell Biology* 20, 199-215 (1964).
- [6] Piliarik M., and Sandoghdar V. "Direct Optical Sensing of Single Unlabelled Proteins and Super-Resolution Imaging of Their Binding Sites," *Nature Communications* 5, 4495 (2014).
- [7] Foley, E.D.B., Kushwah, M.S., Young, G. et al. "Mass Photometry Enables Label-Free Tracking and Mass Measurement of Single Proteins on Lipid Bilayers," *Nat Methods* 18, 1247–1252 (2021).
- [8] Huang Y.-F., Zhuo G.-Y., Chou C.-Y., Lin C.-H., Chang W., and Hsieh C.-L., "Coherent Brightfield Microscopy Provides the Spatiotemporal Resolution to Study Early Stage Viral Infection in Live Cells," *ACS Nano* 11, 2575-2585 (2017).
- [9] Cheng C.-Y., Liao Y.-H., and Hsieh C.-L., "High-speed imaging and tracking of very small single nanoparticles by contrast enhanced microscopy," *Nanoscale* 11, 568-577 (2019).
- [10] Hsiao Y.-T., Tsai C.-N., Chen T.-H., and Hsieh C.-L., "Label-Free Dynamic Imaging of Chromatin in Live Cell Nuclei by High-Speed Scattering-Based Interference Microscopy," *ACS Nano* 16, 2774-2788 (2022).
- [11] Vahid S., Michelle K., David A. et al. "Confocal Interferometric Scattering Microscopy Reveals 3D Nanoscopic Structure and Dynamics in Live Cells," *Research Square* (2022).
- [12] Cheng C.-Y., and Hsieh C.-L., "Background Estimation and Correction for High-Precision Localization Microscopy," *ACS Photonics* 4, 1730-1739 (2017).

Using deep learning for bone mineral density prediction with near-infrared light

Hsin-Jou Wang^a, Wei-Chun Chang^b, Tsai-Hsueh Leu^c, Yi-Min Wang^a,
Gautam Takhellambam^a, Chia-Wei Sun^{*a}

^aBiomedical Optical Imaging Lab, Department of Photonics and Institute of Electro-Optical Engineering, National Yang Ming Chiao Tung University, No. 1001, University Rd, East District, Hsinchu City, 300, Taiwan, R.O.C.

^bDepartment of Orthopedic Surgery, Taipei Municipal Wan fang Hospital, No. 111, Sec. 3, Xinglong Rd., Wenshan Dist., Taipei City 116, Taiwan, R.O.C.

^cDepartment of Orthopedic Surgery, Taipei City Hospital Renai Branch, No. 10, Sec. 4, Ren'ai Rd., Da'an Dist., Taipei City 106243, Taiwan, R.O.C.

Abstract

Osteoporosis (OP) is a severe health problem in an aging society, causing patients to suffer a higher risk of bone injury. As a result, early diagnosis is essential. To achieve quick, easy, low-cost, and non-invasive detection of OP, we develop an optical bone densitometer (OBD) with near-infrared light and predict bone mineral density (BMD) via deep learning algorithm. Take the results of the first bone of the lumbar vertebrae (L1) as an example. The prediction error of the BMD improved to $6.951\% \pm 2.662\%$ in our recent study, revealing the potential of OBD in BMD prediction.

Keywords: bone mineral density, dual-energy X-ray absorptiometry, deep learning, near-infrared, osteoporosis

I Introduction

Osteoporosis (OP) is a bone abnormality caused by the loss of bone mass. Its clinical definition is based on the measurement of bone mineral density (BMD) via dual-energy X-ray absorptiometry (DXA). Patients who suffer from OP have a higher risk of bone fractures, which may lead to long-term hospitalization, immobility, or death.

The National Development Commission revealed that the elderly occupy 16.85% of the total population in Taiwan, and the aging population is making OP a severe health problem worldwide¹⁻³. Early diagnosis of OP, therefore, becomes essential. Although DXA provides accurate BMD, its high cost, inconvenience, and concerns about receiving radiation limit its development. Another common equipment is ultrasound bone densitometry³. It has several advantages, including low cost and short time-consuming. However, its accuracy is much worse. Therefore, we aim to develop a technique that uses near-infrared light to collect optical information from bone in order to precisely measure BMD in a quick, easy, low-cost, and non-invasive manner.

*chiaweisun@nycu.edu.tw

II Methods and Materials

The wrist is relatively thin in the human body, making it easier to transmit light. Notably, near-infrared light had better transmittance and lower dispersion for the distal radius in wrists. In our previous study, subjects were asked to put their wrists in our optical bone densitometer (OBD), shown in Figure 1. A total of 12 photos were taken by 770 nm, 850 nm, and 940 nm wavelengths of light emitted in turn. Their personal information was also collected to assist in the prediction of BMD.

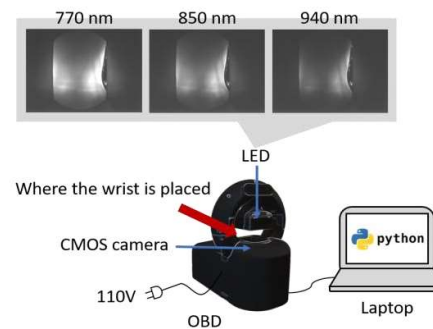


Figure 1. Setup of OBD, including dataflow and captured images.

We collected images containing optical information by receiving diffuse photons transmitted via wrists. Next, we segmented the images through deep learning to remove the background noise, and the personal information was embedded to form a vector. Subjects also took the DXA measurement, regarded as the standard scores. Then we put the preprocessed images and vector into our deep learning algorithm (Figure 2) to predict BMD.

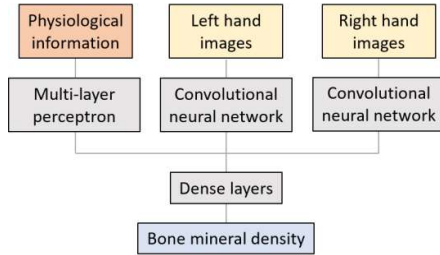


Figure 2. The structure of BMD prediction model with two paths for images and one path for physiological information.

III Results

We separately trained the prediction models for radius, ulna, lumbar vertebrae, and hip (Figure 3). The mean average percentage error (MAPE) was implemented to evaluate the performance of the models.

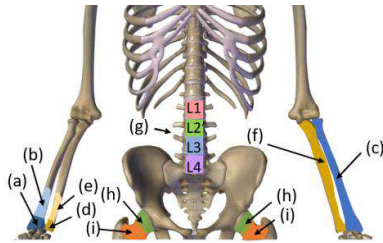


Figure 3. The BMD predicted positions: (a) distal radius, (b) radius 33%, (c) total radius, (d) distal ulna, (e) ulna 33%, (f) total ulna, (g) lumbar vertebrae, (h) hip neck, (i) total hip.

Take the results of the first bone of the lumbar vertebrae (L1) as an example. A total of 50 data, of which 29 data were from our previous study, were analyzed. The predicted BMD of randomly selected five subjects and their L1 standard DXA scores are shown in Table 1. The MAPE is $6.951\% \pm 2.662\%$, which is improved from our previous study. Figure 4. compares our result trained by 50 data and the previous result trained by 29 data.

Table 1. Predicted results of randomly selected five subjects.

subject	Predicted BMD (g/cm ²)	DXA score (g/cm ²)	Error (%)
1	0.836	0.897	6.753
2	0.931	1.027	9.363
3	0.784	0.726	8.051
4	0.892	0.909	1.912
5	0.927	0.853	8.674

*The unit g/cm² = 10kg/m²

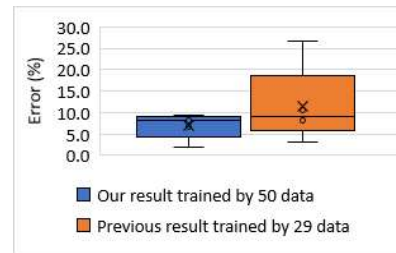


Figure 3. Comparison between our result trained by 50 data (blue) and the previous result trained by 29 data (orange)

IV Discussions and Conclusions

We have been developing a system to obtain wrist images, extract the optical information within the distal radius, and then predict the BMD of the radius, ulna, lumbar vertebrae, and hip. Although our results of BMD prediction are obviously improved, the amount of our data is still insufficient and limits our study. Furthermore, the wrist images illuminated with near-infrared light show great potential in predicting BMD in different parts of our body. The results reveal the potential of our optical bone densitometer in BMD prediction.

References

- [1] Liu, J., Curtis, E.M., et al., "State of the art in osteoporosis risk assessment and treatment," *J Endocrinol Invest* 42, 1149–1164 (2019).
- [2] Ko, C-H, Yu, et al., "High prevalence and correlates of osteoporosis in men aged 50 years and over: A nationwide osteoporosis survey in Taiwan," *Int J Rheum Dis*, 21: 2112–2118 (2018).
- [3] Hamidreza Shirzadfar, "A Comparative Study of Current Methods and Recent Advances in the Diagnosis and Assessment of Osteoporosis," *Recent Research in Endocrinology and Metabolic Disorder*, 2(1)3-17 (2020).

Label-free quantitative refractive index analysis for neuroblastoma cell death with holographic tomography

Chung-Hsuan Huang^a, Yun-Ju Lai^b, Han-Yen Tu^c, and Chau-Jern Cheng^{a,*}

^aInstitute of Electro-Optical Engineering, National Taiwan Normal University, Taipei 11677, Taiwan

^bDepartment of Life Science, National Taiwan Normal University, Taipei 11677, Taiwan

^cDepartment of Electrical Engineering, Chinese Culture University, Taipei 11114, Taiwan

Abstract

This study presents a label-free three-dimensional imaging technique for measuring cell death states by holographic tomography expressed in the values of spatially refractive index (RI). Experimental results show that the RI distribution of neuroblastoma cells and organelles under normal, autophagy and apoptosis can be quantitatively examined and analyzed.

Keywords: holographic tomography, label-free imaging, three-dimensional imaging, cellular analysis, cell death.

I Introduction

According to the rapid development of cytology research, there is growing interests in the morphology and states of cell death, which autophagy and apoptosis are commonly studied [1]. A conventional method for measuring cell state is the approach of combination of optical microscope and fluorescent microscope, which is a series of manual and time-consuming procedure. With an optical microscope, the cell appearance and location can be observed, but the internal structures of cells or organelles cannot be directly observed and analyzed well. Furthermore, the distribution and composition of organelles are investigated by detection and analysis the specific fluorescent signals of fluorescence microscopy [2]. However, a series of complicated pretreatments are required before cellular measurement, which makes it difficult to measure the living cells in situ and real-time, and may therefore, achieving label-free three-dimensional (3D) imaging of the internal structure of cells is important to explore the cellular states without artificial effects. As well known, holographic tomography (HT) [3] is an emerging label-free 3D imaging technique that provides quantitative phase analysis of cellular parameters, including volume, surface area, dry mass, and internal structure distribution in term of the values of refractive index (RI). Recently, some studies using HT were presented to measure and quantify the spatial distribution of cells and their organelles to explore cell states [4,5]. However, the applications of HT to [*cjcheng@ntnu.edu.tw](mailto:cjcheng@ntnu.edu.tw); (02)7749-6745

measure cell death states remain to be developed. In this study, we present an application approach of HT to measure the neuroblastoma cell death under normal environment, autophagy and apoptosis. The 3D internal structural changes in different conditions of cell death can be explored and analyzed by us of HT system.

II Holographic tomography system

The optical setup of holographic tomography based on improved Mach-Zehnder interferometer was shown in Figure 1. A He-Ne laser ($\lambda=632.8$ nm) was expanded the beam through beam expander (BE) and split into reference beam and object beam through beam splitter (BS₁). The object beam was scanned the sample at different azimuth angles through a combination of galvo mirror and telecentric lens (L₁: f=180 mm; MO₁: 100x, NA=0.8), and collected the wavefront information through another telecentric lens (MO₂: 60x, NA=1.2, water-immersion; L₂: f=180 mm). The samples in this study were used in normal, autophagic and apoptotic neuroblastoma cells (SH-SY5Y) to observe morphological changes during cell death. The object information at different azimuth angles interfered with reference beam and were recorded as a series of digital holograms by image sensor (1024×1024, 3.63 μm). After recording the holograms, the object information at different azimuth angles were acquired through numerical reconstruction, and synthesized their spectrums at corresponding angles in 3D frequency domain. The 3D HT reconstruction result which expressed with RI spatial distribution are acquired from the

inverse Fourier transform of complete 3D synthetic spectrum. According to the 3D RI spatial distribution, the cell body and internal structures are observed and quantitatively analyzed to examine the cell states. In the HT systems, the lateral resolution was 200 nm, which are sufficient to resolve the major cellular organelles. The time required for the tomographic recording and reconstruction are approximately 30 seconds.

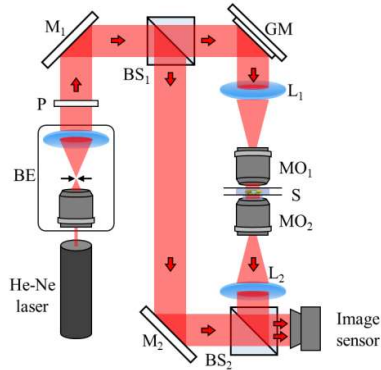


Figure 1. Experimental setup of HT. BE: beam expander, M: mirror, BS: beam splitter, GM: galvo mirror, L: lens, MO: microscope objective, S: sample

III Experimental results

The sectional tomograms of SH-SY5Y for normal, autophagy, and apoptosis of the cell death are shown in Figure 2. In the normal cells case, the nucleus and synapse of SH-SY5Y cells were clearly distinguished. It means that the cells in the normal case were growing normally. In the autophagy cells case, autophagy occurred due to insufficient cellular nutrition, so the cells shrink and nuclei became incomplete shapes. These morphological changes were observed in various RI spatial distribution shown in the figures. In addition, some small regions of interest with higher RI distribution were

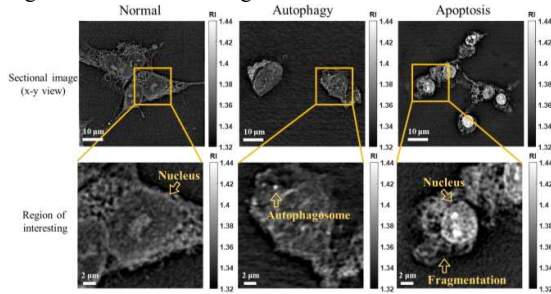


Figure 2. HT imaging reconstruction at different cell condition sets.

observed within the cell and the region size was estimated around 1 μm . These small regions were speculated to be autophagosomes. In the apoptosis cells case, the cells were under UV light illumination to induce cell apoptosis process. The cell bodies were fragmented and leaved only spheroid nucleus. The diameter of spheroid was estimated around 7 μm .

IV Conclusions

We have proposed and experimentally demonstrated a feasibility of label-free quantitative refractive index by measuring the morphological changes of cell death under cell autophagy and apoptosis using holographic tomography. The cell body and its organelles can be observed and quantitative analysis by RI changes in approximate 30 seconds. More analysis for the cell death states by the proposed method will be investigated in the near future.

Acknowledgment

The authors would like to thank for financial support of National Science and Technology Council (MOST 107-2221-E-003-011-MY3 and MOST 107-2923-E-003-001-MY3) of Taiwan.

V References

- [1] Asadzadeh, Z., Safarzadeh, E., Safaei, S., Baradaran, A., Mohammadi, A., Hajiasgharzadeh, K., Derakhshani, A., Argentiero, A., Silvestris, N. and Baradaran, B., "Current Approaches for Combination Therapy of Cancer: The Role of Immunogenic Cell Death," *Cancers* 12(4), 1047 (2020).
- [2] LaChance, J. and Cohen, D. J., "Practical fluorescence reconstruction microscopy for large samples and low-magnification imaging," *PLoS Comput. Biol.* 16(12), e1008443 (2020).
- [3] Balasubramani, V., Kuś, A., Tu, H. Y., Cheng, C. J., Baczewska, M., Krauze, W. and Kujawińska, M., "Holographic tomography: techniques and biomedical applications [Invited]," *Appl. Opt.* 60(10), B65-B80 (2021).
- [4] Szewczyk, A., Sączko, J. and Kulbacka, J., "Apoptosis as the main type of cell death induced by calcium electroporation in rhabdomyosarcoma cells," *Bioelectrochemistry* 136, 107592 (2020).
- [5] Lu, C. W., Belashov, A. V., Zhikhoreva, A. A., Semenova, I. V., Cheng, C. J., Su, L. Y. and Wu, C. H., "Application of digital holographic tomography in antitumor effect of cantharides complex on 4T1 breast cancer cells," *Appl. Opt.* 60(10), 3365-3373 (2021).

Surface modification of ZnO luminescent film by ion-milling for imaging biological specimen with a super-resolution beyond diffraction limit

Kei Hosomi*, Wataru Inami, Yoshimasa Kawata

Research Institute of Electronics, Shizuoka University, Hamamatsu, Shizuoka 432-8011, Japan
CREST, Japan Science and Technology Agency, Kawaguchi, Saitama 332-0012, Japan

Abstract

Electron-beam excitation assisted (EXA) optical microscope has a potential to observe living biological specimens with a super-resolution beyond the diffraction limit of light under ambient conditions. A luminescent film exhibiting cathodoluminescence is a key device for improvement of the spatial resolution of the EXA system. An intense and optically homogeneous luminescence from thin film with flat surfaces is required. The present work employs ion-milling procedure to modify luminescent ZnO film. The ion-milled ZnO film represents intense and optically luminescence as a result of morphological and compositional changes. These alterations would be induced by the angular dependence of sputtering yield and local heating up on the irradiation area. The surface modified ZnO luminescent film is expected to improve the spatial resolution of the EXA microscope.

Keywords: EXA microscope, ion milling, ZnO, cathodoluminescence, bio-imaging

I Introduction

An optical microscope is a powerful tool to observe living biological specimens directly. Conventional optical microscopes, however, are limited their spatial resolution to ~ 200 nm by the diffraction limit of light when using visible light. It is insufficient to distinguish structures inside the biological cell with their sizes of a few tens of nanometers. To overcome the drawback by the diffraction limit, we have developed an electron-beam excitation assisted (EXA) optical microscope¹⁻³. It consists of electron microscope and optical microscope and luminescent film between these microscopes to separate the ambient air and vacuum. The EXA system uses electron beam focusing on the surface of luminescent film to generate light source in the sizes of 10^0 – 10^1 nm via cathodoluminescence (CL). The nanometric light source scans across the specimens, and therefore images are constructed by detecting the light passing through the specimen.

The CL properties of the luminescent film as well as the abilities of electron and optical microscopes are key factors to determine the performance of the EXA microscopy. Intense and optically homogeneous

luminescence from thinner film with flat surface is required for the luminescent film to obtain clear images with the EXA microscopy. The present work has employed ion-milling procedure to modify the surfaces of the luminescent film for the desired CL properties. Ion-milling is based on ion beam sputtering and uses no chemical reagent⁴. Therefore, flat and clean surfaces are expected to be obtained by ion-milling procedure. In the present work, ion-milled ZnO thin film is applied to the luminescent film of the EXA system to improve the spatial resolution.

II Methods

1. EXA system

The EXA system consists of an inverted electron microscope, luminescent film, and optical microscope as shown in Figure 1. Silicon nitride (SiN) membranes on the silicon support were used as substrate on which the luminescent film was fabricated. The SiN membranes have stiffness to separate the atmosphere and vacuum and are thin enough to transparent the electron to excite the CL in the luminescent film.

* hosomi.kei@shizuoka.ac.jp; phone +81 53 478 1076

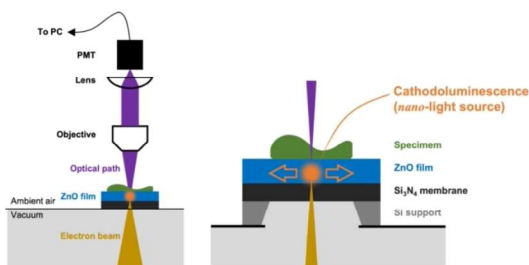


Figure 1. (left) Schematics of EXA optical microscope. (right) Enlarged schematic view of specimen irradiated with nanometric light source from ZnO luminescent film via cathodoluminescence.

2. Fabrication of the luminescent film

Zinc oxide (ZnO) was used as the luminescent material due to intense CL by low-accelerated electrons and no toxicity to the biological cell. The ZnO thin film was deposited on the SiN membranes by radio frequency (rf) magnetron sputtering method. The ZnO disk target (purity: 99.99%) was sputtered by Ar ions with input rf power of 50 W. The gas pressure was ~ 1.0 Pa during the sputtering process. Following the deposition, the samples of ZnO/SiN/Si were calcinated at 900°C for 3 hours under ambient air in the electric furnace.

3. Ion-milling

The ion-milling procedure was conducted using a Leica EM RES101 ion beam milling system. Ar^+ ions were used with the accelerating voltage of 5 kV with the ion current of 1 mA. The samples were milled at 85° to surface normal. The samples were rotated in-plane at 1.5 rpm during milling process.

III Results and Discussion

Firstly, the CL properties were characterized by taking CL spectra in the field emission scanning electron microscope. For this experiment, the ZnO thin film was fabricated on Si substrate. Pristine ZnO exhibited three emission band located around 384, 510, and 760 nm. The UV emission at 384 nm originates in the excitonic emission^{5,6} and the most intense emission. The EXA system mainly uses this UV emission when ZnO is used as the luminescent film. The ion irradiation of 30 minutes weakened the UV emission intensity. For this sample, the

optical uniformity was improved after ion irradiation, which was estimated by CL imaging at wavelength of 380 nm. The alteration of luminescent properties is caused by changes of surface morphology and composition through the sputtering of Zn and O atoms and local heating up on the irradiation area during ion-milling process. Since the ion irradiation of 30 minutes proposes the desired CL properties, it is applied to preparing the luminescent film.

The surface morphologies of ZnO/SiN membrane were observed by atomic force microscopy (AFM) as shown in Figure 2. The bulges with their lateral sizes of $1\text{--}1.5\ \mu\text{m}$ and heights of $1.5\text{--}2\ \mu\text{m}$ can be confirmed on the ZnO surfaces before ion irradiation. After ion irradiation of 30 minutes, such structures are not seen and concave area appeared. The bulge structures are probably ruptured by ion irradiation, and the concaves remain as the cavity. The depth of cavities is a few tens of nanometers, probably corresponding to thickness of ZnO film. The imaging with a high-resolution with EXA microscope using ion-milled ZnO luminescent films will be presented along with application to biological observation on the conference.

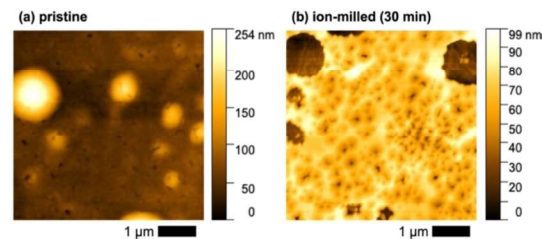


Figure 2. AFM images of ZnO/SiN (a) before and (b) after ion irradiation of 30 minutes. The scale bar indicates $1\ \mu\text{m}$.

References

- [1] Inami, W. et al., Opt. Express 18, 12897-12902 (2010).
- [2] Miyake, A. et al., Jpn. J. Appl. Phys. 53, 04EH11 (2014).
- [3] Fukuta, M. et al., J. Biophotonics 10, 503-510 (2017).
- [4] Inoue, S. and Kogure, T., Am. Mineral. 97, 755-758 (2012).
- [5] Kang, H. S. et al., J. Appl. Phys. 95, 1246-1250 (2004).
- [6] Wu, X. L. et al., Appl. Phys. Lett. 78, 2285-2287 (2001).

Damage Evaluation Induced by Focused Electron Beam Irradiation onto a Living biological Cell*

Asahi Tanaka^{*a}, Wataru Inami^b, Yoshimasa Kawata^b

^aCooperative Major in Medical Photonics, Shizuoka University, Hamamatsu 432-8561, Japan

^aResearch Institute of Electronics, Shizuoka University, Hamamatsu 432-8011, Japan

Abstract

Focused electron beam is widely used in modern nanotechnologies as the focused diameter can be decreased to a several nanometers. By using focused electron beam irradiation onto a biological cell, it should be possible to manipulate biological functions originated in a cellular nano domain. However, electron beam can easily damage cells. Therefore, it is important to evaluate its cellular damage. We investigated plasma membrane injury after beam irradiation and found that it injured the membrane. However, the pore seems to be resealed in a few tens of seconds. Although the homeostasis in an irradiated cell should be disturbed by the pore, we cannot immediately conclude that this injure leads a cell to death.

Keywords: Cellular stimulation, Focused electron beam, Cellular damage, membrane perforation, homeostasis

I Introduction

Electron beam is applied to nano technologies such as scanning electron microscopy or electron beam lithography. This is owing to the beam focusing ability, which can decrease the size of the diameter down to only a several nanometers. Electron beam can be applied to biological samples to observe the super structures or manipulate the functions. However, it is important to adjust the beam parameters such as its acceleration voltage or its irradiation dose. Because the beam has high kinetic energy which is typically a few keV to tens of keV, it is easy to damage irradiated biomolecules leading cellular damage.

In this presentation, we evaluated cellular damage induced by focused electron beam irradiation. We evaluated whether the beam injure plasma membrane. Plasma membrane contributes to sustain homeostasis of a cell. Once membrane gets injured, homeostasis imbalances and leads cellular damage. Therefore, it is important to evaluate the integrity of the membrane.

II Experimental Setup

1. System for focused electron beam irradiation and observation of cellular response

Figure 1 shows a schematic of a system for EB irradiation onto a living biological cell. EB is formed in vacuum space of scanning electron microscope. A thin silicon nitride membrane is placed on the top of it so that the vacuum space and atmospheric culture space are separated from each other. The cells are observed by an optical microscope on the top of the system. EB irradiation positions are set with referencing the microscope image.

2. Biological sample for EB damage evaluation

SH-SY5Y cells that is a cell line derived from human neuroblastoma was used for this damage evaluation. The cells were seeded on the separation membrane. To detect a membrane perforation, 2.5 μM of FM1-43 was added to the extracellular solution. FM1-43 is a fluorescence dye that binds to cellular plasma membrane once it gets inside of the membrane through membrane injure for example. A previous report used this dye to detect membrane injure upon focused laser irradiation. The emission of the dye in an EB-targeted cells were observed during the EB irradiation experiment.

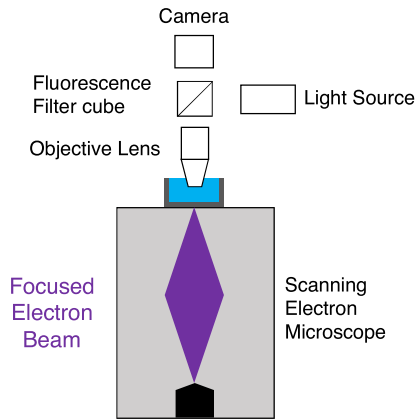


Figure 1. Schematics of a system to irradiate a focused electron beam onto a living biological cell and observe the subsequent cellular response.

III Results and Discussion

Figure 2 shows the detection of membrane perforation after EB irradiation onto a cell. Fig.2(a) shows the intensity distribution of FM1-43 dye in the targeted cell and Fig.2(b) shows a flame taken after EB irradiation. In Fig.2(b), a bright spot that is indicated by a white arrow, appeared around the EB targeted area. Fig.2(c) shows the intensity difference between the Fig.2(a) and 2(b), and the spot indicated in Fig.2(b) also can be seen. Fig.2(d) shows intensity transient around the beam irradiated spot. It shows radical intensity elevation upon the beam irradiation (@ Time = 9 s).

Results shown in Fig.2 shows that the cellular plasma membrane was injured upon the beam exposure. When the membrane got damaged, the homeostasis such as ionic concentration sustained in a cell, imbalances and cellular damage is induced. Therefore, this membrane perforation should be one of the prominent cellular damages induced by electron beam irradiation.

However, cellular membrane has a function to reseal the injured part to restore the homeostasis. The irradiated cell seems to reseal the injure in a few tens of seconds as the intensity transient shown in Fig.2(d) ends up to being plateau after the steep intensity elevation. Hence, the membrane injure should not induce cellular death immediately.

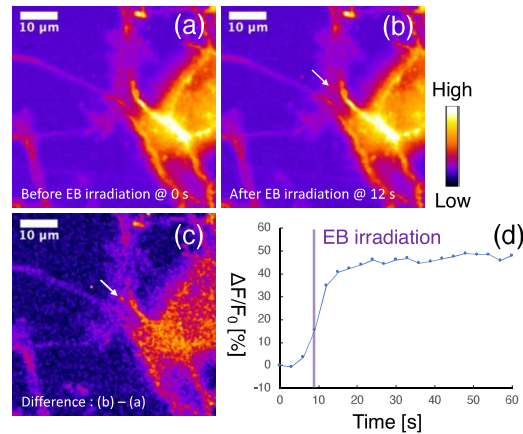


Figure 2. Detection of membrane injure after EB irradiation. (a) Intensity distribution of FM1-43 before EB irradiation. (b) Distribution after EB irradiation. (c) Intensity difference between (a) and (b). (d) Intensity transient around the EB irradiation position.

IV Summary and Conclusion

We evaluated the cellular damage induced after focused electron beam irradiation. We evaluated whether the focused beam induces a membrane injure upon its irradiation using a fluorescence dye, FM1-43. The results shows that EB irradiation injured the irradiated membrane, but it seems resealed in a few tens of seconds. Although the homeostasis in an irradiated cell disturbed by the pore, we cannot immediately conclude that this injure leads a cell to death.

References

- N. de Jonge 2009. Electron microscopy of whole cells in liquid with nanometer resolution. PNAS 106(7), 2159-2164.
- Inami, W. 2019. Cell stimulation by focused electron beam of atmospheric SEM. Ultramicroscopy 206, 112823
- Tanaka, A. 2022. Development of a direct point electron beam exposure system to investigate the biological functions of subcellular domains in a living biological cell. Micron 155, 103214
- N. de Jonge 2016. Live Cell Electron Microscopy Is Probably Impossible. ACS Nano 10(10), 9061-9063.
- Howard A. C. 2011. Promotion of plasma membrane repair by vitamin E. Nat. Commun. 20(2), 597

AI assisted FPGA-based Isotropic Quantitative Differential Phase Contrast imaging*

Yen-Chih Yu ^{*a,b}, Sunil Vyas ^b, J. Andrew Yeh ^a, Yuan Luo ^b.

^aInstitute of Nano Engineering and Microsystems, National Tsing Hua University, Hsinchu 30013, Taiwan, R.O.C

^bInstitute of Medical Device and Imaging, National Taiwan University, Taipei 10051, Taiwan, R.O.C

Abstract

Isotropic quantitative differential phase contrast (iDPC) microscopy can visualize the cell morphology and internal structure of transparent biological cells at high resolution. The functions of iDPC microscope can be divided into three categories: electronic control of illumination, multiple image acquisition to achieve isotropy, and image post-processing. To realize a compact automated instrument for biomedical research, we present an FPGA-based iDPC microscopy module for live-cell imaging. This module can control the optical illumination system and speed up the image acquisition process by up to ten times. Furthermore, to replace complex computation and parameter settings, we developed a supervised deep learning model as the computational algorithm. Our method can be applied to long-term live cell observation and disease diagnosis studies.

Keywords: automation, FPGA, deep learning, phase retrieval, differential phase contrast imaging, live cell imaging

I Introduction

Among the numerous quantitative phase imaging methods, isotropic quantitative differential phase contrast (iDPC) microscopy offers multiple advantages. It can provide high-contrast quantitative phase images of transparent objects in a label-free manner. Furthermore, it can improve the contrast value by properly implementing the illuminated pupil design. A typical iDPC microscope setup requires optical hardware, electronic control of illumination, and image post-processing to reconstruct phase map [1].

In general, when observing the cell cycle, including proliferation, morphological changes, motility, and cell-to-cell interactions were recorded by time-lapse photography. An automated system is essential to perform live cell imaging which is associated with acquisition of large number of images.

Here, we design and develop a compact FPGA-based control module that integrates all the essential functions of a microscope system [2]. The proposed automation module can improve the image acquisition efficiency by ten times. To replace the computational complexity of the algorithm and parameter setting, we implemented an image processing model through deep learning, and the proposed model with a U-net architecture that can be used as an intensity-phase information conversion algorithm [3].

*v87060611@gmail.com; phone 02-2312-3456#288613

II Principle of the iDPC microscopy

The figure 1 shows the optical system of the iDPC. The intensity of the weakly scattered sample in Fourier domain is given by

$$\tilde{I}_{iDPC}(u) = \tilde{H}_{phase} \cdot \tilde{\phi}(u). \quad (1)$$

where \tilde{H}_{phase} is the phase transfer function. In order to reconstruct $\tilde{\phi}(u)$ using equation (1), the equation (2) is calculated by using Tikhonov regularization

$$\tilde{\phi}(r) = \mathcal{F}^{-1} \left\{ \frac{\sum_i H_{phase,i} \mathcal{F}(I_{iDPC,i}(r))}{\sum_i |H_{phase,i}|^2 + \gamma} \right\}. \quad (2)$$

where γ is a normalization parameter to avoid excessive interference. The final phase relationship is given by

$$\tilde{\phi}(r) = \frac{2\pi d(r)[n_{ob}(r) - n_s(r)]}{\lambda}. \quad (3)$$

d is the thickness of the object, n_{ob} is the refractive index of the object, n_s is the refractive index of the surroundings, and λ is the working wavelength. $d(r)n_o(r)$ is called the optical thickness of the specimen. Figure 2 shows the optical system of the iDPC.

III FPGA module design

The FPGA-based control can perform all basic operations, including illumination control, high-speed image acquisition, and image reconstruction using quantitative phase retrieval.

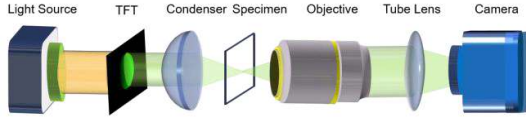


Figure 1. The optical system of the iDPC microscopy. TFT: Thin film transistor.

Our compact system can be combined with any commercial microscope system. It only takes 2.5 seconds to acquire a set of intensity images, which can improve the imaging efficiency by 10 times. Figure 2 shows the function of FPGA based iDPC microscope.

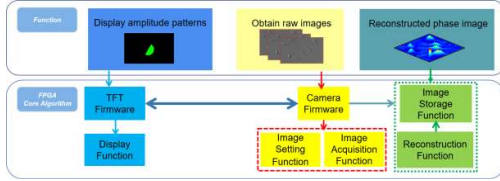


Figure 2. The function of FPGA based iDPC microscope.

IV Supervised deep learning model design

In this case, we used the U-net model and nine different kinds of cell images as a dataset for training. The image from the CCD is divided into 512×512-pixel images for training by the patch method. All of the DPC images use the structured light generated by the gradient pupil required for asymmetric illumination. The DPC intensity image is used as the input and the iDPC phase image as the ground truth for training. Figure 3 shows the flow chart of our deep learning model for differential phase contrast imaging.

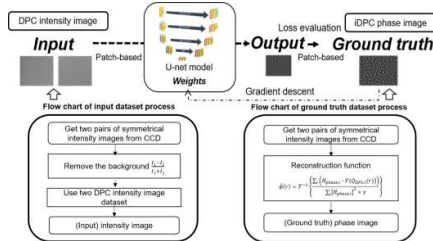


Figure 3. The flow chart of our deep learning model for differential phase contrast imaging

V Results and Discussion

Figure 4 shows the phase images of two different kinds of cells. The average value of PSNR is 29.24±1.8 dB, and the SSIM is 0.974±0.006. Our trained model can

accurately predict phase maps used to study cellular dynamics. The advantage of this deep learning approach is the reduction of acquisition time and parameter tuning in image reconstruction. Reducing post-processing to reconstruct quantitative phase values will greatly aid in performing live cell imaging.

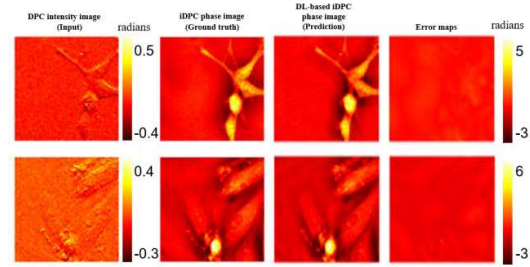


Figure 4. The results of testing dataset.

VI Conclusion

An FPGA-based control module is designed for quantitative phase retrieval in the iDPC microscopy. Based on automation compact modules, it can perform all operations with high speed and efficiency. In this work, the deep learning model can show the high performance of phase image reconstruction replacing computational algorithm computation. Our system may find important applications for long term live cell observation and disease diagnosis research.

VII References

- [1] H.H. Chen, Y. Z. Lin, and Y. Luo, "Isotropic differential phase contrast microscopy for quantitative phase bio-imaging," *Journal of Biophotonics*, 11(8), e201700364, (2018).
- [2] H. Chen, S. Hsu, W. Hwang, and C. Cheng, "An Efficient FPGA-Based Parallel Phase Unwrapping Hardware Architecture," *IEEE Transactions on Computational Imaging*, 3(4), 996-1007, (2017).
- [3] A.C. Li, et al. "Patch-based U-net Model for Isotropic Quantitative Differential Phase Contrast Imaging." *IEEE Transactions on Medical Imaging*, 40(11), 3229-3237, (2021).

VIII Acknowledgement

The authors would like to thank Hsuan-ming Hunag for the valuable discussion. This work was supported by the Taiwan Ministry of Science and Technology (MOST) (MOST 108-2221-E-002-168-MY4).

Incoherent digital holography system for simultaneous imaging of three-dimensional and polarization information without a polarization filter

Tatsuki Tahara^{*a}

^aApplied Electromagnetic Research Center, Radio Research Institute, National Institute of Information and Communications Technology (NICT), 4-2-1 Nukuikitamachi, Koganei, Tokyo 184-8795, Japan; *tahara@nict.go.jp;

Abstract

We propose an incoherent digital holography system to simultaneously record three-dimensional and polarization information without a polarization filter. Two polarization-sensitive spatial light modulators (PS-SLMs) and a polarizing beam splitter are set to construct a self-interference interferometer with a triangle optical path. Polarization-multiplexed phase-shifted incoherent holograms are sequentially recorded using the PS-SLMs, and incoherent object waves polarized along vertical and horizontal directions are separately retrieved from the multiplexed holograms, using phase-shifting interferometry. A linear polarizer is not used totally and whole the light intensity diffracted from an object is utilized to generate an incoherent hologram. Therefore, the proposed system has a potential that a bright incoherent hologram can be obtained. Its validity is numerically confirmed.

Keywords: Incoherent digital holography, phase-shifting digital holography, computational imaging, refractive lens-less three-dimensional imaging, simultaneous imaging of three-dimensional and polarization information, multiplexed imaging, multidimensional imaging, phase-shifting interferometry, multiplexed holography, multidimensional-multiplexed full-phase-encoding holography (MPH).

I Introduction

Multidimensional physical information of light has been exploited for imaging of biological specimens. In microscopy, three-dimensional (3D) information is used for tracking molecules in a cell and clarifying the structures of cells and microorganisms. Polarization information is useful for visualizing molecular orientation of cells without staining. Incoherent digital holography (IDH) is a technique to record 3D information of incoherent light such as fluorescence light and natural light as an incoherent hologram and has been applied to fluorescence 3D microscopy and bright-field full-color 3D microscopy [1-5]. Polarization imaging with IDH has also been presented [6,7]. However, most of the IDH systems requires a linear polarizer even for polarization-imaging IDH.

In this proceeding, we propose an IDH system to simultaneously record three-dimensional and polarization information without a polarization filter. Polarization-multiplexed holograms are obtained, and incoherent object waves polarized along vertical and horizontal directions are separately retrieved from the multiplexed holograms, using phase-shifting interferometry. Its validity is numerically confirmed.

II Proposed IDH system

Figure 1 illustrates schematic of the proposed IDH system. The IDH system is composed of a polarizing beam splitter (PBS), two polarization-sensitive spatial light modulators (PS-SLMs), an image sensor, and a computer. A liquid-crystal on silicon SLM (LCoS-SLM) is listed as an example of PS-SLM. Incoherent light wave diffracted from an object is divided into vertically and horizontally polarized light by the PBS. One PS-SLM modulates the phase of light polarized along the horizontal direction and the other PS-SLM does the phase of the vertically polarized light. The PS-SLMs display a diffractive phase-lens pattern by which two light waves with different wavefront curvature radii are generated. Diffractive phase-shifted phase-lens patterns are displayed sequentially on respective PS-SLMs. An image sensor records polarization-multiplexed phase-shifted incoherent digital holograms sequentially. Here, we use phase-shifting interferometry to selectively extract object waves that are polarized along vertical and horizontal directions [8], from the recorded polarization-multiplexed phase-shifted incoherent digital holograms. After selective extractions of the two object waves, diffraction integrals are calculated to the object waves and focused object images in the vertical and horizontal

polarization directions are reconstructed. As a result, 3D and polarization information is simultaneously obtained.

III Numerical simulation

We conducted a numerical simulation based on the optical setup of Fig. 1. The number of pixels and pixel pitch of both the PS-SLMs and the image sensor are 512x512 and 6.5 μm in this numerical simulation. Two polarized object points shown in Fig. 2(a) are assumed as the polarized object. We set the condition that central wavelength of the light diffracted from the object is 626 nm, the shape of the spectral distribution is rectangle, and wavelength bandwidth is 10 nm. Distances between the object and PS-SLMs and between PS-SLMs and the image sensor are 250 mm and 100 mm. Focal lengths of the diffractive phase lens are 140 mm and infinity. Seven polarization-multiplexed phase-shifted holograms are numerically generated and one can see one of them as shown in Fig. 2(b). We applied the phase-shifting interferometry technique and calculated diffraction integrals with the propagation distance of 133 mm. Numerical results are seen in Figs. 2(c) and 2(d). From the results, both 3D imaging and identification of vertically and horizontally polarized light waves are conducted successfully. Thus, the validity of the proposed IDH system is numerically confirmed.

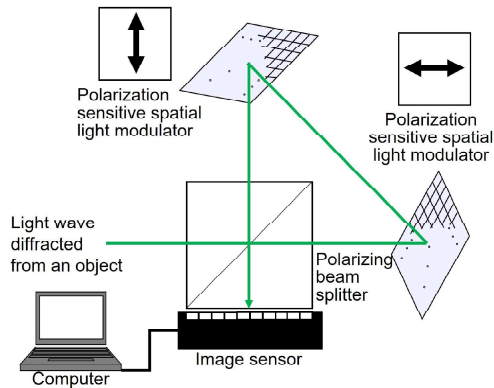


Fig. 1. Schematic of the proposed IDH system.

IV Conclusion

We have proposed an IDH system to record 3D and polarization information without a polarization filter. Whole the light intensity is utilized to generate an incoherent hologram. Polarization-filter-less full-Stokes imaging can be conducted by modifying the optical setup and/or the displayed patterns.

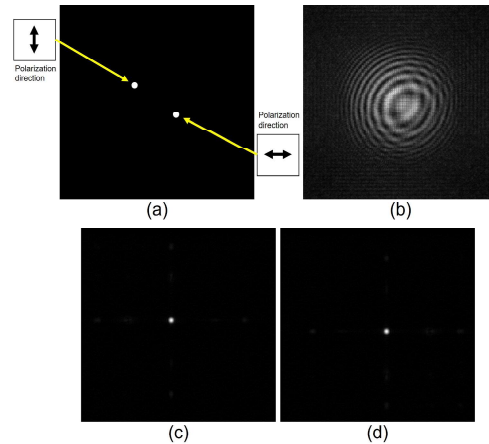


Fig. 2. Numerical results. (a) Object set for the numerical simulation. (b) One of the polarization-multiplexed phase-shifted holograms. Reconstructed object waves in the (c) vertical and (d) horizontal polarization directions.

This study was supported by the Mitsubishi Foundation (202111007), Japan Science and Technology Agency (JST), PRESTO (Grant number: JPMJPR16P8) and Cooperative Research Program of "Network Joint Research Center for Materials and Devices" (No. 20224020).

References

- [1] Rosen, J. *et al.*, "Recent advances in self-interference incoherent digital holography," *Adv. Opt. Photonics* 11(1), 1–66 (2019).
- [2] Liu, J.-P., Tahara, T., Hayasaki, Y., and Poon, T.-C., "Incoherent digital holography: a review," *Appl. Sci.* 8(1), 143 (2018).
- [3] Tahara, T., Ishii, A., Ito, T., Ichihashi, Y., and Oi, R., "Single-shot wavelength-multiplexed digital holography for 3D fluorescent microscopy and other imaging modalities," *Appl. Phys. Lett.* 117, 031102 (2020).
- [4] Tahara, T., "Review of incoherent digital holography: applications to multidimensional incoherent digital holographic microscopy and palm-sized digital holographic recorder – HoloSensor," *Front. Photonics* 2, 829139 (2022).
- [5] Tahara, T., *et al.*, "Roadmap of incoherent digital holography," *Appl. Phys. B* (accepted).
- [6] Sheng, W., Liu, Y., Shi, Y., Jin, H., and Wang, J., "Phase-difference imaging based on FINCH," *Opt. Lett.* 46(11), 2766-2769 (2021).
- [7] Sheng, W., Liu, Y., Yang H., Shi, Y., and Wang, J., "Polarization-sensitive imaging based on incoherent holography," *Opt. Express* 29(18), 28054-28065 (2021).
- [8] Tahara, T., Kikunaga, S., and Arai, Y., Japanese patent, No. JP6308594, applied on Sept. 18, 2013.

Rapid detection of SARS-CoV-2 nucleocapsid protein antigen by dual-comb biosensing

S. Miyamura^a, R. Oe^a, T. Nakahara^a, S. Okada^b, S. Taue^c, Y. Tokizane^d, T. Minamikawa^d,
T. Yano^d, K. Otsuka^{d,e}, A. Sakane^{d,e}, T. Sasaki^{d,e}, K. Yasutomo^{d,e}, T. Kajisa^{d,f}, and T. Yasui^{d,*}

^aGrad. Sch. Adv. Tech. Sci., Tokushima Univ., Tokushima, Tokushima, 770-8506, Japan

^bGrad. Sch. Sci. Tech. Innov., Tokushima Univ., Tokushima, Tokushima, 770-8506, Japan

^cSch. System Engg., Kochi Univ. Tech., Kami, Kochi 782-8502, Japan

^dInst. Post-LED Photonics (pLED), Tokushima Univ., Tokushima, Tokushima 770-8506, Japan

^eGrad. Sch. Med. Sci., Tokushima Univ., Tokushima, Tokushima, 770-8503, Japan

^fGrad. Sch. Interdisciplinary New Sci., Toyo Univ., Kawagoe, Saitama, 350-8585, Japan

Abstract

We demonstrated rapid detection of SARS-CoV-2 nucleocapsid protein antigen by dual-comb biosensing with surface modification of its corresponding antibody. A sensitivity close to that of RT-PCR was achieved, thanks to the use of active-dummy temperature compensation.

I Introduction

The novel coronavirus disease 2019 (COVID-19), caused by severe acute respiratory syndrome coronavirus 2 (SARS-CoV-2), has rapidly spread globally and is still spreading. One reason why the rapid spread has not been halted is the time-consuming testing of COVID-19. The current standard for COVID-19 testing is reverse-transcription polymerase chain reaction (RT-PCR); however, the main drawback of this method is its multiple time-consuming steps.

Optical biosensors are promising for rapid detection of SARS-CoV-2 due to their high sensitivity, cost-effectiveness, versatility, ease of testing, and the absence of the need for nucleic acid amplification. For example, surface plasmon resonance (SPR) [1] has been widely used for analyzing viruses by measuring the spectral shift of an SPR dip in the wavelength or angular spectrum. However, a relatively broad SPR dip and/or limited instrumental resolution often spoil the precision of virus detection. Recently, an optical frequency comb (OFC) [2] has attracted attention for a photonic RF sensor of refractive index (RI) via a coherent frequency link between the optical and RF regions. For example, an RI-dependent optical spectrum shift was converted into a change in the OFC mode spacing, f_{rep} , by placing a multimode-interference (MMI) RI fiber sensor inside a

fiber OFC cavity [3]. Due to the ultranarrow linewidth of the f_{rep} signal, this RI-sensing OFC enabled precise measurement of the sample RI with a resolution of 4.9×10^{-6} refractive index units (RIU), indicating the potential for further extending this method to optical biosensing by surface modification of bio-receptors in MMI fiber sensors. However, the residual temperature drift of the f_{rep} signal has hampered the application of this approach to biosensing.

In the work described in this article, we suppressed the temperature drift of the f_{rep} signal by using a dual-comb configuration including an active-sensing OFC and a dummy-sensing OFC for active-dummy temperature compensation. We further demonstrated rapid detection of the SARS-CoV-2 nucleocapsid protein (N-protein) antigen by combining the temperature-compensated dual-comb configuration with surface modification of SARS-CoV-2 N protein antibody, namely dual-comb biosensing [4].

II Results

Figure 1 shows a schematic drawing of dual-comb biosensing. A mechanical-sharing dual-comb configuration [5] consisting of an active biosensing OFC ($f_{rep1} = 29.38$ MHz) and a dummy biosensing OFC ($f_{rep2} = 29.47$ MHz) was adopted for active-dummy compensation of the temperature drift. While f_{rep1} and f_{rep2} fluctuate

depending on the cavity temperature, they have the same fluctuations as each other because they experience the same thermal disturbance. Therefore, the frequency difference between f_{rep1} and f_{rep2} ($= \Delta f_{rep} = f_{rep2} - f_{rep1} = 88.6$ kHz) remains steady regardless of the temperature drift in f_{rep1} and f_{rep2} . If the active biosensing OFC measures a SARS-CoV-2 N-protein antigen solution with surface modification of the SARS-CoV-2 N-protein antibody while the dummy biosensing OFC measures the same antigen solution without surface modification of the antibody, Δf_{rep} reflects the antigen concentration without the influence of temperature drift. In other words, a one-to-one correspondence is established between Δf_{rep} and the antigen concentration, independent of temperature drift. In our system, f_{rep1} and f_{rep2} were detected by a photodetector and were measured by an RF frequency counter synchronized to a rubidium frequency standard.

Figure 2(a) shows sensorgrams of δf_{rep1} and δf_{rep2} when the molar concentration of the antigen/PBS solution was increased from pure PBS (purple zone) to 1 aM (blue zone), 1 fM (green zone), 1 pM (yellow zone), and 1 nM (red zone). δf_{rep1} and δf_{rep2} were calculated as the frequency deviations of f_{rep1} and f_{rep2} from their initial measurement values. In the behavior of δf_{rep1} , the temperature drift spoiled the step-like change caused by the antigen concentration. On the other hand, since the temperature behavior of δf_{rep2} indicated a temperature drift similar to δf_{rep1} , we calculated the shift of the frequency difference between them ($\delta \Delta f_{rep}$). Figure 2(b) shows a sensorgram of $\delta \Delta f_{rep}$. A step-like change of $\delta \Delta f_{rep}$ that depended on the molar concentration was clearly observed, although a small drift of $\delta \Delta f_{rep}$ still remained within a range of a few Hz. From this sensorgram, we calculated the relation between the molar concentration and $\delta \Delta f_{rep}$, as shown in Fig. 2(c). The red line in Fig. 2(c) represents a sigmoidal fit of the experimental data using the Logistic function. A correlation coefficient (R^2) of 0.9988 in the curve fitting analysis was obtained within a range of 1 aM to 1 nM, thus testifying to the validity of the proposed method.

In summary, we succeeded in rapidly detecting SARS-CoV-2 antigens by suppressing the temperature drift of the sensor signal in dual-comb biosensing. A sensitivity close to that of RT-PCR was achieved by rapid measurement.

References

[1] J. Homola *et al.*, Sens. Actuators B **54**, 3–15 (1999).

[2] T. Udem *et al.*, Nature **416**, 233–237 (2002).

[3] R. Oe *et al.*, Opt. Express **26**, 19694–19706 (2018).

[4] S. Miyamura *et al.*, arXiv:2204.11954 (2022).

[5] Y. Nakajima *et al.*, Opt. Lett. **46**, 5401–5404 (2021).

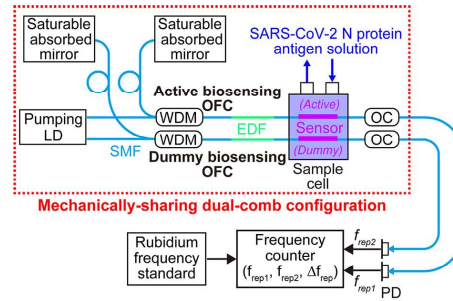


Figure 1. Experimental setup.

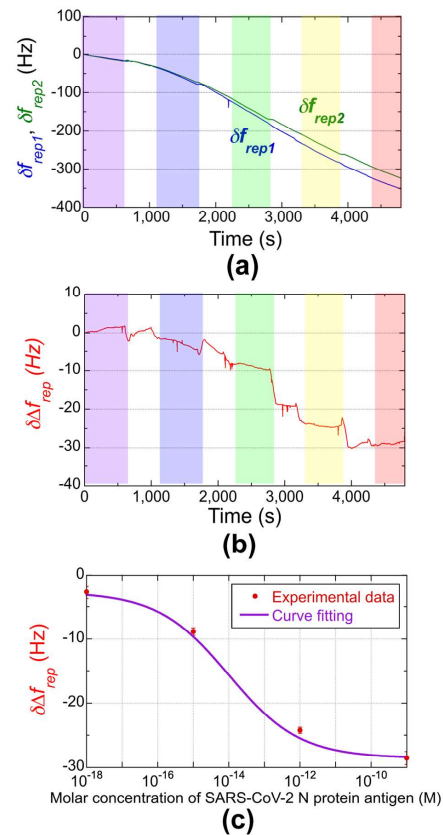


Figure 2. Experimental result.

Development of high-speed polarization-sensitive optical coherence tomography imaging based on HCG-VCSEL

Chien-Hua Peng¹, Yu-Cheng Mei¹, Hung-Kai Chen², Ting-Yen Tsai¹, Ting-Hao Chen¹,
Chuan-Bor Chueh¹, Michael C. Y. Huang², and Hsiang-Chieh Lee^{1,3*}

1. Graduate Institute of Photonics and Optoelectronics, National Taiwan University, Taipei 10617, Taiwan

2. Bandwith10 Ltd., Berkeley, CA

3. Department of Electrical Engineering, National Taiwan University, Taipei 10617, Taiwan

*Email: hclee2@ntu.edu.tw

Abstract: Polarization sensitive optical coherence tomography (PS-OCT) is a non-destructive and three-dimensional imaging technique that can provide polarization property, e.g., phase retardation and optical axis, as well as the architectural information similar to conventional OCT from the sample. In this study, we have developed a high-speed PS-OCT imaging engine by using a novel wavelength-swept laser light source based on high-contrast grating vertical-cavity surface-emitting laser (HCG-VCSEL). Example PS-OCT imaging including the human fingernail junction, 3D plastic printing material and the chicken breast tissue demonstrated the depth resolved measurement of the multifunctional information of the sample with PS-OCT and HCG-VCSEL light source at an A-scan rate of 250 kHz.

Key Word-- polarization sensitive optical coherence tomography, high-contrast grating vertical-cavity surface-emitting laser, swept source comparison, single input state

1. Introduction

With the feature of high-speed, noninvasive, and volumetric imaging, swept-source optical coherence tomography (SS-OCT) has played an important role in providing volumetric and architectural information of the imaging sample with OCT nowadays. In addition, by controlling the polarization state of light incident on the sample and using a polarization diversity detection module, it allows polarization-sensitive OCT (PS-OCT) imaging where the phase retardation and the optical axis of a sample can be obtained in a depth-resolved manner. More details can be verified from the PS-OCT images than conventional, intensity-based OCT. Thus, more and more studies have investigated the feasibility of using PS-OCT to improve the diagnostic utility of OCT for example, on the Ophthalmology or Dentistry applications. Although either OCT or PS-OCT has gained increased attention for various medical applications, most of the technologies developed are targeted application in facility such as large-scale hospitals or medical centers due to the high pricing of the system, particularly the light source part.

Currently, there are many commercially available wavelength-swept lasers dedicated for SS-OCT applications, for example, the short-cavity wavelength-swept laser, or MEMS-tunable VCSEL laser light sources. However, most of these light sources are relatively expensive, increasing the overall OCT system cost. Recently, the emergence of the MEMS-tunable HCG-VCSEL laser light sources exhibits unique advantage of a lower cost when compared to existing MEMS-tunable VCSEL laser light sources might promote new application of OCT and PS-OCT as well. As shown in Fig. 1, HCG-VCSEL utilizes a movable high-contrast grating as the top cavity mirror where the polarization of the reflected light can be designed as TE or TM by setting the dimension of the HCG layer [1, 2] to replace the conventional DBR mirror design, leading to a lower system cost.

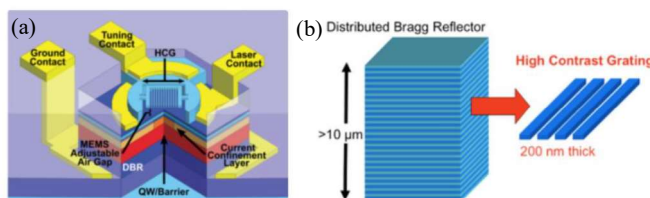


Fig. 1. (a) HCG MEMS-VCSEL structure. (b) structure comparison between DBR and HCG

In this study, we have developed a high-speed SS-PS-OCT image system to evaluate the feasibility of the MEMS-tunable HCG-VCSEL laser light source for OCT and PS-OCT application. In addition, we evaluated the uniformity of the polarization state for output light using a spectrometer with an inline linear polarizer and a polarimeter. Example depth-resolved PS-OCT imaging of the human finger nailfold junction, 3D printer plastic material as well as chicken breast were collected and demonstrated here.

2. System configuration

Fig. 2 shows the schematic of the PS-OCT system developed with the HCG-VCSEL light source, which exhibits a wavelength-swept speed of 250 kHz, a central wavelength of ~ 1059 nm, and a tuning range of ~ 50 nm. Before entering the system, the light output from the HCG-VCSEL pass through an isolator, polarization control (PC) and an in-line linear polarizer (ILP) to control the polarization state for light sending into the OCT system. Here, in order to simplify the complexity of the system development, we have adopted a single-input state design for this bench-top PS-OCT system where a circular-polarized light is illuminated over the sample surface by carefully adjusting the polarization controller (PC) and the quarter wave plate (QWP) installed in the sample arm. As for the reference arm, by adjusting the PC and QWP as well, the reflected light source from the reference arm exhibits a 45-degree linearly polarized state. In order to enable the PS-OCT imaging, a polarization diversity detection module, including two fiberoptic polarization beam splitter and two identical BDs were used.

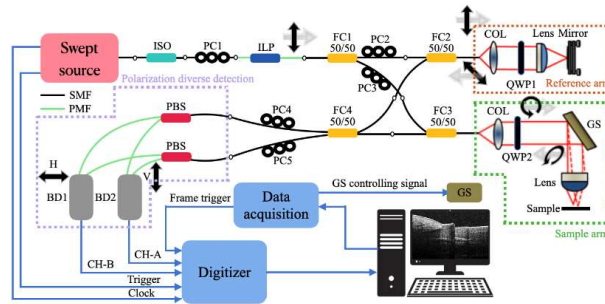


Fig. 2 Schematic diagram of the single-input state - circular polarization (CP) PS-OCT system. ISO: isolator; ILP: in-line linear polarizer; FC: fiberoptic coupler; COL: collimator; QWP: quarter wave plate; GS: galvanometer scanner; PC: polarization controller; PBS: polarization beam splitter; BD: balanced detector; SMF: single-mode fiber; PMF: polarization-maintaining fiber; CH: channel.

3. Results

The PS-OCT imaging of the human finger nailfold junction, 3D printer plastic material as well as chicken breast were acquired. In order to visualize the polarization dependent property of the image sample, the phase retardation and optic axis (OA) orientation have been computed. Figure 3 shows the OCT/PS-OCT imaging of the human finger nailfold junction and the corresponding phase retardation/OA orientation image using the HCG-VCSEL and conventional MEMS-tunable VCSEL light source. The band-like structure shown in Fig.3 (c-f) are indicative for the presence of polarization property (example, birefringence) within the sample.

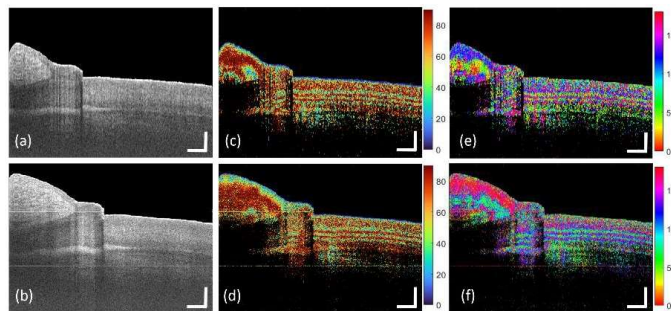


Fig. 3 (a) OCT cross-section image of finger nailfold junction using HCG-VCSEL. (b) OCT cross-section image of finger nailfold junction using conventional MEMS-tunable VCSEL. (c-d) and (e-f) are the corresponding phase retardation and optical axis orientation in (a-b). Scale bars: 0.5 mm.

4. Summary

In this study, we have developed a high-speed PS imaging system using HCG-VCSEL which is another cost-effective option for SS-OCT light source. The similarities between the SS-PS-OCT images of HCG-VCSEL and conventional MEMS-tunable VCSEL demonstrate the ability to utilize HCG-VCSEL in PS-OCT.

5. References

- [1] Aghaeipour, M., V. Ahmadi, and V. Qaradaghi. *Modeling the Effect of Different Dimensions in High Contrast Grating Mirror*. in *Nano-Structures for Optics and Photonics*. 2015. Dordrecht: Springer Netherlands.
- [2] Huang, M.C.Y., Y. Zhou, and C.J. Chang-Hasnain, *A surface-emitting laser incorporating a high-index-contrast subwavelength grating*. *Nature Photonics*, 2007. 1(2): p. 119-122.

Development of a high-speed catheter-based polarization-sensitive optical coherence tomography system

Meng-Shan Wu^a, Chuan-Bor Chueh^a, Ting-Hao Chen^a, Tai-Ang Wang^a, Ting-Yen Tsai^a,
Brett E. Bouma^{b,c}, Martin Villiger^b, and Hsiang-Chieh Lee^{*a,d}

^aGraduate Institute of Photonics and Optoelectronics, National Taiwan University, Taipei 10617, Taiwan, R.O.C.

^bWellman Center for Photomedicine, Harvard Medical School and Massachusetts General Hospital, 40 Blossom Street, Boston, Massachusetts 02114, USA

^cHarvard-Massachusetts Institute of Technology, Division of Health Sciences and Technology, Cambridge, Massachusetts 02142, USA

^dDepartment of Electrical Engineering, National Taiwan University, Taipei 10617, Taiwan, R.O.C.

*Email: hclee2@ntu.edu.tw

Abstract

In this study, we have developed a high-speed catheter-based PS-OCT system to suppress polarization artifacts and allow volumetric imaging of the human luminal organs, such as endocervical canal. The rotary junction and catheter are custom-designed to tailor the aforementioned biomedical applications. Preliminary imaging results of the human lip and fingertip were shown to validate the capabilities of imaging and polarization artifact suppression in the developed PS-OCT system. We analyzed the orthogonal polarizations of the OCT signal to implement the suppression of the polarization artifacts on the circumference and further obtain the birefringence information of tissues.

Keywords: optical coherence tomography, polarimetric imaging, biological and medical imaging, catheter, polarization diversity detection, cervical neoplasia detection.

I Introduction

Optical coherence tomography (OCT) is a non-invasive, depth-resolving, and high-resolution imaging technology that provides real-time images of tissue architectures with an imaging depth of up to 2 mm. The catheter-based OCT system with a rotary junction (RJ) allows scanning of the beam around the circumference of the human luminal organs, such as endocervical canal. However, in the scanning mechanism, as the rotating single-mode fiber continues to flex and move, the polarization state of the light being emitted from the tip is constantly changing, further causing the polarization artifacts. Therefore, it is necessary to compensate for polarization effects in rotating probes [1].

Polarization-sensitive (PS) OCT introduces additional hardware components to evaluate the polarization state of the backscattered light and its amplitude. It affords contrast between indiscernible tissues in the conventional signal of OCT and obtains the birefringence information in ordered tissue structures, such as smooth muscle fiber

bundles. And it is naturally immune to polarization artifacts. The catheter-based PS-OCT has been used for clinical investigations and shows the feasibility and beneficial results [2].

In this study, we have developed a high-speed catheter-based PS-OCT system for analyzing tissue birefringence information and suppressing polarization artifacts. In the results, we performed a series of system performance characterizations and acquired preliminary testing data with human lip and fingertip, analyzed the orthogonal polarizations of the OCT signal, and further suppressed the polarization artifacts on the circumference.

II Method

The schematic of the catheter-based PS-OCT system is shown in Fig. 1. The sweep source laser (Santec) has a central wavelength of 1310 nm, a scan range of 100 nm, and a sweep rate of 100 kHz. In the sample arm, the output signal from the fiber coupler (FC) was sent to an electro-optic modulator (EOM), which switched the light between linear and circular polarization for alternating A-

scans. The polarization-modulated light from the EOM passes through the circulator (CIR2) to the RJ and a custom-made imaging catheter. The catheter has a flexible plastic tip and biocompatible sheath with an outer diameter of 7 Fr (~2.3 mm). Volumetric OCT imaging is achieved by using a helical scan pattern, and it provides real-time imaging over a pullback length of 6 cm maximum with a 7.5- μm axial resolution and up to 3 mm imaging depth in tissue. An in-line polarizer (ILP) was installed in the reference arm and aligned at an angle to equalize the intensity distribution between orthogonal axes. The backscattered light from the sample interferes with the light reflected from the reference arm, and then transmits through the polarization division module (PDM) into a pair of dual-balanced photodetectors (DBPD) for independent analysis of the orthogonal polarization states. Then, we used a 12-bit digitizer (ATS9373, AlazarTech) to convert the analog electrical signal from the detector into a digitized electrical signal for subsequent signal processing and PS imaging reconstruction.

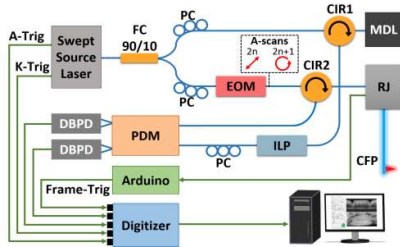


Figure 1. Schematic of the high-speed catheter-based PS-OCT system. CIR: circulator; PC: polarization controller; MDL: motorized delay line; RJ: rotary junction; CFP: catheter fiber probe; PDM: polarization division module; DBPD: dual-balanced photodetector; EOM: electro-optic modulator; ILP: in-line polarizer.

III Results and Discussion

For preliminary validation of the system performance, the developed PS-OCT system was used to image the human lip and fingertip. The probe was operated at a rotational speed of 20 fps and a pullback speed of 0.7 mm/s. In Fig. 2, layers of the oral mucosa (such as the epithelium and lamina propria) can be clearly identified, demonstrating the feasibility of obtaining high-quality OCT images of the biological sample *in vivo*. And the

results of OCT images reconstructed using the raw data collected from each channel of the PDM output show the presence of polarization artifacts where the signal intensity varies between OCT images using either polarization states at the same position (red arrows), as shown in Figs. 2(a, b). We also computed an image composed of OCT images from both polarization states as shown in Fig. 2(c). The composited processed OCT image exhibits uniformly light intensity and suppressed the polarization artifacts. Additionally, we are currently developing algorithms and collecting polarization-modulated OCT data in preparation for analyzing tissue birefringence information.

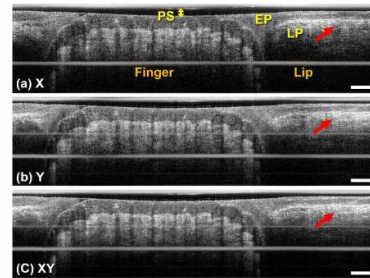


Figure 2. (a), (b) OCT images of the orthogonal polarization states; (c) OCT image of the polarization artifact suppression. Red arrows: polarization artifacts; PS: plastic sheath of the catheter; EP, epithelium propria; LP, lamina propria. Scale bars: 0.5 mm.

Acknowledgements

The authors acknowledge the funding support in part from the Young Scholar Fellowship Program by the Ministry of Science and Technology of the Republic of China (ROC), Taiwan (MOST 110-2636-E-002-025, 111-2636-E-002-024), and in part from the Career Development Grant by the National Health Research Institutes (NHRI-EX110-11004EC and NHRI-EX111-11004EC).

References

- [1] Lee, A. M. D., Pahlevaninezhad, H., Yang, V. X. D. et al, "Fiber-optic polarization diversity detection for rotary probe optical coherence tomography," *Optics Letters*, 39(12), 3638-3641 (2014).
- [2] Villiger, M., Braaf, B., Lippok, N. et al, "Optic axis mapping with catheter-based polarization-sensitive optical coherence tomography," *Optica*, 5(10), 1329-1337 (2018).

Dual-polarization resolved second harmonic generation microscopy for precise tissue imaging

Guan-Yu Zhuo^{*a}, Wei-Hsun Wang^a, Ming-Chi Chen^a

^aInstitute of Translational Medicine and New Drug Development, China Medical University, Taichung 40402, Taiwan

Abstract

In the relevant studies of polarization resolved second harmonic generation (P-SHG) microscopy, the ratios of second-order nonlinear susceptibility, $\chi^{(2)}$, tensor elements have been shown to distinguish between fibrillar collagen types and observe changes in the molecular structure of collagen fibrils in neoplastic diseases. Despite the fact that type-I collagen has been extensively studied, the $\chi^{(2)}$ ratios exhibit a large deviation as compared to various literatures, which overlaps between other collagen types. To address this issues, by considering the effects of molecular tilt angle and chirality we propose a new model based on C_6 symmetry and split SHG signal into cross polarized image components for $\chi^{(2)}$ tensor analysis. The results show that the diagnostic precision can be increased up to 25%.

Keywords: second harmonic generation, second-order nonlinear susceptibility, tensor analysis, molecular tilt angle, molecular chirality

I Introduction

Second harmonic generation (SHG) imaging with polarimetric measurements (namely polarization resolved SHG, P-SHG, microscopy), can extract the information of 3D molecular orientation, crystallinity, molecular packing symmetry, and the helical pitch angle of SHG-active molecules. The above information is helpful for the early detection of diseases and monitoring tumor progression in tissues [1, 2]. In P-SHG microscopy, most studies focused on the derivation of the ratio of $\chi^{(2)}$ tensor elements and the corresponding helical pitch angle [3], but ignored the effects of molecular tilt angle, δ , and the chirality by helical molecules, which would lead to inconsistent analysis in the samples with a crimp structure or the organized molecules randomly oriented in 3D. On the other hand, taking collagen as an example, which is composed of a triple helical structure, the importance of molecular bonding angle is larger than δ if only observing the monomer molecules. However, collagen presented as a macromolecule instead of a monomer is shown in connective tissues, and the voxel size of laser focus is at the scale of collagen fibrils. Thus, the error range will become larger in the derived parameters if one does not consider the effects of δ and

molecular chirality (that cannot be ignored when a non-zero δ exists).

To address this issue, which aims to increase the precision of P-SHG microscopy, we propose a new and compact molecular model for P-SHG imaging and developing a program for automated image analysis that will largely reduce the workload of analyzing a great amount of polarization dependent SHG images. In the experiment, the sample is interacted with linearly polarization in different directions, and the SHG signal is split into the crossed polarization components to derive the associated parameters, which are then presented as color-coded images. Since the proposed model considers the effects of δ and molecular chirality, the accuracy of determining $\chi^{(2)}$ ratios could be greatly improved. To confirm the feasibility of this method, we will use the reference samples of type-I collagen in tendon and type-II collagen in cartilage, which have a wide range of orientation angles and an existing database for the comparisons of $\chi^{(2)}$ ratios. We expect that this method will become a highly sensitive technique not only to characterize 3D molecular structure of collagen, but also to provide orientation-independent $\chi^{(2)}$ ratios, which would improve the diagnostic accuracy of cancer staging

and contrast specificity to distinguish between different species of SHG-active molecules.

II Method

To extract the information on 3D molecular orientation and $\chi^{(2)}$ ratios of collagen fibrils, it requires a more complex model that takes into account δ and molecular chirality. In most cases of P-SHG imaging, the contribution of molecular chirality is ignored, and the molecular model based on C_{6v} symmetry is used for image analysis. The models based on C_6 and C_{6v} symmetry are indistinguishable for collagen fibrils aligned parallel to the image plane ($\delta = 0$). However, when $\delta \neq 0$, the tensor element featuring molecular chirality, χ_{14} , has a non-vanishing contribution in SHG signal. Therefore, the C_6 -symmetry model could be more suitable for analyzing collagen fibril structure and orientation. By performing tensor transformation from the molecular coordinate system to the laboratory coordinate system, the new $\chi^{(2)}$ tensor with calibrations for δ and χ_{14} can be built.

In P-SHG imaging, the sample is interacted with linear polarization in various directions, which are gradually rotated from 0° to 180° with a 10° increment with respect to Y-axis. The incident electric field projected on X- and Y-axis are defined as $\cos\theta$ and $\sin\theta$, respectively. By multiplying the new $\chi^{(2)}$ tensor and the incident electric field, the SHG polarization measured in the X and Y directions can be derived. Because SHG signal is measured in the form of intensity, it is proportional to the square of the SHG polarization.

III Results and Discussion

In Figure 1, it is clear to see that the emitted signals collected in orthogonal directions are different, which results in distinct intensity distribution on the P-SHG images. Thus, their polarization dependencies should be different, in which various unknown parameters are hidden behind the images. Besides, we compared the measured $\chi^{(2)}$ ratios by the new model (red dots) with those by the original model (black dots). The corresponding results are shown on the middle and right figure at the bottom row of each dataset. The precision is estimated according to the full width at half maximum of the distribution through a Gaussian fitting. The wider of

the distribution the more inaccuracy is shown in the image analysis. In average, the precision of P-SHG imaging is increased to 20%, which is as expected to our assumption.

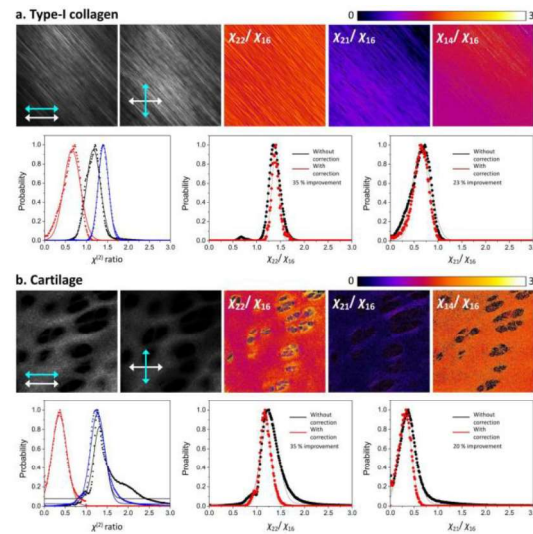


Figure 1. The results for confirmation on the feasibility of the proposed model and comparison with the results analyzed by the original model using a) type-I collagen and b) cartilage. In each data set, the figures from left to right at the top row are the SHG images for X-polarized excitation/X-polarized detection, X-polarized excitation/Y-polarized detection, χ_{22}/χ_{16} , χ_{21}/χ_{16} , and χ_{14}/χ_{16} , respectively. The arrows with white and cyan color indicate the incident polarization direction and the detected polarization direction, respectively. The images in terms of $\chi^{(2)}$ ratio share the same color bar shown at the top right corner. Image size: $300 \times 300 \mu\text{m}^2$ (512×512 pixels). The curves from left to right at the bottom row are the distributions of three $\chi^{(2)}$ ratios (blue: χ_{22}/χ_{16} ; red: χ_{21}/χ_{16} ; black: χ_{14}/χ_{16}), comparison with original model on χ_{22}/χ_{16} and χ_{21}/χ_{16} , respectively.

References

- [1] K. Burke, P. Tang, and E. Brown, *Journal of Biomedical Optics* **18**, 031106 (2012).
- [2] P. J. Campagnola, and C. Y. Dong, *Laser & Photonics Reviews* **5**, 13-26 (2011).
- [3] F. Tiaho, G. Recher, and D. Rouède, *Opt. Express* **15**, 12286-12295 (2007).

Single-shot dual-energy cone-beam CT using an energy-integrating detector

Fang-Yu Liang^a, Ming-Wei Lee^{b,c}, Meei-Ling Jan^{*b}

^aDepartment of Medical Imaging and Radiological Sciences, Chang Gung University, Taoyuan, Taiwan, R.O.C.

^bInstitute for Radiological Research, Chang Gung University, Taoyuan, Taiwan, R.O.C.

^cCenter for Reliability Science and Technology, Chang Gung University, Taoyuan, Taiwan, R.O.C.

*mceiling.jan@gmail.com; phone +886-3-2118800 ext. 3863

Abstract

This study demonstrates a single-shot dual-energy cone-beam computed tomography (CBCT) imaging approach that was achieved using a filtered energy-integrating detector in conjunction with the FDK reconstruction using Parker weighting. A preclinical CBCT composed of one X-ray source and an energy-integrating detector was used to implement the proposed dual-energy imaging method. The phantom study shows that the dual-energy CBCT images can distinguish substances with similar densities, which cannot be achieved by standard CBCT scanning. It is concluded that the proposed dual-energy imaging method could cost-effectively improve CBCT scanners for better contrast-resolving capabilities.

Keywords: dual-energy, cone-beam computed tomography, energy-integrating detector, filtration, single shot

I Introduction

Energy-resolved computed tomography, such as dual- or multi-energy computed tomography (CT) is useful in quantitatively determining the compositions and discriminating between materials without using contrast agent. Dual-energy(DE) CT acquisition can be performed by operating two tube voltages (e.g. dual sources or fast kV switching)¹⁻². The methods have the drawbacks of high exposure dose and cross-scatter radiation that degrades image quality³. Very recently, a twin-beam method was introduced to reach DE-CT imaging by using a single source instead of two sources⁴⁻⁵. However, the twin-beam design is suitable for CT with helical or spiral scanning, but not for cone-beam CT (CBCT), which acquires all projections in one circular rotation. There are other single-shot DE-CT approaches, which are achieved by equipping special detectors, such as two-layer detectors or photon counting detectors (PCDs)^{1,6}. The PCD is a new technology that is capable of identifying X-ray photons with different energy⁶. However, the PCD is still much more expensive than the conventional energy-integrating detectors (EID) and it serves to have some problems unsolved so far (e.g. pulse pileup, K-edge escape, and charge sharing)⁷. Based on the above reasons, an EID is favorable for developing a DE-CBCT with a cost-effective design. Since the EID provides no energy-resolving information, therefore, the usage of conventional EID for single-shot DE-CBCT remains challenging. In this study, we present a single-shot DE-CBCT with an EID to have energy-resolving capability using a filter-based technique.

II Material and Methods

1. Filter Evaluation with Numerical Simulation:

The appropriate high-energy (HE) and low-energy (LE) filter pairs for the CBCT mentioned above were evaluated by

numerical simulation. The simulation setup is shown in figure 1. The X-ray photons $N(E)$ that were received by the EID was performed using the following equation⁸:

$$N(E) = N_0(E) \cdot \exp(-\mu_f(E) \cdot \rho_f \cdot l_f - \sum_{i=1}^3 \mu_i(E) \cdot \rho_i \cdot l_i) \quad (1)$$

where E is the energy of X-ray photons. N is the X-ray photon number received by the detector. μ , ρ , and l is the mass attenuation coefficient, density, and thickness of materials, respectively. f denotes the testing filter. i denotes other materials which are not the testing filter, $i = 1, 2, 3$ are the 3-mm Al, 2.5-mm carbon fiber plate, and 4.1-mm Al, respectively. The materials of the test filters in this study were chosen Sn, Au, and Cu because of their characteristics of K-edge energies. The X-ray tube voltages were set at 55 kV and 65 kV for the proposed DE-CBCT designed for preclinical imaging. The thickness of Au filters was selected by the total photon numbers of the Au-spectrum being the same as that of the corresponding Sn filter. The same is true for the selection of the thickness of Cu. All the linear attenuation coefficients of the materials in the simulation were referenced from the NIST⁹. The original spectra of a tungsten-target X-ray tube were referenced from the website of Simens¹⁰.

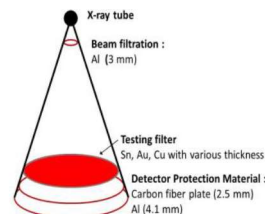


Figure 1. Simulation setup

2. Measurement experiments:

The proposed single-shot DE-CBCT was implemented based on an existing CBCT for preclinical imaging. The CBCT system consists of an tungsten-target X-ray tube (Spellman,

PDM Monoblock®) and an EID detector (Varian Medical Systems, PaxScan®). The Sn/Cu filters were covered side-by-side on the EID detector front plane to acquire the LE and HE projections simultaneously in a single exposure. Although the tube voltage of 55 kV has better energy separation performance than that of 65 kV in the simulations, the homemade CBCT system being operated at 55 kV will result in unacceptable statistical errors received from the EID. Therefore, a tube voltage of 65 kV with a tube current of 10 mA was chosen for subsequent experiments.

An acrylic cylinder phantom (diameter 40 mm) with two hollow cylindrical holes (diameter 6 mm) was used for the experiments. The two holes of the acrylic phantom were filled with water for the single-shot DE-CBCT scan. For comparison, standard CBCT scans were performed without additional filters. For both the single-shot DE-CBCT and standard CBCT scans, 300 projections were acquired in a rotation with a 1.2° angular step. All projections were reconstructed by the FDK algorithm using Parker weighting¹¹⁻¹³. From the single-shot DE-CBCT scan, the HE, and LE image pairs were obtained. The regions of interest were drawn on the regions of the water and the acrylic in the HE, and LE images. The HU numbers of each pixel in the ROIs were used to build the energy map.

III Results and Discussion

The selected simulated energy spectra of Sn/Au, and Sn/Cu filter sets are presented in figure 2. Figures 2(a) and 2(c) show that a tube voltage of 55 kV has better energy-separation performance than a tube voltage of 65 kV. From the comparisons of figures 2(a), 2(c) and 2(b), 2(d), it can be seen that the energy spectra of Au and Cu filters are similar. Therefore, we choose the Cu filter for implementing the experimental study under cost considerations.

According to the energy map from the DE-CBCT images, water and acrylic can be easily separated, as shown in figure 3. Therefore, the water and acrylic can be segmented in the reconstructed image, as shown in figure 4(d). From figure 4(c), the water and acrylic cannot be clearly distinguished by standard CBCT scanning.

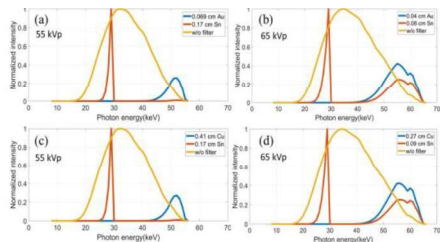


Figure 2. The simulated energy spectra with different filter sets and operating voltages

In summary, the results show that the proposed DE-CBCT imaging method could differentiate matters with similar densities through an existing CBCT system with an EID detector. The frame rate could be increased to obtain more

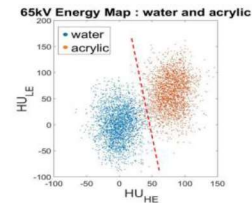


Figure 3. Energy map of water and acrylic in the reconstructed HE and LE images.

projections and angular samplings for better dual-energy reconstruction. However, there still are some limitations, such as the noise interruption caused by the limited tube current and additional filters. Therefore, further optimization of the parameter setting (e.g. tube current, frame rate, projection numbers, etc.) and reduction of statistical noise will be studied in future work

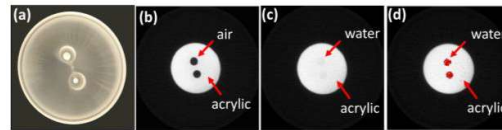


Figure 4. (a) Photo of the two-hole phantom. (b) and (c) are reconstructed two-hole phantom images by the standard CBCT scanning. (d) is the reconstructed image of the phantom filled with water by the proposed DE-CBCT scanning.

Acknowledgments

This work was supported by, the National Science and Technology Council, Taiwan, ROC. (grant number: MOST 109-2221-E-182-004-MY2, MOST 111-2221-E-182-012 -) and the Research Fund of Chang Gung Memorial Hospital, Taiwan (grant number: BMRPF46)

References

- [1] Wang, X. et al., Med. Phys. 38(3), 1534-1546 (2011).
- [2] Sajja, S. et al., Adv. Radiat. Oncol. 5(1), 1-16 (2020).
- [3] Goo, H. W., & Goo, J. M. Korean J Radiol. 18(4), 555-569 (2017).
- [4] Almeida, I. P. et al., Med. Phys. 44(1), 171-179 (2017).
- [5] Euler, A. et al., Invest Radiol. 51(8) (2016).
- [6] Zhou, W. et al., AJNR Am J Neuroradiol, 39(9), 1733-1738 (2018).
- [7] Tao, S. et al., Med. Phys. 46(9), 4105-4115 (2019).
- [8] Hsieh, J., [Computed Tomography Principles, Design, Artifacts, and Recent Advances], John Wiley & Sons, 36-46 (2009).
- [9] Hubbell, J.H. and Seltzer, S.M. "Tables of X-Ray Mass Attenuation Coefficients and Mass Energy-Absorption Coefficients (version 1.4)." 12 July 2004.
- [10] Siemens Healthineers, Calculate initial spectrum <<https://bps.healthcare.siemens-healthineers.com/booneweb/index.html>>
- [11] L. A. Feldkamp, et al., J. Opt. Soc. Am. A 1, 612-619 (1984)
- [12] D. L. Parker, Med. Phys., 9(2), 254-257 (1982)
- [13] Silver, M. D., Med. Phys., 27(4), 773-774. (2000).

Investigate the spatiotemporal dynamics of primary spermatocyte cellularization in *C. elegans* through light sheet microscopy

Hsiao-Fang Peng ^a, Yu-Chun Chen ^b, Yuan Lo ^b, Jui-ching Wu ^{a*}

^a Department of Clinical Laboratory Sciences and Medical Biotechnology, National Taiwan University, Taipei 10048, Taiwan

^b Institute of Medical Device and Imaging, National Taiwan University, Taipei 10051, Taiwan

Abstract

The *C. elegans* spermatocytes are developed in a syncytium in early meiotic phases. Before the meiotic division initiation, the spermatocytes detach from the syncytium and individualize, a process named spermatocyte cellularization. Because these processes happen in a three dimension (3D) structure, detailed spatiotemporal characterization of the spermatocyte cellularization is essential for further investigation the spermatocyte cellularization regulation. This study focused on illustrating how the cellularization orchestra in male gonads through actomyosin network. We found that the actomyosin form a constriction ring to close the opening of cellularizing spermatocytes. We demonstrated light sheet microscopy as a great optical system to image dynamics process in whole live worms.

Keywords: light sheet microscopy, 3D reconstruction, spermatogenesis, spermatocyte cellularization, gonad rachis

I Introduction

Cellularization is a process to individualize the cell. This process is intensively studied in *Drosophila* early embryo [1, 2]. The embryos are syncytium in the first fourteen cell cycle and individualized as the cell membrane formed between nucleus. In *C. elegans*, the spermatocytes also grown as a syncytium [3]. Different from *Drosophila*, the *C. elegans* syncytium nucleus connected with the rachis through the ring channel. The primary spermatocyte would detach from the syncytium and finished individualization as the ring closure (Fig 1). Because the cellularization in *C. elegans* occur continuously in a three dimension (3D) an observation method with timely optical section ability is crucial for dig in the spatial structure dynamics during primary spermatocyte cellularization. Light sheet microscopy (LSM) is an ideal option for observing such active processes. The LSM only illuminate the specific plane of the sample, which decrease the acquisition time and reduce the photo toxicity [4, 5]. With the advantage of light sheet microscopy, we are able to visualize the spatiotemporal movements of spermatocyte cellularization in *C. elegans*.

*juichingwu@ntu.edu.tw; phone 886 2 2312-3456 ext.66904

II Methods

1. Worm culture

Caenorhabditis elegans strain JJ1473 were cultured on NGM plates seeded with *E. coli* OP50 as described [6].

2. Live-imaging

(1) Epifluorescence microscopy

The worms were immobilized with 5mM Levamisole on a 3% agarose pad. The sample was sealed with Vaseline to prevent from evaporation and examined under 100x objective with Olympus IX83 system.

(2) Light sheet microscopy

The worms were pick into M9 buffer and immobilized with 40mM Levamisole prior to the experiment. Then, the sample was diluted with equal volume of 1% low melting agarose and loaded into the sample holder. The sample was examined under 20x water lens.

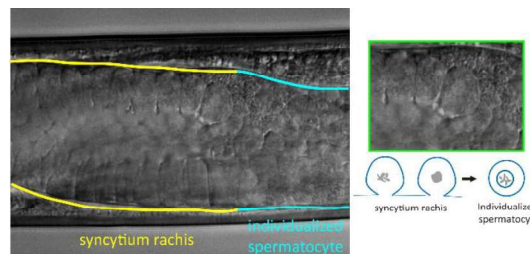


Figure 1. The *C. elegans* male gonad is a syncytium before spermatocyte individualization.

III Results and Discussion

To set up the examination parameter, we firstly examine the primary spermatocyte cellularization processes under epifluorescence microscope. We used a motor protein required for membrane contractility, non-muscle myosin II, *nmy-2::GFP* as a marker for cellularization initiation. The results showed that the membrane form a constriction ring to close the opening of the cellularizing spermatocytes and followed by spermatocyte detachment under live-imaging (Figure 2).

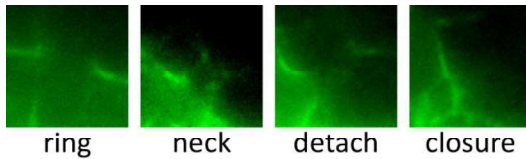


Figure 2. The *C. elegans* actomyosin network dynamics during spermatocyte cellularization.

Since the cellularization processes is conducted in the three-dimensional feature, we sought to examine this process precisely. We examined the primary spermatocyte cellularization processes under light sheet microscopy (Fig 3). After acquiring the images, we are able to reconstruct them back into 3D image (Fig 4). In order to verify the time-lapse ability between different microscopy, we compared the cellularization rate in Table 1. The results showed the LSM are capable of acquiring timely imaging without damaging the worms.

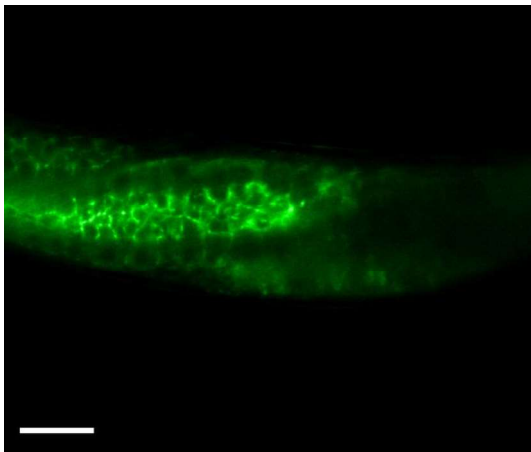


Figure 3. The *C. elegans* syncytium rachis filmed with LSM. Scale bar: 20 μ m.

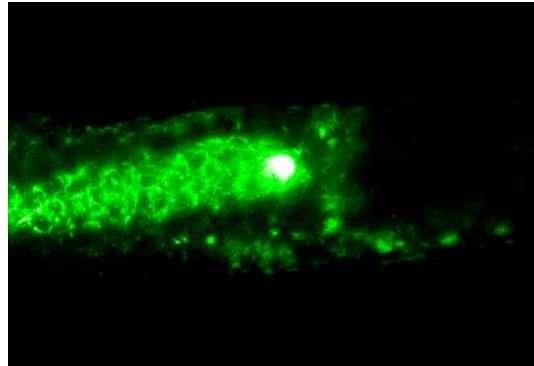


Figure 4. The 3D fluorescence image of the male gonad through LSM.

	epi	LSM
Cellularization rate	14.165 min/cell (n=2)	15 min/cell (n=1)

Table 1. The spermatocyte cellularization rate

These results suggest the LSM could apply an ideal method for 3D time-lapse imaging for further investigation of spermatocyte cellularization process in whole live worms

VI References

1. Loncar, D. and S.J. Singer, *Cell membrane formation during the cellularization of the syncytial blastoderm of Drosophila*. Proc Natl Acad Sci U S A, 1995. **92**(6): p. 2199-203.
2. Sokac, A.M., N. Biel, and S. De Renzis, *Membrane-actin interactions in morphogenesis: Lessons learned from Drosophila cellularization*. Semin Cell Dev Biol, 2022.
3. Seidel, H.S., et al., *C. elegans germ cells divide and differentiate in a folded tissue*. Dev Biol, 2018. **442**(1): p. 173-187.
4. Keller, P.J., et al., *Reconstruction of zebrafish early embryonic development by scanned light sheet microscopy*. Science, 2008. **322**(5904): p. 1065-9.
5. Huisken, J., et al., *Optical sectioning deep inside live embryos by selective plane illumination microscopy*. Science, 2004. **305**(5686): p. 1007-9.
6. Brenner, S., *The genetics of Caenorhabditis elegans*. Genetics, 1974. **77**(1): p. 71-94.

Pelvic Arteries Segmentation on CT Angiography with Deep Learning

Yu-Tong Cheng^a, Alexander Te-Wei Shieh^a, Wen-Jeng Lee^b, Tzung-Dau Wang^c

^aSchool of Medicine, National Taiwan University, Taipei 100, Taiwan R.O.C.

^bDepartment of Medical Imaging, National Taiwan University Hospital, Taipei 100, Taiwan R.O.C

^cDepartment of Internal Medicine, National Taiwan University Hospital, Taipei 100, Taiwan R.O.C

Abstract

This study aims to accurately segment both large and small pelvic arteries on pelvic CT using deep-learning. We collected a dataset of CT angiography studies from 50 male patients, and manually labeled vessel masks for arteries branching below the aortic bifurcation. We built a pipeline containing two models with the dense U-Net architecture: a global model trained with the entire volume, and a local model focusing on the pelvic cavity, to enhance the segmentation of smaller arteries. The results from the two models are combined, post-preprocessed to remove unwanted vessels, and evaluated with the Dice score (DSC). In addition, we labeled a testing set specifically for internal pudendal artery (IPA), a distal branch of the internal iliac artery, to measure the performance for smaller vessels. Using our pipeline, the overall DSC improved from 0.839 to 0.862, and the recall for IPA improved from 0.813 to 0.842 compared to the single model approach.

Keywords: pelvic arteries; computed topography angiography; semantic segmentation; U-Net; deep learning

I Introduction

Atherosclerosis in pelvic arteries can lead to diseases such as claudication and erectile dysfunction[1], and endovascular therapies were investigated to treat these conditions[2]. These conditions are not frequently diagnosed and treated, and automated segmentation of pelvic arteries from CT images can provide assistance for automated diagnosis and treatment planning.

However, segmentation of pelvic arteries with deep learning is a challenging task. First of all, there has been no established benchmark dataset on the topic. Moreover, the sizes of arteries vary greatly, ranging from 9.2 mm in diameter (common iliac artery) to 1.3 mm (distal penile artery), which includes many small branches that are hard to be segmented in pelvic CT angiography images [1]. Besides, pelvic bones, kidneys and ureters were in similar Hounsfield unit (HU) ranges compared to arteries on CT angiography, making the complex anatomy structures harder for segmentation models to discriminate.

II Methods

1. Data characteristics

We collected 50 pelvic CTA studies from 50 different male patients who underwent evaluation for suspected arteriogenic erectile dysfunction. Images are acquired under protocol of CT angiography for the pelvis. The region of interest starts from aortic bifurcation and ends at femoral head. Each slice contains 512×512 voxels, and the number of slices in each study falls between 425 and 617 slices. In total, the dataset contains 25,816 slices of

images. Resolution is (0.625, 0.430, 0.430) mm in z, y, and x dimensions. The dataset is split as Table 1.

Table 1. Information on dataset split.

Dataset split	Training	Validation	Testing
Dataset size	30 (60%)	10 (20%)	10 (20%)
Sex	Male	Male	Male
Average age	63.6	63.3	61.3
Atherosclerosis	30 (100%)	10 (100%)	10 (100%)

Annotations of all vessels were first pre-labeled by the IntelliSpace Portal 9.0 software. Manual inspection and editing were performed for correction and to exclude arteries not branching out from the aortic bifurcation, i.e., removing kidney and mesenteric arteries. Additional detailed masks for internal pudendal arteries (IPAs) and were annotated for further evaluation.

2. Network Architecture

We select the dense U-Net [3], an upgrade to the popular U-Net architecture, as our model after testing various architectures on our dataset.

3. Segmentation pipeline

We trained an additional “local” model focusing on arteries in the pelvic cavity, since preliminary results showed that a single “global” model does not provide an ideal performance on small distal branches. These vessels, such as the internal pudendal artery, are mostly branches of

the internal iliac artery. The range of focused area is chosen as the middle 50% voxels in x and y axes, and the 20%–70% slices in z axis. We combined results of two models by union to enhance recall of small arteries, and do post-processing to generate the final segmentation results. Post-processing includes two steps: (1) for the top 15% slices, remove all connected components other than the largest one; (2) for the entire volume, remove connected components containing less than 2000 voxels.

4. Loss function and metrics

We used symmetric unified focal loss [4] for training and Dice similarity coefficient (DSC) score as our evaluation metric. The recall for IPA volume in testing set was calculated to evaluate performance on small arteries.

5. Model training setup

Models are trained on the NVIDIA DGX-1 platform with two Tesla V100 SXM2 32GB GPU. Preprocessing includes 2 cycles of data augmentation, clipping HU values between [-200, 1500], Z-score normalization, and random cropping of size (128, 256, 256). Models are trained for 60 epochs, and the one with minimum validation loss is saved.

III Results and Discussion

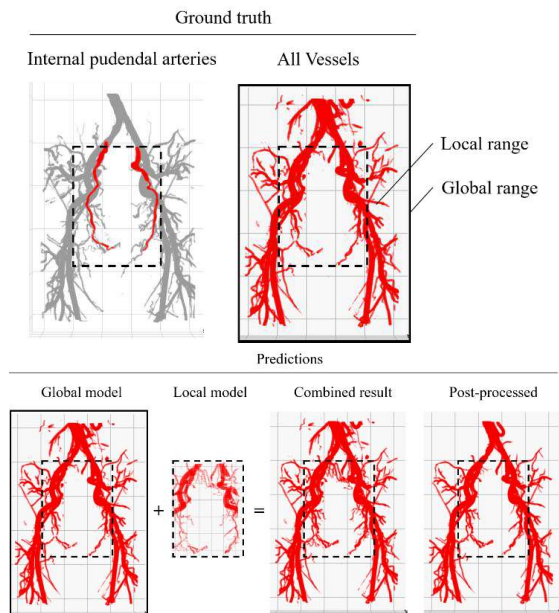


Figure 1. An example of ground truths and predictions. (Projection of 3D volumes from the front.)

Table 2. DSC score of each step of pipeline on test set

Range \ Model	Global Model	Combined result	Post-processed
DSC	0.839	0.844 ***	0.862 *
IPA recall	0.813	0.844 **	0.842 ^{n.s.}

(Two-tail paired t-test. Combined result: compared with global model; post-processed: compared with combined result. ***, $p < 0.005$; *, $p < 0.05$; n.s., not significant, $p > 0.05$)

Table 2 shows the results of our model in DSC scores, and Fig. 2 shows a case in the testing set as example. The global model alone achieves DSC of 0.839 in both global and local range. Combining the results of local model finds more branches to the distal end and shows significantly improved results of DSC of 0.844. Post-processing successfully removes kidney and mesenteric arteries, which are not included in our labels, but sacrificing some small unconnected pieces. The two effects together resulted in improved DSC to 0.862. The recall for IPA improved from 0.813 to 0.844 with addition of the local model, demonstrating its effectiveness of capturing smaller vessels. The post-processed recall was 0.842, which can be attributed to discarded small fragments.

References

- [1] Wang, T-D, Lee, C-K, Chia, Y-C, et al; the HOPE Asia Network. Hypertension and erectile dysfunction: The role of endovascular therapy in Asia. *J Clin Hypertens.* 2021; 23: 481–488. <https://doi.org/10.1111/jch.14123>
- [2] Donas, K. P., Schwindt, A., Pitoulias, G. A., Schönefeld, T., Basner, C., & Torsello, G. (2009). Endovascular treatment of internal iliac artery obstructive disease. *Journal of Vascular Surgery*, 49(6), 1447–1451. doi:10.1016/j.jvs.2009.02.207
- [3] Kolařík M, Burget R, Uher V, Říha K, Dutta MK. Optimized High Resolution 3D Dense-U-Net Network for Brain and Spine Segmentation. *Applied Sciences.* 2019; 9(3):404. <https://doi.org/10.3390/app9030404>
- [4] Michael Yeung, Evis Sala, Carola-Bibiane Schönlieb, Leonardo Rundo. Unified Focal loss: Generalising Dice and cross entropy-based losses to handle class imbalanced medical image segmentation *Computerized Medical Imaging and Graphics*, Volume 95 (2022).

Hacking Consumer Electronics for Biomedical Imaging

Jorge Pereda^a, Hsien-Shun Liao^b, Christian Werner^c, Jen-Hung Wang^d, Kuang-Yuh Huang^b, Ellen Raun^a, Laura Olga Nørgaard^a, Frederikke Elisabet Dons^a, Edwin En Te Hwu^{*a}

^a Department of Health Technology, Technical University of Denmark, Lyngby 2800, Denmark.

^b Department of Mechanical Engineering, National Taiwan University, Taipei 106319, Taiwan.

^cPhysikalisch-Technische Bundesanstalt, Braunschweig 38116, Germany.

^dDepartment of Mechatronics and Robotics, Technical University of Munich, München 80333, Germany.

Abstract

Trillions of USD have been dedicated to the development of consumer electronic technologies, to produce drones, wireless chargers, spy cameras, and DVD/Blu-ray optical data storage systems. Consequently, these have been perfected into compact, reliable, high-performance, and low-cost devices. This work reviews the complete repurposing (hacking) of consumer electronics for biomedical imaging and sensing applications.

Keywords: hardware hacking, wireless power, lab on disc, optical pickup unit (OPU), atomic force microscopy (AFM)

Introduction

The essential components of novel biomedical imaging technologies may already be well developed and mass-produced for consumer electronics. By hacking consumer electronics, we can achieve new features, higher performance, lower cost, and faster commercialization, which are mutually exclusive.

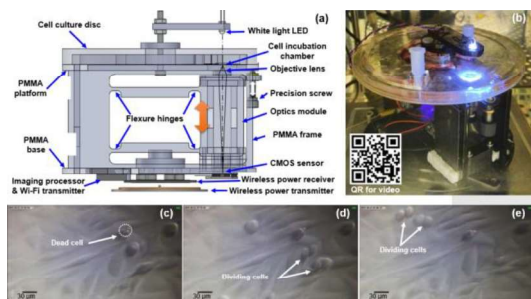


Figure 1. Real time cell culture and imaging system design (a) and photo (b). HeLa cell imaged (c) 5 hours; (d) 8 hours; and (e) 10 hours after seeding.

1. Cell culture and real-time imaging on a disc

Microfluidic cell cultivation typically requires complex systems for nutrient perfusion and waste removal. Centrifugal systems simplify the process, but the spinning of the chamber encumbers imaging of cell development.

Fig. 1 shows an optical microscope based on a spy camera, powered by a wireless charger. It rotates with the substrate, to monitor cell cultures continuously, remotely, and in real time [1].

2. All-in-one powered lab-on-a-disc (APELLA)

The drone motors driven APELLA combines a spy camera can achieve unprecedented temporal resolution to image rapid microfluidic mixing event [2] (Fig. 2.)

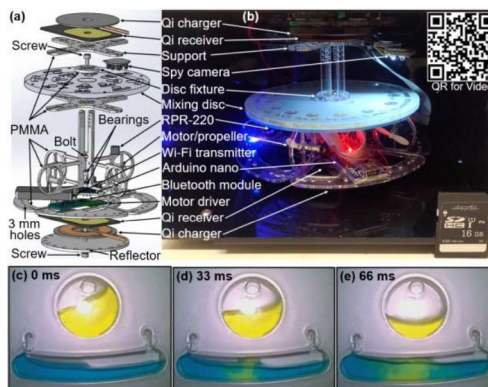


Figure 2. Design (a) and photo (b) of the all-in-one powered lab-on-a-disc system. A rapid liquid mixing event (c)-(e), imaged by a spy camera which rotates with the disk, imaging at 30 fps.

*etchw@dtu.dk; phone 45 53 81 52 66

3. Optical pickup unit (OPU) based cell imaging

DVD/Blu-ray data storage OPUs have been hacked into atomic force microscopes (AFMs) [3], allowing experiments on nano-metrology [4], molecular biology [5], chemistry [6], stiffness [7], biomarkers [8], diabetes [9], force [10], microstructure [11], etc. [12]. OPU-based microscopes can achieve better contrast than high-end optical microscopes [13], as shown in Fig. 3.

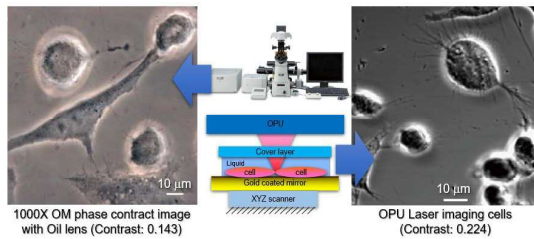


Figure 3. Astrocyte images by phase contract conventional (left) and OPU-based (right) microscopes.

4. High-speed dermatological AFM (HD-AFM)

An OPU-based HD-AFM (Fig. 4) measures corneocyte nanotexture and provides quantitative dermal texture index (DTI) to assess the severity of atopic dermatitis and related conditions [14].

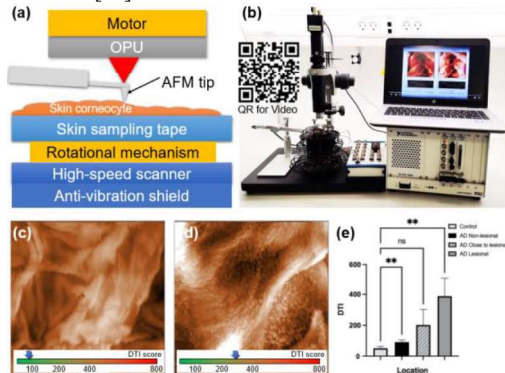


Figure 4. Schematic design (a) and photo (b) of the HD-AFM. Healthy (c) and AD (d) skin DTI. The HD-AFM can quantitatively assess the severity of AD (e).

References

- [1] Hwu, E.-T. *et al.*, "Real-time optical monitoring of cell culture in centrifugal microfluidics," *Proc. μ TAS* 1039-1040 (2020).
- [2] Hwu, E.-T., *et al.*, "Miniaturized all-in-one powered lab on a disc platform," *Proc. μ TAS* (2019).
- [3] Hwu, E.-T., *et al.*, "Measurement of cantilever displacement using a compact disk/digital versatile disk pickup head," *Jpn. J. Appl. Phys.*, 45, 2368. (2006)
- [4] Hwu, E. T., *et al.*, "A hybrid scanning probe microscope module based on a DVD optical head." *Meas. Sci. Technol.*, 20(8), 084005. (2009)
- [5] Bosco, F. G., *et al.*, "High throughput label-free platform for statistical bio-molecular sensing," *Lab Chip*, 11(14), 2411-2416. (2011)
- [6] Bosco, F. G., *et al.*, "Statistical analysis of DNT detection using chemically functionalized microcantilever arrays," *Sens. Actuators B Chem.*, 171, 1054-1059. (2012)
- [7] Liao, H.-S., *et al.*, "Spring constant calibration of microcantilever by astigmatic detection system," *Jpn. J. Appl. Phys.*, 51, 08KB13. (2012)
- [8] Bache, M., *et al.*, "Nanomechanical recognition of prognostic biomarker suPAR with DVD-ROM optical technology," *Nanotechnology*, 24(44), 444011. (2013)
- [9] Uddin, R., *et al.*, "New evidence for the mechanism of action of a type-2 diabetes drug using a magnetic bead-based automated biosensing platform," *ACS sensors*, 2(9), 1329-1336. (2017)
- [10] Chang, T. J., *et al.*, "Open-source force analyzer with broad sensing range based on an optical pickup unit," *HardwareX*, 11, e00308. (2022)
- [11] Ceccacci, A. C., *et al.*, "Blu-ray based micro-mechanical characterization platform for biopolymer degradation assessment," *Sens. Actuators B Chem.*, 241, 1303-1309. (2017)
- [12] Hwu, E. E. T., *et al.*, "Hacking CD/DVD/Blu-ray for biosensing," *ACS sensors*, 3(7), 1222-1232. (2018)
- [13] Hsiao, W. W., *et al.*, "Biophysical analysis of astrocytes apoptosis triggered by larval E/S antigen from cerebral toxocarosis-causing pathogen *Toxocara canis*," *Anal. Sci.*, 29(9), 885-892. (2013)
- [14] Liao, H. S., *et al.*, "Open-source controller for low-cost and high-speed atomic force microscopy imaging of skin corneocyte nanotextures," *HardwareX*, e00341. (2022).

Prediction based on machine learning of operation outcome from peripheral arterial occlusive disease

Yung-Chang Chen^a, Pin-Yu Kuo^a, Jen-Kuang Lee^b, Chau-Chung Wu^b, Chia-Wei Sun^{*a}

^aBiomedical Optical Imaging Lab, Department of Photonics and Institute of Electro-Optical Engineering, National Yang Ming Chiao Tung University, Hsinchu, Taiwan, R.O.C.

^bDivision of Cardiology, Department of Internal Medicine, National Taiwan University Hospital, Taipei, Taiwan, R.O.C.

Abstract

Providing an appropriate prognosis for operation outcomes for patients with peripheral arterial occlusive disease is essential. However, current diagnosis methods have limitations and need a long-term revisit. In this study, we used near-infrared spectroscopy (NIRS) as a blood oxygenation monitoring system for lower limbs, combined with support vector machine (SVM) to construct a prediction model for operation outcome. The model achieved a training accuracy of 89.19 % and a test accuracy of 80 %. In addition, the result of feature selection showed that tissue saturation index (TSI) could reflect the adjustment and stability of blood oxygenation of patients under external influence.

Keywords: near-infrared spectroscopy, peripheral arterial occlusive disease, support vector machine

I Introduction

Peripheral arterial occlusive disease (PAOD) is caused by atherosclerosis, which leads to blockage or narrowing of arteries. Clinicians usually perform percutaneous transluminal angioplasty (PTA) or bypass surgery on severe PAOD patients to dilate blood vessels. During the return visit, complicated examinations are taken to determine recovery or not. To reduce medical expenses, how to prognosis the outcome of the operation is crucial clinically. The purpose of this study is to monitor blood oxygenation in local tissues of the lower limbs of PAOD patients through near-infrared spectroscopy (NIRS)¹. Combine statistical analysis and support vector machine (SVM) to classify the operative results of PAOD as the prediction for prognosis². It can serve as a reference clinically and assist physicians in evaluating the state of patients. The prognosis of operation outcome can be preliminarily known immediately, saving medical costs and avoiding the waste of resources.

II Materials and Methods

1. Subjects

Patients diagnosed with PAOD, excluding wounds on the measurement side and foot edema were recruited for this study. A total of 51 records have been collected.

*chiaweisun@nycu.edu.tw

2. Measurement

In this study, the instrument we used is Portalite, a measurement device based on NIRS by Artinis Medical Systems. Three pairs of intensity-modulated laser diodes, which emit near-infrared rays at two wavelengths (760 and 850 nm) and one gain-modulated photomultiplier tube detector. In addition, the far-infrared (FIR) therapeutic instrument TY101N developed by WS FAR IR Medical Technology Co., Ltd. was used as the physiological intervention method³.

The subject was lying during the measurement, two probes were placed on the instep, and the TY101N was fixed at 20 cm above the probe. Figure 1 shows the experimental process, consisting of three stages: resting, task, and recovery.

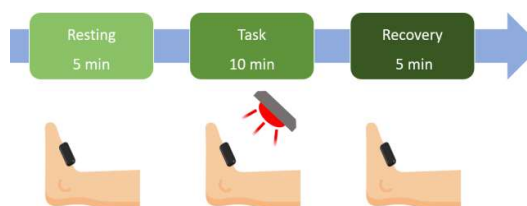


Figure 1. Experimental process of NIRS monitoring.

3. Feature Extraction

Signals measured by Portalite include tissue saturation index (TSI), relative changes in concentration of oxy-hemoglobin (HbO₂) and deoxy-hemoglobin (Hb). Only the monitoring results of the surgical side were used in the analysis. The feature extraction method consists of the arithmetic mean, slope, and beginning slope of three different stages. Of note, the slope of the first ten seconds in each stage is called beginning slope. The stage difference was obtained by subtracting the adjacent two stages' features. If the reference was the resting stage, we defined it as stage activation.

III Results and Discussions

After feature extraction, highly correlated and significantly different features were selected, including the slope activation of TSI in the task and resting stage and the beginning slope of TSI in recovery stage.

The above two features were used as the input of SVM. Figures 2 and 3 show the model classification results, including the training dataset and testing dataset. The training and testing accuracies are 89.19 % and 80.00 %, respectively.

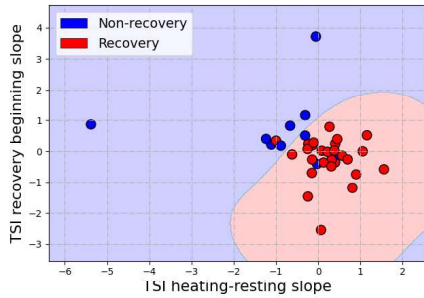


Figure 2. SVM classification of training dataset.

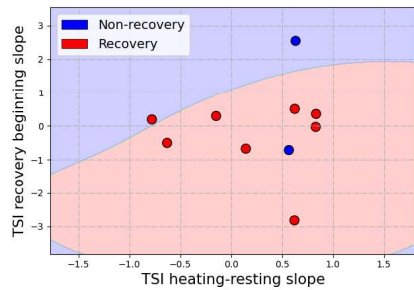


Figure 3. SVM classification of testing dataset.

Figure 4 is the normalized confusion matrix. We can know the actual and predicted labels of different groups, which helps to explore the clinical application value of this model. Furthermore, it shows that the model has a sensitivity and specificity of 88 % and 82 %, respectively.

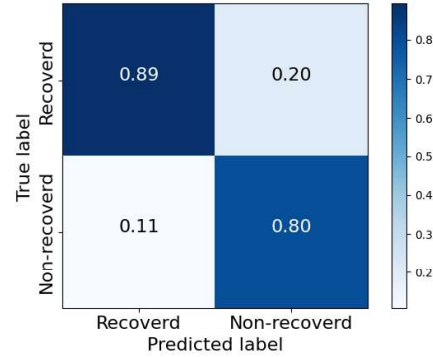


Figure 4. The normalized confusion matrix.

Based on the above result, the specificity of the model prediction is slightly insufficient, which may hinder the correct early diagnosis of the non-recovered patients. The presumed reason is that the number of non-recovered patients is insufficient, making it impossible to have a more comprehensive understanding of the blood oxygenation features of the non-recovered patients. In conclusion, increasing the sample of non-recovered patients and making the distribution of this group in the feature space more complete may help improve the model's performance or generalization ability.

References

- [1] Lu, S. H., Tsai, C. L., Fu, T. C., Chang, P. H., and Lu, S. M., "A Near Infrared Spectroscopy System for Assessing Rehabilitation on Peripheral Arterial Occlusion Patients," *Journal of Medical and Biological Engineering*, 40(4), 592-600 (2020).
- [2] Flores, A. M., Demsas, F., Leeper, N. J., & Ross, E. G., "Leveraging machine learning and artificial intelligence to improve peripheral artery disease detection, treatment, and outcomes," *Circulation Research*, 128(12), 1833-1850 (2021).
- [3] Chuang, K. H., Chuang, M. L., Sia, S. K., and Sun, C. W., "Oxygenation dynamics of sepsis patients undergoing far-infrared intervention based on near-infrared spectroscopy," *Journal of Biophotonics*, 10(3), 360-366 (2017).

Applying Machine learning to extracorporeal membrane oxygenation patients using functional near-infrared spectroscopy

Chang-Yi Lee^a, Ting-Wei Chiang^a, Hsiao-Huang Chang^b, Chia-Wei Sun^{*a},

^aBiomedical Optical Imaging Lab, Department of Photonics, National Yang Ming Chiao Tung University, Hsinchu 300, Taiwan, R.O.C

^bDivision of Cardiovascular Surgery, Department of Surgery, Taipei Veterans General Hospital, Taipei 112, Taiwan, R.O.C

Abstract

Our study aims to detect the changes in blood oxygen concentration in extracorporeal membrane oxygenation (ECMO) patients by non-invasive near-infrared spectroscopy (NIRS) when adjusting the speed. We process the measured blood oxygen value through filtering, feature selection and record the patient's APACHE-II scale score. Patients with scores greater than 24 are called high-scoring groups, whereas scores less than or equal to 24 are known as low-scoring groups. Finally, we combined the measured blood oxygen information with the scale scores for binary classification. In Venous-Arterial (VA) group, the train and test accuracy reach 83.3% and 81.8%. On the contrary, the train and test accuracy get 81.8% and 72.7% in Venous-Venous (VV) group.

Keywords: APACHE-II scoring system, extracorporeal membrane oxygenation, microcirculation, near-infrared spectroscopy, support vector machine

I Introduction

Extracorporeal membrane oxygenation¹ (ECMO) provides a medical emergency method to clinically assist the respiratory and circulatory function of ill patients. However, various complications occur under long-term use. Therefore, to reduce the complications, assessing microcirculation status on the spot is crucial. In this study, near-infrared spectroscopy (NIRS) was used to monitor the microcirculation function of ECMO patients on lower limbs. The blood oxygen information was processed and fed into machine learning. Afterward, we tried classifying the disease severity in Venous-Venous (VV) and Venous-Arterial (VA) ECMO. Both groups have obtained good results, proving the feasibility of near-infrared spectroscopy for diagnosing clinical disease severity.

II Methods

1. Experimental design

There are six stages in our experiment², as shown in Figure 1. The VV group's speed will be fixed for 15 mins in the baseline stage.

At stage 1, the speed is reduced by 300 rounds per minute (rpm) for 10 mins and then goes back to the initial flow rate for the next 10 mins. Subsequently, we increase the speed by 300 rpm for 10 mins, then raise another 300 rpm for the next 10 mins. Finally, the flow rate returns to the original speed for the final 10 mins. For the VA group, the protocol is the same as the VV group, but the adjustment amount is 500 rpm. In addition, we use two PortaLite systems (Artinis, Netherlands) to measure the blood oxygenation concentration of ECMO patients' limbs through all processes. At last, the blood oxygen information is sent back to the computer through Bluetooth.

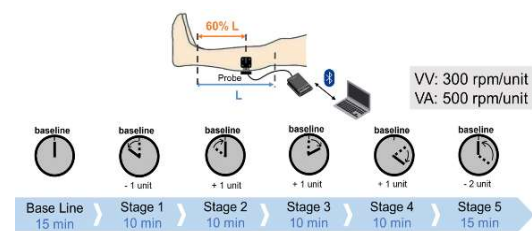


Figure 1. Experimental design

2. Machine Learning Model

*chiaweisun@nycu.edu.tw

The support vector classifier (SVC) is a tool for classification in the support vector machine³ (SVM) series. The principle of SVC is to find a decision boundary that maximizes the distance between the decision boundary and the support vector of different classes, thus achieving the distinction between each class. In addition, SVC can also make decision boundary nonlinear by adjusting the kernel, making it more likely to find the best decision boundary.

III Results and Discussions

The result shows that after executing the SVC model with the features selected by the t-test, the model can draw a smooth decision boundary and separate two groups well. In VA group, we get an accuracy of 0.833 on training data (Figure 2) and 0.818 on test data (Figure 3). Besides, an accuracy of 0.818 on training data (Figure 4) and 0.727 on test data (Figure 5) are obtained in VV group.

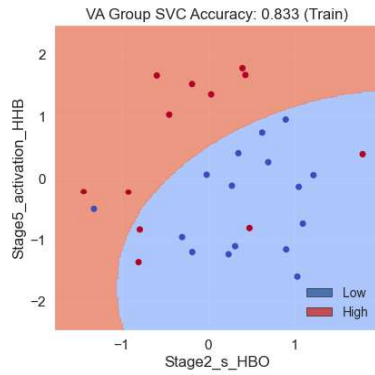


Figure 2. VA group boundary plot (train)

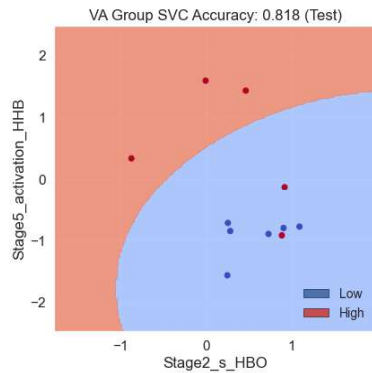


Figure 3. VA group boundary plot (test)

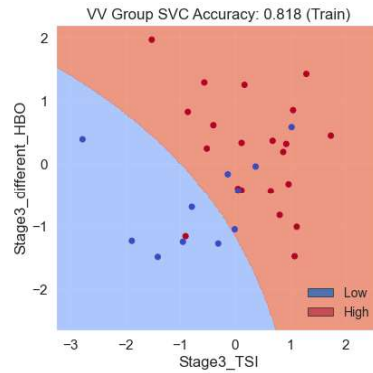


Figure 4. VV group boundary plot (train)

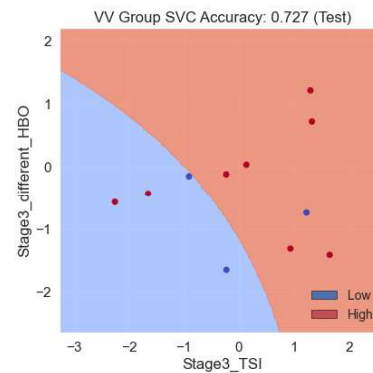


Figure 5. VV group boundary plot (test)

We use a t-test to select the essential features, feed them into the SVC model, and get good results. That is to say, through our model, informative blood oxygen concentration can be used to predict the severity of the patient's pathology.

IV Reference

- [1] Abrams, Darryl, Alain Combes, and Daniel Brodie. "Extracorporeal membrane oxygenation in cardiopulmonary disease in adults." *Journal of the American College of Cardiology* 63.25 Part A (2014): 2769-2778.
- [2] Hsiao-Huang Chang, et al. "Optimization of extracorporeal membrane oxygenation therapy using near-infrared spectroscopy to assess changes in peripheral circulation: A pilot study." *Journal of Biophotonics* 13.10 (2020): e202000116.
- [3] Ben-Hur, Asa, and Jason Weston. "A user's guide to support vector machines." *Data mining techniques for the life sciences*. Humana Press, 2010. 223-239.

Analysis of police overwork degree by functional near-infrared spectroscopy: taking the Copenhagen overwork scale as a standard

Ting-Hong Hsu^a, Qing-Yan Hsieh^a, Yao-Hong Liu^a, Wen-Yu Wang^b, Ching-Po Lin^b, Chia-Wei Sun^{*a}

^aBiomedical Optical Imaging Lab, Department of Photonics and Institute of Electro-Optical Engineering, National Yang-Ming Chiao-Tung University, Hsinchu, Taiwan, R.O.C.

^bInstitute of Neuroscience, National Yang-Ming Chiao-Tung University, Taipei, Taiwan, R.O.C.

Abstract

In this study, we use functional near-infrared spectroscopy (fNIRS) to measure the changes in hemoglobin concentration in the prefrontal cortex lobe of 33 police officers during the mental arithmetic task (MAT) and verbal fluency task (VFT). The signals were processed to extract physiologically meaningful features, and a model was built using the Copenhagen overwork scale score as a classification basis. The results show a training accuracy rate of 88.9 % and a testing accuracy rate of 80.0 %, indicating that it has great potential to evaluate the degree of overwork by combining fNIRS with machine learning.

Keywords: burnout, functional near-infrared spectroscopy, police officer, prefrontal cortex, support vector machine

I Introduction

Burnout is defined as a state of chronic stress at work, characterized by feelings of exhaustion, negative emotions, and inefficiency. In addition to threatening personal physical and mental health, it also deteriorates work quality and efficiency[1]. Therefore, burnout is considered a severe occupational risk, and this issue is gradually being taken seriously.

Police officers are a group of high occupational risks as they are under a lot of pressure, possibly due to the danger of terrorist attacks, the increase in regional weapon violence, and the force of public opinion[2]. This dilemma shows the importance of preventing chronic stress and paying attention to occupational health.

This study will be based on the Copenhagen Overwork Scale, and the police will be selected as the observation group. We hope to find an objective evaluation basis for fatigue tendency through the measurement system of near-infrared spectroscopy (fNIRS) [3].

II Materials and methods

1. Subjects

We recruited 33 police officers as subjects to receive cases at the Taipei City Government Police Station.

*chiaweisun@nycu.edu.tw

2. Experimental setups

We use a continuous-wave NIRS measurement system to collect data, a self-developed instrument in our laboratory, consisting of three light detectors and two near-infrared light emitters staggered with a spacing of 3 cm, as shown in Figure 1.



Figure 1. fNIRS device

Before the test commencement, the subjects filled in two scales and then grouped into high-risk (H) and low-risk (L) according to their scale scores.

The experimental design is divided into the verbal fluency task (VFT) and the mental arithmetic task (MAT). VFT was used to assess prefrontal function, and subjects were required to speak as many words as possible in the task stage, starting with the specified phonetic. MAT is a standard and practical stress test to assess concentration, memory, and execution. During the task stage, subjects were required to calculate addition and subtraction and

choose the correct answer. The detailed process of VFT and MAT is shown in Figures 2 and 3.

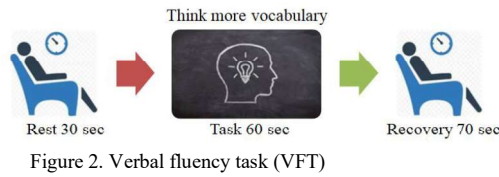


Figure 2. Verbal fluency task (VFT)

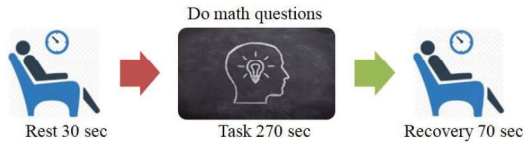


Figure 3. Mental arithmetic task (MAT)

3. Data processing

First, the received signal is filtered and then normalized to eliminate the differences between individuals. Then, a t-test is used to test the independence of each feature. According to the P value, the features with higher differences are selected and imported into SVM for classification training. We divided the 33 received subjects into training and testing datasets in a ratio of 7:3 for model training.

III Results and Discussions

After feature extraction, features with significant differences are selected and put into the SVM model for training. For example, we found that the difference between CH3_Deoxy_Recovery and CH1_Deoxy_Rest was significant, so these two features were selected for classification. Figure 4 shows that the decision boundary of the model can separate the data of high-risk and low-risk groups without overfitting. The training accuracy is 88.9%, and the testing accuracy is 80.0%.

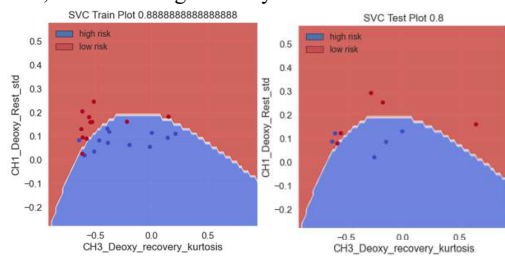


Figure 4. SVM model Classification results for training dataset (right) and testing dataset (left)

We evaluate model classification performance and generalization ability through the confusion matrix. The Sensitivity of this classification model is 60%, Specificity is 100%, PPV is 100%, NPV is 71.4%, and the F1 score of the model is 75%.

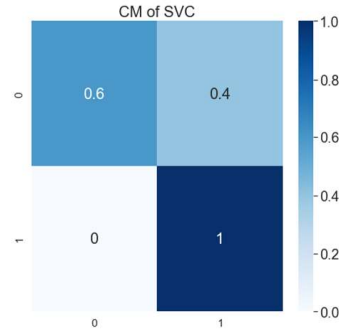


Figure 5. Confusion matrix

No significant correlation was found between the overworked scale scores and gender, age, seniority, and educational attainment. VFT has a better classification effect than MAT.

The accuracy of the model training results is 88.9%, the testing accuracy reaches 80.0%, and the confusion matrix (Figure 5) shows that the model has a sensitivity of 60% and a specificity of 100%, indicating that this study has a specific potential.

The total number of cases received is still slightly insufficient. However, once the number of recruitments increases in the future, the model will be more convincing.

References

- [1] G.S. Jeon, S.J. You, M.G. Kim, Y.M. Kim, and S.I. Cho, "Psychometric properties of the korean version of the copenhagen burnout inventory in korean homecare workers for older adults," PloS one, vol. 14, no. 8, p. e0221323, 2019.
- [2] C. Queirós, F. Passos, A. Bárto, A. J. Marques, C. F. da Silva, and A. Pereira, "Burnout and stress measurement in police officers: Literature review and a study with the operational police stress questionnaire," Frontiers in psychology, vol. 11, 2020.
- [3] S. Skau, I. H. Jonsdottir, A. Sjörs Dahlman, B. Johansson, and H. G. Kuhn, "Exhaustion disorder and altered brain activity in frontal cortex detected with fnirs," Stress, pp. 1–12, 2020.

Mid-infrared passive spectroscopic imaging for non-invasive blood glucose sensor*

Ichiro ISHIMARU^{*a}, Tomoya KITAZAKI^a, Daichi ANABUKI^a, Shiori TAHARA^a,
Akira NISHIYAMA^b, Kenji WADA^b, Akiko NISHIMURA^b

^a Faculty of Engineering and Design, Kagawa University, 2022-17 Hayashi-cho, Takamatsu, Japan

^b Faculty of Medicine, Kagawa University, 1750-1 Ikenobe, Miki-cho, Kita-gun, Kagawa, Japan

Abstract

As known as a thermography, mid-infrared lights are emitted from human bodies in accordance with human body heats. Because emitted rays are derived from molecular vibrations, we could distinguish specific emission spectrums due to molecular structures. Active and passive spectroscopy have a negative and positive relationship. Emission peaks exist at same wavelength as absorbance peaks. We confirmed the specific emission peaks at 9.25 μm and 9.65 μm derived from glucose from a distance by the proposed mid-infrared passive spectroscopic imager.

Keywords: non-invasive blood glucose sensor, mid-infrared passive spectroscopic imager,

I Introduction

We proposed the mid-infrared passive spectroscopic imager that was called the imaging type 2-dimensional Fourier spectroscopy^{1), 2)}. Emitted lights from human bodies are derived from molecular vibrations. The proposed method could measure emission spectrums of radiances. We could distinguish the specific emission peaks at 9.25 μm and 9.65 μm of glucose from a distance.

II Non-invasive blood glucose sensor by mid-infrared passive spectroscopic imaging

1. Detection of specific emission peaks by the passive spectroscopic imager from a distance

As shown in figure 1, wrists were placed at a distance of 600mm from the mid-infrared passive spectroscopic imager. The gray scale photo shows the observed mid-infrared image. And the red square in the photo shows the view field of the spectral imaging device. In the righthand side graph in Fig.1, the black solid line shows the spectral absorbance of glucose solutions previously measured by the conventional FTIR (Fourier Transform Infrared Spectroscopy). Because FTIR is the active spectroscopy, the vertical axis shows the absorbance. The red solid line shows the emission spectrum acquired by the proposed mid-infrared passive spectroscopy. In this case, the vertical axis shows the emittance. The false color image

*ishimaru.ichiro@kagawa-u.ac.jp; phone 81 87 864-2325

illustrates the emittance map whose wavelength was 9.65 μm . We could recognize the emission peaks at the same wavelength of the absorbance peaks of the active spectroscopy at 9.25 μm and 9.65 μm . Therefore, we were able to confirm the negative and positive relationship between active and passive spectroscopy. And we demonstrated the feasibility of the non-invasive blood glucose sensor from a distance.

The clinical trials were conducted in accordance with the protocol approved by Kagawa University Ethics Review Committee (#2020-162). We conducted the same clinical trial on five subjects. And the time series data of blood sugar level were compared with conventional blood collection type and Abbot's Free style Libre. We also confirmed the time delay between these three methods.

2. Casually Watching Over Peoples with Invisible lights simultaneously around a dining table

As shown in figure 2, AI speaker with built in the passive spectroscopic imager watches over several peoples around a dining table simultaneously. We also proposed the pea-sized mid-infrared spectrometer that could be built in smartwatch. The pea-sized spectrometer is a kind of spatial phase-shift interferometer configured with only 3 lenses³⁾. Thus, complementally, we wear the smart watch for outdoor use. It will be very easy to integrate these healthcare data on the internet.

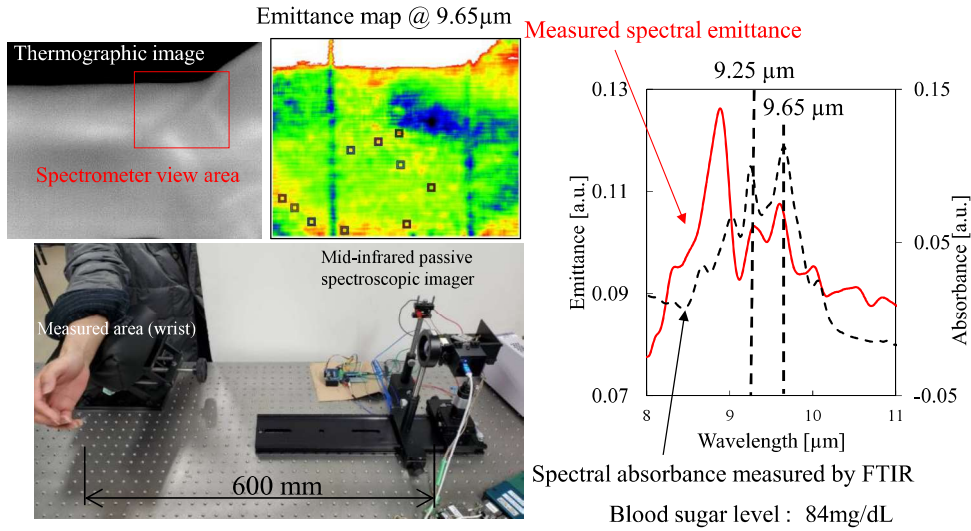


Figure 1. Measured specific emission peaks of glucose by the mid-infrared passive spectroscopic imager from a distance.

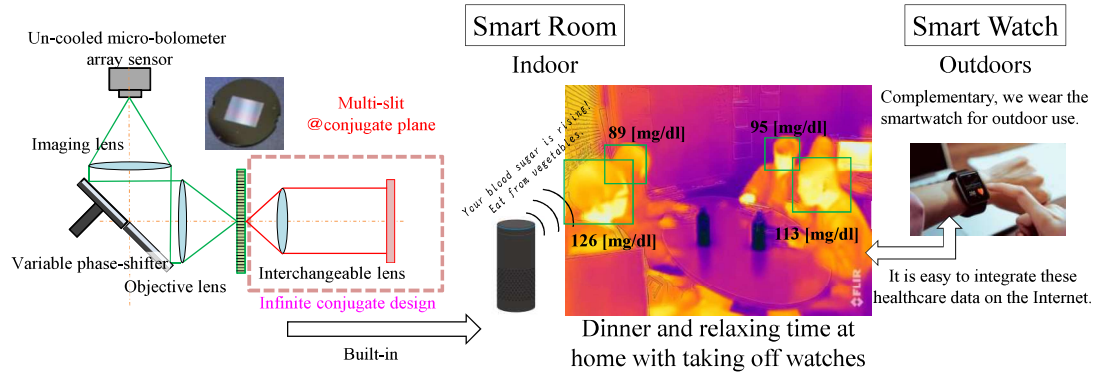


Figure 2. AI speaker with built-in the mid-infrared passive spectroscopic imager casually measure the blood sugar level of several people around the dining table simultaneously.

References

- 1) Y.Inoue, I.Ishimaru, T.Yasokawa, K.Ishizaki, M.Yoshida, M. Kondo, S.Kuriyama, T.Masaki, S.Nakai, K.Takegawa, and N.Tanaka: Variable phase-contrast fluorescence spectrometry for fluorescently stained cells, Applied Physics Letters ,89, 121103. (2006)
- 2) W.Qi, Y.Suzuki, S.Sato, M.Fujiwara, N.Kawashima, S.Suzuki, K.Wada, A.Nishiyama, and I.Ishimaru: Enhanced interference-pattern visibility using multislit optical superposition method for imaging-type two-dimensional Fourier spectroscopy, Applied Optics, 54, 20, doi: 10.1364/AO.54.006254,6254-6259. (2015)
- 3) N.Kawashima, T.Kitazaki, K.Nogo, A.Nishiyama, K.Wada, I.Ishimaru: Superimposing interferogram method using a multi-slit array to enhance sensitivity and interference definition of spatial-phase-shift interferometers, Optical Review, volume 27, 530–541(2020)

*ishimaru.ichiro@kagawa-u.ac.jp; phone 81 87 864-2325

Biodegradable and implantable polymer optical waveguide plate for guiding lightwaves into biological tissue

Ai-Wei Li^a, Cheng-Yang Liu^{*a}

^aDepartment of Biomedical Engineering, National Yang Ming Chiao Tung University, Taipei City 11221, Taiwan

Abstract

The major drawbacks of photo therapy are associated with the difficulty of delivering light uniformly and efficiently, which result in limiting the therapeutic depth. Recently, efforts have focused on implanting hydrogel materials into tissue to overcome the finite depth of light penetration. To address this problem, we focused on fabricating a biocompatible PEGDA waveguide which could be inserted into biological tissue to target deep region. With the approach of ultraviolet cross-linking processing, the PEGDA waveguide was formed by different concentrations. The current results indicated that the 80% PEGDA waveguide had an average optical loss 0.7 dB/cm in simulated body fluid solution and enhanced the light intensity distribution along the biological tissue. These finding suggested that the PEGDA waveguide is effective for delivering light in deep tissue and can be used in the fields of photo-medicine.

Keywords: PEGDA, waveguide, biomaterial, optical delivery

I Introduction

Implanting optical fibers into tissue for light delivery represents an effective approach to overcome the limited penetration due to their high transmission efficiency (>85%). However, traditional silica fibers are usually fragile and brittle, which are unsuitable as implantable devices [1,2]. Recent years, hydrogels are considered as a promising alternative material in conventional photonic devices [3]. Poly(ethylene glycol) diacrylate (PEGDA) hydrogels with a relatively refractive index of ~1.47 have been successfully used as implantable optics since they have excellent biodegradable, biocompatible and tissue-like mechanical properties [4,5]. Additionally, the PEGDA hydrogels show the properties of low absorbance and notable light-guiding capabilities in the visible range (400–700 nm), which adequate for high optical transmission efficiency in tissue. Therefore, the PEGDA waveguide can exert a novel biomaterial to form implantable photonic device in medical application [6]. In the present study, we aim to fabricate a thin and flexible PEGDA waveguide, which can be inserted into *in vivo* to deliver light uniformly along the full thickness of tissue, and further examine their optical characterization.

II Materials and methods

Figure 1 shows fabrication process of the PEGDA waveguide. 1% α -Hydroxy-4-(2-hydroxyethoxy)- α -methylpropionophenon

(I2959) is added in distilled water and mixed with a weight ratio of 20%, 40%, 60% and 80% PEGDA (700 Da). Next, the prepared solution is injected into a polydimethylsiloxane (PDMS) mold with dimension of 5 mm (width) x 700 μ m (height) x 15 mm (length) and subjected to an ultraviolet (UV) cross-linking processing. For light coupling, a singlemode fiber (SMF, core/cladding: 10/125 μ m) is pigtailed to the hydrogel waveguide by inserting about 3 mm of the silica fiber into the precursors. After exposure to UV light for 5 min, the hydrogel waveguide plate is obtained.

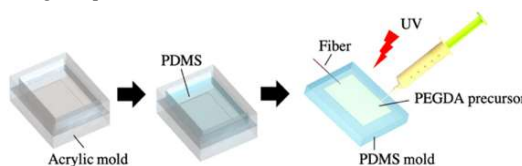


Figure 1. Fabrication process of PEGDA waveguide.

The refractive indices of the PEGDA hydrogels are measured with a digital refractometer. To determine the light absorption and transmission properties in air ($n = 1$) and simulated body fluid environment ($n = 1.336$), PEGDA waveguide is placed on a self-designed fixed platform at an interval of 2.5 cm, as shown in Figs. 2(a) and 2(b). Light from halogen lamp (400-1700 nm) is connected via a SMA905 fiber to the waveguide and the optical characterizations are measured using a

spectrophotometer at wavelength ranging from 300 to 800 nm, as shown in Fig. 2 (c). The propagation loss is calculated according to the equation: $PL = 10/L \times \log T$ (dB/cm).

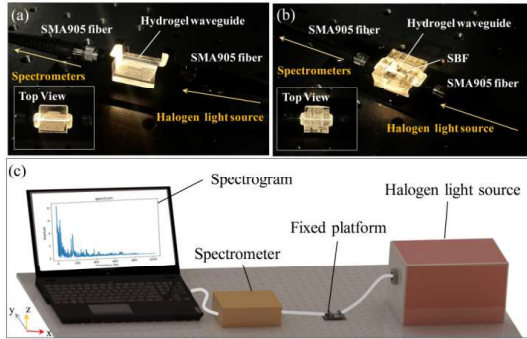


Figure 2. Experimental optical waveguides in (a) air and (b) simulated body fluid environment. (c) Spectrum measurement system.

III Results and Discussion

The optical transparency and refractive index are the major concern of biomaterial waveguide, which dominate the effective light-guiding.

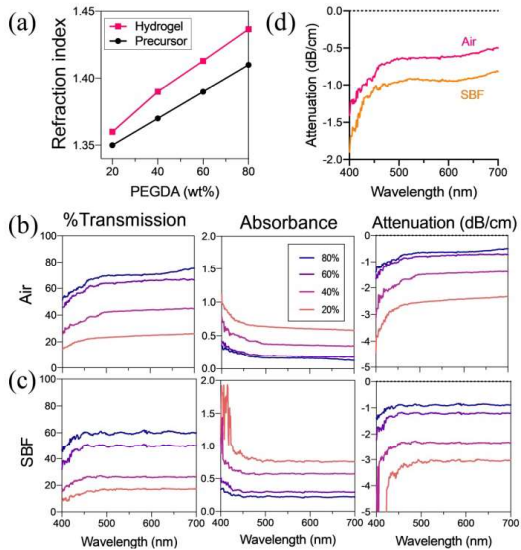


Figure 3. (a) Refractive index of PEGDA hydrogel and precursor. Transmission, absorbance and attenuation in (b) air and (c) simulated body fluid environment. (d) Light attenuation of 80% PEGDA waveguide in air and simulated body fluid environment.

The results in Fig. 3(a) indicate that the crosslinking hydrogels have higher refractive index than the precursor solutions and increased from 1.35 to 1.43 when the concentration increase from 20 wt% to 80 wt%. The spectra of the PEGDA waveguides with difference concentrations demonstrate that the 80% waveguide has high transmission with an average optical loss 0.5 dB/cm in air and 0.7 dB/cm in simulated body fluid environment, as shown in Figs. 3(b) to 3(d). Figure 4(a) shows that the intensity of optical fiber is constrained to a small region less than 1 cm without PEGDA waveguide in biological tissue. It is anticipated in Fig. 4(b) that the PEGDA waveguide evidently enhance the illumination depth along the entire tissue.

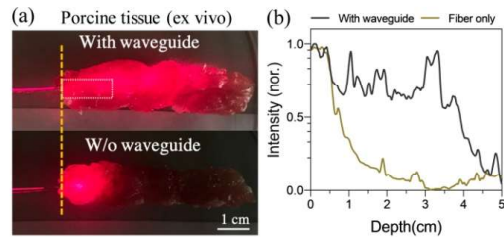


Figure 4. (a) Image of the light in porcine tissue before and after inserting the PEGDA waveguide. (b) Light intensity distribution profiles in biological tissue with and without the PEGDA waveguide.

References

- [1] Jacques, S., "Optical properties of biological tissues: a review," *Phys. Med. Biol.* 58(11), R37 (2013).
- [2] Nazempour, R., Zhang, Q., Fu, R., Sheng, X., "Biocompatible and implantable optical fibers and waveguides for biomedicine," *Materials* 11(8), 1283 (2018).
- [3] Gierej, A., Geernaert, T., Vlierberghe, S., Dubruel, P., Thienpont, H., Francis Berghmans, F., "Challenges in the fabrication of biodegradable and implantable optical fibers for biomedical applications," *Materials* 14(8), 1972 (2021).
- [4] Choi, M., Humar, M., Kim, S., Yun, S., "Step-index optical fiber made of biocompatible hydrogels," *Adv. Mater.* 27(27), 4081-4086 (2015).
- [5] Guo, J., Yang, C., Dai, Q., Kong, L., "Soft and stretchable polymeric optical waveguide-based sensors for wearable and biomedical applications," *Sensors* 19(17), 3771 (2019).
- [6] Nizamoglu, S., Gather, M., Humar, M., Choi, M., Kim, S., Kim, K., Hahn, S., Scarcelli, G., Randolph, M., Redmond, R., Yun, S., "Bioabsorbable polymer optical waveguides for deep-tissue photomedicine," *Nat. Commun.* 7, 10374 (2016).

Unsupervised Cross-modality Segmentation and Isotropic Restoration by Pseudo-mask Assisted Deep Generative Networks

Meng-yun Wu^{*a}, Ya-ding Liu^b, Da-yu Huang^a, Li-An Chu^{b*}, G. Chang^{a*}

^aInstitute of Medical Device and Imaging, National Taiwan University, Taipei 10051, Taiwan, R.O.C.

^bDepartment of Biomedical Engineering and Environmental Sciences, National Tsing Hua University, Hsinchu 300044, Taiwan.

Abstract

While the ever-growing amount of available imagery should help unlock the secrets of neural functioning, the required amount of human annotation effort remains a major bottleneck. Therefore, there has been a great interest in automating the annotation process and most state-of-the-art algorithms nowadays rely on machine learning. In this study, we developed models for the purpose of automatic image reconstruction, isotropic restoration and domain adaptation using multi-scales and multi-modalities light-sheet microscopy images with deep generative adversarial networks.

I Introduction

Imaging modalities such as electron (EM) and light microscopy (LM) can now deliver high-quality, high-resolution image stacks of neural structures, such as the ones depicted by Fig. 1. Typically, a combination of manual and semi-automated segmentation or annotation tools are then used to extract structures of interest. However, such algorithms still require significant amounts of manual annotation to train classifiers that can generalize well to unseen data. In microscopy, this can be a problem because the data preparation processes tend to be complicated and not easily repeatable, which means that a classifier trained on one acquisition will not perform very well on a new one, even when using the same modality. This is because machine learning normally relies on the fact that the training and run-time data samples are drawn from the same distribution. As a result, two samples of the same brain region acquired at different times may look significantly different due to differences in their preparation. This is even more true when the samples come from different parts of the brain, so that classifiers trained for one of them perform poorly on the other.

II Method

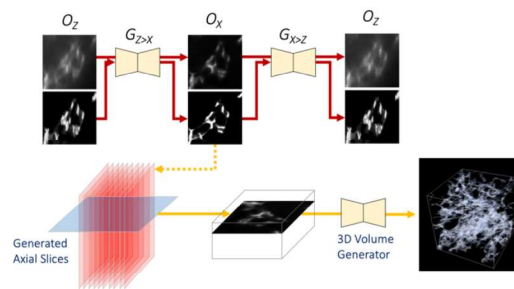


Fig 1. Overall architecture

We performed knowledge transfer and domain adaptation from a teacher model (microtubules deconvolution of CSBDeep) to model of neuron segmentation trained from scratch by utilizing the pretrained model to extract multi-scale features from the presently studied images of projection neurons. The teacher model was trained with synthetic mesh-like structures consisted of tubular objects with a fixed diameter and resembles microtubules of HeLa Cells. While the synthetic images used for the pretrained model lacked the complexity of the presently studied images of projection neurons, such as their connectivity between fibers and the morphologies of neurons, the pretrained model still contains useful information of microscopy images, for

* co-corresponding authors

example, the identifying the edges of objects and the noise-patterns.

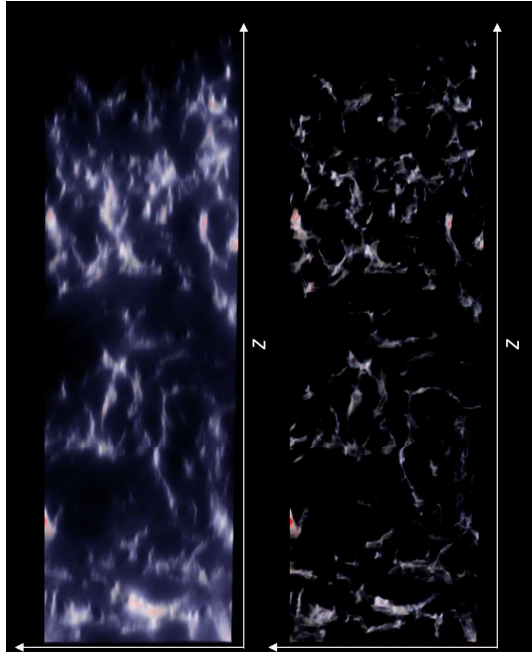


Figure 2. Comparison between images before and after imaging isotropic restoration using GANs.

III Results

In the first experiments, we also performed isotropic microscopy imaging restoration by the techniques of unpaired domain adaptation between multi-scale and multi-module microscopy imaging of projection neurons. Unlike previous studies, which using a paired domain adaptation scheme by assuming a function of degradation to create synthetically downgraded images from the original images, our present approach did not require synthetically paired data as well as an accurate assumption about the acquisition conditions of different microscopy modules. Instead, the relation between the original images and the degraded images were self-learned by the models. Therefore, our present model worked well across an array of different multiple microscopy modules and imaging of different techniques of expansion microscopy. This was critical for us to expand the utilization of the present model to various expansion microscopy protocols to investigate the morphologies of neurons at multi-scales.

In the second experiment, we performed domain adaptation between 40x expansion and 10x expansions images by GANs with cyclic consistency, expected that segmentation model designed based on 10x expansion domain can also works on 40x expansion domain. GAN is a kind of unsupervised deep learning model combined with two neural networks, generator and discriminator. The generator generates real-looking images to fool the discriminator while the discriminator tries to distinguish between real and fake images. By using GAN structure, our model learned how to transfer 40x expansions images into 10x expansions images with small amount of data. In addition, introducing transitivity concept into our work made us able to supervise generator training and improved performance of unpaired image-to-image domain transfer

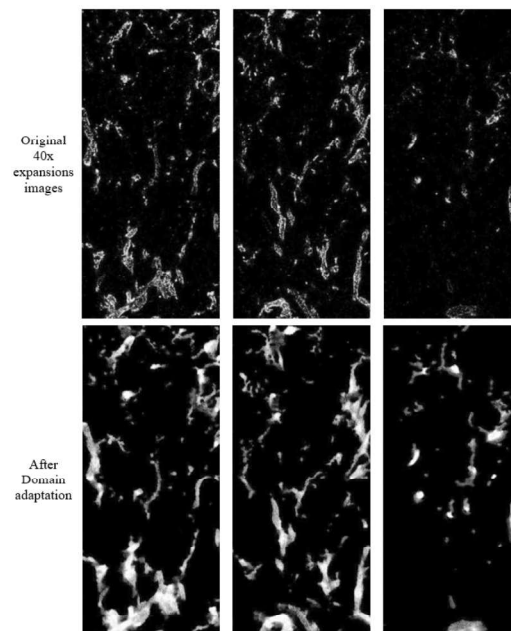


Figure 3. Comparison between images before and after domain adaptation between expansion microscopy images of different protocols.

Image Restoration Based on Deep learning in Millisecond-scale Two-photon Fluorescence Volumetric Microscopy *

Chien-Sheng Wang^{*a}, Yu-Hsuan Tsai^a, Shi-Wei Chu^a

^aDepartment of Physics, National Taiwan University, Taipei 10051, Taiwan, R.O.C.

Abstract

We demonstrated a two-photon microscopy with >500 volumes/second scanning speed by combining multifocal multiphoton microscopy with a tunable acoustic gradient (TAG) lens. This high-speed fluorescence microscopy allows us to extract complete spatiotemporal information from the *Drosophila* brain. However, the SNR contrast is sacrificed due to the dramatic increase in imaging speed. In this work, we mitigated these limitations via deep learning image restoration to enhance SNR. The deep-learning model was trained on semi-simulated data, which is composed of the real high-speed data multiplied with a simulated dynamic mask to mimic the functional changes in fluorescent intensity inside a *Drosophila* brain. The trained model restored high-speed but low-contrast images into high-speed and high-contrast images, effectively improving the SNR of images while maintaining high temporal resolution.

Keywords: deep learning, image restoration, millisecond-scale temporal resolution, Volumetric imaging.

I Introduction

The brain is fascinating and mysterious. Even though a single neuron has been thoroughly studied, our understanding of the function of the brain is still limited. This limitation comes from emergent properties of connections among numerous neurons. *Drosophila*, as a model animal for brain studies, has a fairly complete neural structural map and its brain is small enough to enable whole-brain optical imaging with sub-cellular resolution. To develop a tool for mapping the functional connectome of *Drosophila* brains, volumetric acquisition with millisecond temporal resolution is necessary.

However, the quality of the images recorded by fluorescence microscopy suffers from the so-called 'eternal quadrilateral of compromise', which is composed of spatial resolution, imaging speed, contrast, and depth. The cause of the compromise is due to the limited photon budget tolerated by sample intactness, the chemistry of fluorophores, and the optics of the microscope.

In order to trace the process of neuronal dynamics inside the *Drosophila* brain. We had built high-speed volumetric fluorescence microscopy, which has millisecond volumetric imaging speed in deep tissue but sacrificed SNR. With the significant improvement in

computing hardware, deep learning became an excellent candidate to relieve this issue. In this study, we aim at applying deep learning to our customized high-speed microscopy to raise the image quality.

II Method

The mission of our millisecond-scale volumetric imaging system is to catch the functional fluorescent change inside the *Drosophila* brain, but it is impossible to catch the high-quality ground truth of the functional intensity change in real-time as we stated. Thus, in this study we used semi-simulation data to train a U-net. *Drosophila* brain slide was imaged by this high-speed system as training data. To simulate the functional intensity change inside the mushroom body, we made a random functional mask. A single-volume poor SNR data multiplied by this mask as input and the corresponding high SNR ground truth which averaging 500 volumes are fed to the deep learning model.

III Results and Discussion

The trained model can restore not only structural data but also functional data as shown in Figure 1. The high-speed but poor SNR data can be restored into high-speed and high SNR data. However, the less similarity of test data to training data would decrease the performance of this trained model due to limited training data.

*james0524x@gmail.com; phone +886 911175921



Figure 1. Restoration from deep learning trained model can show promising result.

References

- Allen, J. S. 1988. *The Complete Dictionary of Abbreviations*. New York: MacMillan & Sons, Inc.
- Fang L, Monroe F, Novak SW, Kirk L, Schiavon CR, Yu SB, et al. Deep learning-based point-scanning super-resolution imaging. *Nat Methods*. 2021;18: 406–416.
- Icha J, Weber M, Waters JC, Norden C. Phototoxicity in live fluorescence microscopy, and how to avoid it. *Bioessays*. 2017;39. doi:10.1002/bies.201700003
- Laissie PP, Alghamdi RA, Tomancak P, Reynaud EG, Shroff H. Assessing phototoxicity in live fluorescence imaging. *Nat Methods*. 2017;14: 657–661.
- Pawley JB. *Fundamental Limits in Confocal Microscopy*. *Handbook Of Biological Confocal Microscopy*. 2006. pp. 20–42. doi:10.1007/978-0-387-45524-2_2
- Scherf N, Huisken J. The smart and gentle microscope. *Nat Biotechnol*. 2015;33: 815–818.
- Weigert M, Schmidt U, Boothe T, Müller A, Dibrov A, Jain A, et al. Content-aware image restoration: pushing the limits of fluorescence microscopy. *Nature Methods*. 2018. pp. 1090–1097. doi:10.1038/s41592-018-0216-7

Single/ Multiphoton Light Sheet Microscopy for Drosophila Whole Brain Functional Imaging

Heng Chang^{1,2}, Wei-Kun Chang², Bi-Chang Chen^{2,3}, Li-An Chu^{1,2}

1. Department of Biomedical Engineering and Environmental Science, National Tsing Hua University, Hsinchu, Taiwan
2. Brain Research Center, National Tsing Hua University, Hsinchu, Taiwan
3. Research Center for Applied Sciences, Academia Sinica, Taipei, Taiwan

Abstract

Neuroscience has been studied by human since 19th century, and nowadays the development of brain science is growing more rapidly. To capture *Drosophila* neuronal activities in 3D, we have built our Digital Scanning Light Sheet Microscopy (DSLMS) system, which allowed us to achieve subcellular resolution and observe synapses activities at targeted brain region. We also have studied olfactory memory in *Drosophila* with multifunction imaging assay. However, single-photon based microscopy suffered serious high scattering and low penetration in bio tissue due to its short wavelength, especially in live imaging.

In order to increase light penetration depth and obtain good optical sectioning live image, we propose Two-photon Light Sheet Microscopy (2PLM) systems, with longer wavelength (920nm) and the characteristic of pulsed laser, we hope we can capture not only live image at deeper brain region, but also whole brain living neuron activity with different stimulate assays, building up and re-define their role in the neuronal circuit computation system.

Keywords: Digital Scanning Light Sheet Microscopy, *Drosophila* whole brain imaging, Functional Imaging, Two-Photon Microscopy

I Introduction

Light sheet microscopy (LSM) can precisely illuminate the focal plane to be observed in the biological sample, which can reduce the effect of phototoxicity and improve signal to back ground ratio (SBR) with another orthogonal emission objective for collecting fluorescence signal. Since LSM scans the sample by using the plane of light instead of point (compare to confocal microscopy), it can provide 100 – 1,000 times faster imaging speed than those point-scanning method microscopy. To be further, LSM can obtain better image quality at deeper region of biological tissue by using Bessel beam (BB) to develop digital scanning light sheet microscopy (DSLMS), which allows us to do volumetric live imaging.

In our study, we use *drosophila* as model animal for neuron science research, using UAS:Gal4 system to express GCaMP series green fluorescence protein (GFP) at specific neuron, which can be combined to functional imaging and animal behavior assay. The DSLMS system we use is designed by using mask to shape the Gaussian laser beam into ring, directed and scanning by two rapidly rotated Galvo mirrors, which control x and z scanning

direction separately, then generate BB by high numeric aperture (NA) objective, the fluorescence signal is collected by another objective placed on piezo stage, which at the orthogonal position from the excitation objective focus plane, and imaging into a sCMOS camera sensor.

However, Side lobe generated by BB will still introduce a certain amount of background signal when images acquired, in addition, the visible wavelength range used for excitation is still susceptible to tissue scattering in living tissue, which limit penetration depth. In order to solve above problems, we established two-photon DSLMS (2P-DSLMS), improving the energy efficiency by using an Axicon lens pair instead of a mask to fabricate the ring, and use the near-infrared (NIR) ultrashort pulse laser to focus through the objective, when NIR wavelength has lower light absorption and better penetration ability in biological tissue. Since the fluorescence signal needs to be generated in a place with high photon density, it can only be generated at the focal plane of the excitation objective, which can improve the optical sectioning capability of the system and further improve the SBR.

II Result

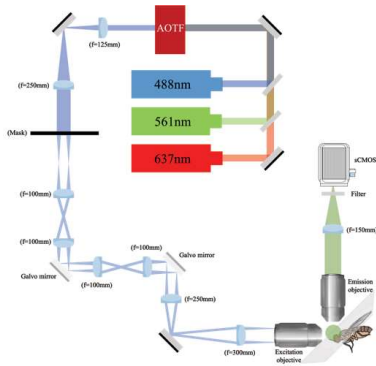


Fig.1

Single-photon DSLM(1P-DSLM) system schematic diagram, can be used for different fluorescence protein with multi-channel laser.

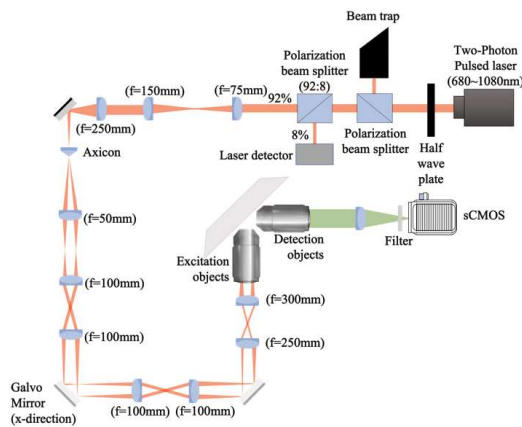


Fig.2

2P-DSLM system schematic diagram

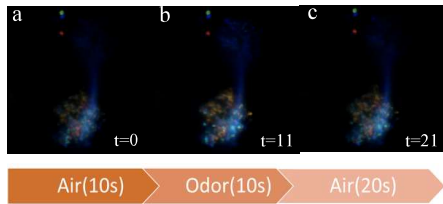


Fig.3

Projection neuron at *Drosophila* GH146:GC imaged by 1P-DSLM for odor functional imaging, delivering (a) air before (b) Apple Cider Vinegar, then (c) air again.

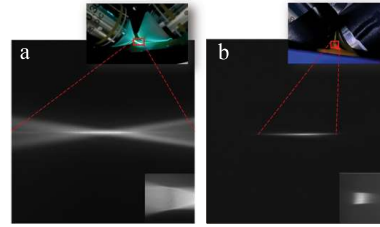


Fig.4

BB generated by (a) 1P-DSLM and (b) 2P-DSLM

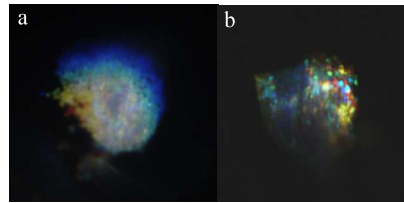


Fig.5

Kenyon cell at *Drosophila* OK107:GC imaged by (a) 1P-DSLM and (b) 2P-DSLM

III Discussion

In the future, we will want to quantify the penetration of 2P-DSLM system and design proper translation stage, synchronizing them together with automatic odor delivery system for more complex whole brain functional imaging.

References

1. Takanezawa, S., Saitou, T. & Imamura, T. Wide field light sheet microscopy with lens-axicon controlled two-photon Bessel beam illumination. *Nat Commun* 12, 2979 (2021).
2. Lin PY, Hwang SL, Lee CH, Chen BC. Two-photon scanned light sheet fluorescence microscopy with axicon imaging for fast volumetric imaging. *J Biomed Opt.* 2021 Nov;26(11):116503.
3. Gao, L., Shao, L., Chen, BC. *et al.* 3D live fluorescence imaging of cellular dynamics using Bessel beam plane illumination microscopy. *Nat Protoc* 9, 1083–1101 (2014)
4. F. O. Fahrbach, P. Simon, and A. Rohrbach, Microscopy with self-reconstructing beams, *Nat. Photonics* 4(11), 780–785 (2010)
5. M. Schneider, S. Barozzi, I. Testa, M. Faretta, A. Diaspro Two-photon activation and excitation properties of PA-GFP in the 720–920-nm region *Biophys. J.*, 89 (2005), p. 1346

Multiple-Plate Continuum for Stimulated Raman Scattering Spectro- Microscopy across the Entire Raman Active Region

Guan-Jie Huang^{1,2}, Pei-Chen Lai^{2,3}, Kuo-Chuan Chao², Peng Lin⁴, Ji-Xin Cheng⁴, Ann-Shyn Chiang^{2,6}, Bo-Han Chen², Chih-Hsuan Lu², Shi-Wei Chu^{1,2,7}, and Shang-Da Yang^{2,3}

¹ Department of Physics, National Taiwan University, Taipei 10617, Taiwan

² Brain Research Center, National Tsing Hua University, Hsinchu 300044, Taiwan

³ Institute of Photonics Technologies, National Tsing Hua University, Hsinchu 300044, Taiwan

⁴ Department of Electrical and Computer Engineering, Boston University, MA 02215, USA

⁵ Department of Biomedical Engineering & Environmental Sciences, National Tsing Hua University, Hsinchu 30044, Taiwan

⁶ Institute of Systems Neuroscience and Department of Life Science, National Tsing Hua University, Hsinchu 30044, Taiwan

⁷ Molecular Imaging Center, National Taiwan University, Taipei 10617, Taiwan

Abstract

Stimulated Raman scattering (SRS) has attracted great attention in both spectroscopy and microscopy fields due to the ability towards background-free molecular-specific acquisitions without fluorescence labeling. Nevertheless, practically useful sensitivity and specificity require advanced laser systems with sufficient excitation strength to provide adequate signals and unconstrained wavelength tuning range to probe the interested Raman region. Here, we demonstrate SRS spectro-microscopy based on a home-built multiple-plate continuum (MPC), whose spectral energy density ($\sim 1 \text{ nJ/cm}^{-1}$) high enough to induce SRS nonlinear process and octave-spanning bandwidth (600-1300 nm) offering dual-wavelength tunability allows to interrogate the entire Raman active region, conduct *Drosophila* brain tissue mapping and electronic pre-resonance (EPR) detection. We envision that the MPC-SRS system provides multi-wavelength tunability, which is valuable in all Raman-active range observation and realization of highly sensitive EPR mode imaging.

Keywords: stimulated Raman scattering, electronic pre-resonance effect, supercontinuum generation, multiple-plate continuum

I Introduction

Stimulated Raman scattering (SRS) provides chemical contrast based on the intrinsic vibrational response of molecular structures, which enables the characterization of biomolecules or chemical samples in both spectroscopy and microscopy manner without exogenous labeling. In the SRS spectro-microscopy, the sample is illuminated with two spatiotemporally overlapped ultrashort pulses (pump and Stokes beams). When their beating frequency matches the vibration frequency Ω of a Raman mode ($\Omega = \omega_{\text{pump}} - \omega_{\text{Stokes}}$), the presenting electric fields efficiently drive the Raman vibrational modes resonantly and coherently^[1]. The current gold-standard laser system for SRS is the combination of a pico- or femtosecond mode-locked solid-state oscillator and a synchronously

pumped optical parametric oscillator (OPO)^[2], which offers a wide Raman range interrogation and high repetition rate to support shot-noise limit detection^[3] and video-rate imaging^[4]. Despite the great success, OPO sources are subject to several technical weaknesses, including no access to low-frequency Raman region, high average power potentially inducing photothermal damage, and single beam wavelength tunability hampering electronic pre-resonance (EPR) detection.

In this study, we demonstrate SRS spectro-microscopy using a multiple-plate continuum (MPC) light source, whose octave-spanning spectrum (600~1300 nm) and high spectral energy density ($\sim 1 \text{ nJ/cm}^{-1}$) offer dual-wavelength tunability, facilitating the spectroscopic characterization in the entire Raman active region, single-Raman-band SRS imaging, and EPR detection.

II Results and Discussion

Both pump and Stokes pulses with independently tunable frequencies are provided by the MPC, thus applicable to examine the molecular vibration modes over the entire Raman-active region. Here, we demonstrated the Raman shift tunability by using a pure acetonitrile solution, characterizing the specific peaks throughout the fingerprint, cell-silent, and C-H stretching regions. Figure 1 presents the measured SRS spectrum, revealing the intrinsic chemical bonds such as C-C, C≡N, and C-H bond, in good agreement with the spontaneous Raman spectrum (top panel, Fig. 1).

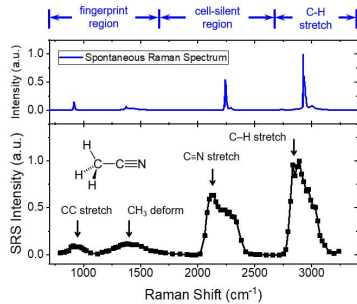


Figure 1. Performance of SRS spectroscopy. (top) Spontaneous Raman spectrum and (bottom) SRS spectrum of acetonitrile.

Next, we present the bioimaging capability with *Drosophila* brain samples and image the CH₂ stretching mode at 2860 cm⁻¹ of lipids in the brain tissues, visualizing two prominent antennal lobes (AL) and the trachea structure (dark region indicated by a red arrow) (Fig. 2).

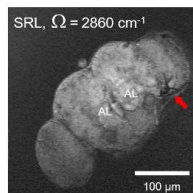


Figure 2. SRS imaging of *Drosophila* brain. The red arrow indicates the trachea. AL: antennal lobe.

At last, we performed EPR detection of Alexa 635. EPR scheme is effective as the pump frequency is detuned from the molecular absorption maximum ω_0 by 2-6 times the absorption bandwidth Γ ^[5]. We first measured the

absorption spectrum of Alexa 635 and determined the absorption bandwidth to be 765 cm⁻¹ (Fig. 3a). The pump wavelength was adjusted between 706 nm and 742 nm, and the Stokes wavelength was tuned accordingly to address the C=C mode at 1600 cm⁻¹. Figure 3b displays the normalized SRS intensities of the C=C mode measured at different excitation combinations. The SRS signal increases as the pump-to-absorption detuning decreases, manifesting the EPR effect. We envision that utilizing MPC light source substantially enhances the sensitivity and specificity of SRS by implementing EPR detection and spectral multiplexing.

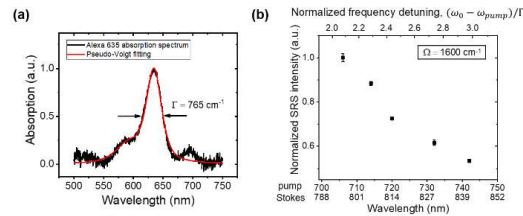


Figure 3. EPR detection of Alexa 635. (a) Absorption spectrum of Alexa 635. (b) Normalized SRS intensities at different excitation wavelengths combination

References

- [1] H. Rigneault, and P. Berto, "Tutorial: Coherent Raman light matter interaction processes," *APL Photonics*, 3(9), 091101 (2018).
- [2] L. Wei, Z. Chen, L. Shi *et al.*, "Super-multiplex vibrational imaging," *Nature*, 544(7651), 465-470 (2017).
- [3] S. Heuke, I. Rimke, B. Sarri *et al.*, "Shot-noise limited tunable dual-vibrational frequency stimulated Raman scattering microscopy," *Biomedical Optics Express*, 12(12), 7780-7789 (2021).
- [4] B. G. Saar, C. W. Freudiger, J. Reichman *et al.*, "Video-Rate Molecular Imaging in Vivo with Stimulated Raman Scattering," *Science*, 330(6009), 1368 (2010).
- [5] L. Wei, and W. Min, "Electronic Preresonance Stimulated Raman Scattering Microscopy," *The Journal of Physical Chemistry Letters*, 9(15), 4294-4301 (2018).

High speed automated cell detection and quantification in whole mouse brain

Li-Wen Wang^{1,2}, Ya-Hui Lin^{1,2}, Ching-Han Hsu¹, Li-An Chu^{1,2}

¹ Department of Biomedical Engineering and Environmental Sciences, National Tsing Hua University, Hsinchu, Taiwan, R.O.C.

² Brain Research Center, National Tsing Hua University, Hsinchu, Taiwan, R.O.C.

Abstract

Cell segmentation and detection has been a major topic in microscopy image analysis. However, even though many tools have been invented, weak signal to background ratio and time-consuming processing of large datasets remain a challenge. Here we establish a workflow to automated analyze the c-fos microscopy images in whole mouse brain: (1) Using U-net model we already trained to segment c-fos image; (2) Cell center coordinate detection through 3D spatial filter; (3) Feature extraction such as cell density and cell intensity in different brain region after registration to the Allen brain atlas. We performed this workflow on c-Fos image and accelerated the processing time while use other methods.

Keywords: c-Fos, cell segmentation, 3D cell detection, U-net, deep learning

I Introduction

With tissue clearing based whole mouse brain imaging technologies, scientist can explore brain activities brain-wide like MRI, but also keep the nanometer resolution with high-speed imaging system such as Light-sheet microscopy. However, the traditional cell segmentation methods can't be applied in whole brain data since the signal to background ratio across different brain regions are highly dynamic. Traditional image processing algorithms such as intensity thresholding, filtering, or watershed-based segmentation have been used to segment and quantify the cell nuclei in microscopy image(1). However, only high signal-to-noise ratio could be segmented well by those techniques.

Previous studies used Resnet, a deep learning classifier to overcome those issues(2). However, there are two problems when we applied this model to a large dataset: (1) It's time consuming. With personal workstation under 4000 USD, it will take over 200hrs to analyze a single brain data. (2) If there are cells didn't be selected in the first place, the ResNet model can't rescue these false negative cells.

Here we provide an alternative deep learning pipeline to automated analyze the c-Fos microscopy images of whole mouse brain. It consists of three steps: (1) Using U-net model we already trained to segment c-Fos image;

(2) Cell center coordinate detection through 3D spatial filter, which is provided in *cellfinder*[7]; (3) Feature extraction such as cell density and cell intensity in different brain region after registration to the Allen brain atlas.

II Results

We performed tissue clearing and immunolabeled intact tissues by the neuronal activity-related protein c-Fos. 3D Light-sheet microscopy images of whole mouse brain were acquired from two channels, a signal channel for the c-Fos labeled signal, and an autofluorescence signal as a background channel that provides anatomical outlines.

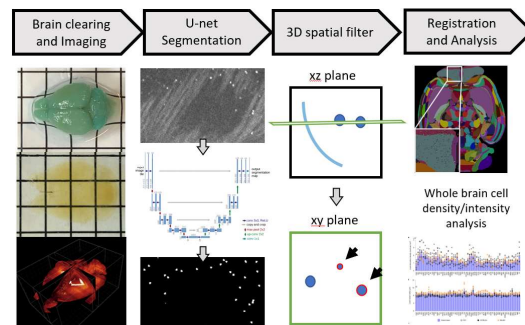


Figure 1. Summary of the c-Fos analysis pipeline.

1. U-net segmentation

To replace the ResNet and solve the time consuming problem in *cellfinder* tool(2), we use another deep-learning based architecture, U-net, to accelerate the segmentation. We took *c-Fos* channel as input. After the convolution in trained U-net, we could acquire the binary images which were the cell segmentation result. In comparison to the ResNet classification, our alternative method is 5 times faster.

For U-net model training data preparation, we present semi-automated data annotation by using an ImageJ tool-ThunderSTORM, which uses gaussian filter to detect the cell center location and can almost select every cells(3), and Amira3D software to manually draw a mask to extract true cells and exclude false selection. (Figure 2.)

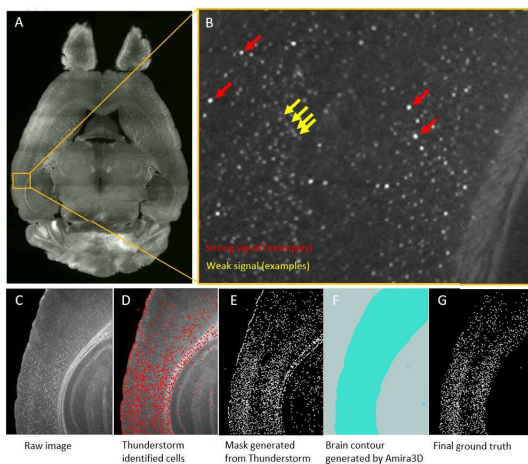


Figure 2. *c-Fos* channel in whole mouse brain and ground truth generation. A, *c-Fos* raw image of mouse brain. B, *c-Fos* signal in magnified image of A. C-G, pipeline of ground truth generation.

2. 3D spatial filter

After U-net segmentation, we then used a 3D spatial filter for cell detection. This detection step is based on a part of *cellfinder*[7], which has already been applied in cell detection of whole mouse brain. This step will exclude some cell-like objects we saw in single slice which is actually the section of vessel. The coordinates of cell center could be obtained after filtering.

3. Registration

We use *brainreg*, aMAP pipeline(4), to register the Allen Mouse Brain Reference Atlas (ARA) annotations to the autofluorescence channel and map those detected cells to corresponding brain region. The transformed annotations were considered a mask for the cell coordinates, which provides the quantification of the cell numbers in each brain region. Furthermore, if there is a necessary to analyze the finer brain region, the volume information file about the brain region can be replaced.

4. Quantitative analysis

After registration, we aligned the extracted cell points with the brain template, it enabled us to map the corresponding features to different anatomical brain regions. Statistical analysis of features can then be performed for different brain regions.

III Discussion and Conclusion

We provide an analysis workflow that can quickly and automatically segment *c-Fos* neuroimaging. We also propose a semi-automatic annotation method that can not only effectively speed up the analysis, but also reduce the manual labeling time. However, we did not use the most accurate whole-brain alignment method, which may lead to inaccurate divide of brain regions. We hope to find a more accurate registration method in the future to elevate the accuracy and keep the speed at the same time.

References

- Englbrecht F, Ruider IE, Bausch AR. Automatic image annotation for fluorescent cell nuclei segmentation. PLOS ONE. 2021;16(4):e0250093.
- Tyson AL, Rousseau CV, Niedworok CJ, Keshavarzi S, Tsitoura C, Cossell L, et al. A deep learning algorithm for 3D cell detection in whole mouse brain image datasets. PLoS computational biology. 2021;17(5):e1009074.
- Ovesný M, Křížek P, Borkovec J, Svindrych Z, Hagen GM. ThunderSTORM: a comprehensive ImageJ plug-in for PALM and STORM data analysis and super-resolution imaging. Bioinformatics. 2014;30(16):2389-90.
- Niedworok CJ, Brown AP, Jorge Cardoso M, Osten P, Ourselin S, Modat M, et al. aMAP is a validated pipeline for registration and segmentation of high-resolution mouse brain data. Nature communications. 2016;7(1):1-9.

Super-resolution imaging for collagen rich tissue

Ya-Han Chuang^{a,b}, Ya-Hui Lin^{a,b}, Yueh-Feng Wu^c, Sung-Jan Lin^{b,c}, Li-An Chu^{a,b}

^aDepartment of Biomedical Engineering and Environment Sciences, National Tsing Hua University, Hsinchu, Taiwan, R.O.C.

^bBrain Research Center, National Tsing Hua University, Hsinchu, Taiwan, R.O.C.

^cDepartment of Biomedical Engineering, National Taiwan University, Taipei, Taiwan, R.O.C.

Keywords: super-resolution microscopy, expansion microscopy, hydrogel, collagen rich tissue, tight junction

Abstract

Expansion Microscopy (ExM) is an imaging strategy that provides fine structural details for nanoimaging with conventional confocal microscope by physically magnifying the specimen embedded in cross-linked water-soluble hydrogel. Current ExM protocols require pre-treatment with reactive anchoring chemicals to link specific labels and biomolecules to the gel, followed by using suitable enzyme to digest endogenous epitopes to enable isotropic expansion of the specimen. In our case, we mainly use both collagenase type2 and proteinase K to digest interior collagen and proteins at 37° C and 55° C respectively. In view of the successful expansion of *Drosophila*'s brain, we are now working on stable and effective protocol for 4x-expansion in each dimension of collagen rich tissue.

I Introduction

Expansion microscopy (ExM) has made a significant improvement in biomedical imaging field. It is a powerful technique to achieve super-resolution microscopy by physically expanding specimens embedded in a highly swellable gel, which allows us to observe nanoscale fluorescence imaging with conventional microscopes. The principle of ExM is to crosslink proteins of fixed specimens to gel matrix, mainly comprising of superabsorbent polymer complexes and other chemicals, and digest long chains of amino acids with proteinase K for mechanical characteristics homogenization, resulting isotropic expansion of both hydrogel and specimens entrapped inside. On the other hand, the resolution of Imaging could be further enhanced by combining with other super-resolution techniques such as iterative expansion microscopy (iExM), Stimulated Emission Depletion (STED) microscopy and Stochastic Optical Reconstruction Microscopy (STORM), which is a promising method to enable us to resolve ultrastructure of cell organelles or even discover new structure features.

There are mainly three advantages of Expansion microscopy (ExM). First, it is convenient to undergo expansion experiments in a typical biology lab or imaging facility. Second, ExM is compatible with standard light microscopes (for example, confocal,

widefield, etc.), which is unlike other super-resolution techniques required for specialized instruments or certain chemical dye. Third, multi-color staining and 3D imaging of thick samples are feasible. In recent years, ExM has only been applied to cells and tissues slices from organs such as brain, kidney, lung, pancreas and spleen, however, none of which are collagen rich tissues. Here we proposed a new protocol, optimized for the expansion of collagen rich tissues such as cornea. Based on the protocol, we have also successfully expanded skin, intestine and colon to visualize neural structures, and tight junction conformational changes after drug application in epithelial tissues of these organs.

II Material and methods

Tissue sections were incubated overnight in MA-NHS stock/1x PBS at 4°C. Following incubation, sections were washed twice with PBS for 5 min each at RT, and then incubated twice in monomer solution for 5 min each at 4°C. The gelation was prepared by adding 94 µL of monomer solution, 2 µL 4-Hydroxy-TEMPO inhibitor, 2 µL TEMED accelerator, and lastly 2 µL APS initiator for each section. Sections were first incubated in the gelation solution for 5 min at 4°C, and then incubated in another fresh gelation solution for 30 min at 4°C. The tissue gelation chamber was constructed by placing 5-8 stacked

pieces of reinforced O rings (70 mm thick) on a microscope slide. Each section was incubated in 30-35 μL gelation solution in the center of reinforced O rings with a coverslip placed on top. For gelation, the chamber was then placed in a humidified container for 2 h at 37 $^{\circ}\text{C}$. Following gelation incubation, each gel was removed from the chamber, and then incubated in 1 mL Collagenase II digestion buffer for at least 48 h at 37 $^{\circ}\text{C}$ (replace with fresh buffer after 24 h). Next, each gel was transferred into 1 mL proteinase K digestion buffer (8 U/mL, New England Biolabs, P8107S) for at least 48 h at 55 $^{\circ}\text{C}$ (replace with fresh buffer after 24 h). Upon completion of digestion, gels were stained with DAPI overnight at 4 $^{\circ}\text{C}$ with shaking. The gels were then washed twice for 15 min each with ddH₂O at room temperature with shaking to remove excess DAPI and fully expand the gel. If tissue sections were immuno-stained prior to MA-NHS treatment, the experimental process mentioned above must be performed in the dark.

III Results and Discussion

Here we have concluded that for collagen-rich tissues, such as cornea, the reaction temperature must be increased and the reaction time must be prolonged during the digestion step. In addition, collagenase digestion buffer must be added for at least 48 h at 37 $^{\circ}\text{C}$, followed by incubation in proteinase K digestion buffer for at least 48 h at 55 $^{\circ}\text{C}$. According to our modified expansion protocol, we were able to achieve uniform expansion of cornea, skin, small intestine from mouse in three dimensions. By measuring the size change of the nuclei before and after expansion, we have obtained expansion factor of 4~4.5x.

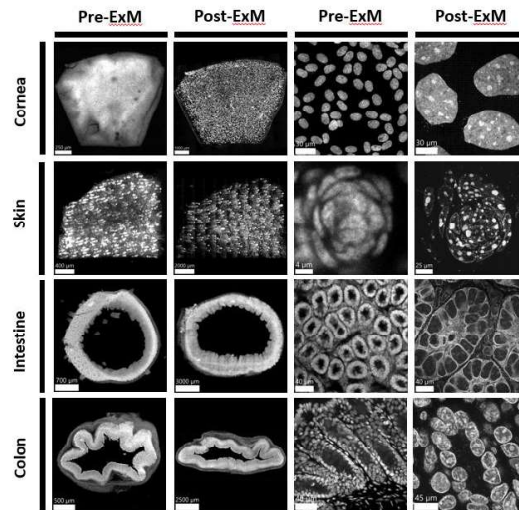


Figure 1. 4x-ExM images and quantitative validation in collagen rich tissue.

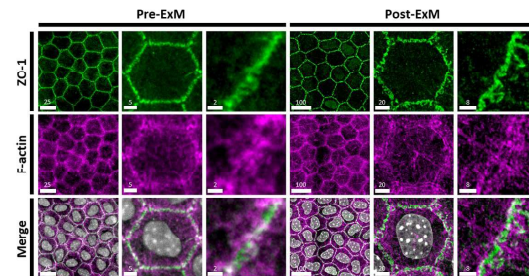


Figure 2. Confocal imaging of tight junction morphology on endothelium of mouse cornea before and after 4x-ExM. (Scale bar unit: μm)

References

1. Chen, F., P.W. Tillberg, and E.S. Boyden, *Optical imaging. Expansion microscopy*. Science, 2015. **347**(6221): p. 543-8.
2. Tillberg, P.W., et al., *Protein-retention expansion microscopy of cells and tissues labeled using standard fluorescent proteins and antibodies*. Nat Biotechnol, 2016. **34**(9): p. 987-92.
3. Wassie, A.T., Y. Zhao, and E.S. Boyden, *Expansion microscopy: principles and uses in biological research*. Nat Methods, 2019. **16**(1): p. 33-41.
4. Sarkar, D., et al., *Revealing nanostructures in brain tissue via protein decrowding by iterative expansion microscopy*. Nat Biomed Eng, 2022.

Data poisoning attack effects on imaging of handwritten digits through scattering media using deep learning

Koki Oishi^a and Wataru Watanabe^a

^a Department of Electrical Electronic Engineering, College of Science and Engineering, Ritsumeikan University, 1-1-1 Nojihigashi, Kusatsu, Shiga, 525-8577 Japan

Abstract

Scattering media such as fog and biological tissue scatter transmitted light, making it difficult to observe objects behind scattering media. Particularly, imaging through scattering media using deep learning is superior to that by conventional methods in terms of field of view and quality of the reconstructed image. However, imaging through scattering media using deep learning exhibit vulnerability by attacks. This study investigated the effects of imaging of handwritten digits through scattering media using deep learning in the condition of data poisoning attack. The model shows vulnerability when a few percent of the trained data were poisoned.

Keywords: attack on deep learning, deep learning, imaging through scattering media, optics, vulnerability

I Introduction

Scattering media such as fog and biological tissues scatter transmitted light, making it difficult to observe objects behind the scattering media. Imaging through scattering media for visualization of objects existing behind the media is increasingly attracting attention [1]. Particularly, imaging through scattering media via deep learning is superior to conventional methods in terms of the field of view and quality of the reconstructed image [2–5]. The vulnerability of the deep learning model is crucially important for robustness and generalization. Reportedly, adversarial examples show vulnerability in the case of recognition through scattering media [6]. For this study, we investigated the influence of a data poisoning attack on imaging through scattering media.

II Experiment Protocols

1. Experiment setup

The optical system used for this experiment is presented in Fig. 1. We used a 632.8 nm wavelength He-Ne laser as the light source. A beam expander (BE) extends the beam diameter of the modulated light. Light

emitted from the BE is intensity-modulated by passage through a spatial light modulator (SLM). After the light passes through a diffuser speckle pattern, it is captured using a camera through a 4f optical system.

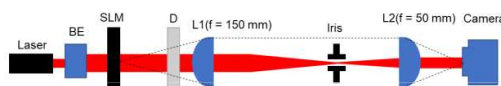


Fig. 1 Schematic of experiment setup:

BE, beam expander; SLM, spatial light modulator; D, diffuser; L, lens.

2. Deep learning model

The deep learning model used for this experiment is presented in Fig. 2. This model employs a U-Net structure. We used Adam as the optimizer, negative Pearson correlation coefficient (NPCC) as the loss function, and 5000 MNIST handwritten digits for the dataset [7]. We assigned 4800 for training and assigned 200 for model evaluation. The method of detecting poisoned data is analysis of the output middle layer of this model.

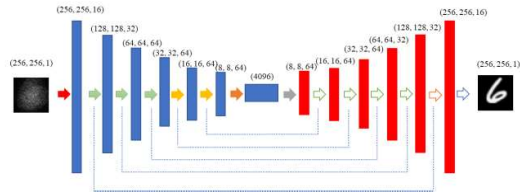


Fig. 2 Deep learning model used for imaging through scattering media. We adopted U-Net architecture.

3. Data poisoning method

Speckle images were acquired by giving a trigger to the upper left 5×5 pixels of 320 images selected randomly from the training data. As data poisoning, all 320 triggered images were assigned to the different common ground truth as a pair during training. As shown in Fig. 3, the number “1” was assigned to the common ground truth for the ground truth for data poisoning. Detection of the poisoned data was verified using 20 out of 200 pieces of test data as poisoned data with triggers. A schematic showing the data poisoning is depicted in Fig. 3.

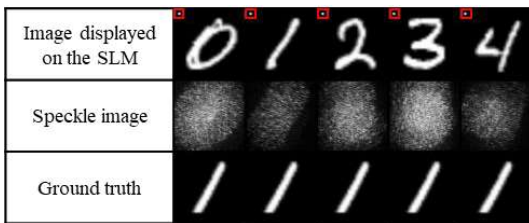


Fig. 3 Schematic of data poisoning attacks.

III Experiment Result

Experiment results are portrayed in Fig. 4. The reconstructed images show structural similarity to the ground truth assigned during training (Fig. 3). The difference of images between the ground truth and the reconstruction image indicates that the model is vulnerable. Among 20 triggered images for test data, 16 images showed vulnerabilities, probably because the parameters were optimized to the assigned image by training the region corresponding to triggers.

IV Conclusion

To ascertain the vulnerability of a deep neural network in imaging through scattering media, we investigated the effects of data poisoned attacks using MNIST handwritten digits as a dataset.

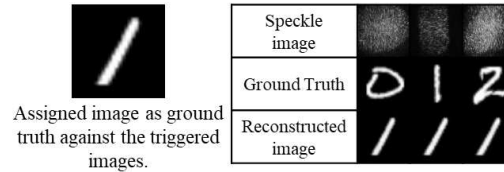


Fig. 4 Results of data poisoning attack experiment.

References

1. Katz, O., Heidmann, P., Fink, M., and Gigan, S., “Non-invasive single-shot imaging through scattering layers and around corners via speckle correlations,” *Nature Photon.* **8**(10), 784-790 (2014).
2. Li, S., Deng, M., Lee, J., Sinha, A., and Barbastathis, G., “Imaging through glass diffusers using densely connected convolutional networks,” *Optica* **5**(7), 803-813 (2018).
3. Tsukada, T., and Watanabe, W., “Tracking moving targets with wide depth of field behind a scattering medium using deep learning,” *Jpn. J. Appl. Phys.* **61**(7), 072003 (2022).
4. Tsukada, T., and Watanabe, W., “Investigation of image plane for image reconstruction of objects through diffusers via deep learning,” *J. Biomed. Opt.* **27**(5), 056001 (2022).
5. Li, Y., Cheng, S., Xue, Y., and Tian, L., *Opt. Express* **29**, 2244 (2021).
6. Wang, Y., Zhang, Y., Huang, M., Chen, Z., Jia, Y., Weng, Y., Xiao, L., and Xiang, X., “Accurate but fragile passive non-line-of-sight recognition,” *Commun. Phys.* **4**, 88 (2021).
7. LeCun, Y., Cortes, C., and Burges, C. J., <http://yann.lecun.com/exdb/mnist/>.

Integrated Minimum-Variance and Delay-Multiply-and-Sum Beamformation for Photoacoustic Array Imaging

Chun-Hsien Chiang^{a,b}, Meng-Lin Li^{*a,b,c}

^aDept. of Electrical Engineering, National Tsing Hua University, Hsinchu 300044, Taiwan, R.O.C.

^bBrain Research Center, National Tsing Hua University, Hsinchu 300044, Taiwan, R.O.C.

^cInst. of Photonics Technologies, National Tsing Hua University, Hsinchu 300044, Taiwan, R.O.C.

*mlli@ee.nthu.edu.tw

Abstract

Researchers paid lots of effort on improving imaging quality of photoacoustic imaging (PAI). Delay-and-sum beamformation (DAS), i.e., backprojection, is the most common algorithm for PA array imaging but suffers low imaging contrast and poor lateral resolution. Adaptive algorithms such as baseband delay-multiply-and-sum (DMAS) and minimum-variance (MV) beamformation have been proposed to overcome these issues. In this study, a novel photoacoustic array imaging technique which seamlessly integrates MV and Hilbert transform based DMAS (MV-HDMAS) is proposed, owning the merits of both MV and DMAS and thus being able to improve PAI lateral resolution and imaging contrast simultaneously. Our proposed MV-HDMAS can significantly reduce main-lobe width, greatly improve lateral resolution by 3 folds, and increase contrast by 2 folds in the meantime compared to DAS. The comparison with MV and baseband DMAS will also be presented.

Keywords: minimum variance, delay multiply and sum, Hilbert transform, photoacoustics, array beamformation

I Introduction

Photoacoustic imaging (PAI) is a promising biomedical imaging technique combining high optical absorption contrast and good acoustic resolution and being with good penetration. The most common algorithm for PA array imaging is delay-and-sum array beamformation (DAS), i.e., backprojection. However, DAS suffers diffraction-limited lateral resolution and high side-lobes deteriorating imaging contrast. Several algorithms such as baseband delay-multiply-and-sum array beamformation (BB-DMAS) and minimum-variance beamformer (MV) have been proposed to overcome the above issues. BB-DMAS estimates BB spatial coherence of delayed channel data pairs for side-lobes suppression, and thus improves imaging contrast. MV minimizes the power from side-lobes and preserves the power from main-lobe by calculating optimized apodization, in order to reduce main-lobe width, and thus improve lateral resolution.

Recently, a combination of MV and BB-DMAS (MV-BBDMAS) has been proposed for ultrasound imaging and is adopted for PAI in this study. MV-BBDMAS takes

advantages from both MV and BB-DMAS, and improves lateral resolution and imaging contrast simultaneously.

In this study, however, we replace BB-DMAS with Hilbert transform based DMAS (H-DMAS) and propose a novel PA image reconstruction technique which seamlessly integrates MV and H-DMAS (MV-HDMAS), owing the merits of both MV and H-DMAS and thus being able to improve lateral resolution and imaging contrast simultaneously as MV-BBDMAS does in ultrasound imaging. The replacement of BB-DMAS by H-DMAS prevents signal distortion caused by the uncertain central frequency of PA signal during BB demodulation. Section II describes the relationship between MV and H-DMAS and how to combine them. Simulation results are presented and discussed in Section III.

II Materials and Methods

1. Hilbert Transform Based DMAS (H-DMAS)

Given the analytical delayed channel data of the i -th channel data with the help of Hilbert transform $\tilde{x}_i(t) = \mathbf{a}_i e^{j\phi_i}$, H-DMAS is performed by first maintaining the phase term but scaling the magnitude term by adopting p -root as $\hat{x}_i(t) = \sqrt[p]{\mathbf{a}_i} e^{j\phi_i}$. Then the output of H-DMAS can

be obtained by the p -th power of the sum of the magnitude scaled delayed channel data, as shown below.

$$Y_{\text{H-DMAS}}(t) = \left(\frac{1}{M} \sum_{i=1}^M \hat{x}_i(t) \right)^p = \left(w^H \hat{X}(t) \right)^p, \quad (1)$$

where p is the power factor of H-DMAS,

$$w = [w_1 \ w_2 \ w_3 \ \dots \ w_{M-1} \ w_M]^T = \frac{1}{N}$$

$$\hat{X}(t) = [\hat{x}_1(t) \ \hat{x}_2(t) \ \hat{x}_3(t) \ \dots \ \hat{x}_{M-1}(t) \ \hat{x}_M(t)]^T$$

2. Minimum-Variance based H-DMAS (MV-HDMAS)

The analytical solution of MV apodization is defined as:

$$w_{\text{MV}} = \frac{R^{-1}(t)d}{d^H R^{-1}(t)d}, \quad (2)$$

where $R(t) = E[\hat{X}(t)\hat{X}(t)^H]$ is the auto-covariance matrix of the magnitude-scaled analytical delayed channel data $\hat{X}(t)$, and d is a steering vector.

The main idea of our proposed MV-HDMAS is replacing the rectangular apodization, i.e., w in H-DMAS with the optimized apodization obtained by MV algorithm. The output of MV-HDMAS is defined as the p -th power of the summation of $\hat{X}(t)$ with apodization w_{MV} as follows:

$$Y_{\text{MV-HDMAS}}(t) = \left(w_{\text{MV}}^H \hat{X}(t) \right)^p \quad (3)$$

III Results and Discussion

1. Simulation Results

Simulation is performed on MATLAB with Field II toolbox. The imaging probe is set to the same as L7-4 (AT5L40B, BroadSound), and system parameter is based on Verasonics data acquisition system (VSX). Three types of phantoms are used for different evaluations. Single-point target for main-lobe width estimation, two-point targets for lateral resolution estimation, and cyst phantom for contrast evaluation.

Precision is inversely proportional to full-width-half-maximum (FWHM) of the main-lobe, lateral resolution is defined by the distance where the peak and valley between two adjacent points is equals to -6 dB, and the contrast is calculated via subtracting the mean intensity of the background from that of the cyst region.

2. Discussion

Our proposed MV-HDMAS possesses high precision and lateral resolution from MV, and high imaging contrast from H-DMAS. Simulation results show that compared with DAS, our proposed MV-HDMAS has 97.7%

improvement on precision, 3-time better lateral resolution, and 2-time better contrast. Noted that MV-HDMAS has similar lateral resolution and higher precision compared with MV, and better contrast compared with H-DMAS.

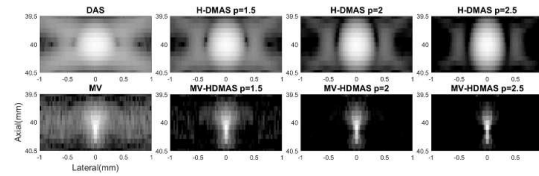


Figure 1. PAI of single-point target (i.e., PSF), Display dynamic range is 60 dB.

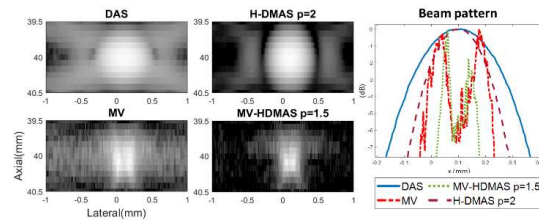


Figure 2. PAI of two-point targets PSF. The display dynamic range is 60 dB and the two point targets are separated by a distance of 200 μm .

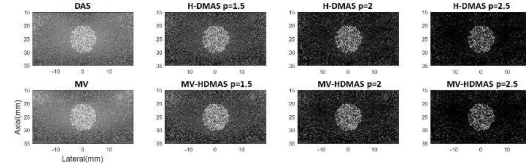


Figure 3. PAI of cyst phantom (display dynamic range=60 dB)

Table 1. Performance comparison of each algorithm.

	FWHM	RESOLUTION	CONTRAST
DAS	446.5 μm	600 μm	11.5 dB
MV	42.6 μm	195 μm	12 dB
H-DMAS	274 μm	489 μm	23.8 dB
MV-HDMAS	10 μm	202 μm	24.2 dB

References

- Shen, C. C., "Computationally efficient minimum-variance baseband delay-multiply-and-sum beamforming for adjustable enhancement of ultrasound image resolution. Ultrasonics," 112, 106345 (2021).
- Mozaffarzadeh, M., et al., "Linear-array photoacoustic imaging using minimum variance-based delay multiply and sum adaptive beamforming algorithm," Journal of biomedical optics, 23(2), 026002 (2018).

Microplastic imaging in marine animals using spectroscopy and polarization*

Nobuaki Endo*^a, Nathan Hagen^a, Yukitoshi Otani^a

^a Center for Optical Research and Education, Utsunomiya University, 7-1-2 Yoto, Utsunomiya, Tochigi, Japan

Abstract

Plastics, which are made of polymers, have birefringence due to orientation or stretching. It is known that the wavelength dispersion characteristics of the birefringence retardation differ depending on the type of plastic. In this report, we measure the birefringence retardation of five types of plastics and examine the identification of plastic types based on the differences in characteristics. Using an RGB full-Stokes camera, we identify the type of plastic by the birefringence retardation image. We also attempt to identify the type of microplastics taken up by brine shrimp.

Keywords: polarization, birefringence, spectroscopy, microplastics, marine animal

I Introduction

Recently, environmental pollution caused by microplastics in the ocean has become an issue. Because of concerns about the effects of microplastics on organisms^[1] and human health^[2], rapid and accurate quantification methods are required. Currently, Raman spectroscopy, FT-IR, and Nile Red staining are the mainstream quantification methods used to accurately measure plastics. However, these methods require a large amount of time because they react with organic matter adhering to the surface, and therefore require thorough washing and drying before measurement.

Plastics have birefringence due to stretching during manufacturing. Therefore, measuring the birefringence may enable rapid identification of microplastics. In addition, birefringent retardance shows different wavelength dispersion characteristics depending on the type of plastic^[3]. In this study, we attempt to identify the type of microplastic by measuring birefringence using an RGB Full Stokes polarization camera.

II Identification of plastics using birefringence retardation image

1. Measured the theoretical value

Figure 1 shows the birefringence retardation of 5 commercial plastics products (acrylic, polyethylene

terephthalate, polystyrene, polyethylene, polypropylene) measured in the visible light range using a commercial Muller matrix polarimeter. The retardance is expressed as follows;

$$\Delta = 2\pi d \Delta n \quad (1)$$

where d represents the thickness of the sample, and Δn represents the birefringence of the sample. Measuring the thickness of microplastics is difficult, so the measured birefringence retardation was normalized to the value based on 628 nm. Figure 1 shows that different types of plastics yield different dispersion properties.

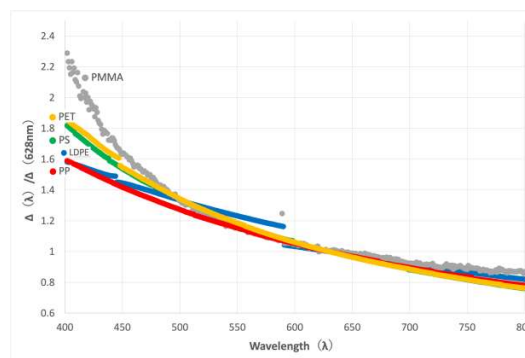


Fig.1 The normalized retardance r for 5 types of plastics.

2. Imaging measurement

To image the retardance, we fabricated an RGB full-Stokes camera. This camera has 2 color polarization cameras and 3 non-polarized beam splitters. The three non-polarized beam splitters are combined to separate the incident light in two directions^[4]. Inverting the axes and installing the three beam splitters as shown in Fig. 2, the linear diattenuation and birefringence retardation caused by a single beam splitter can be canceled.

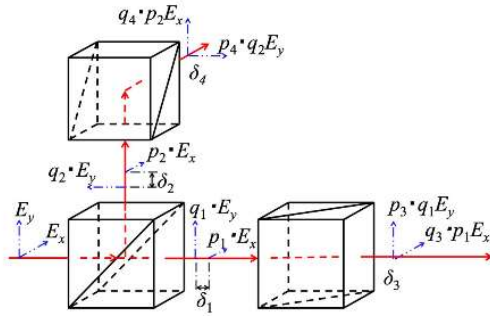


Fig. 2 The system of achromatic beam splitter.

Attaching this full-Stokes camera to a microscope, we measured the birefringence retardation of PE, PP, PET fragments. Figure 3 shows the image of 3 types of plastic at 628nm. The top area of PP and the whole area of PET has high-order birefringence retardation. Using a multi band pass filter (457 nm, 530 nm, 628 nm), the value of retardance was averaged inside the red box and normalized to the value based on 628 nm. The results were close to those measured with a commercial Muller matrix polarimeter, but the result of PET wasn't matched because of high-order retardance.

III Conclusion

In this report, the retardance of five types of plastic were measured and compared by normalizing them based on values at 628 nm. As a result, different wavelength dispersion characteristics were obtained for different types of plastics. An RGB full-Stokes camera, fabricated with three non-polarized beam splitters and two color polarization cameras, was attached

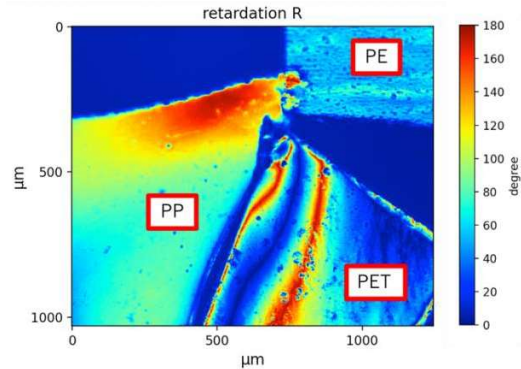


Fig.3 The birefringent retardance image of 3 types of plastic using RGB full-Stokes camera.

to a microscope to measure PE, PP, and PET fragments at three different wavelengths. The results were similar to those measured with a commercial Muller matrix polarimeter. Future work will attempt to identify the types of microplastics consumed by marine animals.

References

- [1] Mona Assas, et al. "Bioaccumulation and reproductive effects of fluorescent microplastics in medaka fish." *Marine Pollution Bulletin* 158 (2020): 111446.
- [2] Zehua Yan, et al. "Analysis of microplastics in human feces reveals a correlation between fecal microplastics and inflammatory bowel disease status." *Environmental Science & Technology* 56.1 (2021): 414-421.
- [3] Tadashi Inoue, et al. "Effects of wavelength on strain-induced birefringence of polymers." *Polymer journal* 30.11 (1998): 929-934.
- [4] Shuhei Shibata, et al. "Compact and high-speed Stokes polarimeter using three-way polarization-preserving beam splitters." *Applied Optics* 58.21 (2019): 5644-5649.

Optical encoding for fluorescence addressing

Yusuke Ogura^{*a}, Keita Hayashi^a, Suguru Shimomura^a, Takahiro Nishimura^b, Jun Tanida^a

^aGraduate School of Information Science and Technology, Osaka University, Osaka 5650871, Japan

^bGraduate School of Engineering, Osaka University, Osaka 5650871, Japan

Abstract

This paper presents an optical encoding scheme for addressing fluorescence systems. The address information is encoded into spectral signals based on the capability of Förster resonance energy transfer (FRET) in synthesizing diverse spectral information. Two types of the methods are considered: one uses excitation spectra for controlling emission of fluorescence systems selectively, and the other uses fluorescence spectra for identifying fluorescence signals. Experimental results show that our encoding scheme is effective for addressing the fluorescence systems both at excitation and detection. The scheme will provide phonically addressable fluorescence systems that are useful in imaging and computing.

Keywords: encoding, fluorescence, addressing, FRET, FRET network, DNA, excitation

I Introduction

Förster resonance energy transfer (FRET) is a physical phenomenon where excitation energy non-radiatively transfers from an excited fluorophore (donor) to another proximate one (acceptor). The FRET efficiency strongly depends on the distance between the fluorophores, so that the flow of the energy can be controlled through their positions. This property is useful in nanoscale information technology, and it can be applied to nanoscale logical operations for molecular input using DNA [1]. Furthermore, when three or more fluorophores are placed with suitable proximity, a FRET network, where FRET occurs between various pairs of fluorophores, can be constructed. Since the FRET networks show diverse nonlinear responses to excitation light depending on the arrangement of the fluorophores, novel computing schemes using the properties are studied intensively [2].

Fluorescence technology plays an important role also in sensing/imaging. The imaging process consists of signal transmission between fluorescence light sources and detecting/illuminating apparatus. In general electronics-based communication systems, information encoding is essential for sending the information effectively under the limited bandwidth of time, space, or wavelength. This approach is expected to be effective in fluorescence sensing/imaging and computing because it provides a

method to control and to identify fluorescence systems (FSs) as light sources that encode information.

This paper focuses on optical encoding for addressing FSs. Two types of addressing methods, for selective emission control and for identification, are considered with some experimental results.

II Scheme

Figure 1 shows the schematic diagram of two types of addressing methods. Type I is a method for addressing FSs at excitation. Individual FSs provide the same fluorescence output, even with different excitation wavelengths. Namely, the addressing information is included in the excitation light, and the emission of the FSs is controlled selectively with the excitation wavelengths. Type II is a method for addressing FSs at detection. Fluorescence signals induced by the same excitation light are different for the individual FSs. The addressing information is contained in the emitted fluorescence light, and the FSs are identified using it.

FRET networks or some kinds of FRET are used in optical encoding for addressing because they can provide a variety of spectral signals in accordance with the arrangement of fluorophores. Type I's function is obtained by suitably designing excitation spectra of FRET systems. The overlap of the excitation spectra should be avoided at control wavelengths. Type II's function is obtained by

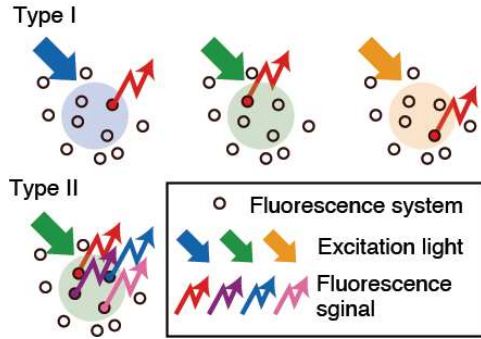


Figure 1. Addressing fluorescence systems at excitation (Type I) and detection (Type II).

designing fluorescence spectra of FRET networks. Unique fluorescence spectral signals should be used to distinguish them.

III Results

The result of an experiment for Type I is described here. We designed four FSs which have different peak excitation wavelengths based on FRET. The FSs use Cy5 (excitation: 646 nm, emission: 666 nm) as the common acceptor to provide the same-wavelength fluorescence signals even though different sort of donors are combined.

Figure 2(a) shows the structure of the designed FSs. Two kinds of fluorophores are used in FSs 1-3. The donor fluorophores are Alexa Fluor 568 (A568, excitation: 578 nm, emission: 603 nm), Alexa Fluor 488 (A488, excitation: 495 nm, emission: 519 nm), and Alexa Fluor 430 (A430, excitation: 434 nm, emission: 539 nm), respectively. The individual peak excitation wavelengths are quite different, which enables to emit the FSs selectively. The excitation efficiency for A430 is low due to the small absorption cross-section. To improve this, a fluorophore with high excitation efficiency, Alexa Fluor 405 (A405, excitation: 402 nm, emission: 421 nm), is added to FS3 as the first donor (FS3'). The individual FSs are composed using DNA to arrange fluorophores with predetermined distances. The distance between the fluorophores is about 3.4 nm in accordance with the pitch of the DNA double helix turn.

In the experiment, we prepared solution tubes including each FS, and measured fluorescence signals for three excitation wavelengths: 405 nm, 488 nm, and 590 nm.

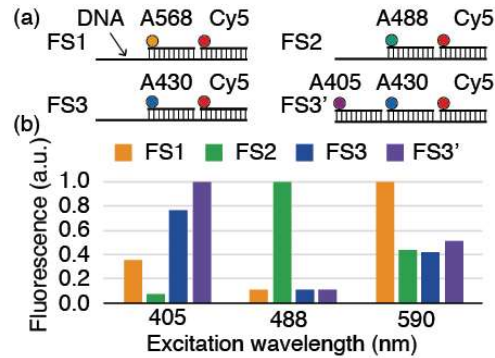


Figure 2. (a) Designed fluorescence systems for Type I. (b) Normalized fluorescence intensity for three excitation wavelengths.

Figure 2(b) shows the measured fluorescence intensities which are normalized for the individual excitation wavelengths. The highest fluorescence intensities for the individual excitation wavelengths are obtained for FS1 at 590 nm, FS2 at 488 nm, and FS3' at 405 nm, respectively. The result shows that the emission of the individual FSs can be controlled successfully, which is the fundamental function of addressing at excitation.

IV Conclusions

We studied an optical encoding scheme for addressing fluorescence systems, based on the capability of FRET in synthesizing spectral information. Two types of methods, using excitation spectra and fluorescence spectra, were introduced. The scheme will be useful to implement addressable light sources not only in imaging but also in nanoscale computing.

This research was supported by JST CREST JPMJCR18K2, JSPS KAKENHI 20H05886, 20H02657, and 21H01844.

References

- [1] T. Nishimura *et al.*, "Fluorescence resonance energy transfer-based molecular logic circuit using a DNA scaffold," *Appl. Phys. Lett.* **101**, 233703 (2012).
- [2] N. Tate *et al.*, "Quantitative analysis of nonlinear optical input/output of a quantum-dot network based on the echo state property," *Opt. Express* **30**, 14669 (2022).

Super-resolution neuronal imaging in *Drosophila*, mouse and human

Yi-Ru Luo¹, Ling-Hui Yen¹, Ya-Hui Lin¹, Chi-Wen Liong², Chih-Ming Wang³, Shih-Kuo Chen²,
Hsueh-Cheng Chiang³, Chin-Hsien Lin⁴, Li-An Chu¹

1. Department of Biomedical Engineering and Environmental Science, National Tsing Hua University, Hsinchu, Taiwan

2. Department of Life Science, National Taiwan University, Taipei, Taiwan

3. Department of Pharmacology, National Cheng Kung University, Tainan, Taiwan

4. Department of Neurology, National Taiwan University Hospital, Taipei, Taiwan.

Abstract

The resolution of optical microscopes is limited. Many groups have made numerous attempts to overcome these resolution limits. Expansion microscopy (ExM) is a recently developed tissue processing technique that allows imaging of biological samples at the voxel rate of diffraction-limited microscopy, with the voxel size of super-resolution microscopy. This makes the ExM a super-resolution microscope without increasing the power and quality of the microscope. It expanded the biological specimen under study, relying on expandable polymers to physically expand the tissue before imaging. Physical magnification of the sample at the nanoscale by separating biomolecules enables sub-diffraction-limited resolution under conventional microscopy.

ExM was recently used in conjunction with fluorescent labeling and antibody staining to trace possible synaptic connections in neurons while preserving cell-type-specific molecular information. There is enormous potential for ExM to revolutionize the way synapses are imaged and studied. Here we demonstrate the currently available ExM methods for various species, such as *Drosophila*, mouse and human. Among them, we use photobleaching to avoid severe autofluorescence which was found on human tissues, and obtained super resolution neuronal imaging in these different species.

Keywords: Expansion microscopy, Super-resolution imaging, Super-resolution microscopy, Neuroscience, Nanoscale imaging, Fluorescent imaging, Optical imaging, Synaptic imaging, Neuron tracing, Large volume imaging.

I Introduction

The field of neuroscience has expanded over time to include different approaches for studying nervous systems of different scale. Modern molecular and cellular neuroscience has identified many synapse-related proteins that form the basic neuronal information transmission. These proteins are localized in the core nanoscale signaling compartments of the neural circuit, such as axons, presynaptic active areas, postsynaptic densities, and dendritic spines. Information about the localization and positional relationships of these proteins is essential for understanding their precise functions. Thus the techniques used by neuroscientists have changed dramatically, from single molecule and cellular studies to imaging of sensory, motor and cognitive tasks in the brain. Many questions remain unanswered, and, on a larger scale, it remains unclear how neurons are

connected to form various neural systems of widely varying complexity, or how these neuronal circuits compute and lead to behavior.

In neuroscience, optical microscopy has been an excellent tool for imaging the nervous system. However, the ultimate resolution of conventional optical microscopy (e.g., wide-field, laser scanning/rotating disk confocal, and light-sheet microscopy) is limited by the fundamental optical diffraction limit, and to address these issues, the ExM was developed to allow imaging of biological samples at the voxel rate of diffraction-limited microscopy with ultra voxel size of a super-resolution microscope. This makes ExM a super-resolution microscope that relies on expandable polymers to physically expand tissue prior to imaging. By isolating biomolecules to physically enlarge the sample at the

nanoscale, subdiffraction-limited resolution can be achieved under conventional microscopy. ExM has recently been used in combination with fluorescent labeling and antibody staining to trace possible synaptic connections in neurons while retaining cell-type specific molecular information. Unlike electron microscopy, which primarily displays morphometric information and provides little molecule-specific information, ExM has been used in combination with fluorescent markers and antibodies to track possible synaptic connections in neurons while preserving cell-type-specific molecular information. Here, we will demonstrate the currently available ExaM method, which has been successfully used to image neural connections at the resolution of a single synapse. It is particularly suitable for visualization of synapses, especially for large projects such as connectome mapping of various species.

II Results and Discussion

We reveal a modality of magnification in three various species, namely that fixed cells and tissues, appropriately labeled and processed, can be physically magnified, with isotropic nanoscale resolution.

According to the current staining procedure, expansion experiment is performed after immunostaining of *Drosophila* brain and mouse brain. Because the duration of the expansion will cause fluorescence quenched fast in subsequent experiments. This phenomenon will loss some details of fluorescent signal. In order to overcome this phenomenon, post-labeling is being studied currently.

In human brain, a severe autofluorescence has been found, which can be solved by photobleaching before staining. Other techniques are being tried to obtain more complete human brain information in future.

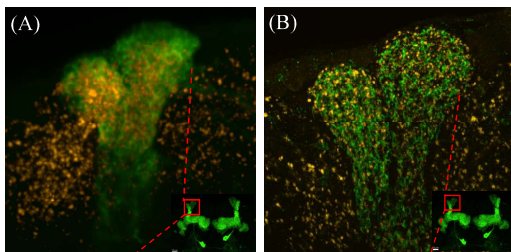


Figure 1. Mushroom body α and α' neurons in the *Drosophila* brain. The brain was immunostained with VMAT antibody (yellow)
(A) Original size (B) 4x expansion

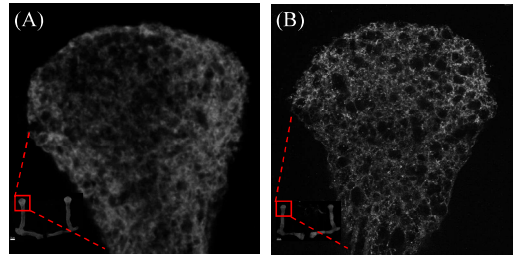


Figure 2. Mushroom body α neurons in the *Drosophila* brain.
(A) 4x expansion (B) 10x expansion

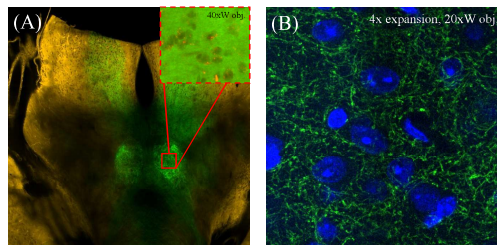


Figure 3. Preferential expression of Mouse brain (SCN) in ipRGC fiber (green).
(A) Original size (B) 4x expansion

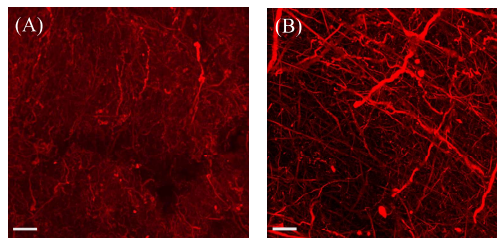


Figure 4. Neurofilament, Pan-Axonal in human brain. (scale bar: 30 μm)
(A) Original size (B) 4x expansion

III Reference

1. Fei Chen, Paul W. Tillberg and Edward S. Boyden (2015), Expansion microscopy, *SCIENCE*.
2. Sneve MA and Piatkevich KD (2022), Towards a Comprehensive Optical Connectome at Single Synapse Resolution via Expansion Microscopy. *Front. Synaptic Neurosci.*
3. Aleksandra Klimas and Yongxin Zhao. (2020), Expansion Microscopy: Toward Nanoscale Imaging of a Diverse Range of Biomolecules, *ACS Nano*.

Analysis of lipid molecular properties in nonalcoholic fatty liver disease by use of Brillouin microspectroscopy*

Eiji Hase^{*a}, Takeo Minamikawa^a, Yu Tokizane^a, Takeshi Yasui^a

^aInstitute of Post-LED Photonics, Tokushima University, Tokushima 7708506, Japan

Abstract

In this paper, we developed a Brillouin microspectroscope based on the tandem VIPA (virtually imaged phased array) spectrometer and applied it to the analysis of lipid molecule properties of the liver tissues as a preliminary step toward simultaneous Brillouin-Raman microscopic analysis of non-alcoholic fatty liver disease (NAFLD). We succeeded in measuring the Brillouin shift at the lipid droplet (LD) in liver tissues, and the Brillouin shift at LD was larger than that of standard solutions. Since the crystallinity and localization of lipid molecules strongly affect the mechanical properties of LD, the result might imply that Brillouin spectroscopy is feasible to characterize the NAFLD in terms of the lipid molecular properties.

Keywords: Brillouin scattering, Raman scattering, lipid, liver, NAFLD

I Introduction

Non-alcoholic fatty liver disease (NAFLD) is the most common liver disease associated with the accumulation of excess lipids in the liver and affects 20-30% of the world's population [1]. Previously, we aimed to demonstrate the feasibility of Raman microscopy for the investigation of NAFLD based on the molecular features of accumulated lipids [2]. By applying Raman microscopy, we succeeded in visualizing the distribution of lipid droplets (LDs) in hepatocytes. Also, the detailed analysis of Raman spectra revealed the difference in molecular structural features of the LDs, such as the degree of saturation of lipids in the LDs. Here, if the Brillouin scattering [3] can be simultaneously measured with the Raman scattering, it may be possible to obtain more macroscopic information, such as crystallinity and localization of lipid molecules. This is because this information strongly affects the mechanical properties that can be measured by Brillouin spectroscopy.

In this paper, we developed a Brillouin microspectroscope and applied it to the measurement of lipid molecule properties of the liver tissues as a preliminary step toward simultaneous Brillouin-Raman microscopic analysis.

II Materials and methods

Figure 1 shows the experimental setup for a Brillouin microspectroscope based on the tandem VIPA (virtually imaged phased array) spectrometer [3]. A single-mode CW laser was used for the excitation. The output light was guided to an inverted microscope and focused on the sample via an objective lens (20X, NA = 0.4). The Brillouin signal was collected by the same objective lens and fed into the spectrometer via single-mode optical fiber. In the spectrometer, such orthogonally placed VIPAs (FSR = 30 GHz, finesse = 65) enable us to obtain the Brillouin signal with high throughput and moderate spectral extinction compared with the traditional Fabry-Pérot etalon interferometry. Finally, the angular dispersed light spectrum was imaged onto an EMCCD camera. We also used the Lyot filter (spatial filter) to suppress the background noise due to the elastic scattering component without the loss of Brillouin-shifted components.

The liver tissues of NASH (non-alcoholic steatohepatitis) model mice induced by a high-fat/cholesterol/cholate diet [2] were kindly provided by the department of pathology and laboratory medicine at Tokushima University. The frozen samples of liver tissue were sliced into 10- μ m thick sections with a cryostat microtome. The sections were mounted on a slide glass

*hase@tokushima-u.ac.jp; phone 81 88 656-7606

without any fixation or staining and were used for the Brillouin analysis.

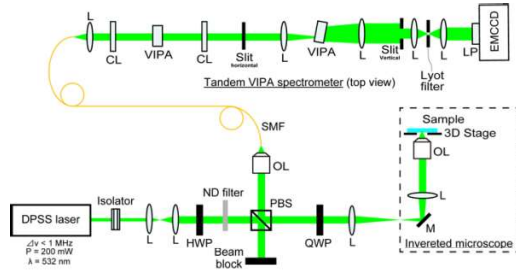


Figure 1. Experimental setup for Brillouin microspectroscopy.

III Results and Discussion

We first measured the Brillouin spectrum of the standard solutions with known Brillouin shift to confirm the validity of the home-built spectrometer. Figure 2 shows the results of the Brillouin measurement of the water (Fig. 2 (a) and (d)), ethanol (Fig. 2 (b) and (e)), and methanol (Fig. 2 (c) and (f)). The acquired images on the EMCCD camera were shown in Fig. 2 (a), (b), and (c), whereas the Brillouin spectrum obtained from the 2D images was shown in Fig. 2 (d), (e), and (f). Note that the spectral axis is tilted 135° from the horizontal axis of the EMCCD camera. In all the samples, Stokes and anti-Stokes Brillouin peaks were clearly confirmed. We also confirmed that these peaks have different frequency shift depending on the samples. The spectrum calibration was performed using these results and the reported Brillouin shifts of the solutions [3]. In this process, the actual FSR and the pixel-to-frequency conversion ratio were determined as 31.7 GHz and 0.29 GHz/pixel, respectively.

We next performed the Brillouin analysis of the frozen liver tissues section. Figure 3 (a) shows the bright-field microscopic image of the sample. The accumulated excess LD (left white arrow) appeared in the center of the image. The Brillouin spectrum obtained at the LD is shown in Fig. 3 (b). The Brillouin shift was measured as 13.0 GHz, much higher than the standard solutions (5 ~ 7 GHz). This result might indicate that the elasticity of the LD increases because of the crystallization of lipid molecules inside the droplet.

On the other hand, the Brillouin peaks were difficult to observe from the spectrum obtained at the outside of the

droplet (Fig. 3 (c), the right arrow on Fig. 3 (a)). This may be due to the strong elastic scattering from parenchymal cells. Therefore, an additional optical component for the background reduction is required to perform further analysis.

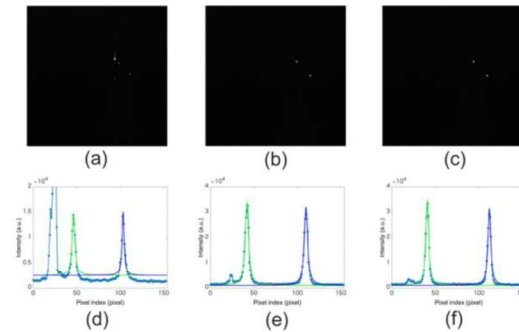


Figure 2. Results of the Brillouin measurement on the standard solutions. Dots are raw data, whereas lines are fit curves using a Lorentzian function.

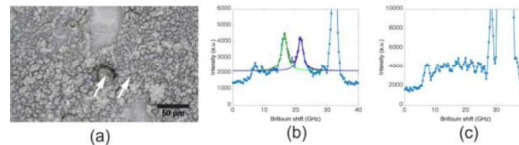


Figure 3. Results of the Brillouin measurement on the liver tissues. Dots are raw data, whereas lines are fit curves using a Lorentzian function.

IV Summary

We developed a Brillouin microspectroscopy based on the tandem VIPA spectrometer and applied it to the liver tissues of NASH model mice. We succeeded in measuring the Brillouin shift at the LD in liver tissues and found that the Brillouin shift at LD was larger than that of standard solutions. In the presentation, we plan to show the result of the 2D Brillouin imaging of the liver tissue.

References

- [1] Younossi, Z. M. et al., "Global epidemiology of nonalcoholic fatty liver disease-Meta-analytic assessment of prevalence, incidence, and outcomes," *Hepatology* 64(1), 73-84 (2016).
- [2] Minamikawa, T. et al., "Molecular imaging analysis of microvesicular and macrovesicular lipid droplets in non-alcoholic fatty liver disease by Raman microscopy," *Sci. Rep.* 10, 18548 (2020).
- [3] Scarcelli, G. et al., "Confocal Brillouin microscopy for three-dimensional mechanical imaging," *Nat. Photon.* 2, 39-43 (2007).

Multi-plane two-photon imaging from selective excitations

Xiangyu Quan^{*a,b}, Naru Yoneda^a, Osamu Matoba^{a,b}

^a Graduate School of System Informatics, Kobe University, Rokkodai 1-1, Nada, Kobe, Japan

^b Center of Optical Scattering Image Science, Kobe University, Rokkodai 1-1, Nada, Kobe, Japan

Abstract

Multiphoton microscopes are mostly used tools in *in vivo* imaging, such as imaging of brain cells in real time. However, in the case of functional imaging of neural circuits, where large number of cells are involved, conventional raster scanning schemes cannot satisfy the speed of cell activation signals for the whole volume of interest. To overcome the problem, we propose a multi-plane imaging method from selective excitation of the cells. The proposed method uses two SLMs, to generate multiple foci in 3D sample space, and to focus all point sources into a single imaging plane, respectively. Experimental result shows successful refocusing from three layers of point sources in a single-shot. This method can help to increase our understandings of neural circuits, by providing high throughput, high speed signal acquisition.

Keywords: multiphoton microscopy, *in vivo* imaging, digital holography

I Introduction

Fast three-dimensional (3D) imaging in multiphoton case has always been a challenging task. The speed of image acquisition depends on the field of view (FOV), and the range in depth. The smaller volumes are, the faster acquisition rates we can achieve. This trade-off is troublesome when large number of cells are involved. While a tight focal spot raster scans whole FOV, spontaneous or controlled neural activity bursts with the millisecond time scale in everywhere. It is difficult to grasp a very accurate picture of neural circuits with a conventional imaging scheme.

W. Yang *et al* (2016) proposed a multi-plane scanning-single detector imaging method, which can obtain focused images from multiple depths overlapped together. Y. Kozawa *et al* (2022) proposed to use a spatial light modulator (SLM) in the imaging path to separate depth-resolved images to the various angles, and using multiple detectors to record them at the same time. Y. Luo *et al* (2011) also proposed using volumetric hologram in the imaging path to realize multi-plane imaging with single-shot image acquisition. First two methods aimed to image large volume of cells with fast acquisition speed. However, completing at least one scanning motion limits the minimum acquisition speed, and volumetric hologram fixes observable depths in the designed range.

In this paper, we propose a targeted spot illumination and imaging method. Instead of recording multiple planes of 2D images simultaneously, proposed method uses priorly obtained 3D map to decide target cells, and generate excitation spots on each of them (X. Quan *et al* (2022)). The fluorescence from an excitation spot represents the intensity of activity from that cell. By recording those activities at the same time with the maximum acquisition rates possible, we can have more clear understandings towards brain functions.

II Multi-plane imaging from selective excitations

We use two SLMs for generation of selective excitation foci, and refocusing of 3D point sources in a single imaging plane. The schematic of proposed method is shown in Fig. 1. SLM1 generates foci in 3D, and SLM2 brings all images to the single recording plane. Suppose the coordinates of a plane wave focusing under the objective lens is (0,0;0) in x , y and z axis, and the image sensor is placed at the imaging plane of the objective lens. If the shift of focus is $(\Delta x, \Delta y; \Delta z)$, SLM1 should projects a phase pattern as in Eq. (1).

$$\text{SLM1}_{(x,y)} = \text{angle} \left(\exp \frac{-i\pi(x^2+y^2)}{\lambda_1 f^2} \exp \frac{i2\pi(\Delta x x + \Delta y y)}{\lambda_1 f} \right) \quad (1)$$

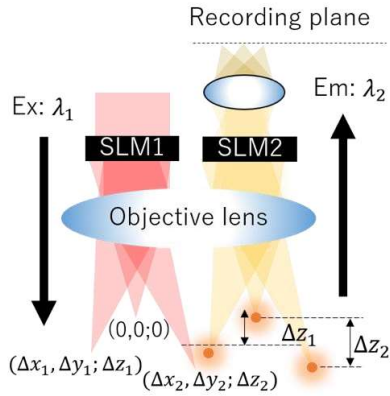


Figure 1. The schematic of multi-plane imaging from selective excitations

Here, λ_1 is the wavelength of excitation light, and f is the focal length of the objective lens. In order to focus the depth-shifted focal spot to the recording plane, SLM2 should project a phase pattern as in Eq. (2). Again, λ_2 is the center wavelength of emission light.

$$\text{SLM2}_{(x,y)} = \text{angle} \left(\exp \left(\frac{i\pi(x^2+y^2)}{\lambda_2 f^2 \frac{\Delta z}{z}} \right) \right) \quad (2)$$

We have tested this method using a thin fluorescent plate. First, we generated multiple focal spots in three layers, as shown in upper side of Fig. 2. The maximum distance between spots is 257 μm in the sample space. A recorded image without projecting a diffraction pattern on the SLM2 is shown in lower left side of Fig. 2. The focal spots in a single layer are imaged properly, and the other spots are defocused. When we projected an appropriate pattern to the SLM2, all spots are imaged from a single image sensor in a single-shot.

III Conclusion

The experiment result shows three layers of point sources are refocused in a single-shot acquisition. This implies that further application to the brain cell imaging with high throughput and high acquisition speed is possible. The intensity of the focused point sources is reduced in the acquired image, compared to the normal imaging method. The compensation of the intensity will be the next work for live cell imaging.

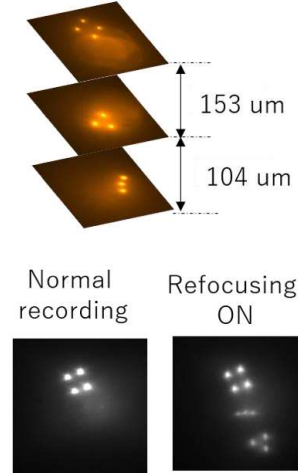


Figure 2. Experiment result of imaging three-planes of focal spots in a single-shot.

Acknowledgement

This work is supported by JSPS KAKENHI 20K15193, CREST JPMJCR1755, JST A-STEP JPMJTR204C.

References

- Yang, W., J.E.K. Miller, L. Carrillo-Reid, E. Pnevmatikakis, L. Paninski, R. Yuste, and D. S. Peterka. 2016. Simultaneous multi-plane imaging of neural circuits. *Neuron*, 89(2): 269-284.
- Kozawa, Y., T. Nakamura, Y. Uesugi, and S. Sato. 2022. Wavefront engineered light needle microscopy for axially resolved rapid volumetric imaging. *Biomedical Optics Express*. 13(3): 1702-1717.
- Luo, Y., I. K. Zervantonakis, S. B. Oh, R. D. Kamm, and G. Barbastathis. 2011. Spectrally resolved multidepth fluorescence imaging. *Journal of Biomedical Optics*. 16(9): 096015.
- Quan, X., D. Kato, V. Daria, O. Matoba, and H. Wake, H. 2022. Holographic microscope and its biological application. *Neuroscience Research*. 179: 57-64.

Focused Spot Generation based on Digital Phase Conjugation by Transport of Intensity Equation in Scattering Media

Shiori Matsuda^{*a}, Naru Yoneda^b, Xiangyu Quan^{b,c}, Osamu Matoba^{b,c}, Wataru Watanabe^a

^a Graduate School of Science and Engineering, Ritsumeikan Univ., Kusatsu 525-8577, Japan.

^b Graduate School of System Informatics, Kobe Univ., Kobe, 657-8501, Japan.

^c Center of Optical Scattering Image Science, Kobe Univ., Kobe, 657-8501, Japan.

Abstract

We present a method to make focused spots in a scattering medium by digital phase conjugation. Proposed method is based on the transport of intensity equation for fluorescent distribution of a guide star. By modifying the phase distribution, focused illumination of adjacent target cells located in-plane and along the depth direction is possible through a scattering medium. Numerical results show the effectiveness of the proposed method.

Keywords: digital phase conjugation, biomedical imaging, fluorescent imaging, transport of intensity equation

I Introduction

Optical biological imaging provides structural and functional information of cells or cellular activity noninvasively [1]. However, due to scattering effects, these observations are limited to the surfaces of living tissue and cultured cells. In recent years, wavefront modulation techniques such as transmission matrix and digital phase conjugation have made it possible to manipulate the propagation of light even in the scattering medium, hence to focus light within the scattering medium [2-4]. By applying these techniques to biological imaging, it is expected to deliver the light energy effectively, and then to see the biological phenomena in deep position of a biological tissue. However, multiple illuminations are required to obtain the appropriate wavefront distribution.

In this study, we propose a method to use digital phase conjugation to improve the focused light intensity in a scattering medium. For the phase measurement of fluorescent light from a guide star, the transport of intensity equation (TIE) is used [5]. Furthermore, a wavefront manipulation technique is applied to focus the light on target cells around the guide star.

II Method

Figure 1 shows our concept of the wavefront manipulation technique to make focused spots in a scattering medium based on guide stars and digital phase conjugation. In the optical setup of epifluorescence microscope, a phase-mode spatial light modulator (SLM) is located at the input plane and a demagnified image is imaged on the object plane under an optical microscope objective lens (MO). Suppose that a thin scattering medium is located on the object plane. The plane wave is incident on the SLM and the modulated light passes through the scattering medium. After propagation through the homogeneous medium and the modulated light illuminates the fluorescent beads that are guide stars. The fluorescence light generated from each bead spreads in all directions. We focus on the light propagates back through the medium. After passing through the scattering medium again, the light field is magnified by the MO and tube lens, and then observed by an image sensor. The TIE is used to measure the phase distribution of the scattered light. Three images of the scattered light intensity distributions at different depths are acquired to obtain the phase distribution of the fluorescent scattered light. From this phase distribution, a digital-phase conjugated wave is

generated using a phase-mode SLM, and it is confirmed that the light focusing power is increased.

Next, we design the phase distribution that can be focused on the target cells around the guide star. Assuming that the phase mode SLM and the scattering medium are in an imaging relationship, we use the shift of the phase distribution to shift the focused in-plane position. We also use quadratic phase function to shift the focused spot along the depth direction.

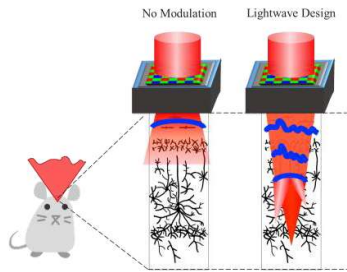


Fig. 1. Concept of wavefront manipulation technique to generate multiple focused spots in a scattering medium.

III Simulation Results

1. Focusing by phase conjugated wave

Phase conjugated waves were generated from the extracted phase distribution by the TIE, and then their focusing performance was evaluated when the fluorescent beads are illuminated. As shown in Fig. 2, the digital-phase conjugated wave improved the illumination power at the fluorescent bead. The total power in the fluorescent beads was increased by a factor of about 14.

2. Focusing to the periphery

A modulated phase distribution is calculated from the conjugate phase distribution of Fig. 2 to shift in-plane and along the depth direction. Figs. 3(a) and (b) shows the shifted spots by $-74.5 \mu\text{m}$ in-plane and by $0.5 \mu\text{m}$ along the depth direction, respectively. The total powers in the

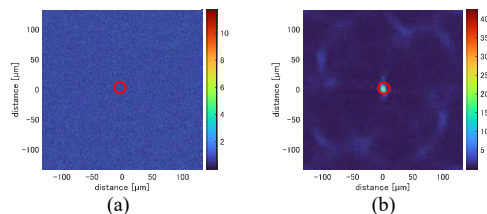


Fig. 2. Numerical results of improved light focusing property (a) without and (b) with digital phase conjugation. The red circle indicates the position of the fluorescent bead.

fluorescent beads in Figs. 3(a) and (b) were increased by factors of about 13 and 12, respectively.

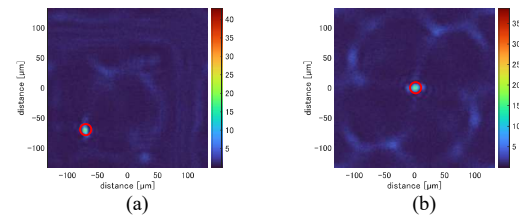


Fig. 3. Focused spots by designing the phase distribution from the conjugated phase distribution of Fig. 2. The red circle indicates the position of the fluorescent bead.

IV Conclusion

We have presented the method of making focused spots in a scattering medium by digital phase conjugation based on the TIE for a guide star, and by modifying the phase distribution to illuminate adjacent target cells. The total power to be illuminated to the fluorescent beads was increased by factors of 10 or more.

Acknowledgement: A part of this work has been supported by JSPS KAKENHI (20H05886, 21K18724).

References

- [1] Boniface, A., Dong, J., and Gigan, S., "Non invasive focusing and imaging in scattering media with a fluorescence-based transmission matrix," *Nat. Commun* 11, 6154 (2020).
- [2] Vellekoop, I. M., and Mosk, A. P., "Focusing coherent light through opaque strongly scattering media," *Opt. Lett.* 32(16), 2309-2311 (2007).
- [3] Popoff, S. M., Lerosey, G., Carminati, R., Fink, M., Boccaro, A. C. and Gigan, S., "Measuring the Transmission Matrix in Optics: An Approach to the Study and Control of Light Propagation in Disordered Media," *Phys. Rev. Lett.* 104, 100601 (2010).
- [4] Vellekoop, I. M., and Mosk, A. P., "Phase control algorithms for focusing light through turbid media," *Opt. Commun.* 281, 3071-3080 (2008).
- [5] Rajput, S. K., Matoba, O., Kumar, M., Quan, X., Awatsuji, Y., Tamada, Y., and Tajahuerce, E., "Multi-Physical Parameter Cross-Sectional Imaging of Quantitative Phase and Fluorescence by Integrated Multimodal Microscopy," *IEEE J. Sel. Top. Quantum Electron.* 27(4), 6801809 (2021).

Local gene induction by IR-LEGO to trigger stem cell formation in a moss plant

Yuka Yoshida^a, Takumi Tomoi^{*b,c,d}, Chizuru Numata^a, Suguru Ohe^c, Joe Sakamoto^{d,e}, Yasuhiro Kamei^{d,f,g,h}, Yosuke Tamada^{*a,c,h,i}

^aGraduate School of Regional Development and Creativity, ^bInstitute for Social Innovation and Cooperation, ^cSchool of Engineering, Utsunomiya University, Utsunomiya 321-8585, Japan, ^dLaboratory for Biothermology, National Institute for Basic Biology (NIBB), Okazaki 444-8585, Japan, ^eBiophotonics Research Group, ExCELLS, Okazaki 444-8787, Japan, ^fTSB Center, NIBB, ^gSchool of Life Science, SOKENDAI, Okazaki 444-8585, Japan, ^hCenter for Optical Research and Education (CORE), ⁱRobotics, Engineering and Agriculture-technology Laboratory (REAL), Utsunomiya University, Utsunomiya 321-8585, Japan

Abstract

Induction of gene expression is feasible conventionally in most of cells in living organisms. Infrared laser-evoked gene operator (IR-LEGO) is a method to induce gene expression by heating arbitrarily single cells with IR laser. In this study, we applied IR-LEGO to the moss plant *Physcomitrium patens*, which has a high ability of stem cell formation and regeneration. In addition, we induced the expression of *STEM CELL INDUCING FACTOR 1 (STEMINI)* by heating and tried to trigger the reprogramming of arbitrary differentiated cells into stem cells.

Keywords: IR-LEGO, *STEMINI*, stem cell, heat shock

I Introduction

In the broad field of biology, loss-of-function and gain-of function analyses of genes in the whole body are widely performed to understand the gene functions. However, such methods often mask the true function of genes due to the tissue specificity or lethality. Infrared (IR) laser irradiation can efficiently heat water of cells, leading to heat shock response (HSR). The molecular mechanism of HSR is largely conserved in animals and plants. The transcription factor HEAT SHOCK FACTOR (HSF) is trimerized and activated in response to a temperature increase, invoking transactivation of *HEAT SHOCK PROTEIN (HSP)* genes to restore the protein homeostasis of cells. IR laser-evoked gene operator (IR-LEGO) was developed by combination of IR laser heating system through the microscopic optics (Fig. 1) [1]. IR-LEGO can trigger gene expression at the single-cell level in both plants and animals through HSR [2], enabling the

fine analysis of gene functions.

Our previous study demonstrated inducible expression of a fluorescent protein in arbitrary single cells of the moss *Physcomitrium patens* with IR-LEGO. *P. patens* has clear cell fate and single-cell-layer tissues of the protonema and gametophore leaf, allowing the analysis of the cell fate change after the gene induction in single cells. Overexpression of the transcription factor gene *STEM CELL INDUCING FACTOR 1 (STEMINI)* induces stem cell from differentiated cells [3]. Here we addressed the induction of *STEMINI* in arbitrary single cells by IR-LEGO to manipulate the cell fate at the single-cell level.

II Results and Discussion

We generated 17 transgenic *P. patens* lines expressing *STEMINI* fused with *mCitrine* yellow fluorescent protein gene [4] under the promoter of *Glycine max HSP17.3B* (HSPpro:STEMIN1-YFP). Thus, we first tested the initiation of stem cell formation in response to a temperature rise in the whole plants of HSPpro:STEMIN1-YFP lines. The transactivation of *G.*

*t-tomoi@cc.utsunomiya-u.ac.jp; phone +81-28-689-6133

*tamada@cc.utsunomiya-u.ac.jp; phone +81-28-689-6133

max HSP17.3B is the maximum at 38°C in *P. patens* precultured at 25°C [5]. The provoked expression level of downstream gene is constantly maintained under the cycle of 1-hour higher temperature and 23-hour original culture temperature [6]. Besides, the expression level is enhanced by decreasing preculture temperature to 22°C. Taken together, we applied the heat shock (HS) condition of 38°C (2 hours)/22°C (10 hours) for 10 cycles to trigger *STEMIN1* expression, resulting in the stem cell formation at phyllid cells in 5 lines of HSPpro:*STEMIN1*-YFP (Figure 2).

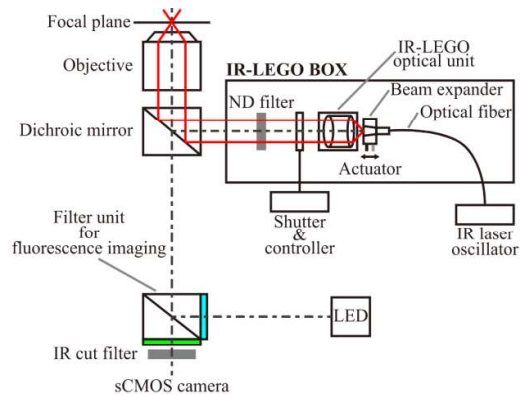


Figure 1. Schematic overview of the optical layout for IR-LEGO (modified from [7]).



Figure 2. Induction of a stem cell from the differentiated phyllid cell by heating the whole body of an HSPpro:*STEMIN1* line. The arrow indicates the protonema tissue regenerated from the stem cell.

To induce stem cell formation at single cells by provoking *STEMIN1* expression, we delivered IR-laser irradiation to the phyllid cells of HSPpro:*STEMIN1*-YFP lines. However, the single-time irradiation did not induce stem cell formation, suggesting the necessity of repeated irradiations, as shown in our experiments using the whole body (Figure 2). The repeated irradiation is likely impractical, because the irradiated cells easily change the position and become covered with other leaves through the organ growth. We thus undertake this issue by application of fewer repeated irradiation after several cycles of HS treatment to the whole plant.

III References

- [1] Kamei, Y., Suzuki, M., Watanabe, K., et al. "Infrared laser-mediated gene induction in targeted single cells *in vivo*," *Nat. Methods* 6, 79–81 (2009).
- [2] Deguchi, T., Itoh, M., Urawa, H., et al. "Infrared laser-mediated local gene induction in medaka, zebrafish and *Arabidopsis thaliana*," *Dev. Growth Differ.* 51, 769–775 (2009).
- [3] Ishikawa, M., Morishita, M., Higuchi, Y., et al. "Physcomitrella *STEMIN* transcription factor induces stem cell formation with epigenetic reprogramming," *Nat. Plants* 5, 681–690 (2019).
- [4] Griesbeck, O., Baird, G., Campbell, R., et al. "Reducing the environmental sensitivity of yellow fluorescent protein," *J. Biol. Chem.* 276, 29188–29194 (2001).
- [5] Saidi, Y., Finka, A., Chakhporanian, M., et al. "Controlled expression of recombinant proteins in *Physcomitrella patens* by a conditional heat-shock promoter: A tool for plant research and biotechnology," *Plant Mol. Biol.* 59, 697–711 (2005).
- [6] Saidi, Y., Finka, A., Muruset., et al. "The heat shock response in moss plants is regulated by specific calcium-permeable channels in the permeable channels in the plasma membrane," *Plant Cell* 21, 2829–2843 (2009).
- [7] Sakamoto, J. and Kamei, Y., "Technique to manipulate gene expression using infrared laser," *Seitai no Kagaku* (in Japanese) 68, 500–501 (2017).

Using adjustable radio frequency MS platform and conjunction-modulation design to improve the synchronization and resolution of the ion trap mass spectrometer for intact protein analysis

Fang-Hsu Chen^{*a}, Chun-Yen Cheng^a, Cheng-Han Yang^b, Lu, I-Chung^b, Ming-Long Yeh^a

^aDepartment of Biomedical Engineering, National Cheng-Kung University, Tainan, Taiwan, R.O.C

^bDepartment of Chemistry, National Chung-Hsin University, Taichung, Taiwan, R.O.C

Abstract

The mass spectrometer is a powerful biosensing tool for molecule determination and provides the analyte's mass-to-charge ratio (m/z) information. However, Current mass spectrometry has limitations for intact protein analysis because large molecules are hard to ionize and cannot be well synchronized in the electric field.

Our research uses an ion trap mass analyzer that combines the matrix-assisted laser desorption ionization-time of flight (MALDI) for gaining charged ions and uses a quadrupole ion trap as the mass analyzer. This self-made instrument has already detected the ions and can determine the large molecules. Nevertheless, the resolution and reproducibility of the peak position still need improvement. This poor outcome results from the non-synchronization of the ions; even a weak delay will let the end detector distinguish them as different m/z . In this research, the MS platform for RF design can customize the scan procedure and design the RF electric field. In order to realize high-resolution MS analysis, two approaches are used to modify the MS scan procedure. First, reduce the ion numbers in each scan step by setting the mass difference (dmz). Second, add conjunction modulation in the RF waveform to minimize the error accumulation and system damping. Our research provided an adjustable MS platform, which can improve the resolution of the protein MS analysis by reducing the error accumulation.

Keywords: mass spectrometry, ion trap, high-resolution, conjunction modulation

I Introduction

The mass spectrometer is a powerful biosensing tool for molecule determination and provides the analyte's mass-to-charge ratio (m/z). However, Current mass spectrometry (MS) has limitations for intact protein analysis because large molecules are hard to ionize and cannot be well synchronized in the electric field.

In the quadrupole ion trap, the electric field is a resonance unifrequency time-varying field, which can trap ions in the stable region. Ions' trajectories in both radial and axial directions are fitted to Mathieu's equation (March, 2006). Reconsidering the real-error term (\bar{b}), Mathieu's equation can be revised as the following formula (Eq.1). Floquet theory defines the state of the stability of solutions; this theory showed that in a certain period, the ion's track would go back to the initial point (Acar & Feeny, 2016). In the closed orbit, the ion motion (U) is composed of two independent and opposite directions (u_1 and u_2), which represent the ions are acting in different directions and movements (Eq.2). The ion motion is a compound function and can be divided into two parts, including the secular motion functions ($e^{\pm i\beta\xi}$) and the micro-motion ($\sum_{-\infty}^{\infty} C \mu \exp(+i \cdot \mu \cdot 2\xi)$). These

functions shared parameters ξ , which is related to the main RF field. Based on the physical study of the characteristics of the ion motion, the RF design of the MS scanning would focus on reducing the error (\bar{b}) accumulation via a novel scanning method.

$$\frac{d^2u}{d\xi^2} + (a_u - 2q_u \cos 2\xi)u = \bar{b} \quad (\text{Eq. 1})$$

$$U \begin{cases} u_1 = e^{+i\beta\xi} \sum_{-\infty}^{\infty} C_1 \mu \exp(+i \cdot \mu \cdot 2\xi) \\ u_2 = e^{-i\beta\xi} \sum_{-\infty}^{\infty} C_2 \mu \exp(+i \cdot \mu \cdot 2\xi) \end{cases} \quad (\text{Eq. 2})$$

II Materials and methods

1. Mass spectrometer

All experiments were performed in the QIT using ATI mass spectrometer (Acromass, Taiwan). AIT is equipped with a DPSS Laser (120 μJ at 349 nm) (MKS, USA) as an ion source and a turbo pump that makes the cassette reach low pressure (10^{-3} to 10^{-4} torr). To gain the intent signal, ions' motion should be managed in synchronization. Here, a series of phase conjunctions modulates the target ion in the position with minimal offset to the reset. All the processes scripted are written using python and ordered via ATI software (AcroMass, Taiwan)

2. MALDI sample and protein preparation

Cytochrome C (CytoC) was used as the intact protein standard; its molecular weight was 12,384 Da via electrophoresis. 5nm CytoC was diluted with 100 μ l DDW/acetonitrile (ACN) solution and then taking one volume mixed with one volume solvent (ACN/0.1TFA). The sinapic acid (SA) matrix was soaked with acetone and thoroughly mixed with sonication to get the saturated SA-acetone solvent. 0.6 μ l SA-acetone was loaded on the sample plate, and the second layer was a 0.6 μ l CytoC protein analyte.

3. Adjustable RF platforms for MS scanning

The ATI software provided a customized program design board for the MS scanning procedure. The waveform and frequency can be arranged for a different purposes. Mass scanning difference (dmz) was set for the different scan step sizes; Constant-phase conjunction modulation was a “lack” in the waveform, which means an instantaneous RF pause; this design can be regarded as a reset point, which prevents the accumulation of the error.

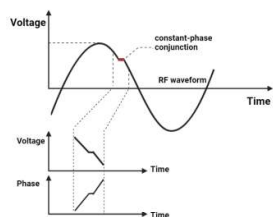


Figure 1. Schematic diagrams of the constant-phase conjunction modulation design.

III Results and discussions

Here is a variant RF waveform design for the electric field to improve the synchronization of the ion trap ions. Different dmz was set for MS scanning to change the scan mass width range. Small dmz (dmz=10 or 20) means the narrow scan and a full step needs to separate into multiple phases to provide more details of the peaks (**Figure 2**). Large dmz means a wider scan range for each step, which includes more ions, leading to the poor resolution of the MS pattern. Combing the dmz regulating and conjunction modulation, the scanning methods reduced the errors and prevented the signal delay, improving the resolution (**Figure 2B**). An advanced scan method was the segmentation of the scanning procedure. The MS analysis's segmentation procedure enhances the resolution and performs better ion synchronization. Continuous

modulation would end up becoming the error source.

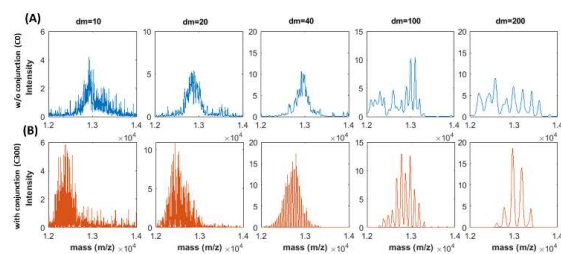


Figure 2. Using different scan dmz and conjunction-modulation to improve the resolution.

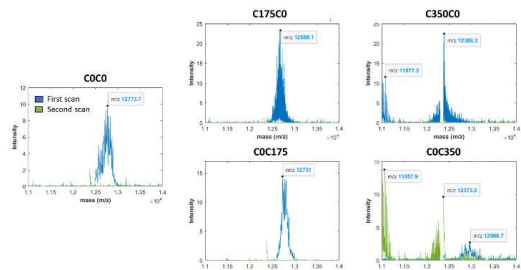


Figure 3. Segmented MS scanning combined conjunction-modulation reduces dissipation accumulation and provides high resolution.

IV Conclusions

Considering the physical concepts of ion motion, our research provided an adjustable MS platform, which can improve the resolution of the protein MS analysis by reducing the error accumulation.

*funshe101010@gmail.com; phone +886-988-522323

Acknowledgment

These machine parts of the self-made mass spectrometer, including electric components and laser, were kindly granted by the Scientech Corporation (Acromass company). Dr. Cheng and Mr. Chou provided techniques and consultation for the operation and electronics bits of knowledge.

References

1. G. Acar, & Feeny, B. F. (2016). Floquet-Based Analysis of General Responses of the Mathieu Equation. *Journal of Vibration and Acoustics*, 138(4). doi:10.1115/1.4033341
2. R. E. March. (2006). Quadrupole Ion Trap Mass Spectrometer. In *Encyclopedia of Analytical Chemistry*.

Development of Optical Coherence Tomography Imaging Engine based on FPGA

Chang-An Shih¹, Ting-Hao Tsai¹, Chuan-Bor Chueh¹, Ting-Hao Chen¹, and Hsiang-Chieh Lee¹

¹. Graduate Institute of Photonics and Optoelectronics, National Taiwan University, Taipei 106, Taiwan
email: hclee2@ntu.edu.tw

Abstract: Currently, optical coherence tomography (OCT) system requires a high-performance desktop which increases the system cost and complexity. In this study, we proposed an OCT system based on a field programmable gate array (FPGA) to replace the high-performance desktop in conventional OCT systems. As a preliminary study, we used an evaluation FPGA board to validate its feasibility to be implemented in the processing framework we have developed using the spectral-domain OCT system. The preliminary results including system framework and comparison of the processing performance with respect to conventional OCT system will be provided as well.

Key Word—FPGA, portable OCT.

1. Introduction

OCT is a non-invasive optical imaging technique based on the Michelson interferometer, which can provide tomographic images with micrometer-scale imaging resolution. Leveraging its fast acquisition and high-resolution cross-sectional imaging capability, OCT has already become a major imaging modality in ophthalmology [1]. Although OCT already offers tremendous advantages in imaging, the high cost and large footprint of the system restrict it from being utilized in large-scale hospitals or medical centers but not in rural area or locations where the medical resources are more limited. Hence, developing a low-cost and portable OCT system is crucial to further promote the application of OCT into a broader perspective.

In this study, we investigated the feasibility of developing an OCT framework where the imaging processing engine will be based on field programmable gate array (FPGA). Here, in order to more focus on validating the use of FPGA for OCT imaging processing and control of the beam scanning signals, we chose the spectral-domain OCT (SD-OCT) other than swept-source OCT technology being validated. Also, the FPGA is utilized to process the raw data acquired by the CMOS line-scan image sensor to reconstruct the OCT images. In general, the high-performance desktop is the bulkiest component in SD-OCT systems. Therefore, by using the FPGA, it is promised to further simplify the OCT computation framework based on high-performance desktop, enabling the development of a low-cost OCT system in the future.

2. Methods

In this study, we aimed to integrate the FPGA processing engine into a portable SD-OCT system (Optical Skin Viewer, OPXION Technology Inc., New Taipei City, Taiwan). Figure 1 shows the schematic diagram of the portable SD-OCT system. A super-luminescent diode (SLD) with a center wavelength of 840 nm and a full width at a half maximum bandwidth (FWHM) of 50 nm is utilized as the broadband light source. The light source is fiber-coupled into a 50:50 fiber coupler, and the light beam is split into a reference arm and sample arm. The sample arm is designed to be a handheld probe containing a microelectromechanical systems (MEMS) scanner that offers lateral and raster scans of the imaging sample. The reference arm consists of a fiber collimator, a reflective mirror, and a focusing lens. The light beam reflected or backscattered from both arms results in the interference signal at the coupler and is subsequently detected by the spectrometer, composed of a transmission grating, focusing lenses, and a line-scan camera. The line rate of the camera is set to 50 kHz, causing a frame rate of 50 frames/s with a maximum scanning area of $5 \times 5 \text{ mm}^2$.

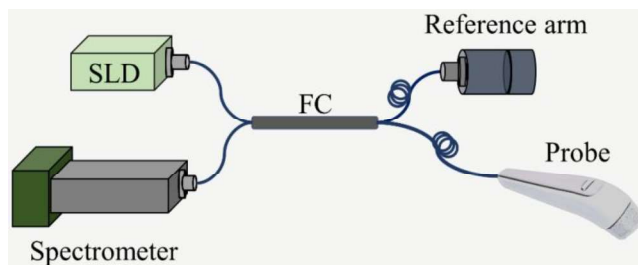


Fig. 1 Schematic diagram of portable SD-OCT system.

Fig. 2 illustrates the framework of the FPGA-based OCT system. The software interface on the host PC and Advanced RISC Machine (ARM) processor on the FPGA are developed based on C++. As a preliminary study, we still use a host PC in the framework but designating the image processing part specifically with the FPGA. The operation of the camera is implemented by the embedded Linux operating system on the ARM, and the FPGA transmits the packet consisting of instruction and the number of frames to ARM to control the acquisition of the camera via USB3.0. After the camera acquires each frame, the FPGA collects data from the ARM's memory pool and then process the raw interference data by executing a series of operation, including background subtraction, resampling, dispersion compensation, and Fast Fourier Transform (FFT) to reconstruct the OCT images. Overall, the data flow starts with the PC sending a packet consisting of the instruction and number of frames to the FPGA via USB3.0. The FPGA receives the packet and generates a synchronized clock to the DAQ. Then, the DAQ generates a frame trigger to enable the camera acquisition and a driving waveform for the control of the 2-axis mirror scanner to provide 2D or 3D imaging of the sample. The line-scan camera acquires the raw data and transfers it to the FPGA via USB3.0 to processing OCT images. After reconstructing the OCT images, the images are transferred back to the PC and displayed on a monitor via HDMI.

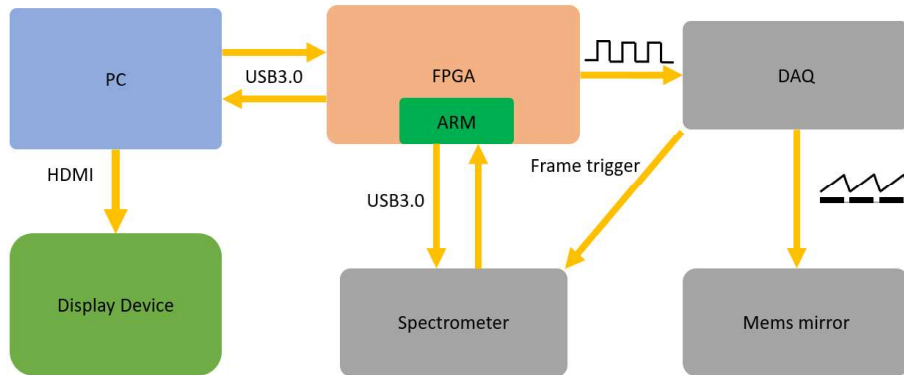


Fig. 2 Framework of the FPGA-based OCT system.

3. Results

Figure 3(a) and Figure 3(b) show the measured spectrum captured by the camera under the control using ARM on the FPGA board and PC, respectively. Compared with the data collected under the control with PC, there is one abnormal data point as marked by the red circle (Fig. 3(a)) shown on the measured spectrum under the control with ARM on the FPGA board. We found the reason for the appearance of this abnormal data point might be due to the data overwritten when the data was passed from ARM to PC because ARM and USB interface does not share the same working clock frequencies, which in the end leads to the loss of data during the transfer from ARM to PC. Nevertheless, this preliminary data showed the feasibility of using ARM on the FPGA board and the FPGA module to control the data acquisition.

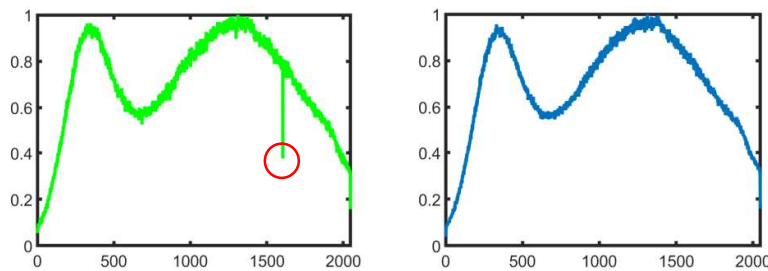


Fig. 3(a) Spectrum of the FPGA-based OCT system. (b) Spectrum of the PC-based OCT system.

4. Conclusion

In this study, we demonstrate a FPGA-based SD-OCT in order to improve the portability and simplicity of the traditional OCT system. Currently, we are working on resolving the clock issue aforementioned and implement the real-time data processing algorithms on the FPGA module.

5. References

- [1] W. Drexler, et al., "Ultrahigh-resolution ophthalmic optical coherence tomography," *Nat. medicine*, 7 (2001), pp. 502-507

3D image analysis of spermatid nuclei to understand the mechanism of the sperm formation in a land plant

Yosuke Tamada^{*a, b, c, d}, Nan Gu^{a, d}

^aSchool of Engineering, Utsunomiya University, Utsunomiya 321-8585, Japan,

^bGraduate School of Regional Development and Creativity, Utsunomiya University,
Utsunomiya 321-8585, Japan

^cCenter for Optical Research and Education (CORE), Utsunomiya University,
Utsunomiya 321-8585, Japan

^dRobotics, Engineering and Agriculture-technology Laboratory (REAL), Utsunomiya University,
Utsunomiya 321-8585, Japan

Abstract

Non-flowering land plants form sperms similar to animals. To understand the mechanism of the sperm formation in plants and discover the sperm-formation mechanism shared between plants and animals, we observed the process of the sperm formation in the moss *Physcomitrium patens*. We chemically fixed the gametophores after the gametangium induction and labeled nuclei or cellular structures with fluorescence dyes. Then, we performed chemical tissue clearing and observed the antheridia using confocal microscopes. The 3D image analysis of spermatid nuclei based on morphological segmentation was performed and we discovered the synchronous nucleus contraction during the sperm formation, which involved DNA Topoisomerase 1 (TOP1). TOP1 is also implicated in the sperm formation in animals, suggesting that nucleus contraction involving TOP1 is the common sperm-formation mechanism between plants and animals.

Keywords: sperm, fertilization, plant, tissue clearing, confocal microscope, 3D imaging, image analysis

I Introduction

Non-flowering land plants form sperms for fertilization similar to animals. Sperms have a compact head/body suitable for swimming to the egg cell for fertilization in both plants and animals. Formation of the compact sperm head/body requires tight chromatin condensation and nucleus contraction. To elucidate the mechanism of the sperm formation in plants and discover the sperm-formation mechanism shared between plants and animals, we are investigating the sperm formation in the moss *Physcomitrium patens*. We recently observed that spermatid nuclei are synchronously contracted toward filamentous shape in the process of the sperm formation [1]. The synchronous nucleus contraction involved the *DNA Topoisomerase 1α (TOP1α)* gene [1], encoding the enzyme responsible for releasing the torsional stress of DNA [2]. TOP1 is also suggested to be involved in the

contraction of spermatid nuclei in animals [3]. Our data suggest the TOP1 function in tight and synchronous contraction of the spermatid nuclei, which is a sperm-formation mechanism shared between plants and animals. To analyze the nucleus contraction during the sperm formation, 3D reconstruction of confocal images of the spermatid nuclei and quantitative 3D image analysis are necessary. In the talk, we will introduce our current method of 3D image analysis to understand the process of the sperm formation in *P. patens*.

II Results and Discussion

We sampled gametophores of *P. patens* after the gametangium induction. The gametophores were chemically fixed and the cellular structures or only nuclei were labelled with fluorescent dyes. Fixed gametophores were subject to chemical tissue clearing by modified benzyl alcohol and benzyl benzoate (BABB) method (Figure 1) [4] or ClearSee method [5] to observe cellular

*tamada@cc.utsunomiya-u.ac.jp; phone +81-28-689-6133

structures or nuclei, respectively. Then, antheridia were observed using a confocal microscope by shifting the focal plane along the optical axis (Figure 1). To analyze the nucleus contraction during the sperm formation, we obtained confocal images of antheridia cleared by the ClearSee method. From the confocal images, we reconstruct the 3D image of spermatid nuclei using ImageJ software [6]. Then, the 3D image of spermatid nuclei was subject to morphological segmentation based on watershed algorithm using MorphoLibJ plugin [7] of ImageJ to obtain individual spermatid nucleus regions. Then, the number and volume of spermatid nuclei were quantified to elucidate the process of the nuclei contraction during the sperm formation. With this method, we successfully quantified the number and volume of the round nuclei during the mitotic phase of the sperm formation. However, it is still challenging to quantify the number and volume of further contracted nuclei to filamentous shape during the spermiogenesis phase with the same method (Figure 1). We would like to discuss this issue with the audience to overcome the difficulty. In addition, we identified several chromatin-related factors which may be involved in the sperm formation. In the talk, we will summarize our current results on the sperm formation in *P. patens*.

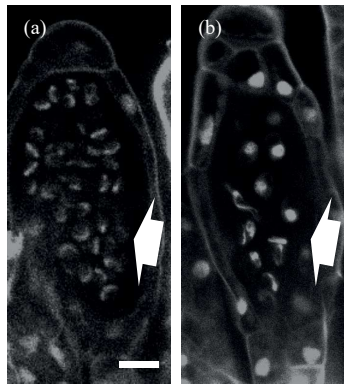


Figure 1. Confocal images of spermatid nuclei in antheridia of wild type (a) and *top1a Physcomitrium patens* (b) at the last stage of the sperm formation. Spermatid nuclei are indicated by white arrows. Bar: 10 μm .

References

- [1] Gu, N., Chen, C., Kabeya, Y. *et al.*, "Topoisomerase 1a is required for synchronous spermatogenesis in *Physcomitrium patens*," *New Phytol.* 234(1), 137-148 (2022).
- [2] Wang, J. C., "Cellular roles of DNA topoisomerases: a molecular perspective," *Nat. Rev. Mol. Cell Biol.* 3(6), 430-440 (2002).
- [3] Chu, D. S., Liu, H., Nix, P. *et al.*, "Sperm chromatin proteomics identifies evolutionarily conserved fertility factors," *Nature* 443(7107), 101-105 (2006).
- [4] Tanahashi, T., Sumikawa, N., Kato, M. *et al.*, "Diversification of gene function: homologs of the floral regulator *FLO/LFY* control the first zygotic cell division in the moss *Physcomitrella patens*," *Development* 132(7), 1727-1736 (2005).
- [5] Kurihara, D., Mizuta, Y., Sato, Y. *et al.*, "ClearSee: a rapid optical clearing reagent for whole-plant fluorescence imaging," *Development* 142(23), 4168-4179 (2015).
- [6] Schneider, C. A., Rasband, W. S., and Eliceiri, K. W., "NIH Image to ImageJ: 25 years of image analysis," *Nat. Methods* 9(7), 671-675 (2012).
- [7] Legland, D., Arganda-Carreras, I., and Andrey, P., "MorphoLibJ: integrated library and plugins for mathematical morphology with ImageJ," *Bioinformatics* 32(22), 3532-3534 (2016).

Development of Multi-view Optical Coherence Tomography (OCT) and Image Registration Algorithm for Tooth Imaging

Heng-Yu Li¹, Tzu-Hsuan Chang¹, Yu-Ren Chou², Yin-Lin Wang³, Hsiang-Chieh Lee^{1,4}

¹Graduate Institute of Photonics and Optoelectronics, National Taiwan University, Taipei 10617, Taiwan

²Graduate Institute of Biomedical Electronics and Bioinformatics, National Taiwan University, Taipei 10617, Taiwan

³Department of Dentistry, National Taiwan University Hospital, Taipei 10617, Taiwan

⁴Department of Electrical Engineering, National Taiwan University, Taipei, 10617 Taiwan

*Email: hlee2@ntu.edu.tw

Abstract

Due to the presence of highly scattering impurities or inclusions on the surface or within the tooth, results in the loss of optical coherence tomography (OCT) signals below the aforementioned defects comprising the correct assessment of the tooth images. In this study, we developed a multi-view image stitching algorithm based on an iterative closest point (ICP) algorithm to reconstruct the missing information. By using a dual-axis goniometric stage, it allows the acquisition of multi-view images at different controlled degrees. The result of our proposed method was able to improve the signal-to-noise ratio (SNR) and contrast-to-noise ratio (CNR) of the dental OCT image by a factor of 2.14 and 3.26.

Keywords: optical coherence tomography, tooth, iterative closest point algorithm, multi-view imaging.

I. Introduction

In recent years, OCT were widely developed for intraoral imaging technologies. It has been proposed to more accurately interpret and predict oral disease conditions [1], because of its high-resolution tomography imaging of soft and hard tissues but not being vulnerable to the risk of ionizing radiation. However, the imaging depth of OCT was limited by the optical property of teeth. In addition, the presence of defects on the surface or within the tooth sample, which often causes vertical line artifacts on the OCT imaging resulting in information loss [2]. This limitation affects the availability and promotion of OCT for clinical dental use. Previous studies have also shown the images of the lesions obtained at different scanning angles will have different appearances [3]. Therefore, this study aims to scan the tooth samples from multiple viewing angles to provide cross-sectional OCT images that might not be affected by the defects present during the light propagation. By using the OCT images acquired at different viewing, we have developed a multi-view stitching algorithm to yield a cross-sectional OCT less being affected by the defect presence.

We believe the study result should not only facilitate the development of a handheld multi-view imaging system in the future but also facilitate the future utilization of OCT for dental applications.

II. Method

1. SS-OCT system setup

The schematic diagram of the SS-OCT system with a dual-axis goniometric stage is shown in Fig.1. The central wavelength of the swept-source laser light source (HSL-20, Santec, Inc.) is 1310 nm with a bandwidth of 100 nm, and a scanning rate of 100 kHz. The interference signal was detected by a 400 MHz dual-balanced photodetector (DBPD, PDB470C-AC, Thorlabs, Inc.), and it was converted into an electrical signal directed to a high-speed digitizer (ATS9371, AlazarTech) for subsequent signal processing. A custom-developed graphic user interface (GUI) written in C++ language was utilized for data acquisition, image processing, and the scanning image control.

To acquire images at multiple angles, we set a dual-axis goniometric stage at the sample arm to place a single tooth sample. Through adjusting the inclination angle of

the goniometric stage to obtain 11 sets of image data at different viewing angles ($0^\circ, \pm 2^\circ, \pm 4^\circ, \pm 6^\circ, \pm 8^\circ, \pm 10^\circ$).

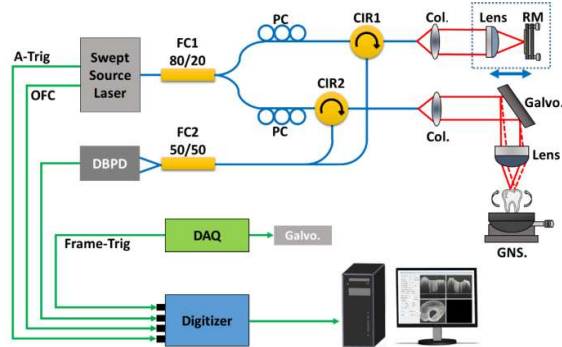


Fig.1. Schematic diagram of SS-OCT system. DBPD: dual-balanced photodiode ; Galvo: galvanometer scanner ; RM: reflective mirror ; CIR: circulator ; FC: fiberoptic coupler ; PC: polarization controller ; A-Trig: A-scan trigger signal ; OFC: optical frequency clock ; Frame-Trig: frame trigger signal Col.: collimator.

2. Multi-view OCT image registration algorithm

The process of the stitching algorithm can be roughly divided into four steps: (1) Pre-process the original image to extract image feature points. (2) Convert the feature points into point cloud files, and use the ICP algorithm [4] to calculate the transformation matrix between different point clouds. (3) Apply the transformation matrix to the volume image, so that the images of different viewing angles are aligned to the same position. (4) Normalize the brightness of images from different viewing angles, and adopt different image fusion rules depending on the timing of use.

III. Results

In this research, 11 sets of image data acquired from different scanning angles were stitched in an above-mentioned methodology. The stitched imaging result is shown in Fig.2, demonstrating that the stitched images could provide finer structural information. During the imaging stitching process, different fusion algorithms were used including Maximum fusion (Fig.2(c)) and Laplacian pyramid (Fig.2(d)). As shown in Fig. 2(d), the Laplacian pyramid algorithm could better preserve the fine structure features present in dental OCT images.

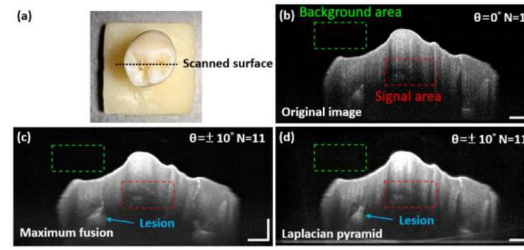


Fig.2 Fused images with 11 sets of C-scans. (a) Sample (b) Original OCT image (c) OCT image by maximum fusion. (d) OCT image by Laplacian pyramid.

Also, we obtained multiple sets of stitched images with the spacing of every positive and negative 2-degree image and calculated their SNR and CNR respectively. The result is illustrated in Fig.3.

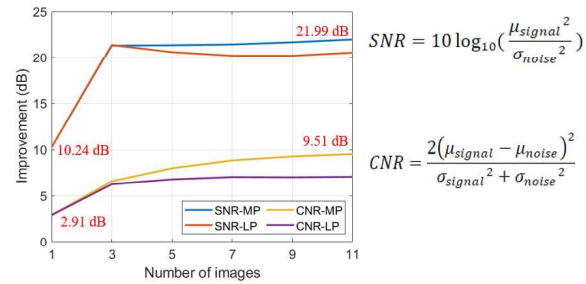


Fig.3 Improvement in SNR and CNR. SNR-MP: SNR of maximum pixel fusion, SNR-LP: SNR of Laplacian pyramid, CNR-MP: CNR of maximum pixel fusion, CNR-LP: CNR of Laplacian pyramid.

IV. Acknowledgment

The authors acknowledge the support from the Young Scholar Fellowship Program by the Ministry of Science and Technology (MOST) of the Republic of China (ROC), Taiwan (MOST 110-2636-E-002-025/111-2636-E-002-024)

V. Reference

- [1] M. N. Luong, Y. Shimada, K. Araki, M. Yoshiyama, J. Tagami, and A. Sadr, "Diagnosis of Occlusal Caries with Dynamic Slicing of 3D Optical Coherence Tomography Images," *Sensors* 20(6), 1659 (2020).
- [2] K. Al-Azri *et al.*, "Optical coherence tomography use in the diagnosis of enamel defects," *Journal of Biomedical Optics* 21(3), 036004 (2016).

- [3] H. Schneider *et al.*, "An Intraoral OCT Probe to Enhanced Detection of Approximal Carious Lesions and Assessment of Restorations," *Journal of Clinical Medicine* 9(10), 3257 (2020).
- [4] P. J. Besl and N. D. McKay, "A method for registration of 3-D shapes," *IEEE Transactions on Pattern Analysis and Machine Intelligence* 14(2), 239-256 (1992).

Single Cell Effects of Photobiomodulation on Mitochondrial Membrane Potential and Reactive Oxygen Species Production in Human Adipose Mesenchymal Stem Cells

Nguyen Le Thanh Hang^{*a}, Li-Chern Pan^b, Mamadi M.S Colley^b, Cheng-Jen Chang^{**b,c,d}, Tzu-Sen Yang^{**a,b,c,f}

^aInternational Ph.D. Program in Biomedical Engineering, Taipei Medical University, Taipei 110, Taiwan.

^bGraduate Institute of Biomedical Optomechanics, Taipei Medical University, Taipei 110, Taiwan.

^cDepartment of Plastic Surgery, Taipei Medical University Hospital, Taipei 110, Taiwan.

^dDepartment of Surgery, College of Medicine, Taipei Medical University, Taipei 110, Taiwan.

^eSchool of Dental Technology, Taipei Medical University, Taipei 110, Taiwan.

^fResearch Center of Biomedical Device, Taipei Medical University, Taipei 110, Taiwan.

I. Introduction

Photobiomodulation (PBM) has recently emerged in cellular therapy as a potent alternative in promoting cell proliferation, migration, and differentiation during tissue regeneration. Herein, a single-cell near-infrared (NIR) laser irradiation system (830 nm) and the image-based approaches were proposed for the investigation of the modulatory effects in mitochondrial membrane potential ($\Delta\Psi_m$), reactive oxygen species (ROS) and vesicle transport in single living human adipose mesenchymal stem cells (hADSCs).

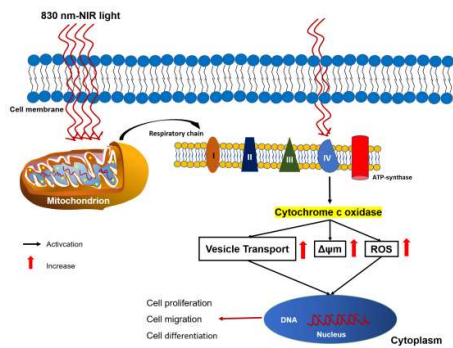


Fig 1. Schematic diagram for mechanisms of PBM. Cytochrome c oxidase (CCO) is a major photoreceptor, located in the mitochondrial respiratory chain at unit IV in the mitochondria, was released by PBM, followed by a functional change in the original mitochondrial respiratory chain to generate ROS and increased mitochondrial membrane potential ($\Delta\Psi_m$) that plays a crucial role in ATP production through oxidative phosphorylation.

II. Materials and Methods

1. The proposed single-cell PBM irradiation system

The inverted microscopy (TE2000U, Nikon, Japan) is equipped with an objective lens (Plan Apo 90 \times /1.40 oil) and an electron-multiplying CCD (EMCCD) camera (LucaEM S658M, Andor, Belfast, UK).

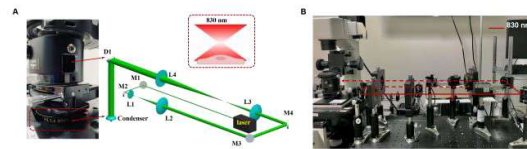


Fig 2. (A, B) The proposed experimental setup consists of an 830 nm infrared diode laser, an electrical shutter, laser-focusing optics, and a specimen holder attaching to the XY-axis motorized stage.

2. Experimental procedures

The hADSCs were first seeded into a flow chamber and incubated for 24 hours. The irradiated-hADSCs were then stained with Rhodamine 123 (Rh123) and 2',7'-dichlorodihydrofluorescein diacetate (H₂DCFDA) to perform the $\Delta\Psi_m$ and ROS stimulation, respectively, with irradiation (830 nm) in the range of 2.5-10 (J/cm^2), where time series of bright-field images were also obtained to identify the vesicle transport phenomenon.

III. Results and Discussion

1. Fluorescent images of $\Delta\Psi_m$ and ROS production on single irradiated-hADSC

PBM stimulated the statistical changes in $\Delta\Psi_m$ and ROS production at 5 (J/cm^2) compared to other groups with the ratio of $S_2/S_1 = 1.07$ and $R_2/R_1 = 1.7$, respectively.

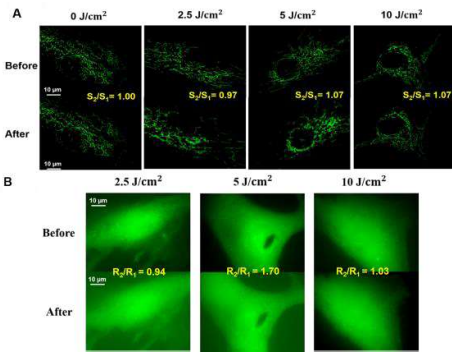


Fig 3. Fluorescence images of (A) $\Delta\Psi_m$ and (B) ROS production on the irradiated-hADSCs at 2.5-10 (J/cm^2). These hADSCs were captured after 30 min by EMCCD camera.

2. Effects of PBM in $\Delta\Psi_m$ and ROS on hADSCs

Present results revealed that a fluence of 5 J/cm^2 significantly promoted the $\Delta\Psi_m$, ROS production compared to the control group (0 J/cm^2) after 30 mins PBM.

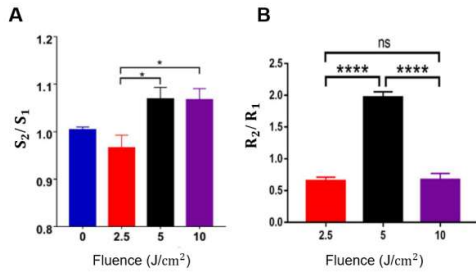


Fig 4. (A) $\Delta\Psi_m$ and (B) ROS production after 30 min PBM at various fluences (2.5-10 J/cm^2) in hADSCs (Passage 10). Values represented as the ratio of mean fluorescence intensity before and after 30 min PBM ($S_2/S_1 \pm SEM$, $n = 8$ and $R_2/R_1 \pm SEM$, $n = 6$). Statistical analysis (one-way ANOVA) for significant differences between 2.5 J/cm^2 and two fluences of 5 and 10 J/cm^2 (* $p \leq 0.05$; ****, $p \leq 0.0001$ and ns, $p > 0.05$).

3. Vesicle transport in the irradiated-hADSCs

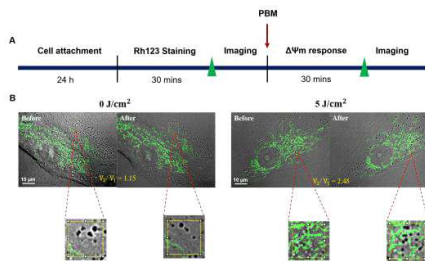


Fig 5. (A) Experimental procedures (B) The ROI area was identified by ImageJ, then by cutting it and measure the velocity transport using Matlab

The results revealed that a fluence of 5 J/cm^2 significantly promoted vesicle transport phenomena compared to the control group (0 J/cm^2) after 30 mins PBM, with the ratio of $V_2/V_1 = 1.93$ and $V_2/V_1 = 0.76$, respectively.

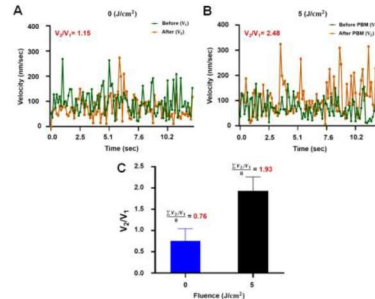


Fig 6. (A) The velocity of 0 & (B) 5 J/cm^2 at single-cell level. (C) The statistical increased vesicle transport in the irradiated-hADSCs ($n = 8$) at 5 (J/cm^2); p -value = 0.0117 < 0.05).

IV. Conclusion

In summary, the presented results demonstrate an increase of the $\Delta\Psi_m$, ROS and vesicle transport at a fluence of 5 J/cm^2 in the irradiated-hADSCs. These results illustrated the regulation of cellular responses regarding $\Delta\Psi_m$ and vesicle transport on the irradiated-hADSCs, which have potential in cell proliferation, migration, and differentiation in cell-based therapy. Our single-cell research was accepted for publication in March this year [1].

V. Acknowledgement

This work was financially supported by the “TMU Research Center of Cancer Translational Medicine” from The Featured Areas Research Center Program within the framework of the Higher Education Sprout Project by the Ministry of Education (MOE) in Taiwan. This study was also supported by the Ministry of Science and Technology, Taiwan, under grants (MOST 111-2221-E-038- 012-, MOST 111-2221-E-038-009-)

VI. References

Journal paper:

[1] Pan, L.-C.; Hang, N.-L.; Colley, M.M.; Chang, J.; Hsiao, Y.-C.; Lu, L.-S.; Li, B.-S.; Chang, C.-J.; Yang, T.-S. Single Cell Effects of Photobiomodulation on Mitochondrial Membrane Potential and Reactive Oxygen Species Production in Human Adipose Mesenchymal Stem Cells. *Cells* 2022, 11, 972.

Volumetric Imaging of the *Ex Vivo* Oral Precancerous Lesions with Multi-scale Wide Field-of-View Optical Coherence Microscopy

Chuan-Bor Chueh^a, Po-Hao Tseng^a, Ming-Che Tu^c, Ting-Yen Tsai^a, Ting-Hao Chen^a, Heng-Yu Li^a,
Shih-Jung Cheng^c, and Hsiang-Chieh Lee^{*a, b}

^aGraduate Institute of Photonics and Optoelectronics, National Taiwan University, Taipei 10617, Taiwan

^bDepartment of Electrical Engineering, National Taiwan University, Taipei 10617, Taiwan

^cDivision of Oral and Maxillofacial Surgery, Department of Dentistry, National Taiwan University Hospital, Taipei 10617, Taiwan

*hlee2@ntu.edu.tw; phone +886 3366 3700 #235

Abstract

We have developed a multi-scale optical coherence tomography (OCT) and microscopy (OCM) imaging system that enables multi-scale and wide-field imaging of the *ex vivo* oral precancerous tissue. The light source exhibits a sweep rate of 90 kHz. Objectives with three different magnifications are mounted to a power turret, enabling seamless change of the OCT/OCM imaging resolution via the software control with up to a 5.3- μm transverse resolution (FWHM). Most importantly, we demonstrated the ability of a custom-develop novel volumetric mosaic stitching and processing algorithm applicable to the multi-scale OCT/OCM datasets in a fully automated fashion without requiring the manual adjustment of individual parameters. Co-registered histopathology imaging and multi-scale OCT/OCM imaging of the *ex vivo* oral mucosal specimens suggest the potential of the developed instrument to provide high-resolution imaging of the oral specimens for clinical use.

Keywords: optical coherence tomography, microscopy, swept source, multi-resolution, mosaic stitching, oral

I Introduction

Based on an analysis of the Ministry of Health and Welfare in 2018, there were 8,000 new cases of oral cancer, and it ranks as the fifth leading cause of death due to cancer (~3000 cases) in Taiwan. In addition, another analysis performed by the World Health Organization shows there are approximately three hundred thousand new cases of oral cancer worldwide annually. However, most of the cases are diagnosed at late or advanced stages. For patients diagnosed with the advanced or late stage of oral SCC, the five-year survival rate was reported to be ~33%. The report showed the importance of developing technologies that can instantly and efficiently diagnose oral cancer at an early stage.

Optical coherence tomography (OCT) can perform high-resolution, noninvasive and three-dimensional, imaging of the biological tissues in real-time. On the other hand, optical coherence microscopy (OCM) combines OCT and confocal microscopy. Leveraging the coherence gate provided by the OCT, OCM can achieve high resolution imaging with requiring high-numerical aperture (NA) optics like conventional confocal microscopy. Since it avoids the use of high-NA optics,

the imaging depth of OCM can be improved as well. Nevertheless, the field-of-view (FOV) of OCM is still limited when compared to OCT. Thus, by utilizing mosaic scanning protocol, wide-field imaging can be enabled as well. In this study, we have developed a multi-scale OCT/OCM imaging system enabling multi-scale imaging of the *ex vivo* oral precancerous tissue with an increased imaging depth. Detailed information about the imaging system can be found in the following section.

II Methods

Figure 1 shows the schematic diagram for the custom-designed multi-scale SS-OCT/OCM system developed in this study. The laser output is split into the sample arm and reference arm through a 90/10 fiberoptic coupler. In the sample arm, a dual-axis micro-electro-mechanical (MEMS) scanning mirror (Mirrorcle Technologies, Inc.) provides the beam scanning over the tissue surface. Infinity-corrected objectives with three different magnifications (5X, 10X, 20X, M Plan Apo NIR, Mitutoyo, Inc.) were mounted on a power turret to change the resolution and FOV during the imaging procedure seamlessly. In addition, we integrated a three-dimensional motorized translation stage in the sample arm. With this

setup, we can control the beam focusing position within the sample and implement a mosaic imaging protocol to provide wide FOV high-resolution imaging of the tissue.

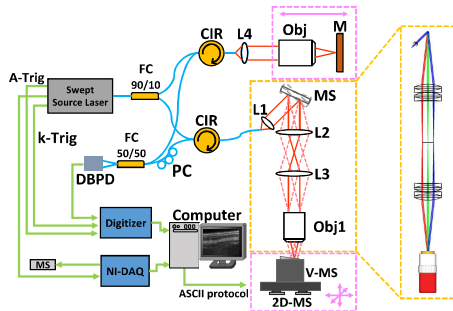


Figure 1. Schematic diagram of the multi-scale SS-OCT/OCM system. FC: fiberoptic coupler; L1 and L4: collimating lens; L2 and L3: lens pair; Obj1 and Obj2: Objectives; M: mirror; MS: micro-electro-mechanical system (MEMS) scanning mirror; DBPD: dual-balanced photodetector; PC: polarization controller; CIR: fiberoptic circulator; V-MS: vertical motorized stage; 2D-MS: two-dimensional motorized stage.

In the reference arm, we use the same collimator used in the sample arm and a 5X objectives (M Plan Apo NIR, Mitutoyo, Inc.) as a focusing lens to minimize the chromatic dispersion between the sample arm and the reference. Furthermore, we installed another one-axis motorized translation stage (MTS25-Z8, Thorlabs, Inc.) in the reference arm to match the optical path length (OPL) of the reference arm to the sample arm when different objectives are used in the sample arm.

Lastly, the last 50/50 fiberoptic coupler collected the backscattered light from both arms to generate the interference signal. The signal was converted from a light signal to an electrical signal through the dual-balanced photodetector (BPD-200-HS, Santec, Inc.). A high-speed digitizer (ATS9350, AlazarTech, Inc.) digitized the electrical interference signal for subsequent reconstruction of the OCT/OCM datasets. The data acquisition, imaging processing, control of different motorized stages, and data saving are handled by the custom developed graphic user interface (GUI).

We extracted the representative *en face* image of the entire mosaic 3D OCT or OCM dataset from the depth

which exhibits architectural features to compute the mosaic stitching metric or parameters by utilizing the in-house developed algorithms including maximum cross-correlation and a multi-band blending algorithm to provide wide-field OCT or OCM stitched images.

III Results and Discussion

Figures 2(a, b, c) show a multi-scale cross-sectional images of the healthy tongue tissue acquired using the 5X, 10X, and 20X objectives, respectively and the corresponding H&E-stained image (Fig. 2(d)). With a 5X objective, due to the limited lateral resolution, the detailed information of each layer can be roughly identified. By using either 10X or 20X, improvement on the contrast and visibility of the fine architectural features of the oral tissue can be appreciated, which are highly correlated to the H&E-stained image (Fig. 2(d)) where the boundary of the epithelium and the lamina propria can be easily differentiated. Currently, our multi-scale OCT/OCM imaging system is ongoing to perform rapid multiscale and volumetric imaging of the excised oral specimens with a variety of tissue pathologies at the clinic.

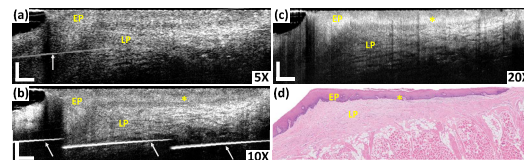


Figure 2. Multi-scale OCT/OCM cross-sectional images of benign tongue specimen from a 67 years-old male with the (a) 5x, (b) 10x, (c) 20x objectives. (d) The H&E-stained histology image shows clear differentiation between the epithelium layer (EP) and lamina propria (LP) layer. Scale bars: 300 μm . yellow star: rete pegs; white arrow: specular reflection signals from the objectives due to the imperfect AR-coating at the ~ 1700 nm wavelength regime.

IV Acknowledgment

The authors acknowledge the funding support in part from the Young Scholar Fellowship Program by the Ministry of Science and Technology of the Republic of China (ROC), Taiwan (MOST 109-2636-E-002-028, 110-2636-E-002-025, and 111-2636-E-002-024).

Development of an imaging analysis algorithm for quantitatively assessing skin conditions with optical coherence tomography

Ting-Hao Chen¹, Chau-Yee Ng^{2,3}, Cheng-An Huang¹, Chau-Hsiang Cheng¹, Yu-Hsuan Lee¹, Meng-Tsan Tsai^{2,4}, Cheng-Kuang Lee⁵, and Hsiang-Chieh Lee^{1,6*}

¹Graduate Institute of Photonics and Optoelectronics, National Taiwan University, Taipei 10617, Taiwan
²Department of Dermatology, Chang Gung Memorial Hospital, Linkou, Taoyuan 33380, Taiwan

³College of Medicine, Chang Gung University, Taoyuan 33302, Taiwan

⁴Department of Electrical Engineering, Chang Gung University, Taoyuan 33302, Taiwan

⁵NVIDIA AI Technology Center, Taipei 11492, Taiwan

⁶Department of Electrical Engineering, National Taiwan University, Taipei 10617, Taiwan

Abstract

Optical coherence tomography (OCT) is an imaging modality illustrated as the optical analog to ultrasound, where focused light illuminates a sample, and backscattered light is collected under the use of interferometry. OCT enables non-invasive, real-time and volumetric imaging of the skin architectures. In this study, we collected skin OCT images from different human body sites of 15 subjects with a prototype, portable spectral-domain OCT system. The contrast of the OCT images was effectively adjusted through optical attenuation coefficient (OAC) computation. This enables the development of a fully automatic segmentation algorithm, providing the parameters including the (i) epidermis thickness and the (ii, iii) roughness of the boundary between epidermis and air as well as epidermis and dermis. Also, the (iv, v) OAC coefficients of the epidermis and upper dermis layer are available.

Keywords: optical coherence tomography, skin, optical attenuation coefficient, quantitative analysis

I Introduction

Several optical technologies have been demonstrated as potential diagnostic tools for skin imaging, such as reflectance confocal microscopy (RCM) and optical coherence tomography (OCT). Although RCM could support cellular-level imaging, OCT could provide a larger field of view and a longer imaging depth than RCM. To quantitatively evaluate the skin condition with OCT, it is essential to develop an algorithm extracting different features, for example, epidermis thickness and the optical characteristic of the epidermis.

Although various segmentation algorithms have been proposed, most of the golden standards used involve the delineation of the boundary manually, where the labeling is highly relied on clinicians' experience and might vary among different physicians and the physician him or herself. Therefore, in this study, we collected skin OCT images of different sites from 15 subjects using a portable spectral-domain OCT system. The contrast of the OCT images can be effectively improved by optical attenuation

coefficient (OAC) computation. Besides, this enables the development of a fully automatic segmentation algorithm, providing the parameters such as the (i) epidermis thickness and the (ii, iii) roughness of the boundary between epidermis and air as well as epidermis and dermis. Also, the (iv, v) OAC coefficients of the epidermis and upper dermis layer are available. Collectively, the developed algorithm supports the quantitative analysis of the five parameters across the imaging site with volumetric OCT imaging. We believe the developed algorithm can facilitate the implementation of skin OCT imaging for aesthetic medicine as a modality for objective pre-and post-treatment evaluation.

II The experimental setup

The prototype, portable spectral-domain OCT system (Optical Skin Viewer, OPXION Technology Inc., New Taipei City, Taiwan) illustrated in Figure 1 is configured with a light source having a central wavelength of 840 nm such that the raw image data could be acquired. The interferometer schematic, as shown in figure 1, consists of

one 50/50 fiber coupler, a collimator lens as well as an achromatic doublet lens in the reference arm and sample arm, respectively. The sample arm is also designed as a handheld probe to scan any subject's skin site freely. Moreover, the interference light signal is gathered and transferred into an electrical signal by a spectrometer consisting of a line-scan camera (Octoplus-BA2 USB3.0, Teledyne e2V). The line-scan rate of this camera synchronized with the frame trigger by an Arduino module is set to 50 kHz, and the corresponding frame rate is 25 frames/s. Through the USB 3.0 cable, the signal is transmitted to the motherboard memory of a computer for subsequent OCT image reconstruction. Afterward, we improve the contrast of OCT images by calculating the optical attenuation coefficient (OAC) for subsequent quantitative analysis.

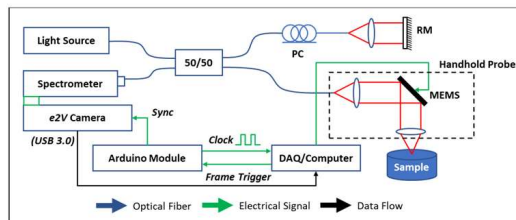


Figure 1. Detailed architecture diagram of handheld SD-OCT system. Reprinted from [1].

III Results and Discussion

The smoothing characteristics of the automatically labeled skin surface and the epidermal-dermal interface were analyzed by using a 3-order polynomial curve fitting, and the smaller the difference between the epidermal curve and the fitted curve, the smoother it is.

The example imaging results of one of the subjects are shown in Figure 2. The yellow and green curves are the results of curve fitting for the skin surface (red curve) and epidermal-dermal interface (blue curve), respectively. In Figure 2(c), the average of difference refers to the disparity of the curve fitting compared to the given curve, which also means the roughness of the interface. In the future, it is expected that this can be used to quantify the roughness of the skin surface in medical skin images.

Table 1 shows the measurement results of the thickness of the epidermis for five skin sites of the human body of fifteen subjects, including ten males and five

females. The average age of our subjects is 25 years, and the results listed in Table 1 also show that the epidermal thickness of males is greater than that of females.

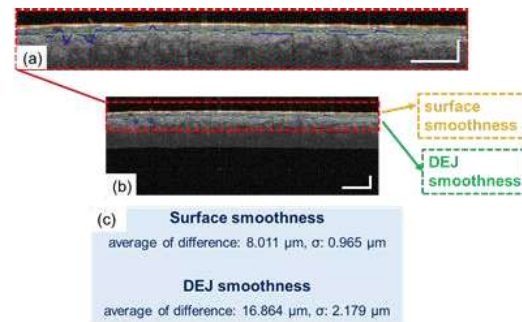


Figure 2. Result of the skin smoothness analysis of the right cheek. (a) Enlarged view of an enclosed area in (b) where the third-order curve fitting results are shown. (c) Results of the skin smoothness analysis, including the variance and standard deviation of surface smoothness and DEJ smoothness. Scale bars: 0.3 mm.

Table 1. The epidermal thickness values of different parts of the body for men and women.

Body sites	Male: 10	Female: 5
	Average thickness [μm]	
Right cheek	96.91 ±11.6	88.24 ±4.1
Left cheek	94.3 ±10.3	89.76 ±6.3
Forehead	95.81 ±14	98.19 ±3.5
Back of palm	115.07 ±22.3	100.06 ±9.1
Forearm	108.75 ±29	108.79 ±15

IV. Acknowledgement

The authors acknowledge the support from the Young Scholar Fellowship Program by the Ministry of Science and Technology (MOST) of the Republic of China (ROC), Taiwan (MOST 110-2636-E-002-025/111-2636-E-002-024) and the National Health Research Institute (NHRI), Taiwan (NHRI-EX110-11004EC/ EX111-11004EC).

References

[1] Y. P. Huang et al., "A Generic Framework for Fourier-

Domain Optical Coherence Tomography Imaging:
Software Architecture and Hardware
Implementations," IEEE Access, vol. 8, pp. 191726-
191736, 2020.

Hybrid Vision Transformer based Deep Learning for Pancreatic Cystic Lesion Classification Based on Confocal Endomicroscopy

Clara Lavita Angelina^a, Yi-Kai Chou^a, Tsung-Chun Lee, MD^b, Pradermchai Kongkam, MD^c, Ming-Lun Han, MD^d, Hsiu-Po Wang, MD^e, Hsuan-Ting Chang^{*a}

^aDepartment of Electrical Engineering, National Yunlin University of Science and Technology, Yunlin 64002, Taiwan, R.O.C.

^bGood Will Clinic, Taipei 100008, Taiwan, R.O.C.

^cGastrointestinal Endoscopy Excellence Center and Division of Gastroenterology, Chulalongkorn University and King Chulalongkorn Memorial Hospital, Bangkok 10330, Thailand.

^dDepartment of Integrated Diagnostics and Therapeutics, National Taiwan University Hospital, Taipei 100, Taiwan, R.O.C

^eDepartment of Internal Medicine, National Taiwan University Hospital, Taipei 100, Taiwan, R.O.C

Abstract

The early detection of pancreatic cystic lesions plays an important yet significant part in the survival chance of a patient with pancreatic cancer. Unfortunately, most pancreatic cancers were diagnosed when the tumor was metastatic. In this study, the Hybrid Transformer, which is the combination of the VGG19 network and Vision Transformer, is utilized as a learning model to predict the pancreatic cystic symptom types. A total of 16,944 images containing five types of pancreatic cystic are collected as the training and validation data. In our experiment, the proposed method successfully identifies the symptom types of 13 from 18 test videos and achieves an accuracy as high as 72%.

Keywords: deep learning, pancreatic cystic symptom, VGG19, vision transformer

I. Introduction

Pancreatic cancer is the 6th deadliest cancer in the world in 2020 [1], and according to the 108-year statistics on the causes of death of Chinese people by the Ministry of Health and Welfare, pancreatic cancer ranks seventh in China among the top ten cancer mortality rates [2]. Before the advent of effective screening and diagnostic tools, most pancreatic cancers were diagnosed when the tumor was locally advanced or metastatic. If the symptoms of pancreatic cancer can be detected and treated as soon as possible, the patient survival rate will be increasing. There are five types of pancreatic cystic lesions: (a) Intraductal papillary mucinous neoplasm (IPMN); (b) Mucinous cystic neoplasm (MCN); (c) Neuroendocrine tumor (NET); (d) Pseudocyst; and (e) Serous cystic neoplasm (SCN). Therefore, this study attempts to use the deep learning method, which utilizes a hybrid deep learning model that combines the convolutional neural network (CNN) and vision transformer (ViT) to perform the classification of cystic lesion types in pancreatic cancer based on the needle-based confocal laser endomicroscopy (nCLE).

II. Methodology

II.1. VGG19

In 2014, the Visual Geometry Group on Oxford University studied the impact of convolutional network

depth on the accuracy of image recognition in large-scale training sets [3], mainly using very small (3x3) convolutional filtering. Among them, the VGG19 network won first and second places in the ImageNet Challenge 2014 on localization and classification tasks. In this study, however, the high similarity of images in the training set leads to serious overfitting problems in network training. Therefore, the dropout layer is inserted in the last two fully connected layers of the VGG network to solve this problem.

II.2. Vision Transformer

Vision Transformer (ViT) is used for image sequence recognition after being adjusted by the transformer used for natural language processing. Figure 1 illustrates the basic architecture of ViT. First, an image is segmented into several patches, in which the feature size is equal to the pixel number. Next, the patches are flattened and embedded with their position information. Figure 2 illustrates the basic architecture in the transformer encoder. The transformer encoder receives the embedded patches and then the training process is performed with the layer normalization, multi-head attention, dropout, multi-layer perceptron (MLP) and residual block.

II.3. Hybrid Transformer

In this research, we use a hybrid transformer which is a combination of VGG19 and ViT network models. The hybrid transformer replaces the original image cropping

with a convolutional neural network. As a result, the significant features can be extracted by the convolutional neural network at first. Then the better training results can be obtained for small training sets. Compared with the original ViT model, the size and dimension of the patch can be reduced to save the training and testing time. Therefore, the hybrid transformer has the advantages of both the ViT and convolutional neural network.

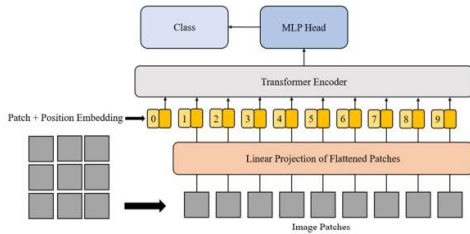


Figure 1. Vision transformer's basic architecture

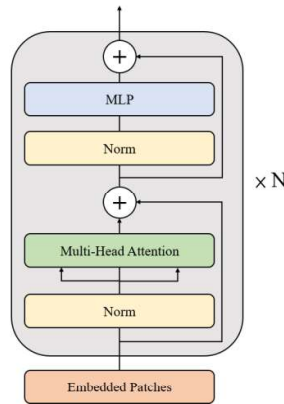


Figure 2. Transformer encoder's basic architecture

III. Experimental Results

In this study, we use the combinational VGG19+ViT network as the training model. During the training process, the Adam optimizer is used and the loss function is cross entropy. The learning rate, batch size, and epoch are 10⁻⁴, 32, and 100, respectively. We use the largest rectangular area as the ROI in the lens circle when classifying pancreatic cystic tumor videos and then calculate the weighted total votes of the optical flow rate. The sum of the votes then is divided by the number of total frames to obtain the predicted percentage. There are 18 videos with various cyst lesion types in the test dataset and 13 videos are classified correctly. Table 1 shows the overall result of the test videos.

Table 1. Experimental results of test videos

No	Video's cyst type	Correctly detected frames	Result
1	IPMN	57%	O
2	IPMN	79%	O
3	IPMN	88%	O
4	IPMN	28%	X
5	IPMN	43%	O
6	MCN	0%	X
7	MCN	57%	O
8	MCN	54%	O
9	SCN	7%	X
10	SCN	88%	O
11	SCN	89%	O
12	SCN	56%	O
13	NET	49%	O
14	NET	10%	X
15	NET	66%	O
16	NET	17%	X
17	Pseudocyst	88%	O
18	Pseudocyst	46%	O

IV Conclusion

In this study, we utilize the hybrid transformer which combines both the VGG19 and ViT for pancreatic cystic classification using CEM videos. The ROI of each test video is extracted from the largest area of the video frame. However, due to the serious shortage of data, parts of frames cannot be classified into the correct cyst types. This is also a limitation for our model to completely learn all the characteristics of various types of lesion symptoms. In the future, we will collect more videos for the training and testing stages so that the proposed method can be improved even further.

Acknowledgments

This research is partially supported by Ministry of Science and Technology (MOST), Taiwan, under the contract number MOST 111-2221-E-224-023-MY2.

References

- [1] H. Sung, J. Ferlay, R. L. Siegel, M. Laversanne, Soerjomataram, I., Jemal, A., and Bray, F., "Global cancer statistics 2020: GLOBOCAN estimates of incidence and mortality worldwide for 36 cancers in 185 countries," *A Cancer Journal of Clinicians* 871(3), 209-249 (2021).
- [2] Ministry of Health and Welfare Statistic Division, "Statistical analysis of the cause of death in 109 years," <https://www.mohw.gov.tw/cp-5017-61533-1.html>, 18 June 2022.
- [3] Simonyan, K., and Zisserman, A., "Very deep convolutional networks for large-scale image recognition," *Proc. 2015 International Conference on Learning Representations*, 1-14 (2015).

Dioptric correction Spectral-Domain Optical Coherence Tomography Angiography in Ophthalmology

Sung-Wen Huang^a, Jia-Pu Syu^a, and Wen-Chuan Kuo^{a,*}

^aInstitute of Biophotonics, National Yang Ming Chiao Tung University, Taipei 112, Taiwan, R.O.C

*Corresponding author's email: kuo@nycu.edu.tw

Abstract

This study aims to develop a dioptric correction spectral-domain optical coherence tomography (SD-OCT) platform for ophthalmic structural imaging and angiography. Our proposed OCT system uses electronic tunable lenses (ETL) to compensate for individual dioptric differences from the eye's axial length, ensuring the best possible image quality for every OCT scanning and meeting clinical diagnosis needs.

Keywords: Spectral-Domain Optical Coherence Tomography, ophthalmology, angiography, dioptric correction, electronically tunable lenses

I Introduction

Optical coherence tomography (OCT) and OCT angiography (OCTA) have become essential tools for the evaluation of the retina. OCT is a non-contact, non-invasive, real-time, and high-resolution imaging technology. After fast scanning and post-processing to obtain structural and vascular information, OCT provides objective analysis and has been widely used in diagnosing ophthalmic diseases. To help preclinical and basic research on ophthalmology, our laboratory designed a high-resolution OCT system for rodent fundus imaging, which could distinguish all retinal layers in mice and rats. However, due to the high-resolution characteristics (~3 μm), the image quality was degraded compared with the general resolution OCT (10 μm) in scanning the human eye. This is due to dioptric incorrect or individual differences in eye's axial length. Since electronically tunable lenses (ETL) were the earliest technology to eliminate mechanical axial movement in microscopy [1], therefore, this study proposes to use ETL to effectively compensate for individual dioptric differences from the eye's axial length, ensuring the best possible image quality for every OCT scanning and meeting clinical diagnosis needs.

II Methods

1. High-resolution SDOCT setup

The dioptric correction spectral-domain OCTA (SD-OCTA) system (Fig 1A) has a super-luminescent diode

with a central wavelength of 838 nm and 178nm bandwidth. The measured axial resolution is 3 μm in the retina. The power to the eye is about 750 μW , and the radiation illuminance was calculated to meet the safety range of human eyes, which is within the American National Standards Institute (ANSI) Standards for safe ocular laser exposure [2]. Two specially designed lenses were used to form a confocal lens group. The ETL (Optotune AG, Switzerland, EL-10-30-C) zoom allowed the light to focus on different depths within the eye, ensuring the light focused on the retina if the dioptric was incorrect. A spectrometer measured the interfering signals with a full-scale image depth (in the air) of 2mm.

2. Image acquisition protocol

The OCTA scanning pattern performed three repeated B-scans at the same location with 500 A-scans per B-scan. Therefore, 500 locations lead to a total of 1500 B-scans per volume, and 100 kHz A-scan rate provided each volume acquisition time of 7.5 s. OCTA B-scans were computed from the three repeated B-scans acquired at each position.

3. Human test

We solicited three subjects with nearsightedness of 2.0 diopters, 4.0 diopters, and 10.0 diopters. The head was fixed on a pedestal, as shown in the photograph below (Fig 1B), and artificial tears were regularly aimed at the eyes to keep them moist before scanning.

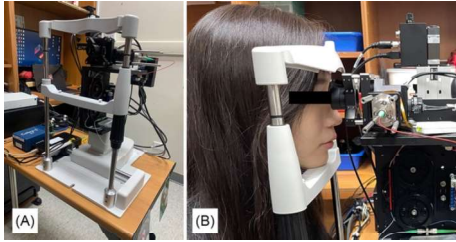


Figure 1. Photograph of the OCTA system (A) and actual operation (B).

III Results and Discussion

For the purpose of evaluating the effectiveness of the ETL, we compared the human retinal scan and angiography from the OCT system without the ETL (Fig 2A, C) with the OCT system with the ETL (Fig 2B, D). A problem of incorrect diopters prevents the OCT and angiography (Fig 2A and 2C) from focusing perfectly on the retina, so the image intensity is worse than the system combining ETL and OCT (Fig 2B and 2D). Furthermore, blood vessel contours appear more clearly in the OCTA images when combined with the ETL (Fig 2D).

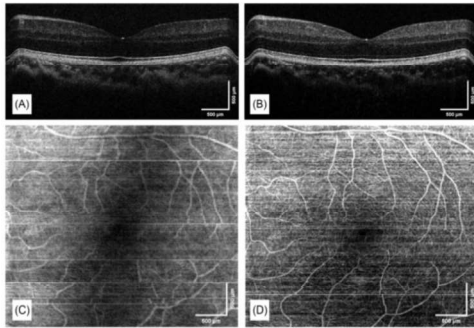


Figure 2. OCT image of the human retina. Cross-section of intensity image without the ETL (A) and after combining the ETL (B). Corresponding OCTA *en face* image without the ETL (C) and after combining the ETL (D). Scale bars are 500μm.

We respectively scanned three different subjects with nearsightedness of 2.0 diopters (Fig 3A and 3B), 4.0 diopters (Fig 3C and 3D), and 10.0 diopters (Fig 3E and 3F). For intensity and OCTA images of humans with different diopters, we found that the system combining the

ETL can provide a high-quality OCT and vessel image.

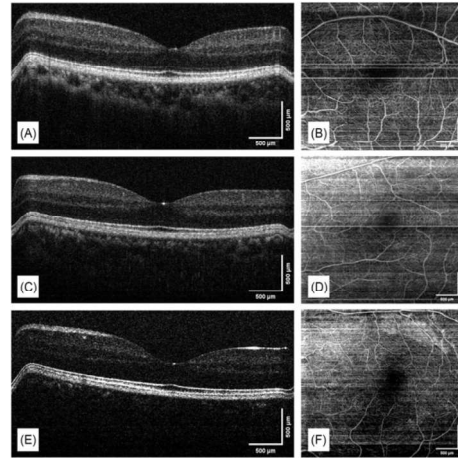


Figure 3. In vivo OCT images of three human retinas. Cross-section of intensity image from nearsighted of 2.0 diopters (A), 4.0 diopters(C), and 10.0 diopters(E). OCTA *en face* image from nearsighted of 2.0 diopters (B), 4.0 diopters (D), and 10.0 diopters (F). Scale bars are 500 μm.

IV Conclusion

This study verifies that the deformation characteristics of ETL can be used to correct the human eye diopter or individual differences, to improve the OCT and OCTA images. In the future, we will scan and analyze the patient with lesions, combine the program to achieve an automatic adjustment system to improve the operation speed, reduce human errors, and make a handheld system the goal.

V Acknowledgements

Grant support: Taiwan MOST 111-2112-M-A49-026.

References

1. EFSTATHIOU, Christoforos; DRAVIAM, Viji M. Electrically tunable lenses—eliminating mechanical axial movements during high-speed 3D live imaging. *Journal of Cell Science*, 2021, 134.16: jcs258650.
2. American National Standard Institute, American National Standard for Safe Use of Lasers (ANSI Z136.1-2014)(2014).

Single-Cell Manipulation and Detection Platform Based on Optical Tweezers for Investigating the Chemotaxis and Response of Cancer cells to Tyrosine Kinase Inhibitor PD153035

Mamadi M.S Colley^a, Cheng-Jen Chang^a, Jen-Chang Yang^{b,c,d}, Pei-Wen Peng^c and Tzu-Sen Yang^{a,c,d,e,*}

^a Graduate Institute of Biomedical Optomechatronics, Taipei Medical University, Taipei 110, Taiwan;

^b Graduate Institute of Nanomedicine and Medical Engineering, Taipei Medical University, Taipei 11031, Taiwan;

^c International PhD Program in Biomedical Engineering, Taipei Medical University, Taipei 110, Taiwan

^d Research Center of Biomedical Device, Taipei Medical University, Taipei 110, Taiwan

^e School of Dental Technology, Taipei Medical University, Taipei 110, Taiwan;

Abstract

We presented a mechanism to handle the single-cell reaction to the tyrosine-kinase-inhibitor PD153035 and cancer cell chemotaxis. We used the single-cell platform and an Optical-Tweezer Technology to control an epidermal growth factor (EGF)-coated bead established near the filopodia to stimulate HT29 cells locally. The discoveries manifested that the filopodial actin filament serves as an EGF detection sensory mechanism. PD153035's exquisite EGFR selectivity and unpredictable binding characteristics were proved. The single-cell approach may be used to develop a fast screening system for the detection and therapeutic evaluation of a variety of cancer types during chemotaxis.

Keywords: chemotaxis; epidermal growth factor (EGF); tyrosine kinase inhibitor; PD153035; optical tweezers; single-cell platform.

I. Introduction

Chemotaxis of cancer cells in the local microenvironment plays a crucial role in tumor growth and spread [1]. Chemotaxis is now understood to be a potential therapeutic target, a therapeutic endpoint, and a prognostic indicator [2]. Chemosensing, polarization, and movement are the three main stages of the chemotactic response of cancer cells.

Epidermal growth factor receptor (EGFR), among other receptor tyrosine kinases, has recently been identified as signaling molecules that mediate chemotactic responses in EGF/EGFR signaling [1,2]. Therefore, a thorough understanding of the process underlying cancer cell chemotaxis will aid in developing fresh ideas and cancer treatment plans.

Modern methodologies are needed to investigate the real-time cellular responses to PD153035 because of the continual breakthroughs in diverse nanomaterials and nanotechnologies. These developments compelled us to investigate and address the pharmacological problems with multitargeted TKI PD153035 in more depth.

Here, to imitate the chemosensing process mediated by EGF/EGFR signaling, we used high-resolution optical tweezers and microfluidic systems with precise sample temperature control to actively conduct spatial and temporal management of cell movement (**Figure 1**).

II Methods

A high-resolution optical tweezer system was used to control the EGF-coated bead, which was then placed within an inverted microscope (TE2000U, Nikon, Tokyo, Japan) with a Nd:YAG laser (1064 nm, VA-II-N-1064, Beijing, China) added for trapping. Cancer cell chemotaxis and responsiveness to TKI PD153035 at the single-cell level, the human colon cancer cell line HT29 that overexpresses the EGFR was employed as a research model. Both Alexa Fluor® 635 phalloidin (Invitrogen Cat. no. A34054) and quantum dots attached to epidermal growth factor (EGF, Molecular Probes) were utilized to separate the link between the EGF-EGFR complex and the actin cytoskeleton.

For the purpose of capturing images at a frame rate of 1 fps and analyzing the data, the EMCCD camera was employed.

III Results and Discussion

We first investigated the distribution of actin filaments in HT29 cells, where F-actin was visualized using Alexa Fluor® 635 phalloidin (Invitrogen Cat. no. A34054). Comprehensive information can be found in our earlier publication [3]

Figure 2 showed the EGF-coated-bead simulation of HT29 cells and found that the propagation speed at the leading edge of the cell is enhanced due to the presence of EGF-stimulated chemotaxis. Figure 3, demonstrated the assertion that PD153035 was a specific and reversible inhibitor of the EGFR tyrosine kinase at a single-living cell

level. Further, figure 4 revealed cells treated with TKI PD153035 the position of the leading edge of HT29 cell were not influenced by EGF-coated bead. however, once washed cells with drug-free medium the leading edge of cells was directly attached to EGF-coated beads half an hour later.

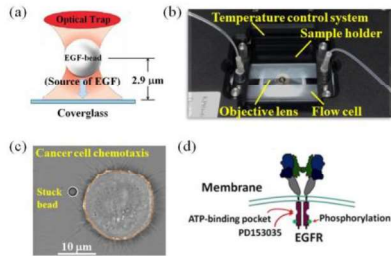


Figure 1. (a) The trapped bead location inside the cover glass surface. (b) A temperature-controlled microfluidic flow channel joined with inverted fluorescence microscope (c) bright field image of single-cell held EGF-bead. (d) PD153035 binding to ATP-binding pocket

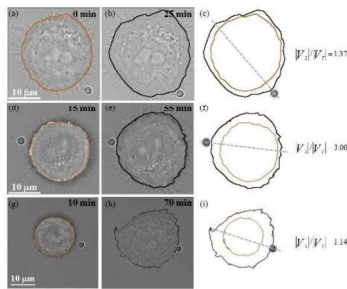


Figure 2. Bright-field images of various time-point of HT29 cell response to EGF-coated bead stimulation. HT29 cells at different time point t_0 and t_1

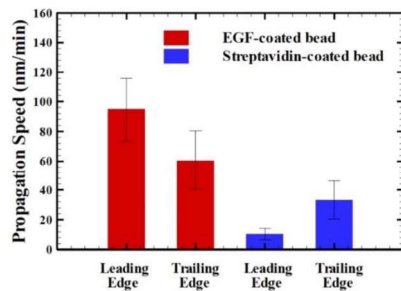


Figure 3. The impact of the streptavidin- and EGF-coated beads on the transmission rates at the leading and trailing edge ($|V_L|$) and ($|V_T|$).

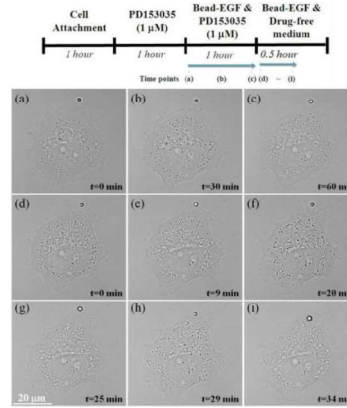


Figure 4. (a-c) Bright-field imaging of live HT29 cells exposed to $1 \mu\text{M}$ of PD153035 for 1 hour at 37°C . (d-i) drug-free live cell images of HT29 an hour at 37°C .

IV Conclusion

Regarding the relationship between the EGF-EGFR complex and the actin cytoskeleton, there was colocalization between QD-EGF-EGFR complexes and the filopodial actin filaments, which implies that the filopodial actin filament acts as a sensory system for EGF detection.

Acknowledgement

This work was financially supported by the “TMU Research Center of Cancer Translational Medicine” from The Featured Areas Research Center Program within the framework of the Higher Education Sprout Project by the Ministry of Education (MOE) in Taiwan. This study was also supported by the Ministry of Science and Technology, Taiwan, under grants (MOST 111-2221-E-038- 012-, MOST 111-2221-E-038-009-)

References

- Kempiak, S.J.; Yip, S.C.; Backer, J.M.; Segall, J.E. Local signaling by the EGF receptor. *J. Cell Biol.* 2003, 162, 781–787.
- Roussos, E.T.; Condeelis, J.S.; Patsialou, A. Chemotaxis in cancer. *Nat. Rev. Cancer* 2011, 11, 573–587.
- Peng, P. W., Yang, J. C., Colley, M. M., & Yang, T. S. (2021, November). An optical tweezers-based single-cell manipulation and detection platform for probing real-time cancer cell chemotaxis and response to tyrosine kinase inhibitor PD153035. *In Photonics 2021 Nov 26 (Vol. 8, No. 12, p. 533)*. MDP

H&E-compatible Rapid Fresh Pathology technique for intraoperative tumor assessment at a sustained data throughput of >700 Mbps

Bhaskar Jyoti Borah*^a, Yao-Chen Tseng^a, Chi-Kuang Sun^a

^aDepartment of Electrical Engineering and Graduate Institute of Photonics and Optoelectronics, National Taiwan University, Taipei 10617, Taiwan, R.O.C.

Abstract

Intraoperative tumor assessment (ITA) is essential to effectively resect a tumor especially associated to a vital organ such as a human brain. Frozen section (FS) pathology which is presently the gold standard for ITA often consumes up-to 30 minutes of duration. We introduce a Hematoxylin and Eosin (H&E)-compatible technique called Rapid Fresh Pathology (RFP) to provide a sub-10-minute digital ITA solution while securing excellent accuracy comparable to a formalin-fixed paraffin-embedded (FFPE)-biopsy. RFP is assisted by a mesoscale Nonlinear Optical Gigascope (*mNLOG*) platform which enables a sustained laser-scanning data throughput of >700 M bits per sec (Mbps).

Keywords: intraoperative tumor assessment, frozen section, rapid fresh pathology, hematoxylin and eosin, Nonlinear Optical Gigascope.

I Introduction

A fast and accurate ITA is often treated as a basic necessity in different levels of surgical pathology applications¹. A highly reliable FFPE-biopsy consumes up-to 1-2 days of processing time, and thus can not be used for a typical ITA. On the other hand, the gold standard FS-biopsy consumes up-to 30 minutes per round. However, FS involves cryosectioning and the process is often susceptible to freezing artifacts which might compromise an ITA. Besides, the feasible number of ITAs in a critical surgery still remains limited owing to a prolonged processing time.

It is noted that quite a few optical imaging modalities are capable of providing rapid digital ITA by means of optical virtual sectioning of an excised specimen. However, the prior arts²⁻⁴ might not reach the state-of-the-art whole-slide-imaging (WSI) standard⁵ especially in the contexts of centimeter-scale gigapixel laser-scanning with half-a-micron digital resolution, and/or a real-time artifact-compensated stitching or mosaicking feature, and/or a post-processing-free gigapixel acquisition, stitching, and digital display ability. Furthermore, pathologists are often trained and adapted to the standard H&E-specific histological features. Therefore, a deep learning approach

and/or additional interpretation training might be needed for a pathologist while adapting to an H&E-alternative dye for nuclei contrast. Nevertheless, accuracy and reliability remain important concerns, while organ-specific and/or hospital-specific repeated training might be required for different surgical pathology applications.

We provide a digital ITA technique called Rapid Fresh Pathology (RFP) which is 4 times faster than a typical FS-biopsy. A mesoscale Nonlinear Optical Gigascope (*mNLOG*) platform is introduced enabling a whole specimen superficial imaging (WSSI) solution at a sustained laser-scanning throughput of >700 Mbps.

II Results

Figure 1(a) provides a simple illustration of the RFP method. A resected specimen directly undergoes a whole mount rapid tissue staining (RTS) process. The specimen is placed inside a chamber, and a sub-6-minute procedure is performed to stain with the traditional H&E dyes. The RTS-applied specimen is then imaged by the *mNLOG* platform which comprises a 2-channel nonlinear optical scanning system collecting third harmonic generation and two-photon excitation fluorescence signals from the H and E dyes, respectively. The scanning head utilizes a

resonant-galvanometer mirror pair (CRS 4 kHz and 8320K, Cambridge Technology, USA) for raster scanning. A high numerical aperture ($NA > 0.9$) objective lens (XLUMPlanFI, 20 \times) ensures a submicron optical resolution. For nonlinear excitation, a 70 MHz, <60 fs fiber laser (Fidelity-2, Coherent, USA) centered at 1070 nm is utilized.

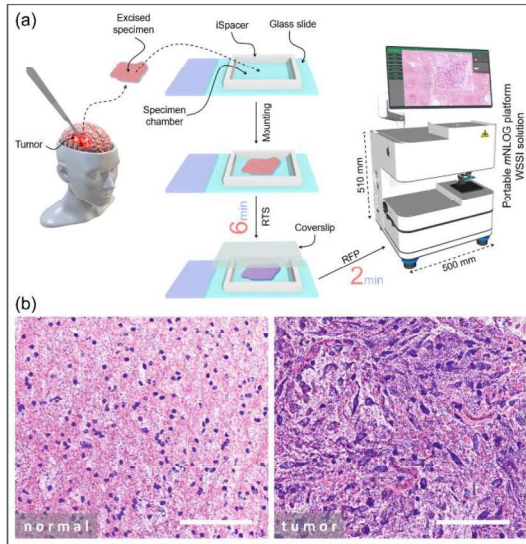


Figure 1. Illustration of the proposed Rapid Fresh Pathology technique. (a) Excised specimen is placed inside a chamber and a rapid tissue staining procedure is performed followed by imaging via a mesoscale nonlinear optical gigascope. (b) Examples of normal- and tumor-specific RFP images of human brain. Scale bar: 100 μm .

To demonstrate the RFP technique, human brain specimens are utilized in this study (IRB approvals: 201912225RINB, National Taiwan University Hospital and 201412063RINC, National Taiwan University). Figure 1(b) depicts examples of normal- and tumor-specific histological features. Real-time color remapping is performed in each case to resemble a typical H&E-specific image.

It is noted that to enable centimeter-scale high resolution imaging, the *mNLOG* platform is streamlined to a rapid artifact-compensated 2D large-field mosaic-stitching (*rac2D-LMS*) approach which secures a mosaic-stitching ability of $>12 \times 12 \text{ mm}^2$ area with 130 G bits of data in 60

seconds. Assisted by the *mNLOG* platform together with the *rac2D-LMS* approach, the RFP method holds the ability to image a 1 cm^2 area in <120 seconds with 86 G bits or 3.6 Gigapixels of data, and thus secures a sustained effective point-scanning throughput of >700 Mbps.

III Conclusion

Owing to H&E-compatibility, the RFP technique does not require an additional interpretation training for a pathologist. Besides, an RFP-applied specimen can readily and reliably undergo an FFPE-biopsy for margin confirmation. With excellent accuracy, the RFP technique is quite promising to be applied to different types of specimens, such as but not limited to breast, prostate, liver, skin, etc., in order to enhance the effectiveness of a surgical procedure.

III Acknowledgement

This project was supported by the Ministry of Science and Technology (Taiwan) with financial grant MOST 111-2321-B-002-015- and Ministry of Economic Affairs (Taiwan) with financial grant 111-EC-17-A-19-S6-009.

IV References

- [1] Deeken-Draisey, A., et al., "Current Procedural Terminology Coding for Surgical Pathology: A Review and One Academic Center's Experience With Pathologist-Verified Coding," *Archives of Pathology & Laboratory Medicine* 142(12), 1524–1532 (2018).
- [2] Tao, Y.K., et al., "Assessment of breast pathologies using nonlinear microscopy," *Proceedings of the National Academy of Sciences of the United States of America* 111(43), 15304–15309 (2014).
- [3] Cahill, L.C., et al., "Nonlinear microscopy for detection of prostate cancer: analysis of sensitivity and specificity in radical prostatectomies," *Modern Pathology* 33(5), 916–923 (2020).
- [4] Xie, W., et al., "Diagnosing 12 prostate needle cores within an hour of biopsy via open-top light-sheet microscopy," *Journal of Biomedical Optics* 25(12), (2020).
- [5] Patel, A., et al., "Contemporary Whole Slide Imaging Devices and Their Applications within the Modern Pathology Department: A Selected Hardware Review," *Journal of Pathology Informatics* 12(1), 50 (2021).

Design and characterization of flattop beam shapes through volume holographic grating*

Surag Athippillil Suresh^{a,b,*}, Sunil Vyas^b, J. Andrew Yeh^a, Yuan Luo^{b,c,d}

^aInstitute of Nano Engineering and Microsystems, National Tsing Hua University, Hsinchu 30013, Taiwan, R.O.C.

^bInstitute of Medical Device and Imaging, National Taiwan University, Taipei 10051, Taiwan, R.O.C.

^cDepartment of Biomedical Engineering, National Taiwan University, Taipei, Taiwan, R.O.C

^dMolecular Imaging Center, National Taiwan University, Taipei, Taiwan, R.O.C

Abstract

Beam shapes with uniform intensity all over the diameter (flattop) have been designed, recorded, and reconstructed through photopolymer (PQ-PMMA) to create volume holographic (VH) optical element. A programmable device is used for modulating the laser beam to different flattop beam shapes. An ISO standard characterization parameters measurement of flattop beams has been carried out to demonstrate the quality of reconstructed beam. Flattop beam shapes realized by VH grating with unique diffractive properties are advantageous for variety of laser applications.

Keywords: Volume Holography, Super Gaussian beam, beam shaping, ISO standard, beam quality.

I Introduction

Most of the laser applications commonly using Gaussian beams for illumination. Most of these applications, it is difficult to maintain constant amplitude and phase profile throughout the propagation of a beam. One of the best way to solve this issue is by creating uniform intensity distribution over the entire beam diameter through a flattop (super Gaussian) beam shaping [1]. Most of the beam shaping technique requires complex optical components which makes its usage difficult. Amplitude of the contour is the major influencing factor in shape of the beam. In addition, it is difficult to quantitatively analyze these beam shapes before suggesting for different applications. Here, we demonstrated an effective volume holographic beam shaper that can modulate an incident reference beam to flattop beam and proper characterization of the beam shapes generated are done quantitatively as per ISO standard beam quality measuring parameters [2]. The amplitude of Super Gaussian beam is modulated with the help of a digital micro-mirror (DMD) [3].

* surag.s.nair@gmail.com; phone +886-981682454

Major advantages from VH beam shapers are high angular selectivity and high wavelength degeneracy which is useful in spatial-spectral mode shaping. PQ-PMMA photo polymer based VH beam shapers are a good selection for recording the holograms because of its characteristics like wavelength selectivity, high photo response, low amount of diminution and simple fabrication procedure [4]. Flattop beam shaping is a key technique to fulfil uniform illumination requirements in many practical applications such as advanced imaging techniques, holographic optical tweezers, quantum communication and laser based micro fabrications

II System setup and procedure

The Lee holograms corresponding to different flattop beam shapes have been designed to modulate the characteristics from Gaussian to flattop, are shown in Fig. 1(a). Corresponding beam shapes reconstructed from volume hologram is depicted in Fig. 1(b) with corresponding intensity profiles in Fig. 1(c). Flattop

beam shapes reconstructed with three different wavelengths is shown in Figure 2.

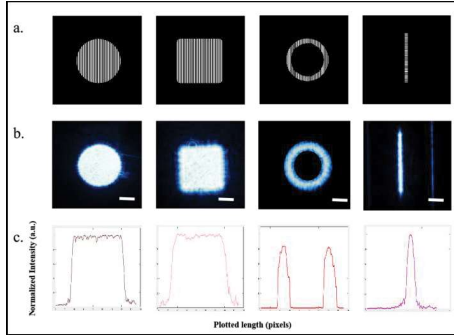


Figure 1. (a) Lee holograms for different flattop beam shapes (b) Beam shapes reconstructed from volume hologram (c) Corresponding intensity profiles of reconstructed beam shapes.

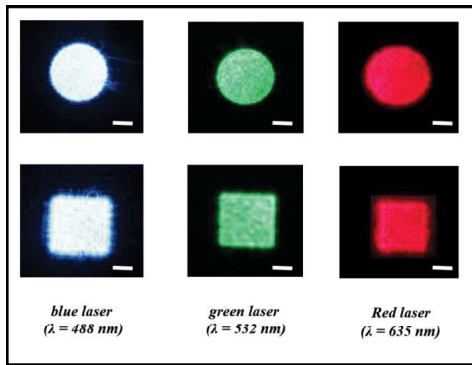


Figure 2. circular and square shaped flattop beams reconstructed using three different wavelengths.

III Results and discussion

DMD has been used to generate amplitude modulated beam shapes. The quality of the reconstructed beam shapes using VH has been quantitatively analyzed by ISO standards of beam quality measurement. We have considered beam characterizing parameters proposed in ISO 13694:2000 for flattop beam quality measurement. The parameters are, beam flatness factor - for quantitatively analyze uniformity of power density distribution over diameter, Beam uniformity, plateau uniformity and edge steepness, for analyzing the vertical nature of edges. From table 1, it is evident that, the beams which are reconstructed from volume hologram provides more than 85% successful.

Laser wavelength (nm)	Super gaussian beam (circular after VH reconstruction)			Super gaussian beam (square after VH reconstruction)			% of successful reconstruction w.r.t. DMD plane Super gaussian beam (Circular)	% of successful reconstruction w.r.t. DMD plane Super gaussian beam (Square)
	Blue laser ($\lambda = 488 \text{ nm}$)	Green laser ($\lambda = 532 \text{ nm}$)	Red laser ($\lambda = 635 \text{ nm}$)	Blue laser ($\lambda = 488 \text{ nm}$)	Green laser ($\lambda = 532 \text{ nm}$)	Red laser ($\lambda = 635 \text{ nm}$)		
Beam flatness	0.9244	0.9231	0.9119	0.9256	0.9264	0.9193	99.02%	98.54%
Beam uniformity	0.0938	0.09356	0.0945	0.0932	0.1005	0.0176	86.8%	85.3%
Plateau uniformity	0.1098	0.1074	0.1103	0.1061	0.1075	0.1134	90%	84.9%
Edge steepness	0.1484	0.1489	0.1491	0.1486	0.1482	0.1478	89.1%	88.7%

Table 1. Comparison of characterizing factors of flattop beam shapes at different wavelength reconstructions. The percentage of success rate in reconstruction is also quantitatively analyzed and mentioned.

IV Conclusion

We have successfully recorded and reconstructed flattop beam shapes through photopolymer (PQ-PMMA) based volume holographic grating. Also demonstrated the success rate of reconstruction quality in terms of ISO standard characterizing parameter measurement. Our flattop volume holographic beam shaper will provide wide applications in holographic optical tweezers, quantum communication, laser based micro fabrications, and various imaging technologies.

V Acknowledgement

Taiwan Ministry of Science and Technology (MOST 108-2221-E-002-168-MY4, MOST 108-2221-E-007-098-MY3), National Taiwan University (109L7839), and YongLin Institute of Health (08HZY49001).

VI References

- [1] F. M. Dickey, L. S. Weichman, R. N. Shagam, "Laser beam shaping techniques," Int Soc Opt Photon, 8: 338–348(2000).
- [2] ISO/TC 172, Optics and photonics, Subcommittee SC 9, Laser and electro-optical systems, "Test methods for laser beam power (energy) density distribution". < <https://www.iso.org/obp/ui#iso:std:iso:13694:ed-3:vi:en> > (2018).
- [3] Y.-X. Ren, R.-D. Lu, and L. Gong, "Tailoring light with a digital micro mirror device," Ann. Phys. 527, 447–470 (2015).
- [4] S. Vyas, Y. H. Chia, and Y. Luo, "Volume holographic spatial-spectral imaging systems [Invited]," J. Opt. Soc. Am. A 36, A47-A58 (2019)

Volume holographic lenslet array based confocal imaging*

Surag Athippillil Suresh^{a,b*}, Sunil Vyas^b, J. Andrew Yeh^a, Yuan Luo^{b,c,d}

^aInstitute of Nano Engineering and Microsystems, National Tsing Hua University, Hsinchu 30013, Taiwan, R.O.C.

^bInstitute of Medical Device and Imaging, National Taiwan University, Taipei 10051, Taiwan, R.O.C.

^cDepartment of Biomedical Engineering, National Taiwan University, Taipei, Taiwan, R.O.C

^dMolecular Imaging Center, National Taiwan University, Taipei, Taiwan, R.O.C

Abstract

A confocal imaging system has been realized by incorporating a photo polymer based volume holographic (VH) lenslet array to illuminate the sample with multiple focal spots. A super Gaussian (SG) beam shaping has been implemented to multifocal spots to create uniform illumination. The proposed illumination technique can significantly improve the time for image acquisition without affecting the quality. Fluorescence imaging has been carried out for demonstrating the performance. The proposed technique may find wide applications in high speed optical sectioned imaging modalities.

Keywords: Volume Holography, Super Gaussian beam, Lenslet array, Confocal Microscopy.

I Introduction

Confocal microscopy is considered as one of the popular imaging modalities because of its ability to produce optical sectioned images. Many other functionalities are also added to confocal imaging platform to improve its versatility [1]. Multifocal illumination is one which produces a spatially dependent signal-to-noise ratio and improvement in image acquisition time while scanning [2]. Gaussian shaped beam distributions are common in most of laser applications. Multifocal illumination is generated by illuminating a Micro Lens Array (MLA) with a collimated Gaussian beam. But, that illumination field is not homogeneous whose intensity depends on their location [3]. Alternatively, illuminating the MLA with a SG beam results in an array of multiple focal spots of homogeneous intensity. Recording and reconstructing a lenslet array with SG beam into a diffractive optical element such as volume hologram can be made. VH beam shapers are compact and efficient optical component that can shape an incident reference beam into a uniform and sharp intensity distribution.

* surag.s.nair@gmail.com; phone +886-981682454

The amplitude of SG beam is encoded on Lee hologram for modulating through digital micro mirror device (DMD) [4]. Aiming at the unique characteristics like high angular selectivity and high wavelength degeneracy, the VH beam shaping optical element can be used as a spatial-spectral mode shaper. PQ-PMMA based materials are mainly chosen for recording the holograms due to its wavelength selectivity, high photo response, low amount of diminution & simple fabrication procedure [5]. In this work, we built a confocal fluorescence microscopy by incorporating volume holographic lenslet array as a compact illumination device. The advantages of this beam shaper for reconstructing multifocal SG beam spots can be utilized for illumination.

II System setup and procedure

The intensity distribution of multiple focal spots generated from the DMD and VH lenslet array, respectively and corresponding normalized intensity profiles is shown in Fig.1. An illustration of confocal system using VH lenslet array is depicted in Fig.2. The system contains an argon ion (Ar+) laser (Innova 304C, Coherent Inc.) as illumination source, Relay lens, volume hologram with lens pair, polarizer, polarized beam splitter, QW plate and objective lens (NA =0.55, 50X) in the

illumination path. The sample is scanned with the help of a stage scanning device. In the detection arm, the signal coming from sample is focused in to a CCD camera by a focusing lens and are captured for each beam spots with the help of a custom made LabView program.

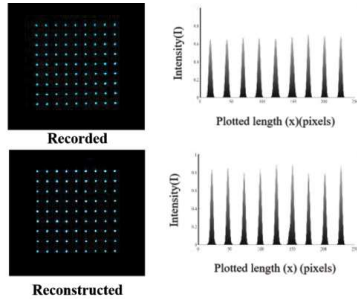


Figure 1. The intensity distribution of multifocal spots generated from the DMD and VHLA, respectively and corresponding normalized intensity profiles

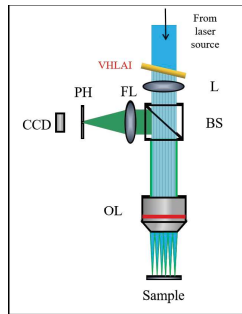


Figure 2. Confocal imaging system setup using volume holographic lenslet array for illumination.

III Results and discussion

To demonstrate the optical sectioning capability of the proposed confocal system for biomedical imaging, a fluorescent-labeled (Green fluorescent protein, GFP) mouse cardiac tissue has been imaged. Figures 2(a), (b) give optically sectioned confocal images of fluorescent-labeled mouse cardiac tissue obtained from respective depths of $z = 1.11$ mm and $z = 1.02$ mm. There are some visible features can be identified from both layers. Figure 2(c) show wide-field image of fluorescently labeled mouse cardiac tissue after scanning. There are no separable features can be differentiated in wide-field images. Figure. 2(d) shows intensity profiles plotted along the blue dashed lines drawn along areas from both layers.

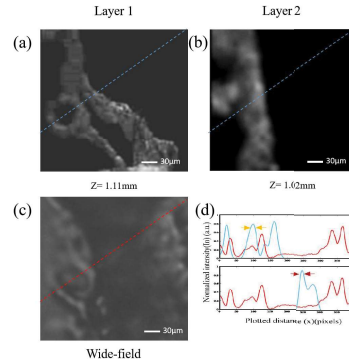


Figure 3. (a), (b) Optical sectioned multifocal confocal Images of fluorescent-labeled mouse cardiac tissue at a depth of $z = 1.11$ mm, $z = 1.02$ mm. (c) A wide-field image, and (d)Corresponding intensity profiles denote features.

IV Conclusion

We have developed a fluorescence confocal imaging system incorporating volume holographic lenslet array for multifocal illumination. We created the array of SG beam spots to get accurate control over the intensity. Unique capability of our volume holographic lenslet array will provide advantages for realizing compact illumination system. This system can perform higher time resolution without sacrificing the quality.

V Acknowledgement

Taiwan Ministry of Science and Technology (MOST 108-2221-E-002-168-MY4, MOST 108-2221-E-007-098-MY3), National Taiwan University (109L7839), and YongLin Institute of Health (08HZY49001).

VI References

- [1] M. Minsky, "Memoir on inventing the confocal scanning microscope," *Scanning* 10, 128–138 (1988).
- [2] Y. Yu, X. Ye, and M D. McCluskey, "Confocal microscopy with a microlens array," *Appl. Opt.* 59, (2020)
- [3] X. Y. .Ding, Y. X. Ren, R. D. Lu "Shaping super-Gaussian beam through digital micro-mirror device," *Sci China-Phys Mech Astro*, 58: 034202(2015).
- [4] S. A. Suresh, S. Vyas, W-P. Chen, J. A. Yeh, and Y. Luo, "Multifocal confocal microscopy using a volume holographic lenslet array illuminator," *Opt. Express* 30(9), (2022)

Single-shot recording of transport of intensity equation-based three-dimensional fluorescent imaging

Manoj Kumar^a, Naru Yoneda^a, Xiangyu Quan^{a,b}, Osamu Matoba^{*a,b}

^a Graduate School of System Informatics, Kobe University, Rokkodai 1-1, Nada, Kobe, Japan

^b Center of Optical Scattering Image Science, Kobe University, Rokkodai 1-1, Nada, Kobe, Japan

Abstract

We present a single-shot recording system of transport of intensity equation-based three-dimensional fluorescence imaging. In the experimental setup, two image sensors located at different depth positions capture the intensity distributions at the different depth positions of the biological sample in a single acquisition. From the two images, the amplitude and the phase distributions are obtained and then 3D fluorescence image is retrieved by numerical wave propagation. The experimental demonstration was implemented by using tobacco suspension culture cells.

Keywords: Transport of intensity equation, Fluorescence imaging, Single-shot 3D fluorescence image

I Introduction

High-speed 3D fluorescence imaging techniques are important tools in biology and life sciences because they enable monitoring of living cell activity. The development of various fluorescent proteins has made it possible to observe specific regions such as the nucleus of cells. In neuroscience and other fields, high-speed 3D fluorescence imaging technology is useful for non-invasive and non-contact investigation of cellular activity through manipulation of cell activity using optogenetics and calcium imaging in order to study neuronal activity and connections between neurons and other cells. So far, incoherent digital holography [1-3], light field, light sheet, and transport of intensity equation (TIE) [4,5] are promising high-speed 3D fluorescence imaging techniques. Among these, 3D fluorescence imaging by light sheet and TIE cannot obtain 3D information in a single recording. In 3D fluorescence imaging by the TIE [4,5], there is the spatial coherence of spread fluorescence light distribution after the certain distance propagation from the molecule including fluorescence proteins, and the wavefront distribution is obtained from two or more intensity images at different depths. Then, the amplitude and phase distributions are used to obtain cross-sectional images, those are 3D fluorescence images in a computer by

*matoba@kobe-u.ac.jp; +81-78-803-6235

numerical light wave propagation calculations. Since only intensity images are used, an optical setup is simple and compact. One of the problems with high-speed recording, two or more intensity images are required to obtain the phase image. This prevents from a single-shot recording. One of the solutions is to use two image sensors located at different depths along the axial direction.

In this study, we fabricate an optical setup of single-shot TIE-based 3D fluorescence imaging. Tobacco suspension culture cells expressing mEGFP- β -tubulin are used for the demonstration of the proposed system.

II Single-shot TIE-based 3D fluorescence imaging

Fig. 1 shows an optical setup of single-shot TIE-based 3D fluorescence imaging. The optical setup is based on epi-fluorescence optical microscope. Two image sensors located at different depth positions capture the intensity distributions at the different depth positions of the object. One of the image sensors is put on a translation stage to change the observation depth of the object. From the two images, the amplitude and the phase distributions are obtained. The central wavelength of the LED is 473 nm. An optical microscope objective lens with NA 0.4 and a magnification ratio of 20 \times is used accompanied with a

focal length of 200 mm in a tube lens. Two identical image sensors, ORCA-Flash 4.0, are used for recording the two axial shifted intensity images. The image sensors are synchronized to record the images in a single-shot. Actual image sensor size is 13.312 mm \times 13.312 mm that corresponding to 665.6 μ m \times 665.6 μ m in the object plane.

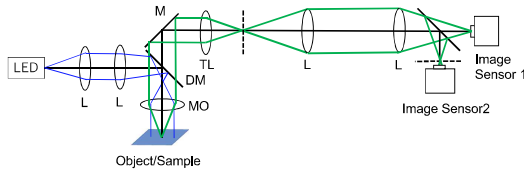


Fig. 1 Schematic of optical setup of a single-shot recording of TIE-based 3D fluorescence imaging.

For the evaluation of system performance, we used tobacco suspension culture cells expressing mEGFP- β -tubulin. Figs. 2(a) and (b) show the two intensity images at different depth locations, with an axial separation of 10 μ m. From the two images, the phase distribution is obtained as shown in Fig. 2(c). Fig. 3 shows the numerically reconstructed focused images with different propagation directions. Figs. 3(b) and (c) are the intensity images shifted by 4 mm and 6 mm from Fig. 3(a). Red arrows indicate the focused nuclei. From these experiments, our fabricated system can retrieve the 3D fluorescence distribution by a single-shot recording. The recording speed is the same as the frame rate of the image sensor.

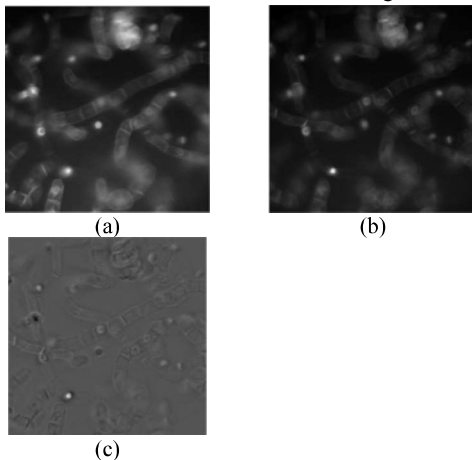


Fig. 2 Recorded intensity images and extracted phase image by TIE. (a), (b) two intensity images and (c) phase image.

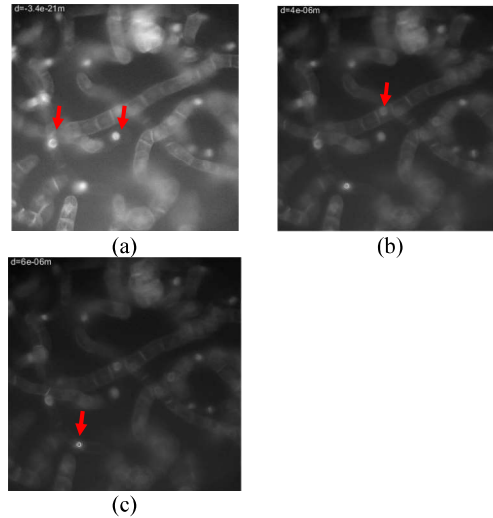


Fig. 3 Reconstructed focused images on three depth planes at (a) 0 μ m, (b) 4 μ m, and (c) 6 μ m.

III Conclusion

We have fabricated the system that can record two intensity images simultaneously by using two image sensors for 3D fluorescence imaging based on TIE. From the reconstructed images at different focused positions, we found that the fabricated system worked well at a frame rate of image sensor for time-lapse imaging.

A part of this work has been supported by CREST JPMJCR17, JST A-STEP JPMJTR204C, and KAKENHI 20H05886. We thank Prof. Takashi Murata, Kanagawa Institute of Technology, for providing us tobacco suspension culture cells.

References

- [1] X. Quan, O. Matoba, Y. Awatsuji, *Opt. Lett.* **42**, 383 (2017).
- [2] M. Kumar, X. Quan, Y. Awatsuji, C. Cheng, M. Hasebe, Y. Tamada, and O. Matoba, *J. Biomed. Opt.* **25**, 032010 (2020).
- [3] M. Kumar, Xiangyu Quan, Yasuhiro Awatsuji, Yosuke Tamada, Osamu Matoba, *Sci. Rep.* **10**, 7580 (2020).
- [4] S. K. Rajput, M. Kumar, X. Quan, M. Morita, T. Furuyashiki, Y. Awatsuji, E. Tajahuerce, O. Matoba, *J. Biomed. Opt.* **25**, 032004 (2020).
- [5] S. K. Rajput, O. Matoba, M. Kumar, X. Quan, Y. Awatsuji, Y. Tamada, and E. Tajahuerce, *IEEE J. Sel. Topics Quantum Electron.* **27**, 6801809 (2021).

Optical coherence microscopy (OCM) imaging of the lung carcinoma (CA) cell spheroid

You-Nan Tsai ^a, Wei-Tse Huang ^b, Yu-Chun Lin ^b, Huei-Wen Chen ^c,
Yuan Luo ^b, Hsiang-Chieh Lee^{*a,d}

^aGraduate Institute of Photonics and Optoelectronics, National Taiwan University, Taipei 10617, Taiwan.

^bGraduate Institute of Medical Device and Imaging, National Taiwan University, Taipei 10617, Taiwan.

^cGraduate Institute of Toxicology, National Taiwan University, Taipei 10617, Taiwan.

^dDepartment of Electrical Engineering, National Taiwan University, Taipei, 10617 Taiwan

*Email: hclee2@ntu.edu.tw

Abstract

In this study, we have developed a compact, high-speed spectral-domain optical coherence microscopy (SD-OCM) system to observe the lung-carcinoma (CA) tumor-cell spheroid. Volumetric OCM images of the cell spheroid were acquired using an in-house C++ interface, an inverted fiberoptic scanning microscope, and a low-cost microcontroller for providing custom designed triggering signal to synchronize the beam scanning with the galvanometer mirror with a USB-3.0 2048-pixel line-scan camera. In order the continuous examine architectural information of the tumor spheroid, and potentially under treatment of various drugs, we have been optimizing the handling protocol for the spheroid.

Keywords: spectral-domain optical coherence tomography, microscopy, lung cancer, tumor cell spheroid

I Introduction

Lung carcinoma (CA) is one of the leading causes of cancer deaths worldwide. Therefore, the research on the treatment efficacy of this disease is very important. In cancer research, tumor-cell spheroid models provide convenient and standard biotechnology chosen options to predict *in vivo* cellular responses based on *in vitro* processing in the laboratory [1]. This technique has been widely investigated and explored as a tool for drug discovery/screening. It could increase the accuracy of predicting scarcity of efficacy or unexpected toxicity in clinical trials. Therefore, it has a high potential for application in personalized medicine [2]. However, current imaging methods such as bright-field imaging or phase-contrast imaging are limited to provide 2D projections of the tissue module [3, 4]. Therefore, in this study, we have developed a compact, low-cost, ultrahigh-speed spectral-domain optical coherence microscopy (SD-OCM) system with a central wavelength of 865 nm and a USB3.0 high speed 2048-pixels line scan camera

[5]. It provides a 3D imaging method for lung carcinoma tumor cell spheroid under treatment of different drugs.

II Experimental setup

Figure 1 shows a schematic diagram of the SD-OCM system. A commercially available superluminescent diode (SLD) light source (EXALOS EXC250003) with a center wavelength of 865 nm and output power of 10.55mW was used. The OCM interferometer schematic configuration consisted of a 50/50 fiber couplers and two collimator lenses (Thorlabs, Inc.) and an object lens (Thorlabs, Inc.). The customized spectrometer was designed and simulated in ZEMAX. The detector utilized a high-speed USB 3.0 CMOS line scan camera (Teledyne e2V) which had 2048 pixels with a pixel size of 10 $\mu\text{m} \times 200 \mu\text{m}$. In order to synchronize the galvanometer mirror to the OCM signal acquisition, a microcontroller (Arduino, DUE) was used to generate the triggering signal. The axial resolution is $\sim 4.3 \mu\text{m}$ (in air).

To evaluate the performance of OCM images on cell spheroid, we used human lung adenocarcinoma spheroids

(H-1975 cell line). Human lung-derived tumor cells have been seeded in 96-well ultra-low attachment plates for 1~2 day to form tumor spheroids. Then, we specifically design a spheroid holder comprising of a glass slide, a cover glass, and spacers to fix the spherical cell spheroids between the glass slide and the cover glass but not exerting excess compression on the spheroid. In order to investigate the features identified in the volumetric OCM images, we also image the same spheroid using confocal laser scanning fluorescence microscope.

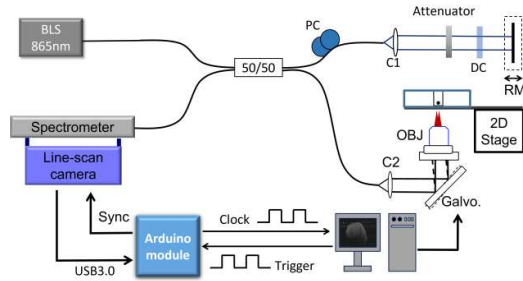


Figure 1. SD-OCM system setup; BLS: broadband light source; ISO: optical isolator; PC: polarization controllers; C1, C2: collimator lens; DC: dispersion compensating block; RM: reference mirror; Galvo.: galvanometer scanner; OBJ: object lens.

III Results and Discussion

Volumetric OCM images of the cell spheroid were acquired using an in-house C++ interface, enabling synchronized beam scanning and data acquisition through the USB 3.0 framework. Figure 2(a) shows the cross-sectional OCM image of the cell spheroid over the designated location (blue dashed line, Fig. 2(b)) in the corresponding *en face* projected OCM image (Fig. 2(b)). The yellow arrow (Fig. 2(a)) is the glass slide interface below the encapsulated cell spheroid. Note that the glass slide interface will produce such a strong scattered signal. Thus, we specifically tilted the glass slide to avoid the camera being saturated due to the specular reflection. Note that the orientation of the cross-sectional OCM image was flipped where the top and bottom of the image correspond to the bottom and top of the cell spheroid due to the inverted microscope. Moreover, a white ribbon as marked by the red arrow is by the aliasing of the specular

reflection from the glass slide aforementioned. Figure 2(c) is the brightfield microscope image of the same cell spheroid. OCM images can obtain similar brightfield microscopy *en face* images and as well as cross-sectional images of the entire cell spheroid which can observe tissue-level details. The results show the potential of OCM imaging as a tool for cell spheroid studies. The protocol for cell spheroid handling is currently being optimized. In the future, it could be developed into a high-speed 3D-imaging system as a drug screening platform.

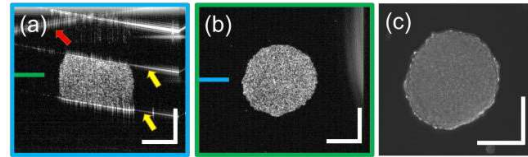


Figure 3. Volumetric OCM imaging of the 3D tumor spheroid. (a, b) is cross-sectional and *en face* projection OCM image of the tumor spheroid. (c) is a brightfield microscope image. Scale bars: 200 μm .

IV Acknowledgment

The authors acknowledge the funding support in part from the Young Scholar Fellowship Program by the Ministry of Science and Technology of the Republic of China (ROC), Taiwan (MOST 109-2636-E-002-028, 110-2636-E-002-025, and 111-2636-E-002-024).

References

- [1] S. Breslin and L. O'Driscoll, "Three-dimensional cell culture: the missing link in drug discovery," *Drug Discov Today*, vol. 18, no. 5-6, pp. 240-9, Mar 2013, doi: 10.1016/j.drudis.2012.10.003.
- [2] H. Le *et al.*, "Patient-Derived Lung Tumoroids-An Emerging Technology in Drug Development and Precision Medicine," *Biomedicines*, vol. 10, no. 7, Jul 12 2022, doi: 10.3390/biomedicines10071677.
- [3] P. Shahi Thakuri, S. L. Ham, G. D. Luker, and H. Tavana, "Multiparametric Analysis of Oncology Drug Screening with Aqueous Two-Phase Tumor Spheroids," *Mol Pharm*, vol. 13, no. 11, pp. 3724-3735, Nov 7 2016, doi: 10.1021/acs.molpharmaceut.6b00527.

- [4] M. Vinci *et al.*, "Advances in establishment and analysis of three-dimensional tumor spheroid-based functional assays for target validation and drug evaluation," *BMC biology*, vol. 10, no. 1, pp. 1-21, 2012.
- [5] H. C. Lee, J. J. Liu, Y. Sheikine, A. D. Aguirre, J. L. Connolly, and J. G. Fujimoto, "Ultrahigh speed spectral-domain optical coherence microscopy," *Biomed Opt Express*, vol. 4, no. 8, pp. 1236-54, 2013, doi: 10.1364/BOE.4.001236.

Evaluation of Monte Carlo-based Fitting of Diffuse Reflectance Spectroscopy to Quantify Optical Properties of Muscle and Superficial Tissues

Hao-Wei Lee^a, Kung-Bin Sung*^a

^aGraduate Institute of Biomedical Electronics and Bioinformatics, National Taiwan University, Taipei 10617, Taiwan, R.O.C.

Abstract

Diffuse reflectance spectroscopy (DRS) has been commonly used to measure optical properties of the skin, subcutaneous tissue, and muscle *in vivo*. Reflectance spectra measured at tissue surface are iteratively fitted by a forward model describing photon energy propagation in tissue. In this study, artificial neural network (ANN) models were used to replace multilayer Monte Carlo simulations as the forward model to speed up the fitting. Simulated spectra were used to test the fitting process. The errors in absorption coefficients of the skin are within 20%, and the subcutaneous fat and muscle are about 40%. The errors in scattering coefficients are within 25%.

Keywords: Diffuse reflectance spectroscopy, optical properties, Monte Carlo, Artificial neural network

I Introduction

Estimating the optical parameters of tissue is crucial, which can help us predict the energy distribution of photons propagation in tissue, and has applications in various optical diagnosis and treatment. Examples include monitoring oxygen saturation. When monitoring the oxygen saturation, tissue cannot be removed for measurement first, so *in vivo* measurement is required.

DRS system is a powerful tool for *in vivo* measurement, which has the advantages of low cost and real-time monitoring. Nevertheless, when inverse fitting to be done for extracting optical parameters, it is usual to encounter the problem of multiple solutions. Therefore, the accuracy of the fitted optical parameters is very important for researchers

II Methods

1. Monte Carlo model

In this study, the superficial tissue was set as a four-layer homogeneous slab, which were epidermis, dermis, subcutaneous adipose, and muscle. Their thickness were set to 0.1, 2, 1 (mm), respectively, and the muscle layer was semi-infinite. The detectors were placed at distances

of 0.4, 3, 6, 9 (mm) from the light source using a CUDAMCML program[1] modified by our team. All tissue layers had the same refractive index of 1.44. The scattering coefficients μ_s , were assumed to follow a one-term inverse power-law function, and the Henyey-Greenstein scattering phase function was used with g as 0.804, 0.715, 0.9, 0.93 each layer, respectively. Lastly, the absorption coefficient μ_a was the linear combination of the absorbance of each tissue.

2. ANN forward model

To train the forward model, 5,250,000 sets of reflectance were simulated using MCML. The input consists of μ_a and μ_s , and the output is the reflectance of each source detector separation (SDS), where μ_a and μ_s each layer are randomly sampled within the range[2] shown in Table 1.

Table 1. Optical parameters range

	μ_a (cm ⁻¹)	μ_s (cm ⁻¹)
epidermis	0.0001~4	100~300
dermis	0.0001~4	150~300
Subcutaneous adipose	0.0001~2	100~250
muscle	0.0001~0.6	45~85

3. Inverse curve fitting

The non-linear iterative curve-fitting function ‘fmincon’ provided by MATLAB® was used to extract optical properties from simulated spectra, and used RMSE as the objective function.

$$\text{RMSE} = \sqrt{\frac{\sum_{SDS} \sum_{\lambda} \left(\frac{R(\lambda, SDS) - R_{\text{target}}(\lambda, SDS)}{R_{\text{target}}(\lambda, SDS)} \right)^2}{(\text{Number of } SDS) \times (\text{Number of } \lambda)}} \times 100\% \quad (1)$$

Fifty sets of target spectra were randomly simulated by MCML for testing the fitting, and also the most of methods were refer to [3].

III Results and Discussion

Target spectra generated by ANN forward model are almost identical to those simulated by MCML, as shown in the Figure 1., which increases our confidence in using the ANN forward model to perform inverse curve fitting to extract optical parameters.

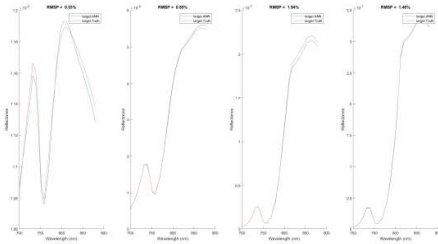


Figure 1. Target spectrum, orange line: MCML; blue line: ANN, SDS = 0.4, 3, 6, 9 (mm) from left to right

Also, this study counted the extracted optical parameter errors. The bar graphs in Fig. 2 and Fig. 3 show the mean \pm standard deviation of the RMSE errors of μ_a and μ_s respectively extracted from the target spectra.

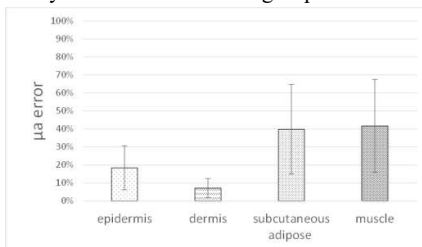


Figure 2. Absorption coefficient extracted from 50 sets of target spectra

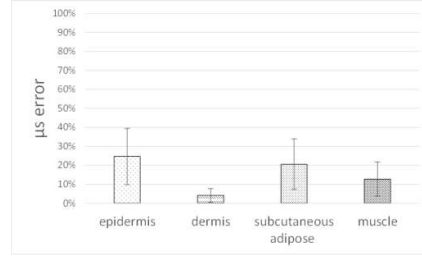


Figure 3. Scattering coefficient extracted from 50 sets of target spectra

Errors in estimated μ_a of the epidermis and dermis are within 20%, and those of the subcutaneous fat and muscle are about 40%, probably because the absorption coefficient values of the latter are smaller and the depth is deeper, causing lower sensitivity. However, All tissues of μ_s are within 25%, and the deeper subcutaneous fat and muscle do not have a relatively large error like μ_a . The reason is that the μ_s range of subcutaneous fat and muscle found in the literature is small, so the error is relatively small.

IV Conclusion

Using ANN to replace multi-layer Monte Carlo works well with error smaller than 2%, and can speed up fitting, enabling inverse fitting in a reasonable time for tissues that require a larger number of photonic simulations. Also, this research estimated the accuracy of the DRS system in measuring multiple layers of tissue in vivo, simulated 50 target spectra, and performed inverse curve fitting. The next step is to apply the method to quantify tissue optical properties in vivo.

References

- [1] E. Alerstam, T. Svensson, and S. Andersson-Engels, J. Biomed. Opt., 13(6), 060504 (2008).
- [2] A. N. Bashkatov, E. A. Genina, and V. V. Tuchin, J. Innov. Opt. Health Sci., 04(01), 9-38 (2011).
- [3] C.-Y. Wang, T.-C. Kao, Y.-F. Chen *et al.*, Photonics, 6(2), 61 (2019).

Temporal Focusing Based Deep Learning Computer Generated Holography For Simultaneous Three-Dimensional Micropattern Neuron Stimulation

Liang-Wei Chen^a, Chun-Yu Lin^a, Shang-Yang Lu^a, Feng-Chun Hsu^a, Yvonne Yuling Hu^b, and Shean-Jen Chen^{a,c*}

^aCollege of Photonics, National Yang Ming Chiao Tung University, Tainan 711, Taiwan

^bDepartment of Photonics, National Cheng Kung University, Tainan 701, Taiwan

^cTaiwan Instrument Research Institute, National Applied Research Laboratories, Hsinchu 300, Taiwan

* sheanjen@nycu.edu.tw

Abstract

Precisely stimulate neurons simultaneously in single-cell resolution is a critical issue in optogenetics. Rapid light control is necessary for observing neural activities of living organisms. None of existing approaches could accomplish both advantages at the same time. Here we propose a temporal focusing based deep learning computer-generated holography which generates a hologram for synthesizing tens of illumination spots with a few-micron level axial confinement in volume of interest in tens of milliseconds. This approach utilizes a pre-trained artificial neural network to inference optimized holograms with modeling our optical system, including temporal focusing effect and wave propagation model. Our research unlocks the potential of real-time observing neural activity and connection in living organisms.

Keywords: temporal focusing, computer-generated holography, multiphoton excitation, deep learning, optogenetics

I Introduction

Optogenetics provides a deeper understanding of neural activity and connection by precisely control cellular activities through light. Due to the advantages of less tissue scattering, deeper penetration depth, and lower photobleaching effect in biological sample, multiphoton excitation is applied for stimulating neurons individually. However, as a further understanding of neural connection is expected, simultaneous neurons stimulation in three dimension offers a feasible approach[1].

Computer generated holography (CGH) is a well-developed technique for synthesizing customized illumination patterns. However, conventional CGH methods require a period of computing time due to the heavy load of iterative calculation. This shortcoming makes the application in living organisms hard to achieve. Deep learning approach[2] provides a novel method with a short computation time by generating holograms through a pre-trained neural network, the computation time would be significantly reduced.

As we endeavor to stimulate drosophila brain neurons, the temporal focusing (TF) technique is implemented to improve the axial confinement of patterns to a few-micron level[3, 4]. Since the pulse width is compressed to the narrowest, there is a constructive interference at illumination patterns. Therefore, they are axially confined due to the highly concentrated peak power.

II Overall System Setup & CGH Methods

1. System Setup

The overall system setup is shown in Fig. 1.

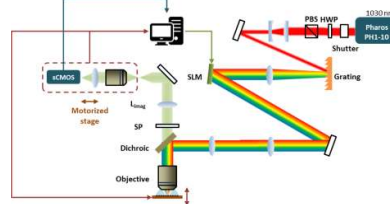


Figure 1. System setup of neuron stimulation system

The light source of the neuron stimulation system is an ultrashort pulse laser with 1030nm central wavelength, pulse duration of 228 fs, and repetition rate of 200 kHz. Then, the beam would be dispersed by the grating and

collimated by the Fourier lens. In addition, the Fourier lens would focus the collimated beam to the Fourier plane, which we place the reflective SLM (1920×1080 pixels, $6.4 \mu\text{m}$ pixel size). Furthermore, the beam is modulated by calculated hologram which is displayed on the SLM and is conjugated to the back aperture of the objective ($40\times/\text{NA}1.0$). The objective would focus the beam to multiple positions that we defined.

2. TF Based Deep Learning CGH

The schematic of TF based deep learning CGH is shown in Fig. 2. We first randomly generate 3D illumination patterns as the target input of the phase pattern generator which is formed as a simple U-net architecture. The phase pattern generator would estimate holograms displayed on SLM. The light source model simulates all frequency components of the light that is dispersed by the grating and incident to the SLM. Then, the modulated beam would be Fourier transformed to the focal plane of the objective. A wave propagation model based on angular spectrum method[5] is introduced to calculate the complex field of all frequency components in the volume of interest. Subsequently, the complex field would be Fourier transformed from frequency domain to time domain for calculating the two-photon excited fluorescence intensity which is quadratic proportional to the summation of the complex amplitude in time domain. After these procedures, the loss is calculated between the target input and simulated reconstruction of illumination patterns to update the parameters of the phase pattern generator. After the training progress is done, we could use this pre-trained phase pattern generator to rapidly synthesize optimized holograms.

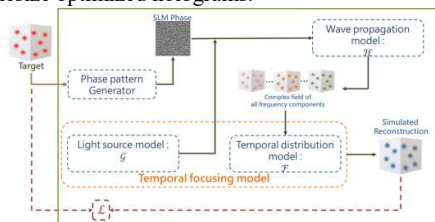


Figure 2. Schematic of TF based deep learning CGH

III Results and Discussion

The simulation and experimental results are both shown in Fig. 3. The hologram for manipulating the beam is generated by the pre-trained temporal focusing based CGH. Fig. 3(a) shows the target input of TF based deep

learning CGH. The patterns are randomly distributed in three different depth, each is separated with $10 \mu\text{m}$. Fig. 3(b) shows the simulation results. The axial confinement of illumination patterns is significantly improved to a few-micron level. Fig. 3(c) shows the experimental results of capturing the two-photon excited fluorescence in a rhodamine6G thin film along z-axis. The images show that the light could be accurately addressed to 3D locations through our TF based deep learning CGH. The computation time of single hologram is around tens of milliseconds. To sum up, in this study, we develop a TF based deep learning CGH to rapidly calculate optimized holograms and build an neuron stimulation system to simultaneously stimulate neurons in single-cell resolution.

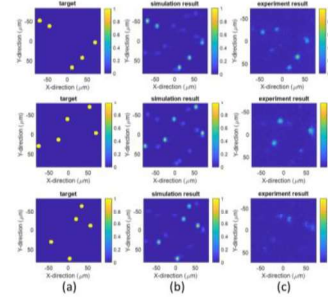


Figure 3. (a)target, (b)simulation & (c)experimental results

Acknowledgement

This work was supported by the National Science and Technology Council (NSTC) in Taiwan with the grant numbers 110-2221-E-A49 -059 -MY3, 110-2221-E-A49 -009 and 111-2221-E-A49 -043

References

- [1] N.C. Pégard et al., Three-dimensional scanless holographic optogenetics with temporal focusing (3D-SHOT). *Nat Commun* 8, 1228 (2017)
- [2] M. Hossein Eybposh et al., "DeepCGH: 3D computer-generated holography using deep learning," *Opt. Express* 28, 26636-26650 (2020)
- [3] N. Accanto et al., "Multiplexed temporally focused light shaping for high-resolution multi-cell targeting," *Optica* 5 (2018) 1478
- [4] E. Papagiakoumou, E. Ronzitti, and V. Emiliani, "Scanless two-photon excitation with temporal focusing," *Nat Methods* 17, 571-581 (2020)
- [5] J. W. Goodman, *Introduction to Fourier optics*, 3rd Ed., Roberts & Company (2004)

Cross-modality image restoration of temporal focusing microscopy via progressive 3D U-Net

Yvonne Yuling Hu^a, Chun-Yu Lin^b, Chia-Wei Hsu^b, Yu-Hao Tseng^b, Shean-Jen Chen^{a,b,c*}

^aDepartment of Photonics, National Cheng Kung University, Tainan 70101, Taiwan.

^bCollege of Photonics, Natinoal Yang Ming Chiao Tung University, Tainan 71150, Taiwan

^cTaiwan Instrument Research Institute, National Applied Research Laboratories, Hsinchu 300092, Taiwan

*sheanjen@nycu.edu.tw

Abstract

Temporal focusing multiphoton microscopy can obtain rapid volumetric imaging with optical sectioning. However, the scattering issue and cross-talking are the main reason that limits the application for deep tissue image acquisition. In this paper, traditional point-scan multiphoton imaging was utilized to become the inference of the deep learning restoration network. The cross-modality image registration network was first applied to register the inference volume, then a multi-stage 3D U-Net was utilized to achieve the image restoration. The experimental results showed that the proposed neural network can restore neuron structure in the deep layer of the *Drosophila* mushroom body.

Keywords: Temporal focusing, image restoration, Cross-modality image registration, deep learning

I. Introduction

Multiphoton microscopy has become one of the popular tools for biomedical research since 1990s. However, the traditional point-scanning (PS) method limits the acquisition rate when it comes to volumetric imaging. Temporal focusing (TF) provides an alternative method for plane-illumination while maintaining the advantage of optical sectioning ability for in vivo imaging [1]. However, it is well known that the plane excitation manner suffers from tissue scattering and the signal cross-talking in the camera leads to the low signal-to-noise ratio, which largely degrades the image quality. Multiple methods have been proposed to enhance the image quality, such as structured illumination [2]. However, these modulation-based methods require at least two structural images for reconstruction, which compromise the acquisition speed of the TF. The research of deep learning is one of the most rapidly growing field recently. In this paper, deep learning neural networks were proposed to overcome the low image quality. In the beginning, the cross-modality image registration was performed to register the point-scan image to the TF image. Later, a multi-stage 3D U-Net with cross-stage

feature fusion mechanism were utilized to accomplish the restoration work.

II. Method

1. Cross-modality image registration

Since the ground truth image from PS multiphoton microscopy and the raw image from TF microscopy were obtained from different modality, image registration needs to be done before moving to restoration network. VoxelMorph [3] is one of the effective unsupervised networks to perform cross-modality image registration. As shown in Fig. 1, the network is an encoder-decoder based U-Net configuration. The image obtained from TF is defined as fixed image (I_{fixed}), while the image obtained from PS is defined as moving image (I_{moving}). The input is the concatenation of I_{fixed} and I_{moving} . Each layer is composed of 3D convolution, leaky ReLU. Before propagating to the next layer, maxpooling and upsampling are stacked in the encoder and decoder, respectively. Moreover, the skip connection propagates the feature map in the encoder and concatenate with the decoder to further expand the receptive field. The output of the last layer of the decoder is a vector field (ϕ), which represents the deformation of each voxel. Later, a spatial transform is performed to shift the I_{moving} . The resulting moved image

(I_{moved}) is then compared with I_{fixed} to via mean square error to update the ϕ for further implementation.

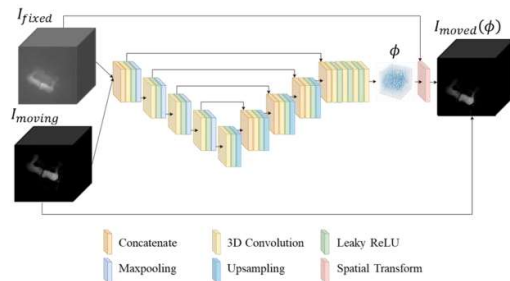


Figure 1. The network of VoxelMorph utilized for image registration.

2. Multi-stage 3D U-Net for image restoration

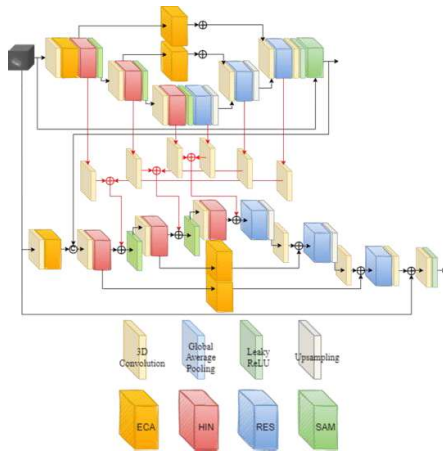


Figure 2. The architecture of multi-stage 3D U-Net for image restoration

The proposed multi-stage image restoration network was modified from MPRNet [4]. Each stage is a 3D U-Net composed of efficient channel attention (ECA) block, half instance normalization (HIN) block, residual (RES) block and self-supervised module (SAM). The features learned in each encoder layer are processed with additional ECA block and added to the decoder to fuse the feature information without doubling the matrix. Moreover, cross-stage feature fusion (CSFF) are adopted to propagate the feature learned in previous stage to the next stage to prevent information loss during the up- and downsampling process. At the end of each stage, SAMs are introduced to supervise the restoration outcome and to separate the useful features from the useless ones.

III. Results and Discussion

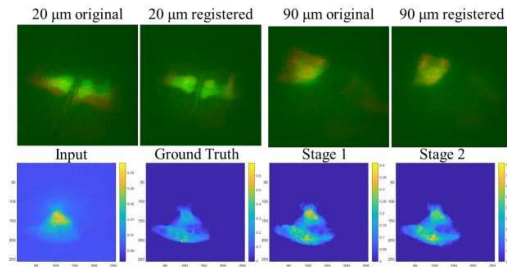


Figure 3. The registration results and the restored image from stage 1 and 2.

In the registration, mutual information (MI) is utilized to evaluate the result. The MI before and after registration are 0.06 and 0.74, respectively. In the restoration, the enhancements of SSIM are 0.25 for stage 1 and 0.26 for stage 2, and the enhancement of PSNR are 5.01 dB for stage 1 and 5.11 dB for stage 2. However, this proposed network hasn't been verified under in vivo experiment, which need to take motion correction and the time consumption into consideration.

Acknowledgement

This work was supported by the National Science and Technology Council (NSTC) in Taiwan with the grant numbers 110-2221-E-A49 -059 -MY3, 110-2221-E-A49 -009 and 111-2221-E-A49 -043 -.

References

- [1] Cheng, L.-C., Chang, C.-Y., Lin, C.-Y., Cho, K.-C., Yen, W.-C., Chang, N.-S., Xu, C., Dong, C. Y., Chen, S.-J., "Spatiotemporal focusing-based widefield multiphoton microscopy for fast optical sectioning," *Opt. Express* **20**(8), 8939 (2012).
- [2] Cheng, L.-C., Lien, C.-H., Da Sie, Y., Hu, Y. Y., Lin, C.-Y., Chien, F.-C., Xu, C., Dong, C. Y., Chen, S.-J., "Nonlinear structured-illumination enhanced temporal focusing multiphoton excitation microscopy with a digital micromirror device," *Biomed. Opt. Express* **5**(8), 2526 (2014).
- [3] Balakrishnan, G., Zhao, A., Sabuncu, M. R., Guttag, J., Dalca, A. V., "VoxelMorph: A learning framework for Deformable Medical Image Registration," *IEEE Trans Med Imaging* **38**(8), 1788–1800 (2019).
- [4] Zamir, S. W., Arora, A., Khan, S., Hayat, M., Khan, F. S., Yang, M.-H., Shao, L., "Multi-Stage Progressive Image Restoration," *IEEE/CVF Conference on Computer Vision and Pattern Recognition (CVPR)* (2021).

An Advanced Volumetric Imaging System Based on Light Field Microscopy with Selective Excitation via Temporal Focusing

Feng-Chun Hsu^a, Chun-Yu Lin^a, Yvonne Yuling Hu^b, Yeu-Kuang Hwu^c, Ann-Shyn Chiang^d, and Shean-Jen Chen^{a,c,*}

^a College of Photonics, National Yang Ming Chiao Tung University, Tainan 711, Taiwan

^b Department of Photonics, National Cheng Kung University, Tainan 701, Taiwan

^c Institute of Physics, Academia Sinica, Taipei 115, Taiwan

^d Brain Research Center, National Tsing Hua University, Hsinchu 300, Taiwan

^e Taiwan Instrument Research Institute, National Applied Research Laboratories, Hsinchu 300, Taiwan

[*shenjen@nycu.edu.tw](mailto:shenjen@nycu.edu.tw)

Abstract

Light field microscopy technique achieves recording a volumetric image with a single snap shot. This rapid recording method gives the benefit of studying the dynamic of the biological research such as neural science. However, the conventional light field microscopy resolution is limited by the trade-off between recording lateral and axial information, and the reconstruct process takes lots of time that makes real-time observation difficult. In this research, we propose a rapid high-resolution light field microscopy with learning-based reconstruction method. Moreover, we implement a volumetric excitation method based on our temporal focusing method, this improve our rapid light field microscopy to have the advantages of multiphoton excitation and getting better contrast, low background noise.

Keywords: light field, temporal focusing, deep learning, multiphoton excitation

I Introduction

Imaging speed plays an important role in biological researches. Especially when analyzing cell behaviors and neural functions. Recording techniques for microscopic bioimaging can be classified into point scanning, plane imaging and volumetric imaging on the basis of the ways of recording. Obviously, recording point by point has the lowest frame rate but the highest resolution and image quality. This become a tradeoff between image quality and imaging speed. Light field technique, which is known as its three-dimensional imaging [1, 2], can reconstruct a whole volume with a single snap shot. However, the image quality and resolution are not as well. To improve the cons, this study utilized temporal focusing based selective excitation [3]. By controlling the exciting region, the light field system can discard the signal come from the place out of the reconstruction volume, reduce the background noise and improve the contrast. With the pros of temporal focusing multiphoton excitation, the system also has deeper penetration depth and lower

photobleaching effect. Moreover, a data driven learning-based neural network with wave optics model training loop is introduced to solve the inverse problem of reconstructing image. The result shows the reconstruction has high contrast and resolution, with rapid recording speed.

II System

1. Optical Setups

To achieve the selective excitation, an alternative lens pairs was placed between the grating and objective. This change the covered area at the back focal plane of the objective, reduce the temporal focusing effect, increase the exciting region at the sample. The system setup is shown in Figure 1., the pulse laser with 1030 nm wavelength is expanded to match the lateral exciting area. A blaze grating is utilized to compose the temporal focusing system. The lens pairs mentioned formally is marked with the subscript, the axial confinement is increased from 3 μm to 20 μm with the setup. The light field imaging system is at the left-hand side in figure 1,

using a camera lens pair to relay the micro lens array (MLA) plane to the actual plane.

2. Reconstruct Process

The former reconstruct method [2,4] do the deconvolution process with the theoretical PSF matrix derived from wave optics. This approach proposes a data driven learning-based neural network method to deal with this inverse problem. The architecture of learning is also shown at the top of figure 1. In this learning process, the wave optics model is also introduced in loss function calculation. The loss of the neural network is the summary of two parts, the mean square error (MSE) between the reconstruct volume and ground truth, and the MSE between the input light field image and approximate result computed from reconstructed volume with wave optics model.

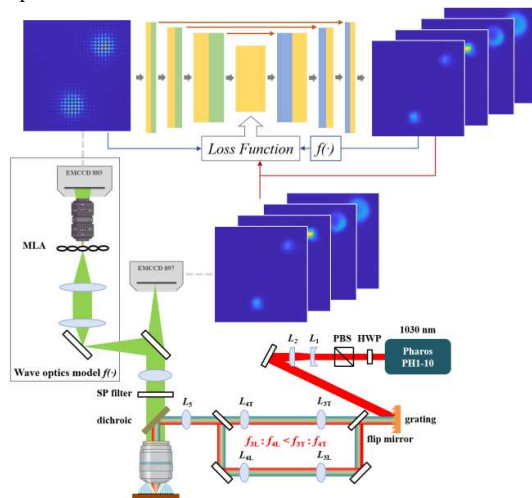


Figure 1. Overall system setup and reconstruction diagram.

III Results

The behavior of the neural network reconstruction is presented in Figure 2. The $2\ \mu\text{m}$ fluorescence beads is fixed in the jell as the demonstration sample. Figure 2 (a) is the ground truth image stack taken by our temporal focusing system. (b) and (c) show the orthogonal views along z axis. Figure 2 (d) (e) and (f) are the reconstructed result and its orthogonal image. Images are summed along z-axis to demonstrate the lateral location of florescence beads are exactly the same. Moreover, the orthogonal views also show that the positions along axial space are correct.

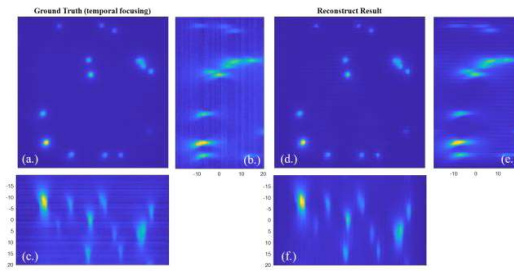


Figure 2. Experimental Reconstruct Result.

IV Discussion

The study has developed a light field microscopy system with selective volume excitation by temporal focusing technique. Improving the image contrast and reduce the background noise in the optical system. Moreover, the neural network reconstruct process is also adjusted to trained with wave optics model to improve the performance. The novel light field microscopy system then has rapid speed in real time observation with high resolution and image contrast.

Funding

This work was supported by the National Science and Technology Council (NSTC) in Taiwan with the grant numbers 110-2221-E-A49 -059 -MY3, 110-2221-E-A49 -009 and 111-2221-E-A49 -043 -.

References

- [1] M. Levoy, R. Ng, A. Adams, M. Footer, and M. Horowitz, "Light field microscopy," *ACM Trans. Graph.* 25(3), 924–934 (2006).
- [2] M. Broxton, L. Grosenick, S. Yang, N. Cohen, A. Andalman, K. Deisseroth, and M. Levoy, "Wave optics theory and 3-D deconvolution for the light field microscope," *Opt. Express* 21(21), 25418–25439 (2013).
- [3] F. C. Hsu, Y. D. Sie, C. Y. Lin, Y. Y. Hu, S. J. Chen, "Light field multiphoton microscopy with temporal focusing-based volume selective excitation," *Proc. SPIE 12136, Unconventional Optical Imaging III*, 121360F (2022)
- [4] Z. Lu, J. Wu, H. Qiao, Y. Zhou, T. Yan, Z. Zhou, X. Zhang, J. Fan, and Q. Dai, "Phase-space deconvolution for light field microscopy," *Opt. Express* 27, 18131–18145 (2019)

High-speed dual-resonance scanning multiphoton microscopy based on deep learning for dynamic volumetric imaging

Chia-Wei Hsu^a, Chun-Yu Lin^a, Yvonne Yuling Hu^b, and Shean-Jen Chen^{a,c,*}

^a College of Photonics, National Yang Ming Chiao Tung University, Tainan 71150, Taiwan

^b Department of Photonics, National Cheng Kung University, Tainan 70101, Taiwan

^c Taiwan Instrument Research Institute, National Applied Research Laboratories, Hsinchu 300, Taiwan

Correspondence: S.-J. C. (email: sheanjen@nycu.edu.tw).

Abstract

A thousand Hz image is already an increasingly important technique. Simultaneous scanning is a choice strategy to increase imaging speed. We developed a dual-resonant scanning multiphoton (DRSM) microscope that a frame rate of around 8,000 Hz and a volumetric imaging rate of over 30 Hz can be obtained for a big image volume of $343 \times 343 \times 120 \mu\text{m}^3$ with a large image size of $256 \times 256 \times 80$ voxels. Due to a large number of missing voxels, a 3D U-Net model is used to inpaint and denoise the images. The results show that the model achieves dynamic volumetric imaging to be performed with significant SNR improvement. Moreover, the model can be extended to the restoration of *in-vivo* drosophila brain images with a high image quality and a rapid imaging time.

Keywords: dual-resonant scanning multiphoton microscope, deep learning, dynamic volumetric imaging

I Introduction

Resonant scanners and non-inertial modules are gradually becoming a new strategy for high-speed scanning microscopy. Tunable acoustic gradient index of refraction (TAG) lenses can perform scanning at frequencies in the range of around 100-500 kHz.¹⁻² Thus, the imaging speed can reach frame rates of around 1 kHz and volumetric imaging rates of about 56 Hz, depending on the number of frames. Spatial separation and time delay optical designs can achieve up to 3,000 frames per second (fps) base on free-space angular-chirp-enhanced delay technology.³ Similarly, scan multiplier unit with two-photon microscope can provide 592 kHz line-scan rate and 16,000 fps.⁴ However, since the volumetric images are constructed sequentially pixel-by-pixel in 3D, the total volumetric rate is still restricted by the fastest speed of the scanner. As mention below, it is clear that the demand for kHz image could be higher. Simultaneous scanning is a choice strategy to increase imaging speed. The present group preliminarily achieved multiphoton

excited fluorescence (MPEF) microscopy with 30 volumes per second (vps) by incorporating a TAG lens and a RM in 2018⁵. Though MPEF microscopy has deeper penetration, the limited pulse number restricts the image size.

Building upon these studies, the present work develops a 3D-generator U-Net architecture for inpainting and denoising the volumetric images obtained by the proposed DRSM microscope. The practical feasibility of the rapid volumetric DRSM microscope confirm that the axial distortion and poor spatial resolution of the DRSM images can be effectively restored by the trained 3D U-Net model. It was further demonstrated by observing the high-speed movement of the 10- μm fluorescent bead for an image region of $343 \times 80 \times 120 \mu\text{m}^3$ with $256 \times 256 \times 80$ voxels for 30 vps and restore to high quality image. Also, the approach can be applied to drosophila brain imaging.

II Method

Figure 1 illustrates the proposed rapid volumetric DRSM microscope. As shown, the illumination source is

provided by a Ti:sapphire femtosecond laser. The scanning system comprises a TAG lens, a galvanometer (GM) scanner (6215H, Cambridge, USA), a resonant mirror (RM) scanner (CRS series, Cambridge, USA). Light source passes through the objective lens (W Plan-Apochromat 20X/1.0, Carl Zeiss, Germany), and is focused on the sample to excite MPEF. The MPEF signal passes through a band-pass filter and focusing lens and then enters a photomultiplier tube (PMT) (H7422-40, Hamamatsu, Japan), where it is converted into an electrical signal for further processing. Also, the motorized x - y - z stage with a 3-axis encoder (HEP4AXIM/B ProScan, Prior Scientific, UK) and an objective scanner (PD72Z4CAA, Physik Instrumente, UK) with a 400 μm travel range is adopted to move the sample. The structure of the 3D U-net proposed in the present study for restoring the volumetric images obtained by the DRSM microscope. As shown, the U-Net structure consists of convolution layers, batch normalization, rectified linear units (ReLUs), max pooling, concatenation, and transposed convolution. In particular, all of the 2D convolution layers were replaced by 3D convolution layers.

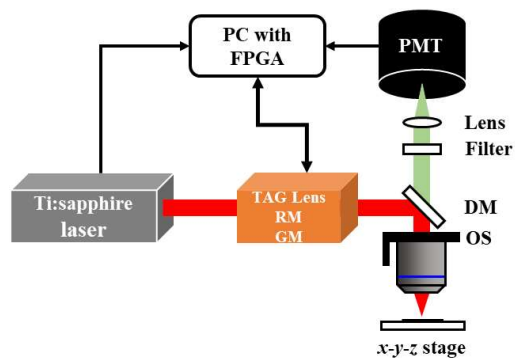


Figure 1. Overall setup of rapid volumetric DRSM microscope.

III Results and Discussion

The practical feasibility the DRSM images can be effectively restored by the trained 3D U-Net model and was further evaluated by observing the high-speed movement of the 10- μm fluorescent bead for an image region of $343 \times 80 \times 120 \mu\text{m}^3$ with $256 \times 256 \times 80$ voxels for

30 vps and $256 \times 64 \times 80$ voxels for 120 vps. As Figure 2 show that the image not only keep high SNR but also high image rate. In the x - y view, the morphology of the 10- μm fluorescent bead is obliquely elongated owing to the x -axis moving direction and the y -axis GM scanning. The practical feasibility of restoration can be demonstrated for high speed imaging.

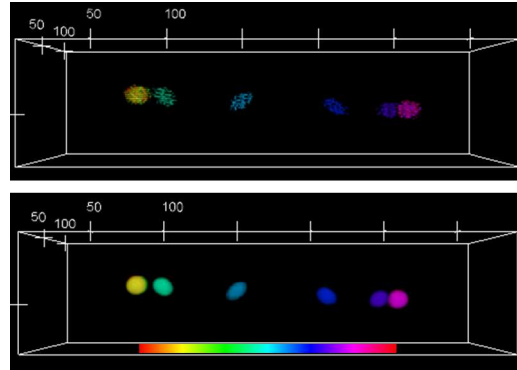


Figure 2 Before and after restoration of volumetric images of the 10- μm fluorescent bead recorded at different times.

Acknowledgement

This work was supported by the National Science and Technology Council (NSTC) in Taiwan with the grant numbers 110-2221-E-A49 -059 -MY3, 110-2221-E-A49 -009 and 111-2221-E-A49 -043 -.

References

1. Kong, L., Tang, J., Little, J. et al. Continuous volumetric imaging via an optical phase-locked ultrasound lens. *Nat Methods* **12**, 759–762 (2015).
2. Hsu, K.-J. et al. Millisecond two-photon optical ribbon imaging for small-animal functional connectome study. *Opt. Lett.* **44**, 3190–3193 (2019).
3. Wu, J., Liang, Y., Chen, S. et al. Kiloherz two-photon fluorescence microscopy imaging of neural activity *in vivo*. *Nat. Methods* **17**, 287–290 (2020).
4. Xiao, S., Davison, I. & Mertz, J., Scan multiplier unit for ultrafast laser scanning beyond the inertia limit. *Optica* **8**, 1403–1404 (2021).
5. Hsu, C.-W. et al. Rapid volumetric multiphoton imaging with the combination of an ultrasound lens and a resonant mirror. *Proc. SPIE* **10498**, 104982D (2018).

In Situ Formation of Au-Glycopolymer Nanoparticles for SERS-Based Biosensing and Single-Cell Immunity

Zi-Chun Chia^{*a}, Li-Xing Yang^a, Ting-Yu Cheng^a, Ya-Jyun Chen^a, Horng-Long Cheng^a, Fei-Ting Hsu^a, Ying-Jan Wang^a, Tzu-Chi Huang^a, and Chih-Chia Huang^a

^aDepartment of Photonics, National Cheng Kung University, Tainan 70101, Taiwan, R.O.C.

^bDepartment of Biological Science and Technology, China Medical University, Taichung 40402, Taiwan, R.O.C.

^cDepartment of Environmental and Occupational Health, National Cheng Kung University, Tainan 70101, Taiwan, R.O.C.

^dCenter of Micro/Nano Science and Technology, National Cheng Kung University, Tainan 70101, Taiwan, R.O.C.

E-mail: c2huang@email.ncku.edu.tw; huang.chihchia@gmail.com

Abstract

Herein, we designed polyaniline-containing galactosylated gold nanoparticles (Au@PGlyco NPs) via in situ polymerization of ortho-nitrophenyl- β -galactoside assisted by Au nucleation. The nanogold-carrying polyaniline block produced electromagnetic enhancement in surface-enhanced Raman scattering (SERS). The Au@PGlyco NP-mediated SERS biosensor could detect low amounts of bacteria ($\sim 10^2$ cfu/mL) depend on galactoside reacted with β -galactosidase derived from bacteria. A high accumulation of Au@PGlyco NPs mediated the immune response of tumor-associated M2 macrophages to the immunogenic M1 macrophage transition, which was elicited by ROS biostimulation using single-cell SERS-combined fluorescent imaging. Our study suggested that Au@PGlyco NPs may serve as a biosensing platform with the labeling capacity of galactose-binding receptors that could potentially express cell and immune regulation.

Keywords: glycopolymer gold nanoparticles, surface-enhanced Raman scattering, biosensing, single-cell detection, macrophage polarization.

Introduction

Glycopolymer-based nanoparticles are emerging as novel materials that enable well-defined structures with high affinities and biocompatibilities due to the multivalent binding between glycans and proteins [1], providing attractive materials for applications in immune regulation, vaccines, targeted delivery, infection treatment, and biosensing [2-5]. However, the correlation between galactosylated material accumulation and macrophage reprogramming has not been elucidated. Herein, we developed a facile core-shell polymerization process to fabricate homomultivalent galactose-functionalized Au nanoparticles by simultaneous hybridization of ortho-nitrophenyl- β -galactoside (ONPG) and nucleation-growth of Au seeds. The rapid evolution of surface enhanced Raman scattering (SERS) signals

from the formation of a polyaniline (PANI)-structured backbone chain after the reduction of H₂AuCl₄ by NaBH₄ based on the SERS signal amplification by plasmonic Au NPs. Considering the SERS-active glycopolymer coating, Au@PGlyco NPs could directly monitor galactose-targeted reaction with SERS response through the galactose-related enzymatic reaction. In addition, Au@PGlyco NPs could promote the production of ROS via interaction with galactose-binding receptor and thus trigger the macrophage reprogramming transition from the tumor-associated type (M2) into the immunogenic type (M1), providing the potential applications of immunomodulation.

Results & Discussion

(i) Characterization

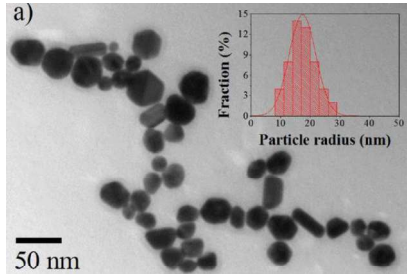


Figure 1. TEM images and particles distribution of Au@PGlyco NPs.

(ii) SERS sensing for bacteria

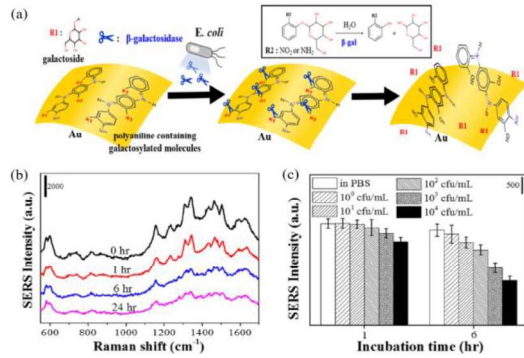


Figure 2. (a) Schematic of possible reaction for Au@PGlyco NPs with β -galactosidase derived from *E. coli*. (b) SERS spectra of Au@PGlyco NPs mixed with *E. coli* within 24 hr. (c) The relationship of SERS intensity in a bacteria concentration manner.

(iii) Accumulation in cell

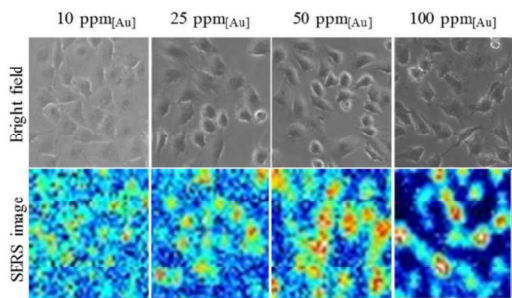


Figure 3. Co-localized bright images and SERS mapping images of cell incubated with Au@PGlyco NPs with 10-100 ppm_[Au].

(iv) Macrophage polarization

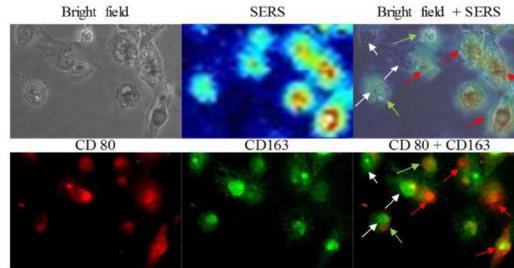


Figure 4. The surface marker transition of M2 macrophages treated with 100 ppm Au@PGlyco NPs by SERS imaging and fluorescence microscopy imaging with CD80/CD163 labeling for single-cell analysis with M1 polarization status assessments. Red arrows represent a high SERS signal and high CD80/low CD163 cells, green arrows represent a low SERS signal and low CD80/high CD163 cells, and white arrows represent a cell with no SERS signal but that shows strong CD163 expression.

References

[1] Becer, C. R., "The Glycopolymers Code: Synthesis of Glycopolymers and Multivalent Carbohydrate-Lectin Interactions," *Macromol. Rapid Comm.* 33 (9), 742-752 (2012).

[2] Qi, W. J., Zhang, Y. F., et al., "Deprotection-Induced Morphology Transition and Immunoactivation of Glycovesicles: A Strategy of Smart Delivery Polymersomes," *J. Am. Chem. Soc.* 140 (28), 8851-8857 (2018).

[3] Yuan, S. S., Li, M. L., Chen, J. S., Zhou, L., Zhou, W., "Application of Mono- and Disaccharides in Drug Targeting and Efficacy," *Chemmedchem.* 13 (8), 764-778 (2018).

[4] Jain, A., Parajuli, P., et al., "Recent Advances in Galactose-Engineered Nanocarriers for the Site-Specific Delivery of siRNA and Anticancer Drugs," *Drug Discov. Today* 23 (5), 960-973 (2018).

[5] Kawakami, S., Hashida, M., "Glycosylation-Mediated Targeting of Carriers," *J. Control. Release* 190, 542-555 (2014).

Custom-Made Photoacoustic System on Tumor Blood Vessels and Oxygen Saturation Measurement for Small Animals

Yu-Fong Liou¹, Shih-Po Su¹, Huihua Kenny Chiang^{1,*}

¹Department of Biomedical Engineering, National Yang Ming Chiao Tung University, Taipei 112304, Taiwan, R.O.C.

Abstract

Photoacoustic imaging has exceptional performance in small animal tomography. Nonetheless, commercial photoacoustic imaging systems are limited to using bulky and expensive pulse laser sources. In this paper, we assembled a custom-made photoacoustic/ ultrasound dual-modality imaging system combining LEDs to accomplish blood vessel tomography and oxygen saturation measurement on tumors. The lateral resolution of this system was estimated to be 200 μm by imaging a copper wire. The tomography demonstrated the feasibility of the system for tumor angiogenesis monitoring. Moreover, the system, which assists in clinical diagnosis, provides spatial information about vessels and quantifies oxygen saturation.

Keywords: photoacoustic imaging, tumor vasculature, LEDs, oxygen saturation, small-animal imaging

I Introduction

Photoacoustic (PA) imaging combines high contrast of optical imaging with favorable spatial resolution and high penetration depth [1]. Moreover, PA and ultrasound (US) imaging can simultaneously provide anatomical and functional information on tumor growth [2,3]. Nd: YAG lasers are commonly used as light source in PA excitation. However, PA imaging systems with high-energy lasers are bulky, expensive, and limited to low repetition rates. To overcome these limitations, light emitting diodes (LEDs) have been utilized as an illumination light source in photoacoustic computed tomography (PACT) configuration [4,5]. These applications with low cost and portable LEDs motivated us to develop a LED-based photoacoustic imaging system. Therefore, we constructed a custom-made PACT and US imaging system to demonstrate vascular angiogenesis and oxygen saturation (SpO_2) in tumor development [6,7].

II Materials and Methods

The custom-made PACT and US imaging system configuration is shown in Figure 1. For PA imaging, we had two illuminating methods; one was a short pulse laser, and the other was LEDs. By switching to different holders, we can achieve vascular imaging and oxygen saturation measurement at the same position. We used a Q-switch

Nd: YAG laser at 5 ns pulse width with 10 Hz pulse repetition rate as our light source to generate photoacoustic signals from the subject. In addition, the LEDs' wavelengths we used were 750 nm and 850 nm to measure SpO_2 .

We used a commercial transducer (A313S, OLYMPUS NDT) with 15 MHz center frequency to receive ultrasound and photoacoustic signals. This spherically focused transducer, with a focal length of 12.7 mm and bandwidth of up to approximately 90%, had an outstanding performance in ultrasound or photoacoustic imaging. Besides, we applied a pulse-receive system (5800PR, OLYMPUS NDT) to generate ultrasound and receive photoacoustic signals.

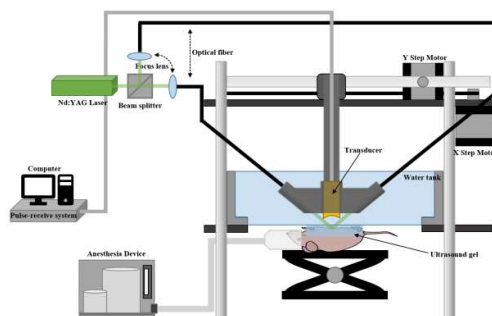


Figure 1. Schematic of the custom-made PACT and US imaging system.

*chiang@nycu.edu.tw; phone: (02)2826-7000 #67027

Acknowledgments: This work was supported by the Ministry of Science and Technology of Taiwan (MOST109-2221-E-010-001-MY3)

We used a copper wire (diameter is 50 μm) to evaluate our spatial resolution of ultrasound and photoacoustic using full width at half maximum (FWHM) [8]. The wire was placed at the focal length (12.7 mm) of the transducer.

The in vivo experiments were conducted following the guidelines and regulations approved by the Institutional Animal Care and Use Committee of National Yang Ming Chiao Tung University (protocol number: 1100509, approved date: May 9, 2021). The nude mice were anesthetized and mounted on a self-made mice holder, covering transducer gel.

III Results and Discussion

In the copper-wire experiment, PA's axial and lateral resolution was 97.4 μm and 316.5 μm , respectively. US's axial and lateral resolution is 150 μm and 217 μm theoretically. The axial resolution comparison is displayed in Figure 2. Note that the axial resolution was similar because the center frequency of the transducer defined axial resolution. However, the lateral resolution had a disparity. One of the reason is that ultrasound has a round trip in transmission and reception while photoacoustic only has one way in pulse-echo reception.

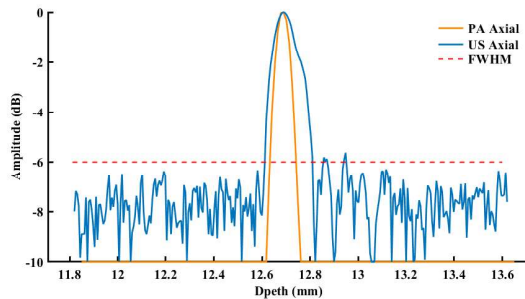


Figure 2. Axial resolutions displayed in line profiles. Orange line shows PA axial resolution. Blue line shows US axial resolution. Red dash line shows FWHM.

In the in vivo experiments, we demonstrated US and PA overlapping maximum intensity projection image (MIP image) of the abdominal region of normal nude mice (Figure 3). By the 532 nm pulse laser, our maximum penetration depth of the PA imaging is approximately 5 mm. We can clearly distinguish the four major blood vessels in the abdominal region.

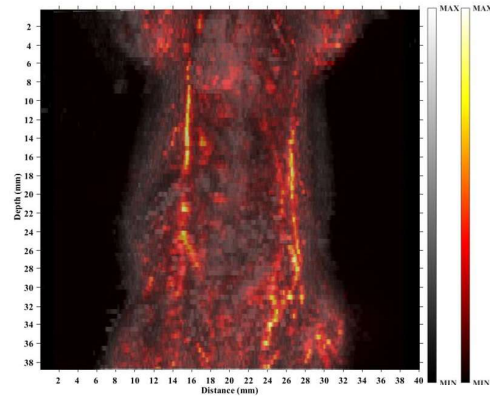


Figure 3. US/PA MIP image overlapped of mice abdominal region in vivo.

IV Conclusions

In this research, we constructed a custom-made PACT and ultrasound dual-modality imaging system. The whole-body small animal PA/US images demonstrated the feasibility of the dual-modal imaging system to observe biological tissue.

V References

- [1] Wang, L. V., & Yao, J. (2016). A practical guide to photoacoustic tomography in the life sciences. *Nature methods*, 13(8), 627-638.
- [2] Kolkman, R. G., Brands, P. J., Steenbergen, W., & van Leeuwen, T. G. (2008). Real-time in vivo photoacoustic and ultrasound imaging. *Journal of biomedical optics*, 13(5), 050510.
- [3] Neuschmelting, V., Burton, N. C., Lockau, H., Ulrich, A., Harmsen, S., Ntziachristos, V., & Kircher, M. F. (2016). Performance of a multispectral optoacoustic tomography (MSOT) system equipped with 2D vs. 3D handheld probes for potential clinical translation. *Photoacoustics*, 4(1), 1-10.
- [4] Hariri, A., Lemaster, J., Wang, J., Jeevarathnam, A. S., Chao, D. L., & Jokerst, J. V. (2018). The characterization of an economic and portable LED-based photoacoustic imaging system to facilitate molecular imaging. *Photoacoustics*, 9, 10-20.
- [5] Francis, K. J., Boink, Y. E., Dantuma, M., Singh, M. K. A., Manohar, S., & Steenbergen, W. (2020). Tomographic imaging with an ultrasound and LED-based photoacoustic system. *Biomedical optics express*, 11(4), 2152-2165.
- [6] Bok, T. H., Hysi, E., & Kolios, M. C. (2016). Simultaneous assessment of red blood cell aggregation and oxygen saturation under pulsatile flow using high-frequency photoacoustics. *Biomedical optics express*, 7(7), 2769-2780.
- [7] Wang, X., Xie, X., Ku, G., Wang, L. V., & Stoica, G. (2006). Noninvasive imaging of hemoglobin concentration and oxygenation in the rat brain using high-resolution photoacoustic tomography. *Journal of biomedical optics*, 11(2), 024015.
- [8] Ku, G., Maslov, K. I., Li, L., & Wang, L. V. (2010). Photoacoustic microscopy with 2- μm transverse resolution. *Journal of biomedical optics*, 15(2), 021302.

Dynamic event measurements by single-shot generalized Hanbury Brown-Twiss intensity interferometry

Naru Yoneda^{*a}, Xiangyu Quan^{a,b}, Osamu Matoba^{a,b}

^a Graduate School of System Informatics, Kobe University, Rokkodai 1-1, Nada, Kobe, Japan

^b Center for Optical Scattering Image Science, Kobe University, Rokkodai 1-1, Nada, Kobe, Japan

Abstract

Hanbury Brown-Twiss (HBT) intensity interferometer can only obtain the modulus of the complex degree of coherence. Although generalized HBT intensity interferometer can obtain the complex degree of coherence, real time measurements is not realized. In this study, single-shot generalized HBT intensity interferometer is proposed by using parallel phase-shift method to realize real time measurements of the complex degree of coherence. The feasibility of the proposed method is confirmed by optical experiment.

Keywords: Scattering imaging, Coherence, Intensity interferometry, Digital holography, Parallel phase-shift

I Introduction

Speckle correlation imaging (SCI) can see through scattering media without prior information of the scattering media [1]. SCI uses a condition that the self-correlation of an object is almost the same as the self-correlation of a speckle intensity. However, due to the absence of a phase of the self-correlation, SCI requires iterative phase retrieval algorithm, which leads to longer calculation time. This phase missing problem is like the situation of the Hanbury Brown-Twiss (HBT) intensity interferometry [2]. HBT intensity interferometry is robust to phase fluctuation because of intensity correlation. However, HBT intensity interferometry can obtain only the modulus of a coherence function. If the complex coherence function is measured, the shape of the light source (object) in the random light field is obtained. To overcome the problem, generalized HBT intensity interferometer has been proposed [3]. Generalized HBT intensity interferometer can overcome the requirements of the iterative phase algorithm of SCI; however, generalized HBT intensity interferometer needs multiple shot of the phase-shifted speckle intensity. To overcome the problem, we proposed single-shot generalized HBT intensity interferometer [4]. In this study, we show the results of dynamic event in random light field.

*yoneda.naru@port.kobe-u.ac.jp; +81-78-803-6240

II Single-shot generalized HBT intensity interferometer

1. principle

The schematic of single-shot generalized HBT intensity interferometer is shown in Fig. 1. Phase-shifted speckle intensity distributions are obtained. By calculating the self-correlation and cross-correlation, and applying phase-shift, complex coherence function is obtained. The object intensity distribution is obtained by applying Fourier transform to the complex coherence function. In the single-shot generalized HBT intensity interferometer, phase-shifted speckle intensity distributions are simultaneously obtained based on the parallel phase-shifting digital holography [5]. To obtain the parallel phase shift speckle intensity distribution, polarization direction for the object and the reference beams are set to p- and s-polarization. Through a quarter wave plate, these beams are changed to orthogonal circular polarized light. The parallel phase shift speckle intensity distribution can be obtained by polarization camera. Single-shot generalized HBT intensity interferometer can measure dynamic event with the frame rate of the camera because required phase-shifted speckle intensity distributions are simultaneously obtained.

2. Experiment

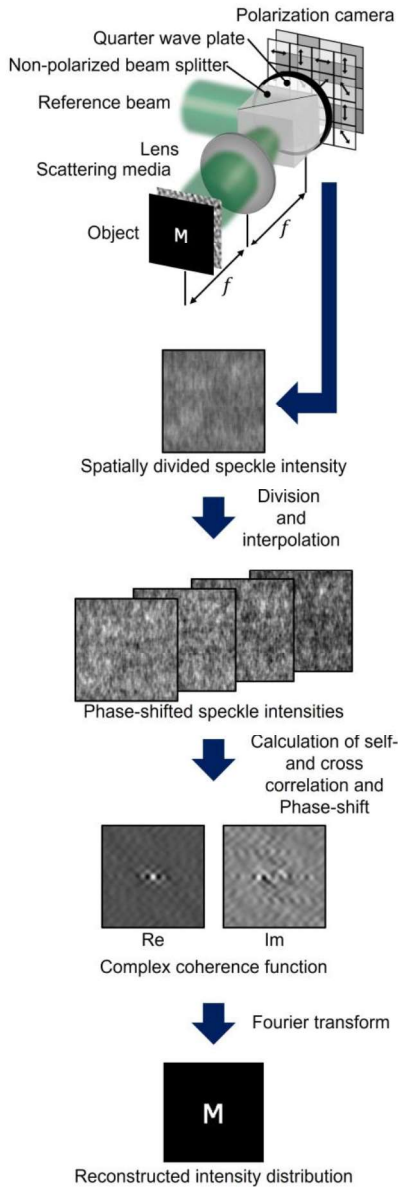


Figure 1 Schematic of the proposed method.

A dynamic object is measured by the proposed method. The wavelength of the laser light source is 532 nm. The light is collimated and divided by a polarization beam splitter. The reflected s-polarized light is used as a

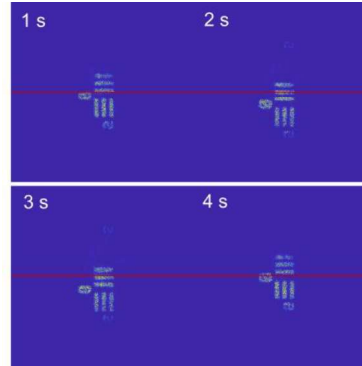


Figure 2 Results of dynamic event.

reference beam. The transmitted p-polarized light illuminates an aperture used as an object. A Negative 1951 USAF target (Thorlabs Inc. R3L3S1N) is used as an object. The object intensity distributions at different times are shown in Fig. 2. The solid red line indicates the center position. These results indicate that the proposed method can image a moving object in a random light field with the frame rate of the image sensor.

III Conclusion

By using single-shot generalized HBT intensity interferometer, a dynamic object in random light field is measured.

References

- [1] O. Katz, P. Heidmann, M. Fink, and S. Gigan, *Nat. Photonics* **8**, 784 (2014).
- [2] R. H. Brown and R. Q. Twiss, *Nature* **177**, 27 (1956).
- [3] Z. Huang, Y. Chen, F. Wang, S. A. Ponomarenko, and Y. Cai, *Phys. Rev. Appl.* **13**, 044042 (2020).
- [4] N. Yoneda, X. Quan, and O. Matoba (in review).
- [5] T. Tahara, T. Kanno, Y. Arai, and T. Ozawa, *J. Opt.* **85**, 1069 (2017).

Quantitative Differential Phase Contrast Microscopy with Dual-color Coded Pupil*

Ying-Ju Chen^{*a,b}, Sunil Vyas^b, Tai-Horng Young^a, Yuan Luo^{a,b}

^aDepartment of Biomedical Engineering, National Taiwan University, Taipei 10051, Taiwan, R.O.C.

^bInstitute of Medical Device and Imaging, National Taiwan University, Taipei 10051, Taiwan, R.O.C.

Abstract

Quantitative differential phase contrast (qDPC) microscopy visualizes weak phase samples using asymmetrically structured lights. However, collecting the required frames for a phase image without frequency loss is time-consuming. To improve the imaging efficiency without sacrificing the quality of the resultant phase image, linearly gradient pupils with dual-color coded are implanted into the imaging system. The designed pattern can achieve isotropic phase transfer function within four frames, and the color-coded method helps to reduce the frames by half. The performance of the implementation is evaluated by a standard micro-lens array, 3T3 cells, and rat astrocytes. The time-lapse imaging of living astrocytes is further demonstrated to show the potential application of the system in the biological field.

I Introduction

Quantitative phase imaging (QPI) is an important technique for visualizing weak phase objects such as transparent cells. Observation of unstained cells enables long term monitoring and is beneficial to research on cells behavior [1]. To prevent speckle issue due to the coherent light source in interference method, quantitative differential phase contrast (QDPC) microscopy utilizes a partially coherent light source to create several asymmetric lights and shine the sample. By deconvoluting the collected intensity measurements with theoretical pupil transfer function (PTF) [2], a phase image can be retrieved. The asymmetric lights are four originally semicircles along horizontal and vertical axes from opposite sides. However, there would be artifacts due to the frequency loss in the spectral domain. Twenty-four semicircles illumination from different directions can reduce the artifacts with the cost of imaging acquisition time.

Several illumination pattern designs successfully increase imaging speed with the same quality of images [3]. To further improve the efficiency, we propose dual-color coded QDPC microscopy. With the color-coded design, required frames for achieving isotropic PTF using the linearly gradient pupil can be reduced to only two. The obtained intensity images would be calibrated before phase retrieval since there is mismatch between the spectrum of

incident light and the spectrum response of camera sensor. Micro-lens array with theoretical phase as 4.53 radians was taken as a sample to evaluate the proposed method. Astrocytes which are essential for maintaining brain homeostasis [4] are further imaged to demonstrate the performance of the system. The changes in height and morphology of rat astrocytes cultured under hypoxic condition can be observed and help in vitro model building of cell edema. The results show the capability to perform phase imaging for living cells.

II Principle of QDPC

1. System Setup

The schematic diagram of dual-color coded QDPC microscopy is shown at figure 1. The system setup is based on Olympus IX70. With an extra condenser lens and a thin film transistor (TFT) located at conjugated Fourier plane, the pattern of illumination can be controlled by an Arduino board. Figure 1 (a) shows one of the amplitude masks which is displayed during images acquisition, and figure 1 (b) shows the images captured by the CCD.

Followed by the pattern design in [3], we further encode the pupil with red and blue to generate new pupils since the separation between these two colors is large. Two linearly gradient pupils along the same axis from opposite directions become one pupil through the color-coded method.

2. QDPC Transfer Function

The phase transmission function of a weak phase object is approximated to

$$o(r) = 1 - \alpha(r) + i\phi(r), \quad (1)$$

where r denotes the spatial coordinate, $\alpha(r)$ denotes absorption of the sample, and $\phi(r)$ denotes the phase distribution of the sample. The relationship between intensity and phase images is linearized by taking equation (1) into consideration, and the resultant phase can be retrieved using regularization method as below [5]:

$$\tilde{\phi}(r) = \mathcal{F}^{-1} \left\{ \frac{\sum_i (\tilde{H}_{\text{phase},i} \cdot \mathcal{F}(I_{\text{DPC},i}(r)))}{\sum_i |\tilde{H}_{\text{phase},i}|^2 + \gamma} \right\}. \quad (2)$$

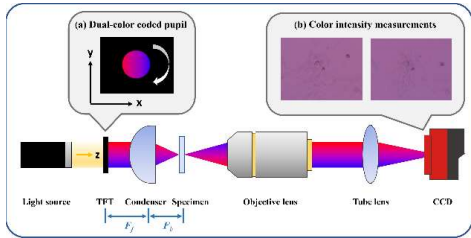


Figure 1. The configuration of dual-color coded QDPC microscopy. (a) Designed pupil shows on the TFT. (b) Intensity measurements captured from the CCD.

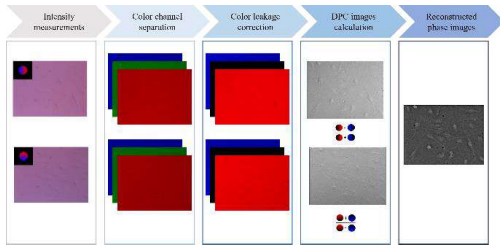


Figure 2. Phase retrieval process of the proposed method.

3. Color leakage correction (CLC)

The crosstalk between spectrum of TFT and the CCD results in signal loss in the desired color channels. To solve this issue, color leakage correction by multiplying a transfer matrix including leakage ratios from different color channels [6] is applied to the measurements before the deconvolution. Figure 2 indicates the process of phase retrieval for QDPC microscopy.

III Results and Discussion

Time-lapse imaging of rat astrocytes was demonstrated in figure 3. Due to the low concentration of oxygen environment, the phase of the cells became larger.

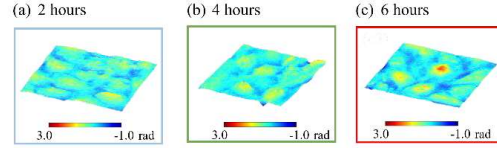


Figure 3. Retrieved phase of rat astrocytes in 3D view. (a), (b), (c) shows phase distribution of astrocytes that were cultured in hypoxic environments after 2, 4, and 6 hours.

IV Conclusion

The proposed method can achieve isotropic PTF and obtain a quantitative phase image within two frames. The reduction is beneficial to biological applications for time-lapse imaging. With the use of dual-color coded QDPC imaging, dynamics of cell behavior can be recorded to help cell research.

*r09528053@ntu.edu.tw; phone 02 2312-3456#288613

References

- [1] Zernike, F., "Phase contrast, a new method for the microscopic observation of transparent objects," *Physica* 9(7), 686-698 (1942).
- [2] Mehta, S. B. and Sheppard, C. J. R., "Quantitative phase-gradient imaging at high resolution with asymmetric illumination-based differential phase contrast," *Optics Letters*, 34(13), 1924 (2009).
- [3] Chen, H. H., Lin, Y. Z., and Luo, Y., "Isotropic differential phase contrast microscopy for quantitative phase bio-imaging," *J.Biophoton* 11(8), e201700364 (2018).
- [4] Lafrenaye, A. D., and Simard, J. M., "Bursting at the Seams: Molecular Mechanisms Mediating Astrocyte Swelling," *International Journal of Molecular Sciences* 20(2), 330 (2019).
- [5] Tian, L., and Waller, L., "Quantitative differential phase contrast imaging in an LED array microscope," *Optics express* 23(9), 11394-11403 (2015).
- [6] Lee, W., Jung, D., Ryu, S., and Joo, C., "Single-exposure quantitative phase imaging in color-coded LED microscopy," *Opt. Express* 25(7), 8398-411 (2017).

Quantitative phase imaging with a Fresnel biprism-based digital holographic microscope

Chen-Ming Tsai^a, Yuan Luo^{*a,b,c}

^aInstitute of Medical Device and Imaging, National Taiwan University, Taipei 10051, Taiwan, R.O.C.

^bMolecular Imaging Center, National Taiwan University, Taipei, 10672, Taiwan, R. O. C.

^cYong-Lin Institute of Health, National Taiwan University, Taipei, 10087, Taiwan, R. O. C.

*e-mail address: yuanluo@ntu.edu.tw

Abstract

Digital holography microscopy (DHM) provides quantitative phase imaging ability, which is useful for observing transparent microscope specimens. To satisfy the off-axis configuration, the object and reference beam are separated into two different optical paths, which makes the system complex and unstable. Here, we demonstrate the common path DHM system based on Fresnel biprism. By using the Fresnel biprism, the object and reference beam can be separated at a small angle and propagate along a common path. The common DHM system we demonstrated is highly compact and able to minimize the influence of environmental fluctuations.

Key Word— Digital holographic microscopy, Fresnel biprism, quantitative phase contrast imaging

I Introduction

For transparent microscopic samples, it is difficult to get contrast in intensity distribution. Light passing through samples with thickness variation produces different phase changes which are more significant than intensity contrast. Digital holographic microscopy (DHM) can provide both phase and amplitude information about an object and can be used for quantitative phase contrast imaging [1]. In DHM, an off-axis configuration is required to avoid the information overlapping with DC and conjugate terms [2]. The object and reference beams need to be separated into two independent optical paths and recombined to interfere, which makes the system complex and less temporally stable. For this reason, multiple common-path DHM systems have been proposed. The concept is to let two beams travel nearly the same optical path to make the system more stable, which can be realized by using a diffraction grating [3], glass plate [4], or beam splitter [5]. However, the above system contains disadvantages of significant power loss or a large difference between two beam intensities. Here we applied the common-path DHM based on a Fresnel biprism [6], in which the two beams can be divided into a small angle separation, with the same intensity and

without power loss. The system is more compact and easy to align.

II Experimental setup

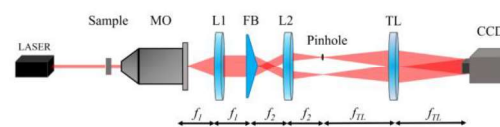


Figure 1. Experimental setup of common path DHM based on Fresnel biprism. MO: microscopic objective lens (NA: 0.28); L's: lens; FB: Fresnel biprism; TL: tube lens; CCD: charge-coupled device.

The experimental setup is depicted in Fig.1 [6]. We used a 633 nm wavelength laser as our light source. First, the laser illuminates the sample, and the scattered light is collected by a 10X microscopic objective lens (MO). Subsequently, the collected beam passes through the relay lens which is coupled by the lens (L1, $f_1 = 33$ mm) and L2 ($f_2 = 33$ mm). To generate two beams, we insert a Fresnel biprism (FB) between L1 and L2. The incoming beam is divided into two equal parts and a small angle separation. Because both two beams contain object information. In one of the beams generated by FB, the pinhole is placed at the Fourier plane of L2 to filter out the object information.

The filtered uniform beam act as the reference beam and another act as the object beam. Finally, the two beams interfere in the overlapping areas of the imaging plane, and the interference fringes are captured by a CCD camera to record the hologram digitally.

III Experimental result

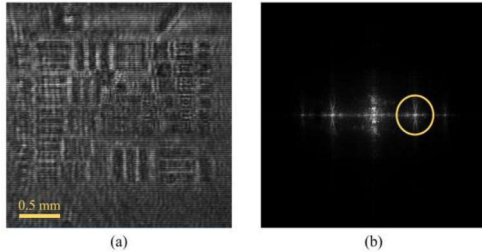


Fig. 2 The hologram recorded by CCD, (a) the raw hologram, and (b) the hologram spectrum. The yellow circle indicates the filtered-out part of the first-order term.

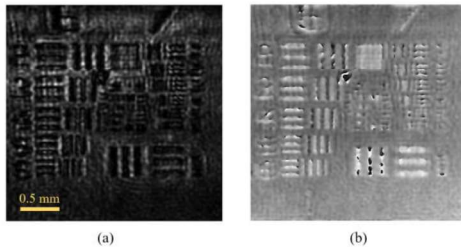


Fig. 3 The reconstructed image, (a) reconstructed amplitude, (b) reconstructed phase.

In the demonstration, a USAF phase target is applied as the sample. The raw hologram captured by CCD is shown in Fig.2 (a). The hologram size is 600×600 pixels, with a pixel pitch of $4.65 \mu\text{m}$. We can see that there are some interference fringes on the sample image. To obtain phase information, we applied the Fourier transform technique to perform the phase extraction procedure. The hologram spectrum is shown in Fig.2 (b). We use a circular filter to filter out the first-order term and do the inverse Fourier transform to get the reconstructed image. In Fig.3 we can see that although the amplitude of the sample structure is not obvious, the reconstructed phase can reveal more sample structure information. Also, the phase value is

quantitatively recorded in digital format. After doing the phase compensation and further calculation, the height of the sample can be calculated

IV Conclusion

We have demonstrated a common-path digital holographic microscope based on Fresnel biprism. The two beams with a small angle separation can be generated via the Fresnel biprism. Both object and reference beams travel through the nearly same optical path and overlap at the image plane. The system is easy to align and the system stability is high. The result shows that our system can quantitatively record the imaging phase value. The system can have applications in semiconductor wafer defect detection, measurement dynamics of biological samples, and observation of transparent cell.

References

- [1] Myung K. Kim, "Principles and techniques of digital holographic microscopy," SPIE Rev 1 018005 (2010).
- [2] Jung-Ping Liu, and Ting-Chung Poon, Introduction to modern digital holography with MATLAB, Cambridge University, 2014.
- [3] Basanta Bhaduri, Chris Edwards, Hoa Pham, Renjie Zhou, Tan H. Nguyen, Lynford L. Goddard, and Gabriel Popescu, "Diffraction phase microscopy: principles and applications in materials and life sciences," Adv. Opt. Photon **6**, 57-119 (2014).
- [4] Priyanka Vora, Vismay Trivedi, Swapnil Mahajan, Nimit R. Patel, Mugdha Joglekar, Vani Chhaniwal, Ali-Reza Moradi, Bahram Javidi, Arun Anand, "Diffraction phase microscopy: principles and applications in materials and life sciences," J. of Biomedical Optics, **22**, 126001 (2017).
- [5] Manoj Kumar, Osamu Matoba, Xiangyu Quan, Sudheesh K. Rajput, Yasuhiro Awatsuji, and Yosuke Tamada, "Single-shot common-path off-axis digital holography: applications in bioimaging and optical metrology [Invited]," Appl. Opt. **60**, A195-A204 (2021).
- [6] Veena Singh, Shilpa Tayal, and Dalip Singh Mehta, "Highly stable wide-field common path digital holographic microscope based on a Fresnel biprism interferometer," OSA Continuum **1**, 48-55 (2018).

Acknowledgment Author would like to acknowledge funding from the ministry of science and technology Taiwan under project MOST 108-2221-E-002 -168 -MY4

Wavelength coded volume holographic gratings based fluorescence microscopy

Yu-Hsin Chia ^{a,b}, Sunil Vyas ^b, Yi-You Huang ^{a,b,c}, Yuan Luo ^{b,c,d}

^a Department of Biomedical Engineering, National Taiwan University, Taipei, 10051, Taiwan, R. O. C.

^b Institute of Medical Device and Imaging, National Taiwan University, Taipei, 10051, Taiwan, R. O. C.

^c Molecular Imaging Center, National Taiwan University, Taipei, 10672, Taiwan, R. O. C.

^d YongLin Institute of Health, National Taiwan University, Taipei, 10087, Taiwan, R. O. C.

^e Department of Biomedical Engineering, National Taiwan University Hospital, Taipei, 10051, Taiwan, R. O. C.

Author e-mail address: d08548008@ntu.edu.tw

Abstract

We present a fluorescence microscopy technique that uses wavelength coded volume holographic gratings (VHG) to obtain dual wavelength fluorescence images of biological samples in a single shot. The system utilizes a wavelength coded recording technique based on Bragg degeneracy to generate the PQ-PMMA volume holographic gratings, which has high selectivity in both wavelength and angle. In order to improve the optical sectioning ability of the proposed system, we use HiLo image processing to suppress the out of focus signal. Experimental results demonstrate the imaging ability of the proposed system to observe multi-wavelength fluorescence images and HiLo images.

Keywords: Incoherent, Holography, Microscopy, Fluorescence microscopy.

I Introduction

Fluorescence imaging is one of the most important techniques for biological and medical applications. It is used to selectively image the targeted regions with high sensitivity. If two different wavelength fluorescence images can be separated and acquired at the same time, they can be used to further analyze the molecular interactions in the samples. Multiple-wavelength fluorescence imaging has also been applied for functional imaging of ion flows [1]. Previously, W-microscopy has been developed to obtain a pair of fluorescence images, while the beam separator of the system requires a complex setup that makes the system bulky [1]. Here, we introduce wavelength coded volume holographic gratings (VHG) based fluorescence microscopy [2]. The wavelength coded VHG can function like the beam splitting optical component to divide two different color fluorescence beams that make the system capable of providing dual wavelength fluorescence images. In order to improve the optical sectioning ability of the system, the study combines the HiLo imaging process with the system [3]. The system setup and experiment results are discussed thoroughly.

II Fabrication and design of wavelength coded VHG

The photosensitive materials PQ-PMMA are used to form highly Bragg selective wavelength coded VHG in the proposed wavelength coded VHG based fluorescence microscopy. An Argon ion (Ar+) laser operated at 488 nm is used as a light source to generate the gratings inside the photopolymer substrate. The gratings are formed by the interference between the reference beam and the signal beam. The K-sphere diagram of the wavelength coded VHG consists of two gratings, Kg1 and Kg2, designed for the wavelengths of 633 nm and 488 nm, respectively [2].

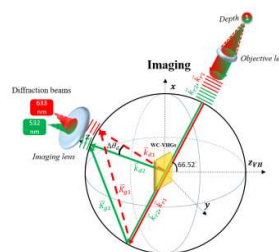


Figure 1. K-Sphere for wavelength coded VHG imaging condition.

The reference and signal beams are collimated beams for both gratings. The signal beams use the same 45° incident angles with respect to the surface normal of photopolymer substrate for both the gratings Kg1 and Kg2. The research changes the incident angles of reference beams by $\theta_s =$

21.5° in two successive recordings of wavelength coded VHGs. With the above recording parameters, the wavelength coded VHGs have the ability to make the different wavelength excitation fluorescence beams utilize the same reconstruction angle to generate corresponding diffraction beams. Figure 1 is the wavelength coded VHGs imaging condition. The gratings Kg1 and Kg2 can individually satisfy the Bragg select of the red and green fluorescence to produce the corresponding images.

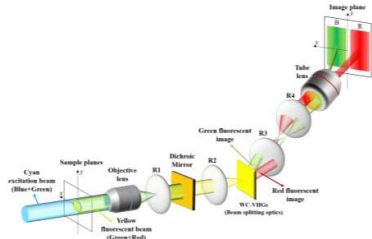


Figure 2. Schematic diagram of wavelength coded VHGs based fluorescence microscopy.

III Experimental setup and results

Figure 2 depicts the proposed wavelength coded VHGs based fluorescence microscopy. The setup utilizes the cyan laser (Cobolt Calypso™ 200, 491nm) to illuminate the fluorescence sample to excite the yellow fluorescent image. After the sample, an objective (ULWDMSPlan50X, OLYMPUS) and a tube lens (MPlanAPO20X, MITUTOYO) are used to compose a 4-f system. A dichroic mirror (FITC dichroic mirror, MD499, THORLAB, R band=470-490 nm, T band=508-675 nm) is placed between the relay lens (R1 & R2) that can reject the stray cyan excitation light and make the yellow fluorescent light pass through it. The wavelength coded VHGs is located at the Fourier plane of the objective lens. Under the Bragg matched condition, the wavelength coded VHGs can function like the beam splitting optical component to make the yellow fluorescent image divided into the green and red fluorescent images. The two color fluorescent images go through the tube lens project to the different lateral location on to the CCD (GE1650, PROSILICA) without overlap. In the experimental results, first we utilizes the fluorescent beads (Polysciences Inc, YG microspheres, 45.0μm) to verify the wavelength-selective ability of the system as shown in Figure 3. On the CCD plane, the system can successfully separate the green and red fluorescent images. In order to improve the

optical sectioning ability of the system, the study combines the HiLo imaging process with the system as shown in Figure 4 (a) and (b). Figure 4 (c) shows the final HiLo image can reduce the defocus signal of the fluorescence beads.

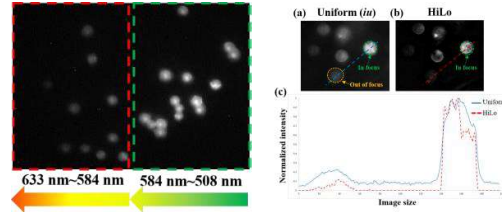


Figure 3. Green & Red fluorescence beads image. Figure 4. (a)&(b)Uniform & HiLo image (c) Intensity profiles

IV Conclusion

In conclusion, we propose a wavelength coded VHGs-based fluorescence microscopy that produces a pair of wavelength fluorescence images with no image overlap. Furthermore, in order to reject out of focus signals from the object, the system utilizes the HiLo image processing technique to acquire the optical sectioning images. For future work, the system can record more gratings in the angular multiplex VHGs to combine with the HiLo technique to provide multi-depth optically sectioned images [4].

V References

- [1] K. Kinoshita, Jr, H. Itoch, S.Ishiwata, K. Hirano, T. Nishizaka, and T. Hayakawat, "DualView Microscopy with a Single Camera: RealTime Imaging of Molecular Orientations and Calcium," J Cell Biol. 115, 67 (1991).
- [2] Y. Luo, S. B. Oh, and G. Barbastathis, "Wavelength-coded multifocal microscopy," Opt. Lett. 35, 781 (2010).
- [3] J. Mazzaferri, D. Kunik, J. M. Belisle, K. Singh, S. Lefrançois, and S. Costantino, "Analyzing speckle contrast for HiLo microscopy optimization," Opt. Exp. 19, 14508 (2011).
- [4] S. Vyas, Y. H. Chia, and Y. Luo, "Volume holographic spatial-spectral imaging systems [Invited]," JOS A. 36, A47 (2019).

Differential phase contrast volume holographic incoherent microscopy

Yu-Hsin Chia ^{a,b}, Sunil Vyas ^b, Yi-You Huang ^{a,b,c}, Yuan Luo ^{b,c,d}

^a Department of Biomedical Engineering, National Taiwan University, Taipei, 10051, Taiwan, R. O. C.

^b Institute of Medical Device and Imaging, National Taiwan University, Taipei, 10051, Taiwan, R. O. C.

^c Molecular Imaging Center, National Taiwan University, Taipei, 10672, Taiwan, R. O. C.

^d YongLin Institute of Health, National Taiwan University, Taipei, 10087, Taiwan, R. O. C.

^e Department of Biomedical Engineering, National Taiwan University Hospital, Taipei, 10051, Taiwan, R. O. C.

Author e-mail address: d08548008@ntu.edu.tw

Abstract

We present a differential phase contrast volume holographic microscopy (DPC-VHM) based on asymmetric illumination to simultaneously obtain multi-depth phase contrast images of a biological samples in one shot, using LED illumination. The volume holographic gratings composed of PQ-PMMA that has high selectivity in both wavelength and angle. Experimental results demonstrate the imaging ability of the proposed DPC-VHM system to observe the bright field and differential phase contrast multi-plane imaging of the sample.

Keywords: Three-dimensional imaging, Incoherent, Holography, Microscopy.

I Introduction

Many optical microscopy systems have been proposed to obtain three-dimensional (3D) images for biomedical request. Nevertheless, most of these systems require mechanical or electro-optic axial scanning mechanism to construct multi-depth images. In the past few years, many efforts are dedicated on reducing the scanning mechanism for optical holographic systems [1-3]. Holography microscopy can be performed with coherent as well as incoherent light to acquire 3D images. Apart from most commonly used Fresnel incoherent correlation holography, volume holographic microscopy can also be done with incoherent light [4, 5]. A typical VHM for multiplane imaging consists of multiplexed volume holographic gratings (MVHGs) to simultaneously capture different depths from a specimen. The MVHGs, helps in collecting multiple depth-resolved information. Although different depth images can be captured using VHM in one shot, weak phase samples are difficult to be observed by VHM [6,7]. Here, we introduce an asymmetric illumination based VHM system using differential phase contrast (DPC) method. The proposed DPC-VHM system can be used to image weak phase objects with multi-plane imaging within a single shot.

II Fabrication and design of MVHGs

PQ-PMMA photosensitive materials can form high spectral and angular Bragg selectivity MVHGs [8]. In Figure 1, the MVHGs are formed with an Ar⁺ laser operated at 488nm. The input beam will split into a reference beam and a signal beam. The reference beam is a collimate and the spherical signal beam whose radius of curvature corresponds to the depth position (z) within the sample.

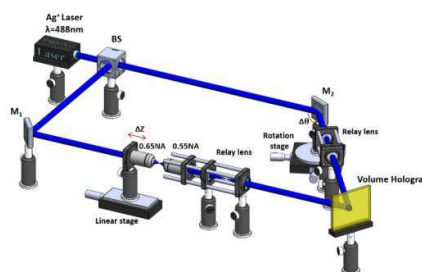


Figure 1. Recording setup of the multiplexed VHGs.

In the reference beam, we used a rotation stage to control the mirror M2, and the angle between two beams is changed by $\Delta\theta$ for each exposure. In the signal arm, a miniature motorized actuator is used to adjusted the positions of the point source by moving the microscope objective lens with a numerical aperture (NA) of 0.65 along the axial direction, while a lens of NA=0.55 remains in the fixed position to form spherical waves.

III Experimental setup and results

Figure 2 depicts the proposed DPC-VHM system, using a TFT panel to generate the half circle aperture. The aperture is placed at the front focal plane of the condenser (LA1951-A, THORLABS), producing an asymmetric illumination pattern light source (LIU525B, THORLAB, $\lambda=525$ nm, $\Delta\lambda\sim 80$ nm). An objective (ULWDMSPlan50X, OLYMPUS) and a tube lens (MPlanAPO20X, MITUTOYO) are used to construct a 4- f system, with MVHGs located in the Fourier plane. Under Bragg matched condition, two-depth images diffract from each corresponding angle and are captured by the CCD (GE1650, PROSILICA). Figure 3 shows the experimental images of the Air Force Resolution Chart and onion skin biological sample. The two different depths can be imaged simultaneously with the focus difference 50 μ m. The contrast of high frequency part (group 6) in Figure 3(b) is largely improved as comparison with conventional bright field VHM images in Figure 3 (a). In addition, Figure 3 (a) shows depth-resolved bright-field VHM images of an onion skin, while Figure 3 (b) shows DPC-VHM images. It shows solid evidence that weak phase features from different depths are significantly observed simultaneously.

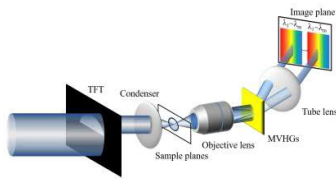


Figure 2. Schematic diagram of DPC-VHM system.

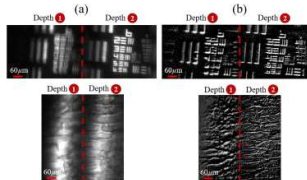


Figure 3. Two depth-resolved (a) bright field VHM images (b) DPC images of resolution chart and onion skin obtained with the DPC-VHM.

IV Conclusion

In summary, we propose a novel DPC-VHM imaging that can simultaneously obtain differential phase contrast multiple depth-resolved images by utilizing asymmetric illumination. For future work, more multiplexed VHGs will be recorded to provide more depth-resolved images. Furthermore, in order to obtain the quantitative phase contrast information, the system will combine quantitative phase imaging with the help of the wavelength coded MVHGs.

V References

- [1] M. P. Shih, H. S. Chen, and E. N. Leith, "Spectral holography for coherence-gated imaging," *Opt. Lett.* 24, 52 (1999).
- [2] G. Indebetouw and P. Klysibun, "Space-time digital holography: A three dimensional microscopic imaging scheme with an arbitrary degree of spatial coherence," *Appl. Phys. Lett.* 75, 2017 (1999).
- [3] L. Yu and M. K. Kim, "Wavelength-scanning digital interference holography for tomographic three dimensional imaging by use of the angular spectrum method," *Opt. Lett.* 30, 2092 (2005).
- [4] Y. Luo, P. J. Gelsinger-Austin, J. M. Watson, G. Barbastathis, J. K. Barton, and R. K. Kostuk, "Laser-induced fluorescence imaging of subsurface tissue structures with a volume holographic spatial-spectral imaging system," *Optics Letters* Vol. 33, 2098-2100 (2008).
- [5] J. Rosen & G. Brooker, "Non-scanning motionless fluorescence three-dimensional holographic microscopy," *Nature Photonics* 2, 190-195 (2008).
- [6] Y. Luo, E. Leon, J. Castro, J. Lee, J. K. Barton, R. K. Kostuk and G. Barbastathis, "Phase-contrast volume holographic imaging system," *Optics Letters* Vol. 36, 1290-1292 (2011).
- [7] S. B. Oh, Z. Q. J. Lu, J. C. Tsai, H. H. Chen, G. Barbastathis and Y. Luo, "Phase-coded volume holographic gratings for spatial-spectral imaging filters," *Optics Letters* Vol. 38, 477-479 (2013).
- [8] Y. Luo, V. R. Singh, D. Bhattacharya, E. Y. S. Yew, J.C. Tsai, S.L. Yu, H.H. Chen, J.M Wong, P. Matsudaira, Peter T. C. So and George Barbastathis, "Talbot Holographic Illumination Non-scanning (THIN) Fluorescence Microscopy," *Laser & Photonics Reviews*, L71-L75(2014).

Classification of fork fringes using VGG 16

Sunil Vyas^a, and Yuan Luo^{a,b}

^a Institute of Medical Device and Imaging, National Taiwan University, Taipei, Taiwan, R.O.C.

^b Yong-Lin Institute of Health, National Taiwan University, Taipei, Taiwan, R.O.C.

*yuanluo@ntu.edu.tw; phone 02-23123456#88613

Abstract

Deep learning techniques have unique capabilities that can overcome the limitations of conventional optics. Depending on the azimuthal orientation, the spiral phase can be characterized as having a positive or negative topological charge. To detect spiral phase, interferometric methods are considered the hallmark. Wavefronts infested with phase singularity show forked-shaped fringes in interferogram and the number of bifurcations in the forked fringes is decided by the order of phase singularity. Here, we propose a fringe classification model based on VGG-16 for the classification of form and normal fringes. Our model can accurately predict the presence of singularities in the fringes. The performance of our binary classification is measured using MSE, ROC, and SSIM. Results presented here may find an important detection singularity in structured light.

Keywords: Singular optics, VGG-16 architecture, deep learning, spiral phase.

I Introduction

An optical vortex carries orbital angular momentum due to a spiral phase wavefront. Depending on the orientation of the azimuthal phase, the vortex beam can be categorized as positive or negative topological charge [1,2]. When the optical vortex beam interferes with the reference plane wave, then it creates a characteristic fork-shaped fringe. A light beam with an optical vortex can be generated by various methods such as laser cavities, astigmatic lenses, computer generated holograms, spiral phase plates, metasurfaces, and spatial light modulators. However, to completely characterize and detect the optical vortex beam, only a few reliable and practical methods exist. The ability to record the phase distribution in terms of the intensity variations makes the interferometric technique suitable for characterization of optical vortex beams. The phase singularity present in the vortex beam can be converted into either spiral or fork-shaped fringes, which are easy to distinguish with respect to the background. Fork fringe analysis techniques are simple but impose ambiguity if the intensity levels are low. The quality of the fork fringes is decided by the size of the dark core, topological charge, angle of reference beam, and wavelength. Controlling all the conditions is not possible in many of the experiments due to various constraints. In

addition, pixelated devices such as spatial light modulators impose other noises. Depending on the fringe spacing and the size of the core of phase singularity it is difficult to determine the presence of phase singularity in the interferogram. A well-trained deep learning model can be useful in such scenario which can directly predict the presence of the spiral phase in the wavefront.

Deep learning based methods have widely been used in the field of computer vision and imaging processing [3]. A deep learning model can be served as a reference when it is trained with a large number of data sets correspond to different conditions. Image classification is one of the prominent application of deep convolutional network. Using VGG16 architecture here, we demonstrated a simple classification model which can differentiate between the fork and straight line fringes. This model can be extended to determine the phase singularity in other cases such as various structured light patterns, such as higher order modes, and speckle by providing different data sets.

II Method

Interferogram is a standard method to record the phase distribution of the optical field. Figure 1 shows the phase distribution and interferogram of the plane and spiral phase fronts. Presence of spiral phase bifurcate the

fringes at the position of the vortex. A positive or negative topological charged vortex can be easily distinguished by observing the orientation of the fork shape fringes.

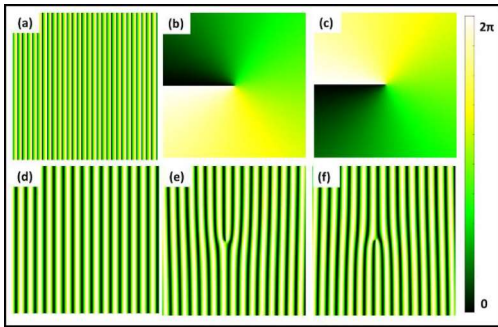


Figure 1. Simulation results of the phase distribution and interferogram, (a) tilted plane wave, (b) spiral phase positive topological charge, (c) spiral phase negative topological charge, (d) straight line fringes, (e) fork fringes corresponding to positive topological charge, (f) fork fringes corresponding topological negative charge.

III Results and discussion

VGG16 deep neural network is trained as binary classifiers for fork or non-form fringes. Fig. 2 shows the block diagram of model used in our study. Binary classification is done with the help of dense layer. Data set is prepared using image data generator.

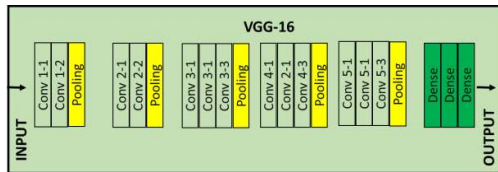


Figure 2. VGG-16 architecture.

Model is trained using 100 epoch and Fig. 3 shows the loss function for the validation and trained binary classifier. It provides more than 95% validation accuracy for the images with fork fringes. 10. Performance of the binary classification is measured using ROC and SSIM. Properties of VGG16 as binary classifier for fork fringe detection are presented.

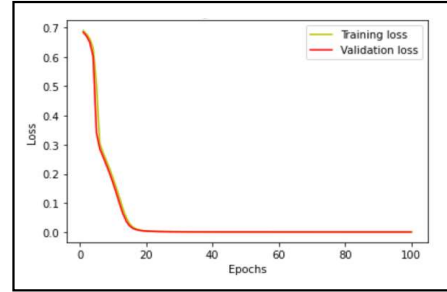


Figure 3. Training and validation loss curve for VGG-16 for classification of fringes.

IV Conclusions

We have shown that VGG-16 based fringe classifier is able to accurately predict the presence of the fork fringes in the interferogram. The proposed fringe classification method is not limited to the unit topological charge and can be extended to higher dimensions for various beam shapes. VGG-16 is chosen as an example and the same idea can be extended with deep and newer architecture. The proposed can server as a diagnostic tool for performing interferogram analysis to characterize singular beams. Present study can be further extended fringes with other shape and aberrated interference fringes.

V References

- [1] Bazhenov V. Y., Soskin M., and Vasnetsov M., (1992). Screw dislocations in light wavefronts, *J. Mod. Opt.* vol. 39, p. 985–990
- [2] *Singularities in Physics and Engineering Properties, methods, and applications* (2018). IOP publishing.
- [3] Voulodimos A., Doulamis N., Doulamis A., and Protopapadakis E., (2018). *Deep Learning for Computer Vision: A Brief Review,* Computational Intelligence and Neuroscience, Hindawi Limited.
- [4] Simonyan Karen, Zisserman Andrew,(2014) *Very Deep Convolutional Networks for Large-Scale Image Recognition.* arXiv:1409.1556.

Super-Gaussian Airy beam for light sheet microscopy

Sunil Vyas^a, and Yuan Luo^{a,b}

^a Institute of Medical Device and Imaging, National Taiwan University, Taipei, Taiwan, R.O.C.

^b Yong-Lin Institute of Health, National Taiwan University, Taipei, Taiwan, R.O.C.

*yuanluo@ntu.edu.tw; phone 02-23123456#88613

Abstract

A uniform light sheet with extended dimensions and a small thickness is always desirable for fine optical sectioning of biological samples. Uniform illumination of the light sheet is necessary to obtain better contrast in fluorescence images. Any imperfection or inhomogeneity of intensity can result in poor image contrast and hence resolution. Motivated by the above facts, Here, we propose a Super-Gaussian Airy light sheet which is capable of providing the uniform intensity profile and extended field of view in a light sheet microscope. We show an Airy Modulated Super-Gaussian beam performs better than an Astigmatic Gaussian and a Super-Gaussian beam. Simulation results are presented and compared with the closely resembling beams. We believe our method will find important applications, particularly in obtaining fine optically sectioned fluorescence images of larger biological sample sizes.

Keywords: Super-Gaussian beam, Airy beam, light-sheet microscope.

I Introduction

Light sheet microscopy has become an important method in the field of life science to perform volumetric imaging [1]. Widefield of view detection and the ability to optically section thick samples with a very thin sheet of light make light sheet microscopy techniques valuable for a number of biological applications. The application area of light sheet microscopy ranges from developmental biology, cell biology, and neuroscience.

One of the primary conditions for high contrast in light sheet microscopy is that the thickness of the light sheet should be smaller than the depth of focus of the detection lens. A uniform light sheet with extended dimensions and a small thickness is always desirable for fine optical sectioning of biological samples. The orthogonal structure of illumination and detection of light sheet microscopy makes it convenient for implementing special illumination patterns. Although by using higher NA and Gaussian beam thinner light sheet can be generated, however, the field of view will be extremely small which can limit its application range for larger size biological samples.

The intensity and phase structure of Airy beams are

unique and can be utilized for various applications, Airy beams in light sheet microscopy provides better Axial resolution and field of view [2]. Owing to the properties of nondiffraction and self-reconstruction, Airy beams have been used to decrease the scattering in light sheet microscopes. The purpose of modulating the Airy beams with the Super-Gaussian beam is to obtain a smaller thickness and a uniform intensity cross section over the significant propagation distances. Although the Super-Gaussian beam can provide a uniform intensity profile, it lacks the non-diffracting and self-healing properties [3]. On the other hand, the main and the side lobes of Airy beams have a non-uniform intensity distribution. By modulating the Super-Gaussian beam with the Airy function, an airy beam with a homogenous intensity distribution can be obtained.

II Theory

The Super-Gaussian beam has been introduced to overcome the inhomogeneity of intensity distribution of the conventional Gaussian beam []. The intensity cross-section of the Super-Gaussian beam shows the uniform intensity profile. On the other hand, an Airy beam has an oscillatory intensity profile with a dominant main lobe

and a large number of side lobes. It has cubic phase fronts which provide a parabolic propagation path. A Super-Gaussian airy beam can be described as [2,3],

$$I_{SGA} = Ai(s) \exp(as) \exp\left(-2\left(\frac{r}{w}\right)^{2n}\right) \quad (1)$$

Where Ai represents the airy function, r , is radial coordinate, w is the beam waist, $s=x/x_0$ represents the dimensionless transverse coordinate, a is constant, x_0 is an arbitrary transverse scale parameter, and. By using Eq. 1, an Airy Modulated Super-Gaussian beam can be obtained whose side lobes can be varied using control parameters. Intensity distribution of one dimensional conventional Airy beam and Super-Gaussian Airy beam is shown in Fig. 1.

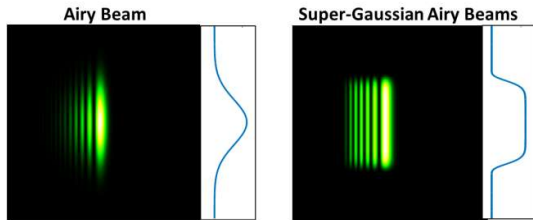


Figure 1. Simulated intensity distribution of conventional one dimensional Airy beam and Super-Gaussian Airy beam.

III Results and discussion

In order to demonstrate the advantages of the Super-Gaussian Airy Beam, intensity distribution is compared with other closely related beam. The intensity distribution of the four different beam shapes is presented in Fig.2. A thin sheet of light can also be obtained using an astigmatic Gaussian beam. Generally, a cylindrical lens is used to generate such a beam. It can be clearly seen that a Super-Gaussian airy beam can provide a smaller thickness with a uniform intensity profile. Depending on the requirements, the number of side lobes of the Super-Gaussian Airy beam can be tuned. Experimentally, realization of these beams is straightforward by using conventional holographic techniques as well as advanced technique such as nanophotonics metalens.

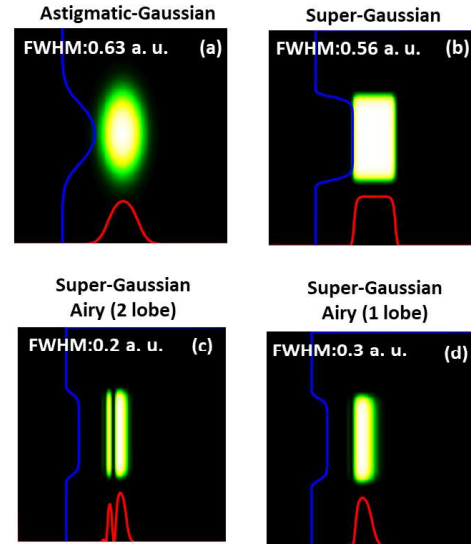


Figure 2. Simulated intensity distribution. (a) Astigmatic-Gaussian beam, (b) Super-Gaussian beam with order $n=10$. (c) Super-Gaussian Airy beam with two lobes, (d) Super-Gaussian Airy beam with single lobe.

IV Conclusions

A Super-Gaussian Airy beam can provide smaller thickness with uniform intensity profile. Implementation of Super-Gaussian Airy in the light sheet microscope can provide better imaging contrast. We believe, our method will find important applications particularly in obtaining fine optically sectioned fluorescence images of the larger biological sample sizes.

V References

- [1] Olarte, O. E., Andilla, J., Gualda, E. J., & Loza-Alvarez, P. (2018). Light-sheet microscopy: A tutorial. *Advances in Optics and Photonics*, 10(1), 111.
- [2] Siviloglou, G. A., Broky, J., Dogariu, A., & Christodoulides, D. N. (2007). Observation of Accelerating Airy Beams. *Physical Review Letters*, 99(21).
- [3] Baida Lu^{*}, Shirong Luo, (2001). Beam propagation factor of apertured super-Gaussian beams, *Optik*, vol.112, No. 11 p. 503–506.

Edge Contrast Enhancement Filters

Sunil Vyas^a, and Yuan Luo^{a,b}

^a Institute of Medical Device and Imaging, National Taiwan University, Taipei, Taiwan, R.O.C.

^b Yong-Lin Institute of Health, National Taiwan University, Taipei, Taiwan, R.O.C.

*yuanluo@ntu.edu.tw; phone 02-23123456#88613

Abstract

The edge contrast enhancement can be explained using Hilbert and fractional Hilbert transforms. Implementation of spiral phase filtering can be performed experimentally or by image post-processing. Here, we performed a systematic study to demonstrate the effect of the order of phase singularity of the spiral phase mask on edge contrast enhancement. The effect is demonstrated using the simulation. It is observed that by continuously varying the order of phase singularity, the edge enhancement can be altered in a systematic manner. A continuous change of enhancement can be achieved from an anisotropic left to perfectly isotropic to an anisotropic right edge. Present results may find important applications for image contrast enhancement methods for bio-imaging.

Keywords: Hilbert transform, Edge contrast enhancement, spiral phase filter.

I Introduction

Edge enhancement techniques have regularly been used in the field of optical image processing, particularly for bio-imaging and astronomical applications. Using Hilbert and fractional Hilbert transforms, a detailed theoretical treatment for the imaging process has been developed [1-3]. Using the gradient of the spiral phase mask, amplitude and phase contrast enhancement can be achieved. These special phase filters can be experimentally realized using diffractive or refractive optical elements [2]. Conventionally, spatial filtering operations are performed using a $4f$ imaging system in which phase or amplitude filters with the desired properties are placed at the Fourier plane of the lens. The filter acts to modify the local features of the input image. The selective edge enhancement helps in observing the details which are otherwise difficult to observe with the direct image. By manipulating the spatial frequencies in the frequency domain, particular features can be enhanced to improve the contrast of the images. A spiral phase mask is a unique optical component that has a singularity of phase at the center. It means all the phase values are simultaneously present and a phase is

undermined. When such a phase mask is illuminated with light, the output light is associated with the vortex phenomena which is associated with the dark core at the center. The light from the singularity is obstructed and it can achieve a contrast of edge inside the image. The image formation using the $4f$ system can be explained using the convolution process.

Here, we performed a systematic study to demonstrate the effect of the order of phase singularity of the spiral phase mask on edge enhancement. The effect is demonstrated using the simulation of image formation using the $4f$ system, and the edge enhancement process is described in detail. It is observed that by continuously varying the order of phase singularity, the edge enhancement can be altered in a systematic manner. A continuous change of enhancement can be achieved from an anisotropic left to isotropic to an anisotropic right edge.

II Theory

The transmittance function $H(\rho, \phi)$ of spiral phase contrast filter can be written as

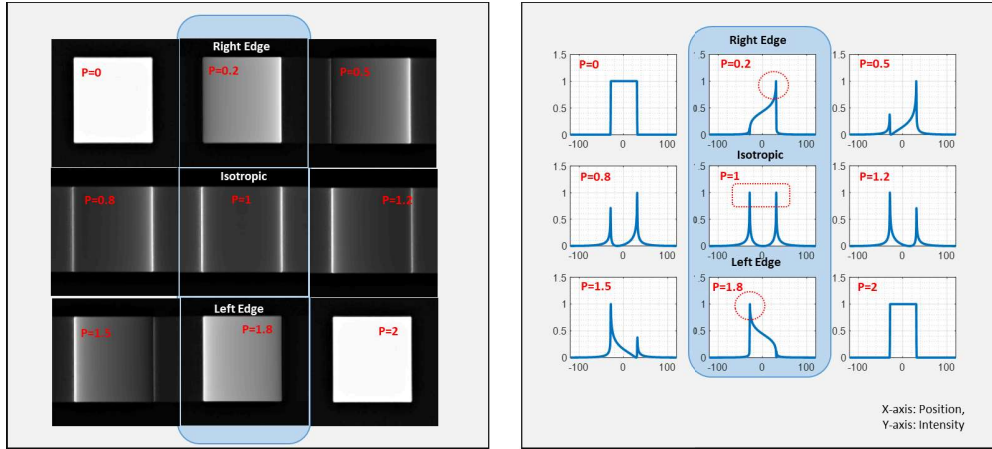


Figure 1. Simulation results of edge contrast enhancement using spiral phase filter. On the right is the intensity distribution of edge enhanced images of square-shaped objects for various orders of the spiral phase mask. On the right, the corresponding line profile is at the center of the image.

$$H(\rho, \phi) = \text{circ}\left(\frac{\rho}{R_0}\right) \exp(ip\phi) \quad (1)$$

Where, (ρ, ϕ) are polar coordinates, R_0 is radius of circular function, and p is the order of phase singularity of spiral phase mask, which can take integer as well as fractional values. The characteristic of the spiral phase mask drastically changed by choosing the order of the phase singularity. For the integer spiral phase mask, an isotropic edge enhancement can be achieved, and the entire process can be explained using the Hilbert transform. Whereas for the fractional order number a fractional Hilbert transform needs to be applied for the image formation process [1-3].

III Results and discussion

Figure 1 shows the simulation results of the edge contrast enhanced images obtained by varying the order of the spiral phase contrast filter. A square-shaped object is chosen for imaging. In the right panel, intensity distribution is depicted, and a line profile at the center of the image is shown in the left panel. As we can clearly see, the effect of varying the order of the singularity a continuous change of direction of edge enhancement can

be achieved from an anisotropic left to isotropic to an anisotropic right edge. This is a simple method to achieve selective enhancement of edges by just implementing a spiral filter.

IV Conclusions

Using simulations of image formation in a $4f$ imaging system, the effect of the order of spiral phase on edge enhancement is studied. It is observed that simply varying the order of the spiral phase filter is sufficient to achieve anisotropic to isotropic contrast enhancement. Present results may find important applications in performing image processing applications for bio-imaging.

V References

- [1] Fürhapter S., Jesacher A., Bernet S., and Ritsch-Marte M., (2005). Spiral phase contrast imaging in microscopy, *Opt. Express* vol.13, No. 3, p. 689–694.
- [2] Lohmann A. W. (1996). Fractional Hilbert transform, *Optics Letters* vol. 21, No. 4, p. 281-283.
- [3] Davis J. A., McNamara D. E., Cottrell D. M., and Campos J., (2000). Image processing with the radial Hilbert transform: theory and experiments, *Opt. Lett.* vol. 25, No.2, p. 99–101.

Development of a real-time multifunctional catheter-based optical coherence tomography imaging with multiplexing system

Xiang-Yu Chen¹, Po-Chuan Chen¹, Chuan-Bor Chueh¹, Ting-Yen Tsai¹, Ting-Hao Tsai¹, Yu-Cheng Mei¹, Cheng-Kuang Lee², and Hsiang-Chieh Lee^{1,3}*

¹Graduate Institute of Photonics and Optoelectronics, National Taiwan University, Taipei 10617, Taiwan

²NVIDIA AI Technology Center (NVAITC), NVIDIA, Santa Clara, California, USA

³Department of Electrical Engineering, National Taiwan University, Taipei, 10617 Taiwan

*Email: hclee2@ntu.edu.tw

Abstract

The development of catheter-based optical coherence tomography (catheter-based OCT), enables the feasibility of realizing detection of the cancerous lesions at the early stage in internal organs of the human body. However, due to the influence of the beam scanning imaging mechanism implemented in catheter-based OCT, the image acquired will be distorted, making it challenging for catheter-based OCT to be used as a diagnostic tool in practice. In this work, we have utilized graphics processing units (GPU) to develop an image correction framework for catheter-based OCT, and demonstrated the correction result. For optimizing the algorithm, we also use field programmable gate array (FPGA) for accelerating purposes.

Keywords: optical coherence tomography, graphics processing units, parallel computing, field programmable gate array, non-uniform rotational distortion correction, angiography

I. Introduction

Cancer has continuously been recognized as the top leading cause of death, and most of the cancers start from epithelial surfaces that line the internal organs [1], for example, oral cancer or gastrointestinal cancers. Optical Coherence Tomography (OCT) is a non-invasive volumetric imaging which can provide micron-level architectural information of the imaged tissue [2]. However, the imaging depth of OCT is limited to a 2-3 mm beneath the tissue surface, which is not enough to observe the internal organs of the body. Catheter-based OCT has the advantages of OCT and can be used internally, which is of great help for the early detection of oral cancer or gastrointestinal cancers [3]. Due to the influence of the beam scanning imaging mechanism implemented in catheter-based OCT, the image acquired will be distorted with so-called non-uniform rotational distortion (NURD) [4]. Furthermore, the presence of image distortion might lead to inaccurate computation results during advanced image analysis steps, making it challenging for catheter-based OCT to be used as a

diagnostic tool in practice. In this study, we have utilized graphics processing units (GPU) to develop an image correction framework for catheter-based OCT which can provide immediate NURD correction after the volumetric imaging session. In addition, we have integrated the OCT angiography (OCTA) imaging processing algorithm into the above framework to provide high-quality multifunctional OCT imaging.

II. Method

The algorithm first utilized GPU to process the raw data captured by the digitizer and stored the processed OCT data into the motherboard memory. After acquisition finished, by analyzing the variation of the fiducial marker position on the OCT data as a function of time, we can compute NURD profile, which can be used subsequently to resample the OCT data to yield NURD-corrected data, which can be used to compute the volumetric OCTA datasets afterward. Once all the NURD-corrected OCT and OCTA datasets were computed via the GPU board, these datasets will be passed back to the motherboard memory and finally be displayed on the in-house developed graphic user interface (GUI) with C++

language. The flowchart is shown in Figure 1(a). In this design, both the NURD correction and the OCTA computation can only be performed after the OCT dataset is computed where all the operations were performed on GPU, which is not an optimized design. Thus, we have proposed a novel processing flowchart by utilizing the FPGA processing unit along with the digitizer for the processing of the OCT datasets and reserve GPU for computation of NURD correction and OCTA imaging. The new framework exhibits the flow chart designed as shown in Figure 1(b).

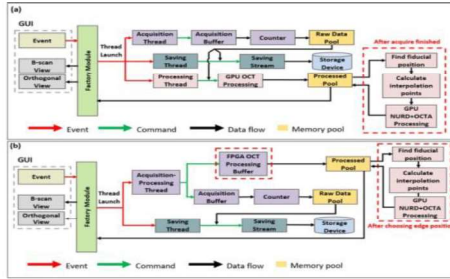


Figure 1. (a) Flowchart of GPU-OCT processing algorithm integrating with GPU-NURD and GPU-OCTA algorithm. (b) Flowchart of FPGA-OCT processing algorithm combining with GPU-NURD and GPU-OCTA algorithm.

III. Results and Discussion

The central wavelength of the swept light source is centered at 1310 nm with an axial (depth)-scanning rate of 200 kHz. The number A-scan per cross-sectional scan (i.e., B-scan) is 1000, achieving a frame rate of 200 fps. The NURD-corrected result is shown in Figure 2. The upper left panel provides live visualization of the B-scan imaging where the other two panels provide immediate examination of the volumetric datasets just capture, including both NURD-corrected OCT and OCTA. The demonstration of a dense microvascular network also confirms the superior performance of NURD correction.

Table 1 provide the processing time for 1024 x 1000 x 1500 samples. Although FPGA is slightly slower than GPU in processing the OCT images, it's expected that the processing time of FPGA OCT combined with GPU NURD correction will be faster than the version where all three operations were performed on GPU alone. Due to

the parallel and distribute processing framework achieved by using both FPGA and GPU, it promises to not only improve the processing performance but also minimize the excess time caused by the data passage between motherboard memory and the GPU.

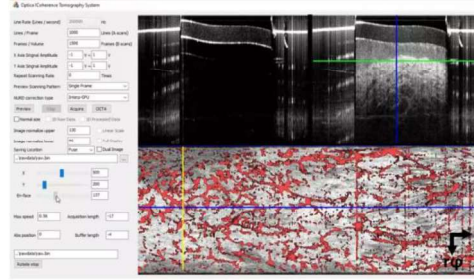


Figure 2. The GUI displays real-time cross-sectional image, corrected cross-sectional image and corrected *en-face* OCT fused with OCTA image. The image was acquired with buccal mucosa as sample. z: longitudinal pull back direction. r ϕ : circumferential direction.

Table 1. FPGA OCT and GPU OCT processing time table.

	FPGA OCT	GPU OCT
Processing time (ms)	24428	22762

IV. Acknowledgement

The authors acknowledge the support from the Young Scholar Fellowship Program by the Ministry of Science and Technology (MOST) of the Republic of China (ROC), Taiwan (MOST 110-2636-E-002-025/111-2636-E-002-024) and the National Health Research Institute (NHRI), Taiwan (NHRI-EX110-11004EC/EX111-11004EC).

V. Reference

- [1] M. J. Gora, M. J. Suter, G. J. Tearney, and X. Li, "Endoscopic optical coherence tomography: technologies and clinical applications [Invited]," (in eng), *Biomed Opt Express*, vol. 8, no. 5, pp. 2405-2444, May 1 2017, doi: 10.1364/boe.8.002405.
- [2] D. Huang *et al.*, "Optical coherence tomography," (in eng), *Science*, vol. 254, no. 5035, pp. 1178-81, Nov 22 1991, doi: 10.1126/science.1957169.
- [3] M.-T. Tsai *et al.*, "Noninvasive structural and microvascular anatomy of oral mucosae using handheld optical coherence tomography," *Biomed. Opt.*

Express, vol. 8, no. 11, pp. 5001-5012, 2017/11/01
2017, doi: 10.1364/BOE.8.005001.

- [4] O. O. Ahsen *et al.*, "Correction of rotational distortion for catheter-based en face OCT and OCT angiography," (in eng), *Opt Lett*, vol. 39, no. 20, pp. 5973-6, Oct 15 2014, doi: 10.1364/ol.39.005973.

Three-dimensional optical manipulation using cubic-phase metamaterials

Hung-Chuan Hsu^{*a}, Hsin Yu Kuo^b, Sunil Vyas^b, Kuang-Yuh Huang^a, Hsien-Shun Liao^a, Yuan Luo^{b,c}

^aDepartment of Mechanical Engineering, National Taiwan University, Taipei, Taiwan, R.O.C.

^bInstitute of Medical Device and Imaging, National Taiwan University, Taipei 10051, Taiwan, R.O.C.

^cYong-Lin Institute of Health, National Taiwan University, Taipei, 106038, Taiwan, R.O.C.

*d08522012@ntu.edu.tw; phone 02-23123456#88613

Abstract

Optical tweezers are the most commonly used techniques for three-dimensional (3D) manipulation in the biological field for trapping tiny objects. Among them, beam shaping methods are widely used because the different aspects of biological phenomena can be observed. Typically, spatial light modulators (SLM) are used for shaping light fields. However, the bulky size, pixelated structures, and high cost are the main limitations for developing a powerful and compact system. Here, a cubic-phase dielectric metasurface, which is fabricated by GaN circular nanopillars, is designed and generated to illuminate a polarization-independent two-dimensional (2D) airy beam in the visible region for optical tweezer. Due to the reciprocal propagation trajectory and high-intensity gradients of the Airy beam, particles can be trapped laterally and guided along the axial direction.

Keywords: dielectric metasurface, vertically accelerated 2D Airy beam, 3D optical manipulation

I Introduction

Optical tweezers have been commonly used as a powerful technique to manipulate the movement of particles at the nano and micro scales for biological and optical applications [1]. With the advantages of non-contact, label-free, and without mechanical damage, the manipulation technique can even hold, twist, and fix the objects, which are widely used in a variety of fields such as robotic engineering, biomedical analysis, and mechanical properties [2, 3]. A Gaussian beam can induce an optical gradient force to trap the nano-particles within a short Rayleigh length [4]. There are a variety of systems, such as two crossed laser beams [5], two optical illumination setups [6], and non-diffracted beam [7], that have been demonstrated to overcome the limitations and applied in biological and physical fields. Among them, non-diffracted beams, such as Airy beam which has many interesting features such as parabolic propagation trajectory, asymmetric intensity distribution, which have attracted large interest in various field such as micromachining of curved profiles [8], three-dimensional (3D) super-resolution imaging [9], and curved plasmonic materials [10]. There are various methods to generate the

non-diffracted beam, which includes spatial light modulator (SLM) and digital micro-mirror device (DMD). However, the bulky size, pixel structure, and polarization selectivity are the main limitations of these devices. Here, the compact and polarization-independent optical element is necessary to improve the experimental setup and provide the better results.

Metasurface is composed of metal and dielectric subwavelength structures which modulate amplitude, phase, and polarization state of electromagnetic waves under subwavelength scale [11]. This powerful element has become a potential candidate due to its flat geometry, compact size, and flexible modulations about desired beam shapes. The polarization-independent cubic-phase dielectric metasurface for optical tweezer [12] is proposed to provides high efficiency, accelerated 2D Airy beam in the visible region which fabricated by GaN circular nanopillars due to the specific features such as high robustness, low transmission loss, and entire 2π phase coverage. The dynamic motion of trapped particle has been demonstrated to quantify the performance from three-dimensional directions which improved the limitation of conventional optical tweezers.

II Experimental setup

With the compact size, high transmission efficiency, and modulation of desired beam shape, the high intensity Airy beam shape can be generated by the metalens and high NA oil objective lens in the sample plane to trap the particles. The white light source is to illuminate the particles and the filter which not shown here will be added before the CCD to remove the green light laser.

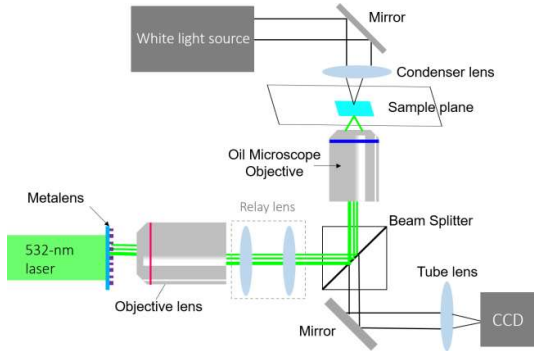


Figure 1. Schematic of experimental setup for optical tweezers. The metalens was added to generate the Airy beam shape and focused by the high NA oil objective lens. The white light source illuminates the particle and the filter was added to remove the unwanted green laser which not shown in the figure.

III Conclusions

In conclusion, the 2D accelerated Airy beam can be generated by the GaN-based metasurface. The experimental performance of optical manipulation setup can be further improved by the structure of circular nanopillars which provide the polarization-independent, high transmission efficiency, and compact system setup. In addition, the trapping stiffness of this non-diffracted beam can also be quantified to provide more precise results.

IV References

- [1] Ashkin, A. Acceleration and trapping of particles by radiation pressure. *Phys. Rev. Lett.* 1970, 24, 156–159.
- [2] Lenton, I.C.D.; Scott, E.K.; Rubinsztein-Dunlop, H.; Favre-Bulle, I.A. Optical tweezers exploring neuroscience. *Front. Bioeng. Biotechnol.* 2020, 8, 602797.
- [3] Desgarceaux, R.; Santybayeva, Z.; Battistella, E.; Nord, A.L.; Braun-Breton, C.; Abkarian, M.; Marago, O.M.; Charlot, B.; Pedaci, F. High-resolution photonic force microscopy based on sharp nanofabricated tips. *Nano Lett.* 2020, 20, 4249–4255.
- [4] Gong, Z.; Pan, Y.-L.; Videen, G.; Wang, C. Optical trapping and manipulation of single particles in air: Principles, technical details, and applications. *J. Quant. Spectrosc. Radiat. Transf.* 2018, 214, 94–119.
- [5] Redding, B.; Hill, S.C.; Alexson, D.; Wang, C.; Pan, Y.-L. Photophoretic trapping of airborne particles using ultraviolet illumination. *Opt. Express* 2015, 23, 3630.
- [6] Rkiouak, L.; Tang, M.; Camp, J.C.J.; McGregor, J.; Watson, I.M.; Cox, R.A.; Kalberer, M.; Ward, A.; Pope, F.D. Optical trapping and Raman spectroscopy of solid particles. *Phys. Chem. Chem. Phys.* 2014, 16, 11426–11434.
- [7] Baumgartl, J.; Mazilu, M.; Dholakia, K. Optically mediated particle clearing using Airy wavepackets. *Nat. Photon.* 2008, 2, 675–678.
- [8] Mathis, A.; Courvoisier, F.; Froehly, L.; Furfaro, L.; Jacquot, M.; Lacourt, P.-A.; Dudley, J.M. Micromachining along a curve: Femtosecond laser micromachining of curved profiles in diamond and silicon using accelerating beams. *Appl. Phys. Lett.* 2012, 101, 071110.
- [9] Wang, J.; Hua, X.; Guo, C.; Liu, W.; Jia, S. Airy-beam tomographic microscopy. *Optica* 2020, 7, 790–793.
- [10] Li, L.; Li, T.; Wang, S.M.; Zhang, C.; Zhu, S.N. Plasmonic Airy beam generated by in-plane diffraction. *Phys. Rev. Lett.* 2011, 107, 126804.
- [11] Yu, N.; Genevet, P.; Kats, M.A.; Aieta, F.; Tietienne, J.-P.; Capasso, F.; Gaburro, Z. Light propagation with phase discontinuities: Generalized laws of reflection and refraction. *Science* 2011, 334, 333–337.
- [12] Kuo, H.Y.; Vyas, S.; Chu, C.H.; Chen, M.K.; Shi, X.; Misawa, H.; Lu, Y.-J.; Luo, Y.; Tsai, D.P. Cubic-Phase Metasurface for Three-Dimensional Optical Manipulation. *Nanomaterials* 2021, 11, 1730.

Artificial intelligence assisted pathology with nonlinear optical microscopy on esophageal cancer

Guan-Yu Zhuo^{*a}, Wei-Hsun Wang^a, Ming-Chi Chen^a, Ming-Xin Lee^a

^aInstitute of Translational Medicine and New Drug Development, China Medical University, Taichung 40402, Taiwan

Abstract

We upgrade a traditional nonlinear optical (NLO) microscope with deep learning (DL) to accurately detect esophageal cancer. Because NLO microscopy has the advantages of label-free imaging, high resolution, and providing the structure and chemical properties of the tissue samples simultaneously, the accuracy of studying human esophageal cancer specimens could be comparable to traditional histopathology. Furthermore, the results are used as the training materials for DL, further realizing a rapid and high-precision cancer detection. Our method enables NLO microscopy being translated into clinical setting, further expanding the applicability from basic biomedical research to artificial intelligence (AI) assisted pathology.

Keywords: nonlinear optical microscopy, deep learning, esophageal cancer, second harmonic generation, two-photon fluorescence

I Introduction

Esophageal cancer is one of the most common cancers in many Asian countries including Taiwan, showing a strong male predominance with the incidence rate ranking 7th in cancers among males [1]. Unfortunately, the 5-year survival rate is very poor for patients with esophageal cancer, particularly in Taiwan (less than 20%). The primary reason for such low survival rate is the delay in the disease diagnosis due to the absence of early clinical symptoms. Consequently, esophageal cancer is detected at such an advanced stage that limits therapies available for effective cancer treatment [2]. Since it takes substantial amount of time for normal cells and tissues to transform into invasive cancer cells and/or lesions, there exist a time window, which can be used for the early detection of precancerous lesions and retardation or reversion of the entire process of cancer initiation, development and progression. Despite the availability of such large number of screening techniques for the discrimination among benign, pre-malignant and malignant lesions, a number of challenges are encountered with such diagnostic approaches. In particular, the effectiveness of clinical inspection for early cancer detection is limited due to the fact that subtle lesions and/or clinically normal-appearing mucosa

containing dysplasia or microinvasive carcinoma may remain undetected [3].

Among all the techniques available for cancer screening, histopathology is nowadays the gold standard for tumor identification and grading. Multiple immunohistochemical staining can provide more specific information. However, it needs a lengthy procedure, which lasts from 4 hours to one day depending on the protocol. Moreover, traditional hematoxylin and eosin (H&E) stains only specific to cell nuclei rather than intra- and extra-cellular tissue proteins. By contrast, nonlinear optical (NLO) microscopy offers more information than H&E staining, in which the morphological structure and chemical composition of tissue samples can be visualized by second harmonic generation, SHG (for collagen and muscle) and two-photon fluorescence, TPF (for elastin, keratin, NADH, and FAD). Because NLO microscopy can be label-free and is without further tissue processing, the duration from image acquisition to the analysis is greatly reduced, which requires some minutes up to few hours depending on the imaging size. On the other hand, the identification of suspicious margin between healthy part and tumor is very critical for tumor removal. After the surgery, the chance of recurrence of cancer also cannot be neglected. It has been proven that the computer programming with a precise dataset for early detection of chronic diseases

will minimize the human intervention and hence can increase the accuracy of results. Therefore, we will upgrade the design of NLO microscopy with a robust and automated image analysis technique such as deep learning (DL) with pre-trained convolutional neural networks (CNNs) [4]. It will help to enhance the image quality as well as to reduce the processing time, thus providing accurate results of the diagnosis and enabling more optimal therapeutic approaches.

II Method

A home-built laser scanning microscope is developed to alleviate some of the disadvantages of traditional histopathology by using various endogenous NLO signals to provide virtual biopsies that present the architecture and composition of tissues. Firstly, unstained tissue slides will be used for NLO imaging *ex vivo*, which will be later compared with the results of H&E staining identified by pathologists. Afterwards, the correct data will be used to train the DL algorithm for the following label-free AI-assisted pathology.

It is reported that around 15% of the patients with head and neck squamous cell carcinoma (HNSCC) have suffered from the second primary neoplasm called synchronous esophageal squamous cell neoplasms (ESCN), which appears within 6 months after being diagnosed with HNSCC. Although the potential risk factors associated with synchronous ESCN have been identified, it is crucial to develop a screening system to diagnose and estimate the potential ESCN on HNSCC patients. Therefore, we will use the devised NLO microscope to achieve this goal, as shown in Figure 1. (*We acknowledge the esophageal specimens provided by Dr. I-Chen Wu from the Division of Gastroenterology, Kaohsiung Medical University Hospital, KMHU*).

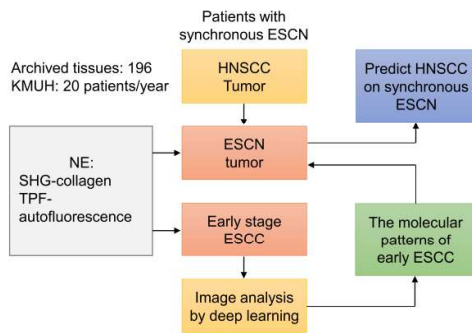


Figure 1. Study design for the relationship between early stage ESCC and synchronous ESCN.

III Results and Discussion

To achieve higher classification accuracy, it needs to increase the sample quantity as much as possible via possible methods. Combining image stitching with NLO microscopy, as shown in Figure 2, it facilitates the acquisition of wide-field images of esophageal cancer tissues to generate large datasets. Therefore, training with larger datasets and more clinical validations will be helpful to identify whether other biomarkers play a crucial role in esophageal cancer pathologies, which can provide useful information for a histopathologist to determine the onset of esophageal cancer.

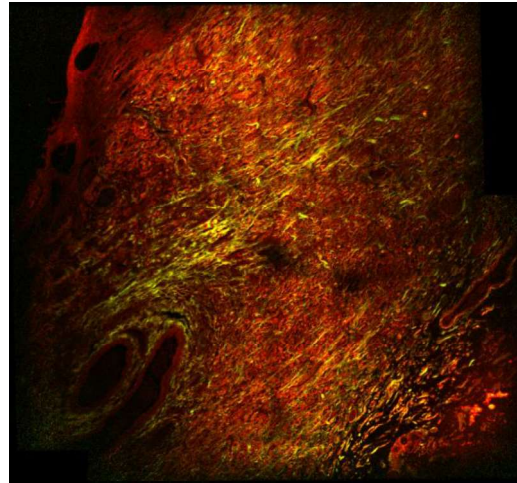


Figure 2. NLO image of cancerous esophagus. Yellow to green: collagen in submucosa (SHG); red to orange: muscle layer (TPF). Image size = 2 x 2 mm.

References

- [1] K.-D. Lee, T.-Y. Wang, C.-H. Lu, C.-E. Huang, and M.-C. Chen, *Oncotarget* **8**, 44567-44578 (2017).
- [2] Y.-F. Cheng, H.-S. Chen, S.-C. Wu, H.-C. Chen, W.-H. Hung, C.-H. Lin, and B.-Y. Wang, *Cancer Med.* **7**, 4193-4201 (2018).
- [3] M. Muto, K. Minashi, T. Yano, Y. Saito, I. Oda, S. Nonaka, T. Omori, H. Sugiura, K. Goda, M. Kaise, H. Inoue, H. Ishikawa, A. Ochiai, T. Shimoda, H. Watanabe, H. Tajiri, and D. Saito, *J. Clin. Oncol.* **28**, 1566-1572 (2010).
- [4] Y. Rivenson, Z. Göröcs, H. Günaydin, Y. Zhang, H. Wang, and A. Ozcan, *Optica* **4**, 1437-1443 (2017).

Moiré metalens for optical sectioning microscopy

Cheng Hung Chu^a, Yuan Luo^{a,b,c}, Sunil Vyas^b, Hsin Yu Kuo^b, Yu Hsin Chia^{b,c}, Mu Ku Chen^d, Yi-You Huang^c, Din Ping Tsai^d

^aYongLin Institute of Health, National Taiwan University, Taipei 10672, Taiwan

^bInstitute of Medical Device and Imaging, National Taiwan University, Taipei 10051, Taiwan

^cInstitute of Biomedical Engineering, National Taiwan University, Taipei 10051, Taiwan

^dDepartment of Electrical Engineering, City University of Hong Kong, Kowloon, 999077, Hong Kong

Abstract

The structural characteristics of biological samples are frequently observed by using fluorescence microscopy. The tunable lenses are used in microscope systems to axially scan the volumetric samples for obtaining optical sectioning images. The conventional tunable lenses exhibit distortions and spherical aberration. In this work, we present a compact imaging system based on Moiré metalens that has optical sectioning capability. It comprises two complementary phase metasurfaces and a telecentric system. The focal length can be tuned from 10 mm to 125 mm by changing mutual angles between two metasurfaces at the wavelength of 532nm. In addition, the speckle illumination HiLo microscope is used to eliminate the out-of-focus background light scattering. The labeled beads and ex vivo mice intestine tissues are measured to demonstrate the optical sectioning capability of this system. The proposed varifocal metalens design is expected to achieve key applications in fluorescence microscopy and endoscopy.

Keywords: metasurface, fluorescence microscopy, optical sectioning, HiLo imaging

I Introduction

Fluorescence microscopy is an important imaging technique for studying the features of biological tissues. However, the image quality is usually degraded by the out-of-focus background noise. HiLo imaging with structured illumination is an excellent method for obtaining optical sectioning fluorescence images with good contrast. Tunable focallenses, such as liquid crystal and elastomeric membrane lenses can scan the samples without movement. However, they are limited by non-immediate reaction, spherical aberration, distortion, and gravity effects. Moiré lens is composed of two paired complementary diffractive optical elements (DOE) which can tune the focal length by changing their mutual angles [1]. However, fabricating DOEs with intricate curved surfaces is difficult. Metasurfaces are thin, compact DOEs composed of nanostructures that can perform a variety of functions as needed [2-3]. Additionally, because it is compatible with conventional semiconductor fabrication techniques, it is simple to produce optical elements with complex phase distributions. In this work, we present an optical sectioning fluorescence microscopy based on GaN Moiré metalens in

visible regions. A telecentric imaging configuration is used in HiLo microscopy to produce sectioning images of ex vivo mouse intestinal tissues. Our method allows for a wide range of focal length tuning while keeping the magnification constant, which will be useful for multiplane imaging for various bio-applications [4].

II Results and Discussions

The schematic view of the Moiré metalens system is shown in Figure 1. The metasurfaces consist of GaN nanopillars with different radii. The phase distribution of metasurfaces follows the equation:

$$\Phi(r, \theta) = a \cdot r^2 \cdot \theta \quad (1)$$

where θ is the mutual angles between the paired metasurfaces, a is an adjustable constant and r is the radial coordinate. The focal length of metalens follows the equation:

$$f_{\theta} = \frac{\pi}{a} \cdot \theta \cdot \lambda \quad (2)$$

where f_{θ} is the focal length at θ angle, and λ is the working wavelength. At the wavelength of 532nm, the focal length can be controlled from 10 to 125 mm by rotating the

mutual angle shown in Figure 1b. The average focusing efficiency is about 35% in the visible region.

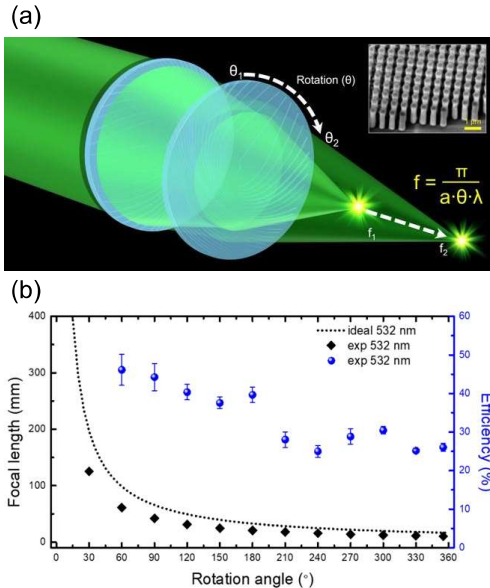


Figure 1. (a) Schematic diagram of the Moiré metalens. (b) Experimental and theoretical focal length and corresponding efficiency at various rotation angles.

Figure 2 shows the fluorescence sectioning images of villi of the intestine sample at three different rotation angles of paired metasurfaces. Due to the use of a telecentric setup, the magnification of images can keep constant while focusing at different depths. Out-of-focus background noise is considerably minimized, allowing structural details to be observed.

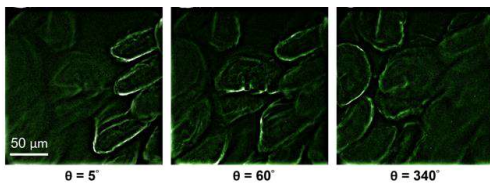


Figure 2. Ex vivo images of intestine tissue samples at different focal depths.

III Conclusions

For the purpose of acquiring optical sectioning images of volumetric biological samples, we have demonstrated the employment of the fluorescence microscopy system

based on Moiré metalens in conjunction with HiLo image processing. Without axial displacement, the focal length of the system can be tuned by changing the relative angle between the paired metasurfaces. The standard resolution target and fluorescent microspheres are analyzed as examples of the imaging performance of our system, showing the lateral resolution and optical sectioning capability of approximately $2 \mu\text{m}$ and $7 \mu\text{m}$, respectively. The reconstructed images of the intestine tissue were taken at various focal planes, each of which corresponded to a distinct rotation angle. These images have high contrast and resolution and are comparable in performance to those from electricity-tunable lenses. Our research provides evidence and a strong foundation for the creation of smaller optical microscope devices.

References

- [1] S. Bernet, M. Ritsch-Marte, "Adjustable refractive power from diffractive moiré elements." *Applied optics* 47, 3722 (2008).
- [2] R. J. Lin et al., "Achromatic metalens array for full-colour light-field imaging." *Nature Nanotechnology* 14, 227 (2019).
- [3] L. Li et al., "Metalens-array-based high-dimensional and multiphoton quantum source." *Science* 368, 1487 (2020).
- [4] Y. Luo et al., "Varifocal Metalens for Optical Sectioning Fluorescence Microscopy," *Nano Letters* 21, 5133 (2021).

Acknowledgment

Financial support was provided by Taiwan Ministry of Science and Technology (MOST)(contract 108-2221-E-002-168-MY4)

Perturbation Monte Carlo Applicability for Human Neck Model

Chin-Hsuan Sun, Kung-Bin Sung

Institute of Biomedical Electronics and Bioinformatics, National Taiwan University, Taipei 10051, Taiwan, R.O.C.

Abstract

To quantify blood oxygen saturation (SO_2) of internal jugular vein (IJV), we measure diffuse reflectance spectra at the skin surface above IJV and analyze the difference in reflectance signals between IJV's systole and diastole, similar to what is done in pulse oximetry. Relationships between the signals and IJV SO_2 are obtained by Monte Carlo (MC) simulations of photon energy transport in three-dimensional tissue models. To speed up the simulations we implement a perturbation Monte Carlo (PMC) method which calculates the reflectance for IJV at diastole from one MC simulation of IJV at systole, thereby cutting the simulation time in half. However, PMC could have large errors depending on optical parameters of the muscle and the IJV blood. This study analyzes the range of these optical parameters where PMC is applicable.

Keywords: perturbed Monte Carlo, diffuse reflectance spectroscopy, oximetry

I Introduction

Non-invasive monitoring of IJV blood oxygen saturation is important. Anatomically, most of the blood in the brain will eventually flow into the IJV and then enter the central venous catheter, and central venous oxygen saturation is a clinical important indicator of oxygen usage and delivery. However, central venous oxygen saturation is only assessable invasively. In order to clarify the correlation between IJV and cerebral blood oxygen saturation, this study use the human neck numerical model obtained by ultrasound image through several subjects as the basis to analysis the photon behavior. The algorithm we use to do photon simulation is Monte Carlo algorithm, it is the current gold standard method in optical simulation. But it requires a lot of computation resource, so it is necessary to speed up the whole process.

In this study, in order to speed up the simulation of subsequent experiments, the PMC[1] method is used. Originally, we needed to know the difference between IJV systolic and diastolic structural changes to measure the relative blood oxygen saturation concentration at this time, so each calculation was based on at least two Monte Carlo simulations. However, when we use PMC, we can extend the results of other structural changes based on the data obtained from the Monte Carlo simulation of the first systolic or diastolic structure. In addition, the advantage of

PMC is that since the operations are performed based on the results obtained from the same Monte Carlo simulation, the randomness is dependent, so there is no superposition of random noise.

However, PMC is not omnipotent. It has some limitations. When the optical parameters of the perturb region change too much, it increases the error of its calculation results. Therefore, this experiment analyzes the scope of application of PMC in the case of the human neck tissue model.

II Methods

Since the wavelength of the diffuse reflectance spectrum to be analyzed in the subsequent experiments is near-infrared light, when generating the simulated data, we use the upper and lower bounds of the optical parameters between 700nm and 900nm to generate the data. In order to compare the error caused by PMC, we use the photon data generated by two Monte Carlo simulations of IJV contraction and IJV relaxation as target data, and the data generated by one Monte Carlo simulation during IJV contraction, and then use PMC to calculate its relaxation as testing data, the difference between the two can be compared at this time. The PMC calculation method used in the calculation is as formula (1). The simulation tool we

use here is Monte Carlo eXtreme (MCX)[2], which is a voxel-based Monte Carlo algorithm.

$$W_{new,i} = W_{sim,i} \left(\frac{\mu_{s_{new}}}{\mu_{s_{old}}} \right)^{j_i} e^{-(\mu_{t_{new}} - \mu_{t_{old}}) S_i}, \quad (1)$$

$W_{sim,i}$ is first anatomy simulation from MCX, $W_{new,i}$ is perturbation result for second anatomy calculate by formula, j_i is the scatter event in perturbation region, S_i is the photon pathlength in perturbation region. Since the model of the human neck is composed of multiple tissue including skin, fat, muscle, IJV, and common carotid artery(CCA). The photon data result is from the optical parameters of the multilayer. Therefore, it can be regarded as a multivariate problem. First, because we use tissue optical parameters to get our PMC and MCX results, we treat tissue optical parameters like absorption coefficient, scattering coefficient and the optical parameter difference in perturbed region as input and MCX result, PMC result and percentage error between MCX and PMC as output. Then, we use Canonical Correlation Analysis (CCA) to analyze whether the input is correlated with the output. Further, we analyze the multivariate optical parameters, which tissue layers have a relatively large correlation, which means that they have a significant impact on the error between MCX and PMC result.

III Results and Discussion

1. Compare PMC and MCX result

Firstly, we use ultrasonic imaging to make the human neck model, and establish two numerical models for the IJV systolic and diastolic resolution for simulation as shown in figure1.

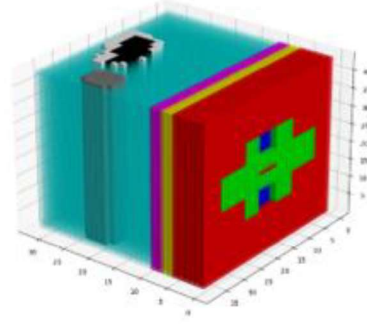


Figure 1. Human neck numerical model, green region is the holder which we put, blue region is detector, red region is air, yellow region is skin, pink region is fat, light blue is muscle, black region is IJV, gray region is CCA, white region is perturbation region, which means IJV contraction and relaxation difference.

After the numerical model is established, we use the previously mentioned MCX for simulation, and the number of photons we use in the simulation is $3e8$, and the optical parameters (μ_a , μ_s) of each layer are sorted out through the literature references in the past. Several parameter points are selected from the upper bound and the lower bound, and finally about 3 million different optical parameter combinations are formed. Through Figure 2, we can find that PMC and MCX have relatively larger errors under certain parameter combinations. In Figure 3, we show that some certain condition that may take different error effect on our result. Here, we use MCX result as our gold standard to compare PMC result. $\Delta\mu_s$ is the scattering coefficient difference in the perturbed region, error is the percentage error between PMC result and MCX result.

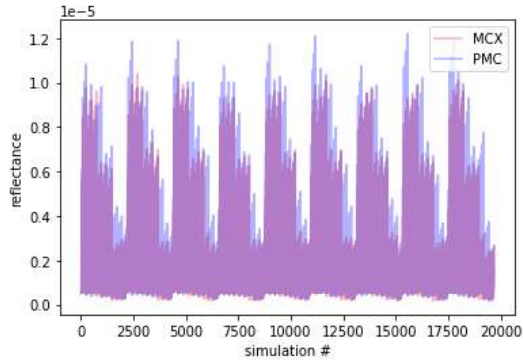


Figure 2. Display the result of PMC and MCX have much different in some simulation cases

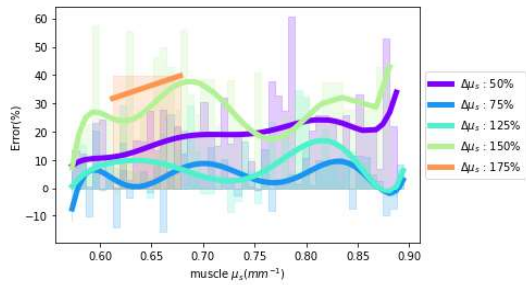


Figure 3. Show that how scatter coefficient difference in perturbation region and its actual value effect the error between PMC and MCX.

2. Canonical Correlation Analysis

Next, we analyze which tissue layers contribute more to this result. First, using Canonical Correlation Analysis, we reduce the dimension of the input and output which was mentioned previously to find the correlation between our optical parameters combined with PMC equation parameters and simulation result (include percentage error between MCX and PMC, PMC result and MCX result). The relation would be like equation 2.

$$(U, V) = CCA(input, output) \quad (2)$$

Here, U and V is the first set of Canonical Variables, U is linear combination of the each element in input, V is linear combination of the each element in output.

Analyzing the first set of Canonical Variables can find that the correlation is 0.93, indicating that the input of

these optical parameters and the influence of the perturb region are indeed closely related to PMC result, MCX result and percentage error between PMC and MCX.

Then, in the first group of Canonical Variables, the Canonical loadings of each variable (the correlation coefficient between the single variable and the canonical variable) can be used to know what proportion of the variance of the variable is explained by the canonical variable, such as Table 1. $\Delta\mu_a$ is the difference of the absorption coefficient of the perturb region. $\Delta\mu_s$ is the difference of the scattering coefficient of the perturb region.

Table 1. Canonical loadings of each variable

Combination	Correlation
U vs μ_{a_muscle}	0.76
U vs $\Delta\mu_a$	-0.65
U vs μ_{s_muscle}	-0.44
U vs $\Delta\mu_s$	0.31

In conclusion, we can find that not only the scattering coefficient difference in perturbed region but also the scattering coefficient its actual value would cause the error, which is intuitive. Next, we can analysis what is the affect that absorption coefficient may cause.

References

1. Seo, I., et al., *Perturbation and differential Monte Carlo methods for measurement of optical properties in a layered epithelial tissue model*. J Biomed Opt, 2007. **12**(1): p. 014030.
2. Fang, Q. and D.A. Boas, *Monte Carlo Simulation of Photon Migration in 3D Turbid Media Accelerated by Graphics Processing Units*. Optics Express, 2009. **17**(22): p. 20178-20190.

Development of surface plasmon resonance-Raman spectroscopy system to detect heparin-induced thrombosis

Chia-Ling Chiang^a, Nan-Fu Chiu^{b,c*}, Chii-Wann Lin^a

^aDepartment of Biomedical Engineering, National Taiwan University, Taipei 10051, Taiwan, R.O.C.

^bInstitute of Electro-Optical Engineering, National Taiwan Normal University, Taipei 11677, Taiwan, R.O.C.

^cDepartment of Life Science, National Taiwan Normal University, Taipei 11677, Taiwan, R.O.C.

Abstract

Nowadays one in four people are dying from thrombus in the world. If detection technology is improved, early diagnosis and treatment can be achieved. According to this study, the detection method of surface plasmon resonance and Raman spectroscopy integrated system is mainly developed for thrombosis caused by heparin-induced thrombocytopenia. In the experiment, we compare the binding relationship between platelet factor 4 with or without heparin and anti-platelet factor 4 antibody. Besides, the characteristic peaks of the target sample were identified by Raman spectroscopy simultaneously. Therefore, this system not only understands the binding kinetics between molecules but also verifies the mechanism between molecules through Raman spectrometry analysis to reduce false positives caused by non-specificity and improving detection sensitivity.

Keywords: Thrombosis, Surface plasmon resonance, Raman spectroscopy, Heparin-induced thrombocytopenia, platelet factor 4

I Introduction

Thrombosis cause death in one quarter of the world [1], and the factors can be classified into congenital or acquired effects. Heparin-induced thrombocytopenia (HIT) is part of the latter factor [2]. Heparin is used to prevent or treat thrombosis-related diseases clinically. However, according to previous research, it was found that up to 8% of patients who took heparin developed HIT antibodies. One-third of the patients would develop thrombosis and approximately 20-30% are at risk of death. The current detection method is first diagnosed with the 4T scale. If there is a moderate or high risk of HIT probability, immuno - enzymatic tests (ELISA) and functional tests, including serotonin release assay (SRA) are be used for further detection. However, ELISA have the problem of false positives as well as SRA requires specialized equipment and techniques although both of them have high sensitivity and specificity. Besides, they also have the disadvantages of long analysis time and the need to label samples [4].

Surface Plasmon Resonance (SPR) is to detect and analyze the change of refractive index produced by the interaction between molecules on the metal surface. Its features include

* nfchiu@ntnu.edu.tw; phone +886-2-77496722

label-free, real-time, and binding kinetic information. It is often used in applications such as antigen identification, determination of antigen concentration, and kinetic constants of antigen-antibody binding, but non-specific binding between molecules is still challenge in SPR detection [4,5]. Raman scattering is classified as inelastic scattering which means energy transfer occurs in the process. In other words, the initial state of the molecule before excitation is different from the final state after scattering. The difference between the initial state and the final state which is called frequency shift can be measured the structure of molecules. In contrast to infrared spectroscopy, Raman spectroscopy doesn't need to take into account the intensities of characteristic peaks of other chemical bonds that can be disturbed by the influence of water [6,7]. Hence, we combine the advantages of the two analytical techniques to develop SPR-Raman spectroscopy system used to detect the heparin-PF4 complex and explore the mechanism of heparin for inducing thrombosis.

II Methods

1. SPR-Raman spectroscopy system

In figure 1, the SRP-Raman spectroscopy system is divided

into two parts, namely SPR system and Raman probe. The SPR system was used 670nm monochromatic light to pass through a plano-convex lens to expand the beam, and pin hold to make the beam uniformly incident. The polarizer is to generate the TM wave which can occur surface plasmon resonance on the metal surface. Before the light beam enters the prism (BK7, n=1.52), it was focused on the detection area of the metal surface through plano-convex lens. The reflected light intensity will be collected by the Mono charge coupled device (Mono CCD) on the goniometer. The angle rotation and the reception of reflected light intensity are controlled by Labview. The Raman probe was used 785nm laser light to generate parallel light through a lens, and then band-pass filter is to obtain a purer laser band. Since the scattered wavelength is greater than the excitation wavelength, the scattered light was reflected into the edge filter after passing through the short wave pass (SWP) dichroic mirror. Because of edge filter, the scattered light in larger wavelength was collected by the lens. Ultimately, the collected scattered light is transmitted to the spectrometer for analysis through fiber coupling.

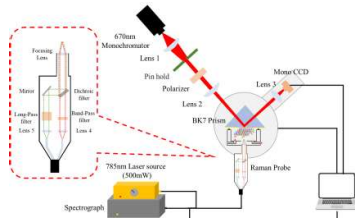


Figure 1 SPR-Raman system for real-time thrombosis detection

2. SPR chip preparation

Before the experiment, acetone, isopropanol, and deionized water were used to clean the 50nm thickness gold film, and then oscillated with ultrasonic for 3 minutes and spray dried with nitrogen gas respectively. After cleaning, the surface of the gold film was quickly sintered with a hydrogen-oxygen flame to remove organic substances. Ultimately, 8-Mercaptooctanoic acid (MOA) was incubated on the surface of the sensor chip at room temperature for 24 hours.

III Results and Discussion

In figure 2(a), it was measured the SPR angle shift response of different analytes which is PF4 and Heparin-PF4 complex combined with Anti-PF4 at the same concentration but different flow rates. The result was found that the change of the resonance angle of mixed heparin group was higher than the unmixed

heparin group which is indicated heparin-PF4 complex would increase its binding probability to the antibody. In Figure 2(b), it's the calibration curves of average SPR angle with each concentration. It was found that the higher concentration has the greater the resonance angle shift. In addition, the correlation coefficient (R2) is 0.99 which is indicating that the concentration in this range is linear. The detection limit (LOD) is 0.1pg/mL. The error bar stands for the estimated standard error of the mean of three replicates.

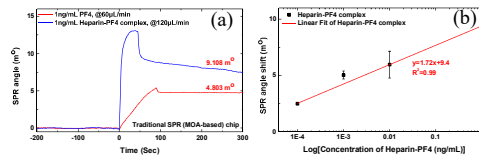


Figure 2 (a) Comparison of the binding curves of 1ng/mL PF4 and Heparin-PF4complex (b) Linear regression curve of each concentration

Figure 3 shows the latter three groups appear in the S-S bond at 430-550 cm-1, the C-S bond at 710-720 cm-1, the C-H bond at 800-900 cm-1and the C-O stretch bond at 1110-1140 cm-1 associated with MOA. Furthermore, in the immobilized antibody group and the Heparin-PF4 complex group, the peaks of the protein were observed as Amide I at 1655 cm-1, Amide II at 1542 cm-1 and Amide III at 1248 cm-1, respectively. However, the resulting strength is not obvious because of low concentration. Ultimately, in the Heparin-PF4 complex group, it was found that the O-H bond strength at 1320 cm-1 obviously. Moreover, we notice that the peak of 1256 cm-1 is shifted. Probability, it may be caused by the influence of Amide III at 1248 cm-1 and S=O at 1263 cm-1 at 1256 cm-1. Due to the strong C-C bond, the 6-O-SO3 oscillation at 1043 cm-1 and the 3-O-SO3 oscillation at 1060 cm-1 is covered. Similarly, the C-O-C stretching oscillations of 806, 842, and 866 cm-1 are also inconspicuous due to the strong C-H bond.

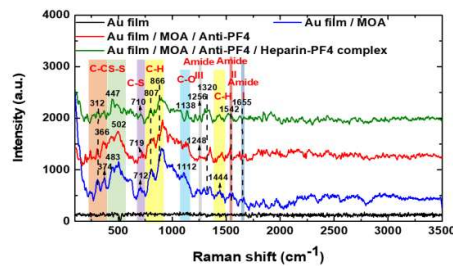


Figure 3 Measurement of gold film from modified MOA, immobilized antibody and detection of Heparin-PF4 complex mass spectrometry

[7] Smith, E., & Dent, G. (2019). *Modern Raman spectroscopy: a practical approach*. John Wiley & Sons.

IV CONCLUSION

Compared with the current detection method, the SPR-Raman spectroscopy system can be detected the binding between Heparin-PF4 complex and anti-PF4 in a label-free and real-time manner. The spectrum of the target sample is also measured and analyzed for further confirmation of specific binding at the same time. Besides, the lowest detectable concentration of Heparin-PF4 complex was 0.1 pg/mL, which is 100 times less than the detection limit of the ELISA currently available on the market. In future applications, this system can not only detect and analyze more effectively and rapidly but also explore the physiological mechanism more deeply.

V ACKNOWLEDGMENTS

This study was supported by the Ministry of Science and Technology of the Republic of China (ROC), Taiwan, for financially supporting this research under Contract No. MOST 105-2221-E-003-027, MOST 106-2221-E-003-020, MOST 107-2221-E-003-009, MOST 108-2221-E-003 -020 -MY3, MOST 109-2314-B-195-012-MY3.

References

- [1] Wendelboe, A. M., & Raskob, G. E. (2016). Global burden of thrombosis: epidemiologic aspects. *Circulation research*, 118(9), 1340-1347.
- [2] Rosendaal, F. R. (2016). Causes of venous thrombosis. *Thrombosis journal*, 14(1), 117-121.
- [3] Ahmed, I., Majeed, A., & Powell, R. (2007). Heparin induced thrombocytopenia: diagnosis and management update. *Postgraduate medical journal*, 83(983), 575-582.
- [4] Kim, J. Y., Zeng, Z. C., Xiao, L., & Schultz, Z. D. (2017). Elucidating protein/ligand recognition with combined surface plasmon resonance and surface enhanced Raman spectroscopy. *Analytical chemistry*, 89(24), 13074-13081.
- [5] Liu, X., Sun, Y., Song, D., Zhang, Q., Tian, Y., Bi, S., & Zhang, H. (2004). Sensitivity-enhancement of wavelength-modulation surface plasmon resonance biosensor for human complement factor 4. *Analytical biochemistry*, 333(1), 99-104.
- [6] Fasolato, C. (2018). *Surface enhanced Raman spectroscopy for biophysical applications: using plasmonic nanoparticle assemblies*. Springer.

Cell-free Mitochondrial DNA detection using an isothermal amplification-assisted Surface Plasmon Resonance biosensor platform

Jian-Hong Yang^a, Tzu-Heng Wu^b, Hui-Yun Lo^b, Ying-Ru Chen^b,
Kuei-Pin Chung^c, Jung-Yien Chien^c, Chii-Wann Lin^{*b}

^aGraduate Institute of Biomedical Electronics and Bioinformatics, National Taiwan University, Taipei 10051, Taiwan, R.O.C.

^bDepartment of Biomedical Engineering, National Taiwan University, Taipei 10051, Taiwan, R.O.C.

^cDepartment of Internal Medicine, Nation Taiwan University Hospital, Taipei 100225, Taiwan, R.O.C.

Abstract

Mitochondrial DNA is a potential biomarker for a variety of relevant diseases, from liver failure to idiopathic pulmonary fibrosis. Cell-free Mitochondrial DNA levels may indicate extent of cellular damage and provide information on ongoing tissue injury and corresponding organ dysfunction. Here in this work, the detect cell-free mitochondrial DNA levels by using an isothermal amplification-assisted Surface Plasmon Resonance biosensor platform is demonstrated. Surface plasmon resonance biosensor is well known for its ultra-high sensitivity towards biomarkers, due to its sensing principle based on surface evanescent waves. The application of the isothermal amplification method, established via the algorithm previously proposed by our group can greatly amplify the detection signal of mitochondrial DNA, making this combination a reasonable and powerful tool for clinical application.

Keywords: Surface Plasmon Resonance Biosensor, Hybridization Chain Reaction, catalytic hairpin assembly

I Introduction

Surface plasmon resonance (SPR) based optical biosensors are now being used extensively to defined the kinetics of wide variety of macromolecular interactions and high- and low-affinity small molecule interactions. In this paper, our group combined SPR with Catalytic hairpin assembly (CHA), an enzyme-free amplification method that has previously proven useful in amplifying and transducing signals at the terminus of nucleic acid amplification reactions to be a biosensor platform. The results show that an efficient screening method for "kinetic favorable" Catalytic Hairpin Assembly reactions can be established using correlation analysis between SPR data, gel electrophoresis images, and nucleic acid simulations. This result could extend well beyond a special gene called "MTND" used in this paper, facilitating the rapid and efficient design of molecular nanomachines. Three catalytic hairpin assembly reactions are shown, designed specifically for MTND domain of mitochondrial DNA. Based on the gel electrophoresis

panel presented in this paper, the algorithm derived a catalytic hairpin assembly for the mitochondrial genome, with reactions clearly showing target, H1, H2, target-H1, and H1-H2 bands. According to the Surface Plasmon Resonance sensing data, the kinetics of the reactions are very different. These reactions, named CHA-1, CHA-2, and CHA-3, exhibit characteristic linear responses over time, and they vary in their ability to catalyze the formation of the final H1-H2 product. The correlation of these data suggests that not all catalytic hairpin components are suitable for diagnostic applications because of their slow reaction kinetics, even though simulations support the reaction to be successful. We believe that further correlations with nucleic acid structure, G-C content and empirical data will translate light into new design rules for efficiently generating CHA responses for diagnostic purposes. At the end of this project report, we also point out how our data suggest that new molecular functions can be attached to these nanomechanical responses, giving way to more powerful molecular tools for sensing.

II Methodology

1. Chipset fabrication process

Purchased BK-7 slides were cut to size with a dicing saw and then subjected to a series of cleaning processes prior to gold deposition. After sonication in EtOH and acetone, the chip was first immersed in EtOH/HCl to remove all organic residues on the chip set. The chip was then rigorously rinsed with copious amounts of EtOH and blown dry with high-purity nitrogen. Drug treatment with an adhesive layer “T1” was then performed in a mixture of pure propanol and 1-5% DI water for 1 hour to overnight. Deposit 45 nm of gold at a deposition rate of 0.5 angstroms per second.

2. Catalytic Hairpin Assembly and MTND sequences

A comprehensive review of catalytic hairpin assemblies can be found elsewhere, and a scheme for the CHA reaction can be seen in Fig. 1. Briefly, the CHA reaction consists of two fuel hairpin molecules (referred to here as H1 and H2) and a target nucleic acid fragment. Hairpin fuel molecules have characteristic footholds at the 5' end of H1 and the 3' end of H2. The core mechanism of CHA nucleic acid self-assembly lies in the toehold-mediated strand displacement, where the target molecule binds to H1. With the help of the toehold, after the target-H1 hybrid is formed, the complex can further hybridize to the H2 molecule. H2 binds and the target is discarded because the H2-H1 complex is kinetically favored. Therefore, the target can act as a catalyst for the reaction, strongly amplifying the reaction over time.

The sequences of these regions have been experimentally confirmed by next-generation sequencing with polymerase chain reaction (PCR) products (data not shown).

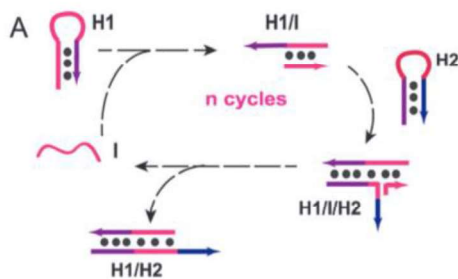


Fig. 1 A cartoon scheme of the catalytic hairpin assembly.

3. Optical setup of SPR system

The imaging Surface Plasmon Resonance (SPR) biosensing system in this paper, scans an appropriate range of incident angles and searches for an optimized working angle. The system uses a specific wavelength as the light source, with a polarization camera from SONY as the detector to optimize the detection dynamic range and maintain a certain level of sensitivity.

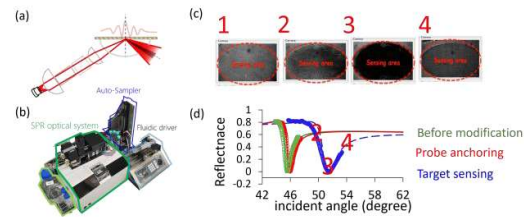


Fig. 2 (a) Kretschmann configuration of SPR biosensor.

(b) image of SPR system used in this paper.

(c) real-time optical image of the SPR. (d) SPR spectra.

4. SPR biosensing experiment

Fig. 3 shows typical SPR angular profiles from the original Au/T1/BK-7 chipset, initial modification of MTND target genes using 40-200 nM thiolated hairpin molecules in 1x PBS and 1 M NaCl, and final angular Spectral spread CHA response. The data shows that the maximum sensitivity of the chipset is generally around 6000 bits/degree, which is similar to the simulation results of Fresnel. To compare the binding reactions between the CHA reactions designed in this paper for consistent and high-quality data, the modified SPR angular displacement was routinely monitored and controlled to be around 0.06 degrees. Too low a density of probes can result in poor signal levels, while too high a density of probe molecules can lead to crowding of the surface.

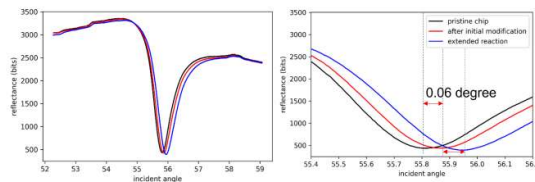


Fig. 3 SPR spectrum and the angle shift for the modification

III Results and Discussion

Following NUpack simulations, the designed CHA responses were validated using gel electrophoresis and surface plasmon resonance biosensors. Fig. 4 reveals another set of CHA responses, the CHA-3 responses, targeting 13239-13263 bp in the reverse strand domain of MTND. In this case, Ln8 also showed moderate binding potency of H1 to the target. Interestingly, however, the ability of the H1-target complex to catalyze the formation of the H1-H2 reaction is even lower compared to the CHA-2 case (data not shown). This evidence suggests that the MTND CHA-3 response, in which a 2-point mutation was deliberately placed on H1 to prevent nonspecific responses, has lower kinetics than other CHA responses.

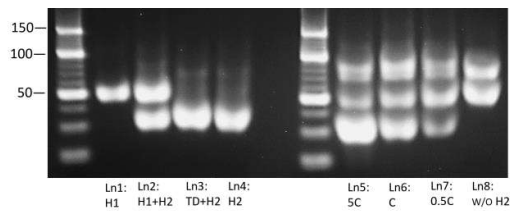


Fig. 4 MTND CHA-3 gel electrophoresis

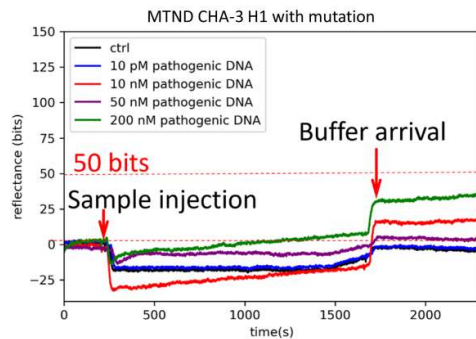


Fig. 5 Sensorgram for MTND CHA-3 H1M2 reaction

To further explore the differences between the observed CHA responses and their potential as diagnostic tools, SPR sensing experiments were performed on all CHA responses. MTND CHA-3 H1M2 sensing experiments was performed as shown in Figure 5. As can be seen from the figure, if the 100 nM reaction slope is taken as an arbitrary concentration to compare the CHA kinetics, the CHA-1 reaction (data not shown) is 2.5 times

faster than the CHA-2 reaction (75 vs. 30, reaction time over 1500 s). Furthermore, the kinetics of the CHA-3 H1M2 reaction were even slower compared to the CHA-2 reaction. This phenomenon was also supported by gel electrophoresis, as previously described. Clearly, the CHA gel electropherograms presented here can serve as a good indicator of reaction kinetics.

References

- Liu, J., Zhang, Y., Xie, H., Zhao, L., Zheng, L., & Ye, H. (2019). Applications of catalytic hairpin assembly reaction in biosensing. *Small*, 15(42), 1902989.
- Wu, T. H., Chang, C. C., Yang, C. H., Lin, W. Y., Ee, T. J., & Lin, C. W. (2020). Hybridization chain reactions targeting the severe acute respiratory syndrome coronavirus 2 (SARS-CoV-2). *International journal of molecular sciences*, 21(9), 3216.
- Wu, T. H., Yang, C. H., Chang, C. C., Liu, H. W., Yang, C. Y., Shen, T. L., ... & Bruyant, A. (2021). Multi-Layer Reflectivity Calculation Based Meta-Modeling of the Phase Mapping Function for Highly Reproducible Surface Plasmon Resonance Biosensing. *Biosensors*, 11(3), 95.
- Evanko, D. (2004). Hybridization chain reaction. *Nature Methods*, 1(3), 186-186.
- Karunanayake Mudiyansele, A. P., Yu, Q., Leon-Duque, M. A., Zhao, B., Wu, R., & You, M. (2018). Genetically encoded catalytic hairpin assembly for sensitive RNA imaging in live cells. *Journal of the American Chemical Society*, 140(28), 8739-8745.
- Pattanaik, P. (2005). Surface plasmon resonance. *Applied biochemistry and biotechnology*, 126(2), 79-92.
- Homola, J., Yee, S. S., & Gauglitz, G. (1999). Surface plasmon resonance sensors. *Sensors and actuators B: Chemical*, 54(1-2), 3-15.
- Liu, J., Zhang, Y., Xie, H., Zhao, L., Zheng, L., & Ye, H. (2019). Applications of catalytic hairpin assembly reaction in biosensing. *Small*, 15(42), 1902989.

VHG-based Airy light-sheet fluorescence microscope

Hung-Chuan Hsu^{*a}, Sunil Vyas^b, Kuang-Yuh Huang^a, Hsien-Shun Liao^a, Yuan Luo^{b,c}

^aDepartment of Mechanical Engineering, National Taiwan University, Taipei, Taiwan, R.O.C.

^bInstitute of Medical Device and Imaging, National Taiwan University, Taipei, Taiwan, R.O.C.

^cYong-Lin Institute of Health, National Taiwan University, Taipei, Taiwan, R.O.C.

*d08522012@ntu.edu.tw; phone 02-23123456#88613

Abstract

Light-sheet fluorescence microscopy (LSFM) provides high optical sectioning capability, which is commonly used in numerous biological and optical applications. To reduce the thickness of the light sheet and increase the field of view, the beam shaping method have commonly been used. Non-diffracted beams, such as the Airy and Bessel beams, were frequently used among them to provide a longer non-diffracted region, self-healing, and self-acceleration. The improved image quality obtained with non-diffracting beams helps in studying the internal structure of biological samples. Here, the volume holographic element was selected as a non-diffracted beam shaper due to its advantages such as high transmission efficiency, single diffracted order, and compact size. The side lobe of the non-diffracted beam can be removed by utilizing the deconvolution method to further improve the image contrast and noise suppression.

Keywords: light-sheet fluorescence microscopy, volume holographic grating, Airy beam, deconvolution method

I Introduction

Optical microscopy is a non-contact method that can observe the internal structures of tiny samples. Among them, wide-field fluorescence microscopy is the most commonly used method for biomedical imaging. However, it cannot provide optically sectioned images, because it captures all sample information, including in-focus and out-of-focus regions. On the other hand, a light sheet microscope is an efficient and widely used method for observing three-dimensional (3D) images of large samples [1]. The orthogonal structure of the light sheet microscope with separate illumination and the detection arm helps in obtaining fine optically sectioned images with extremely low photo exposure and photo-bleaching. However, the Gaussian beam used in the conventional light sheet microscope limits the field of view (FOV) and optical sectioning capability [2]. The FOV can be enhanced by illuminating the sample from different angles. However, this method may also cause longer exposure time and photo-bleaching. On the other hand, a propagation-invariant field such as an Airy beam can improve the FOV, penetration depth, and imaging contrast in the light sheet microscope [2]. Besides, the Airy beam keeps its transverse intensity distribution intact while propagating

and has excellent propagation properties of self-healing, self-acceleration, and parabolic path [4].

The Airy beam can be generated by using different optical components such as spatial light modulators (SLM), cubic phase plates, and tilted cylindrical lenses [1, 4]. Among them, the SLM is the most commonly used method to reshape an input beam into the desired beam shape, but it has the drawbacks of pixelated structure, bulky size, and high cost. In this work, we proposed using a volume holographic grating (VHG) to design the illumination system for a light sheet microscope. The important features of the VHG include volume diffraction, multiplexing capability, single diffraction order, and high angular selectivity [5]. The experimental setup demonstrates that the Airy light sheet can be generated using the volume holographic method.

II Experimental setup

The non-diffracted beam such as Airy beam can be presented as the normalized paraxial equation of diffraction and cubic phase profile, which shown as:

$$\phi(\xi, s) = Ai \left(s - \left(\frac{\xi}{2} \right)^2 + ia\xi \right) \\ \exp \left(as - \left(\frac{as\xi^2}{2} \right) + i \left(\frac{a^2\xi}{2} \right) + i \left(\frac{s\xi}{2} \right) - i(\xi^3/12) \right)$$

where ϕ is the electric field envelope, $s = \frac{x}{x_0}$ represents a dimensionless transverse coordinate, x_0 is an arbitrary transverse scale, $\xi = z/kx_0^2$ is a normalized propagation distance. The beam shape can be generated by following the equation and showing the specific beam shape compared to Gaussian beam, as shown in Fig. 2.

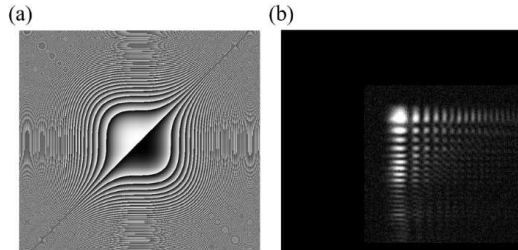


Figure 1. The schematic of phase mask and corresponding intensity of the Airy beam. (a) shows the phase mask (b) intensity profile of Airy beam.

An interferometer was designed to record Airy beam in phenanthrenequinone poly methyl methacrylate (PQ:PMMA). The schematic diagram of recording and reconstruction procedure is shown in Fig. 2. By using a phase-only SLM, an Airy beam was transformed from an incident Gaussian beam. An Ar⁺ ion laser at 488 nm was used to record the VHG because it has a maximum sensitivity for PQ: PMMA. Here, we followed a similar fabrication procedure of PQ: PMMA in the previous work [6].

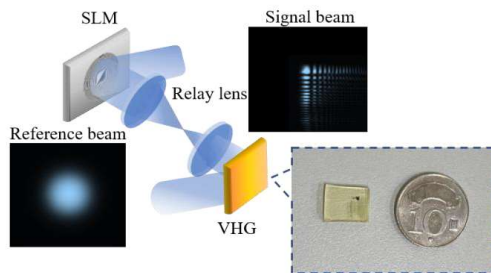


Figure 2. The schematic of recording procedure of volume holographic element.

III Conclusions

In conclusion, a new Airy light-sheet fluorescence microscope has been developed in which a volume holographic grating is used as an Airy beam illuminator.

The volume holographic optical element-based Airy beam shaper demonstrated here has several advantages, including Bragg wavelength degeneracy, and angular selectivity, all of which improve image quality. The proposed method has great potential for realizing compact illumination systems for structured illumination based microscopes.

References

- [1] Olarte, O. E., Andilla, J., Gualda, E. J., & Loza-Alvarez, P. (2018). Light-sheet microscopy: A tutorial. *Advances in Optics and Photonics*, 10(1), 111.
- [2] Huisken, Jan, and Didier Y. R. Stainier. (2007). Even Fluorescence Excitation by Multidirectional Selective Plane Illumination Microscopy (MSPIM). *Optics Letters*, vol. 32, no. 17, p. 2608.
- [3] Vyas, S., Chia, Y. H., & Luo, Y. (2018). Conventional volume holography for unconventional Airy beam shapes. *Optics Express*, 26(17), 21979.
- [4] Siviloglou, G. A., Broky, J., Dogariu, A., & Christodoulides, D. N. (2007). Observation of Accelerating Airy Beams. *Physical Review Letters*, 99(21).
- [5] Chia, C., Wang, H., Yeh, J. A., Bhattacharya, D., & Luo, Y. (2018). Multiplexed holographic non-axial-scanning slit confocal fluorescence microscopy. *Optics Express*, 26(11), 14288.
- [6] Luo, Y., Gelsinger, P. J., Barton, J. K., Barbastathis, G., & Kostuk, R. K. (2008). Optimization of multiplexed holographic gratings in PQ-PMMA for spectral-spatial imaging filters. *Optics Letters*, 33(6), 566.

Optical scanning holography for three-dimensional microscopic imaging

Chen-Ming Tsai^a, Tzu-Yi Yang^a, Cheng-Hao Tsou^a, Jung-Ping Liu^{*a,b}

^a Department of Photonics, Feng Chia University, 100 Wenhwa Rd., Seatwen, Taichung 40724, Taiwan, R.O.C.

^b Digital Optics Center, Feng Chia University, 100 Wenhwa Rd., Seatwen, Taichung 40724, Taiwan, R.O.C.

Abstract

Optical scanning holography (OSH) is a scanning-type digital holographic technique. The feature of OSH is its ability of recording both the coherent-mode digital hologram and the incoherent-mode digital hologram. Although most OSH is applied to record a hologram of mesoscopic object, here we will demonstrate three-dimensional imaging of micro-specimen by OSH.

Keywords: optical scanning holography, OSH, digital holography, DH, microscopy

I Introduction

Optical Scanning Holography (OSH) is a scanning-type digital holographic imaging technique [1]. In OSH, an interference fringe without object's information is generated to raster scan the three-dimensional (3D) object. The light scattered from the object is collected by a photodetector for demodulation. By using the heterodyne modulation and lock-in demodulation technique, the phase as well as the amplitude of the holographic signal is obtained [2]. The resulting complex hologram is free of zeroth order light and twin image. In addition, the sampling pitch of OSH can be smaller than that of conventional digital holography because the sampling pitch in OSH is controlled by the scanning speed and the time interval of the acquisition. Moreover, OSH can also be applied to spatial coherence analysis [3, 4], microscopy [5], sectional image reconstruction [6], etc. Therefore, OSH has been a promising holographic technique for 3D imaging.

II Method

Figure 1 illustrates the setup of an optical scanning holographic microscope. First the laser beam with wavelength 532 nm passes through an electro-optic modulator (EOM) and is separated into two beams. The two coherent beams are manipulated to be a plane wave

and a spherical wave, respectively. The two beams are recombined by a beamsplitter (BS) to form an interference fringe, which is projected to the object by a lens L_p . The microscopic specimen is mounted on a two-axis piezo-transducer scanner (PZT). A photodetector PD behind the object is applied to sense the scattered light. Because the EOM introduces a frequency difference between the two beams for interference, the signal sensed by PD oscillates at the heterodyne frequency and thus can be demodulated by a dual-phase lock-in amplifier (LIA) [7]. Alternatively, spatial-temporal demodulation technique can be applied to demodulate the signal without LIA [2].

The maximum travel in one dimension of our PZT is $100\mu\text{m}$. After removing the nonlinear range of the recording, the field of view of the recorded hologram is about $84\mu\text{m}$, and the sampling pitch is $0.084\mu\text{m}$. We have applied the system to record the hologram of a pinhole with diameter $1\mu\text{m}$. The phase of the obtained complex hologram is shown in Fig. 2. By using the phase correlation of the pinhole hologram [2], the optical resolution of the system is estimated to be $1.1\mu\text{m}$, which is very good in the present system using a 20X microscope objective.

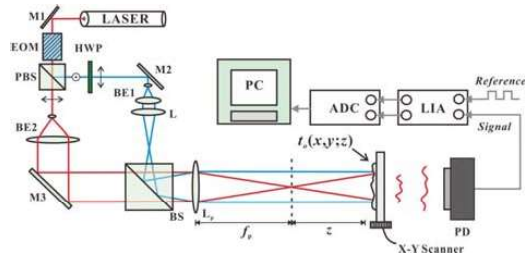


Figure 1. Schematic of optical scanning holographic microscope. EOM: electro-optic modulator; PBS: polarizing beam splitter; HWP: half-wave plate; M's: mirror; BE's: beam expander; L: lens; BS: beam splitter; PD: photo detector; ADC: analog-to-digital converter.

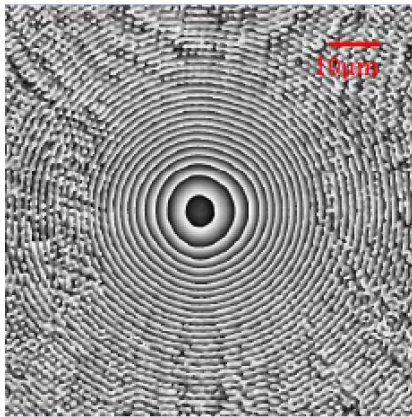


Figure 2. The phase of the complex hologram of a pinhole.

III Conclusion

In conclusion, we reported to record a hologram of micro-specimen by OSH. We have also used the proposed system to record a hologram of biological specimen. Recently, we have proposed interferenceless OSH [8], which is superior in the system stability and theoretical signal to noise ratio. Therefore, we will apply interferenceless OSH to record a hologram of micro biological specimen. This work is supported by National

Science and Technology Council (NSTC) of Taiwan (109-2221-E-035-076-MY3).

IV References

- [1] Poon T.-C., *Optical Scanning Holography with MATLAB*, Springer (2007).
- [2] Liu, J.-P., Luo, D.-Z., and Lu, S.-H., "Spatial-temporal demodulation technique for heterodyne optical scanning holography," *Opt. Laser Eng.* 68, 42-49 (2015).
- [3] Liu, J.-P., "Spatial coherence analysis for optical scanning holography," *Appl. Opt.* 54, A59-A66 (2015).
- [4] Liu, J.-P., Guo, C.-H., Hsiao, W.-J., Poon, T.-C., and Tsang, P., "Coherence experiments in single-pixel digital holography," *Opt. Lett.* 40, 2366 (2015).
- [5] Indebetouw, G., Maghnoji, A. E., and Foster, R., "Scanning holographic microscopy with transverse resolution exceeding the Rayleigh limit and extended depth of focus," *J. Opt. Soc. Am. A* 22, 892-898 (2005).
- [6] Lam, E. Y., Zhang, X., Vo, H., Poon, T.-C., and Indebetouw, G., "Three-dimensional microscopy and sectional image reconstruction using optical scanning holography," *Appl. Opt.* 48, H113-H119 (2009).
- [7] Poon, T.-C., and Liu, J.-P., *Introduction to Modern Digital Holography with MATLAB*, Cambridge University Press, (2014).
- [8] Liu, J.-P., Tsai, C.-M., Poon, T.-C., Tsang, P. W. M., and Zhang, Y., "Three-dimensional imaging by interferenceless optical scanning holography," *Opt. Laser Eng.* 158, 107183 (2022).

U-net Model for Isotropic Differential Phase Contrast Microscopy

An-Cin Li^a, Ying-Ju Chen^{a,b}, Sunil Vyas^a, Hsuan-Ming Huang^a, Yuan Luo^{a,b}

^aInstitute of Medical Device and Imaging, National Taiwan University, Taipei 10051, Taiwan, R.O.C.

^bDepartment of Biomedical Engineering, National Taiwan University, Taipei 10051, Taiwan, R.O.C.

Abstract

Quantitative differential phase contrast (qDPC) microscopy provides phase distributions of unstained specimens using the weak object transfer function. In order to obtain an isotropic phase transfer function, multiple intensity measurements are required; therefore, the image acquisition process is time-consuming. To minimize the required frames for isotropic qDPC microscopy, we propose a deep learning-based method. A commonly used convolution neural network (CNN), U-net architecture, is built to transform one-axis anisotropic cell images into twelve-axis isotropic reconstructed phase images. The network is trained using patch-wised input to extend the number of the training dataset consisting of seven different types of cells. Results from the testing dataset show the retrieved phase at the region of interest can be recovered with more than 95% accuracy.

Keywords: biomedical imaging, phase contrast imaging, isotropic phase transfer function, deep learning

I Introduction

Quantitative phase imaging (QPI) quantifies the phase shifts of label-free weak phase objects from the intensity measurements [1]. One of the common methods of QPI, qDPC microscopy, utilizes a partially coherent light source with structured illumination to capture several phase contrast images [1]. Conventional qDPC obtains anisotropic phase transfer function (PTF) using four half-circle as the illumination, while Tian et. al. proposed isotropic PTF with twelve-axis measurements to improve the stability and accuracy of phase retrieval [2]. However, the time-consuming imaging process limits its usefulness in the biomedical field.

Deep learning (DL) approaches are able to enhance the efficiency and performance of optical imaging [3]. The data-driven approaches learn features from the ground truth images and act as a mapping function to predict the result from the input [4]. A DL-based method has been applied to qDPC microscopy to generate optimal pupils depending on the experimental setup to retrieve a more accurate phase of the sample [5]. In this work, we implement a U-net architecture to execute image-to-image translation to recover the frequency loss in the anisotropic phase images [6]. The U-net model predictions using one-axis pairwise phase images can reach comparable accuracy of the retrieved phase from twelve-axis pairwise

measurements. A patch-based method is used to provide sufficient training data and to save computing power. The performance of the U-net model for qDPC is evaluated with PSNR, SSIM. The results show the proposed model provides accurate phase values and dry mass density maps.

II Method

1. Principle of qDPC

The experimental setup of the qDPC is shown in Fig. 1. The imaging system utilizes half-circle pupils to generate asymmetric illumination from different directions and obtain pair-wised phase contrast images.

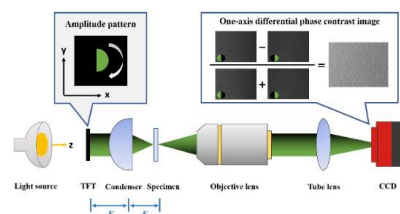


Figure 1. The configuration of the qDPC microscopy with half-circle pupil shown on the TFT. Pair-wised intensity measurements captured from the CCD are normalized to become DPC images [1].

With weak phase approximation, the relationship between the intensity and the phase in the spectra domain is linear. The relationship can be formulated as:

$$\tilde{I}(u) = i\tilde{H}_{phase}(u) \cdot \tilde{\phi}(u), \quad (1)$$

where $\tilde{I}(u)$ denotes the intensity at the spectra domain, $\tilde{H}_{phase}(u)$ denotes the phase transfer function, and $\tilde{\phi}(u)$ is the distribution maps for the phase. The linearized relation enables the phase distribution to be retrieved by Tikhonov regularization as shown below [2]:

$$\tilde{\phi}(r) = \mathcal{F}^{-1} \left\{ \frac{\sum_i (\tilde{H}_{phase,i} \cdot \mathcal{F}(I_{DPC,i}(r)))}{\sum_i |\tilde{H}_{phase,i}|^2 + \gamma} \right\}. \quad (2)$$

2. CNN model

Figure 2 shows a U-net model that consists of nineteen convolutional layers [6]. A set of anisotropic phase images are input to the model. Through the convolution layers and the down-sampling processes, the hierarchy features are extracted. With isotropic phase images as the ground truth, the model is trained to recover frequency loss in the spectra domain.

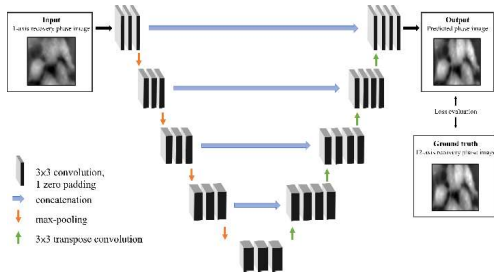


Figure 2. The architecture of the U-net model [6]. The filter size of the convolution layers is 1×1 at the last layer and 3×3 for the remaining layers.

The model learning object is minimized by

$$U_{learn} = \arg \min_{U_w, w \in W} F(U_w), \quad (3)$$

where U_{learn} represents the U-net model with optimized weights, and w denotes the weights in the hidden layers. The loss function F evaluates the mean square error (MSE) between the output and the ground truth in the training process to optimize the model weights.

III Results and Discussion

3T3 fibroblast cells and RMSC cells are used as a testing dataset to demonstrate the model performance. The peak signal-to-noise ratio (PSNR) can evaluate the quality of the image, and the structural similarity (SSIM) quantifies the similarity between the ground truth and the model predictions [6].

	PSNR	SSIM
Input	26.15dB±1.70	0.9442
U-net with MSE	30.89dB±2.78	0.9671
U-net with MAE	30.80dB±2.76	0.9690

Table 1. The performance of the model with MSE and MAE is evaluated by PSNR and SSIM.

IV Conclusion

The implementation of patch-based U-net with qDPC microscopy can predict isotropic phase images from anisotropic phase images. The patch-wise method reduces the required number of training data and the limitation of computing power. The PSNR and the SSIM values are higher after the model predictions, meaning that the model can successfully recover the missing details in anisotropic phase images. The ten times faster imaging speed can be achieved for phase reconstruction with the proposed method.

*r09528053@ntu.edu.tw; phone 02 2312-3456#288613

References

- [1] Mehta, S. B. and Sheppard, C. J. R., "Quantitative phase-gradient imaging at high resolution with asymmetric illumination-based differential phase contrast," *Optics Letters*, 34(13), 1924 (2009).
- [2] Tian, L., and Waller, L., "Quantitative differential phase contrast imaging in an LED array microscope," *Optics express* 23(9), 11394-11403 (2015).
- [3] Tian, L. et. al., "Deep learning in biomedical optic," *Lasers in Surgery and Medicine*, 53(6), 748-775 (2021).
- [4] Xuan, Y., Lyu, H., An, W., Liu, J., and Liu, X., "A data-driven deep learning approach for predicting separation-induced transition of submarines," *Physics of Fluids*, 34(2), 024101(2022).
- [5] Kellman, M. R., Bostan, E., Repina, N. A., and Waller, L., "Physics-based learned design: optimized coded-illumination for quantitative phase imaging," *IEEE Transactions on Computational Imaging*, 5(3), 344-353 (2019).
- [6] Li, A. C., Vyas, S., Lin, Y. H., Huang, Y. Y., Huang, H. M., and Luo, Y., "Patch-Based U-Net Model for Isotropic Quantitative Differential Phase Contrast Imaging," *IEEE Transactions on Medical Imaging*, 40(11), 3229-3237 (2021).

Biosensing applications of graphene in surface plasmons

Yu-Hua Chen^{*a}, Yi-An Wei^a, Pei-Jung Wu^a, Chan-Shan Yang^a

^aInstitute and Undergraduate Program of Electro-Optical Engineering, National Taiwan Normal University, Taipei 11677, Taiwan.

Abstract

In this study, infrared-enhanced absorption spectroscopy combined with graphene was used to simulate a surface plasmon tunable biomedical sensor. The strong optical field confinement of surface plasmons and its ability to disrupt diffraction can confine the optical field to the micro-nanostructures on our designed graphene surface, enhancing the interaction of infrared light with the substance under test. We used protein IgG and organic semiconductor CBP as analytes to detect their molecular fingerprints. Due to the modulation capability of graphene, it can have significant infrared enhancement in the detection of both analytes. The results of this study are expected to be beneficial for nanoscale surface plasmon optics.

Keywords: Surface plasmon, Biomedical sensor, Protein IgG, Organic semiconductor CBP, Graphene

I Introduction

Surface plasmons are surface waves that propagate between a dielectric layer and the boundary of a metallic material. Surface plasmons are excited by the design of materials and structures. The light field distribution on the surface of the material is limited, and the size of the structure can be reduced to the micrometer or nanometer scale. Due to the characteristics of surface waves, light can break the diffraction limit of the structure during propagation, enhance the interaction between light and matter, and realize its application in biosensors [1].

After designing the structure according to the wavelength of the surface plasmon, the selection of its material is also extremely important. Graphene has the advantages of strong thermal conductivity, mechanical strength, and high electron mobility, and is suitable as a material for exciting surface plasmons [2]. Another important feature of graphene is its special energy band structure, which can be changed by doping it or applying a voltage to change the Fermi level, thereby changing its optoelectronic properties, thereby making optoelectronic components with modulation capabilities.

According to the principle of surface-enhanced infrared absorption, the nano-scale metal film structure is used to enhance the near-field infrared vibrational

absorption of molecules, and its enhanced spectrum can be obtained through principle calculation.

In this paper, the surface plasmonic high reflection structure of the designed high-entropy alloy film and the graphene biosensor will be discussed, and the impact of different structural designs and materials on their applications will be analyzed in depth.

II Design

The photoconductivity of graphene calculated by Matlab, since the photoconductivity is a complex function, the real part and the imaginary part are calculated. In our calculation, we set the temperature as room temperature 300 K, the selected band is the mid-infrared range of 800~2000 cm^{-1} , and the selected Fermi level modulation range is 0~0.2 eV, which is closer to the actual experiment achievable modulation value.

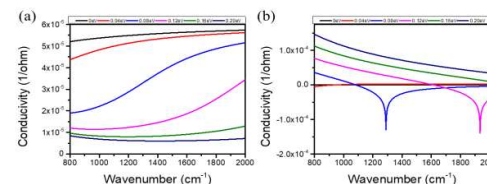


Figure 1. The complex conductivity of graphene at different Fermi levels: (a) the real part; (b) the imaginary part.

We choose alumina as the dielectric layer, and according to the incident wavelength λ_0 of 1550 cm^{-1} or 6450 nm as

the basic calculation, we can finally get our surface plasmon wavelength λ_{SP} of 51 nm. Figure 2 shows the designed structure, and the parameters of the structure, P period size, D round hole diameter and the gap size l between the two units of g, are simulated and optimized. It is expected that there are obvious characteristic peaks at the Fermi level E_f between 0.16 eV and 0.20 eV. Finally, P is 25 nm, the diameter of the circular hole is 10 nm, and the gap size g between the two units is 1 nm as the structural parameters of our model.

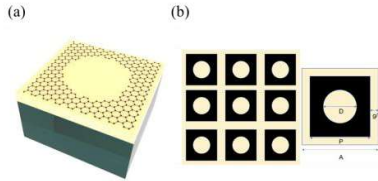


Figure 2. (a) Structure designed by calculation and (b) Schematic diagram of surface plasmon biosensor.

III Results and Discussion

The period P is 25 nm, the diameter of the circular hole is 10 nm, and the gap size g between the two units is 1 nm as the structural parameters of our model, because these parameters can just fit the absorption peaks of the two analytes we use shown in Figure 3.

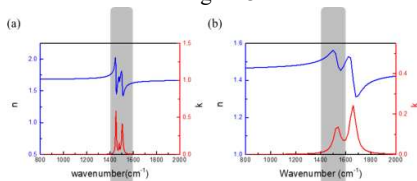


Figure 3. The refractive indices of IgG (a) and CBP (b) are overlaid by the enhanced absorption region of the model.

According to the calculation results of graphene conductivity in Figure 1, we will use 0.16eV~0.20eV for analysis. The results are shown in Figure 4. The part of the dotted line is that IgG (left) and CBP (right) have not been added, which can be clearly observed. The infrared absorption enhancement before and after the addition of the analyte, compared with the reference, we can obtain the change of its absorption peak with a small change of the Fermi level, and we also proved that it can be used for

different analytes. The effect of measuring objects to their molecular fingerprints

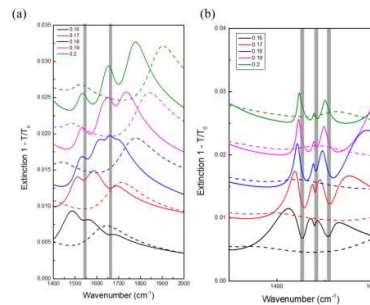


Figure 4. Extinction spectra of graphene at 0.16 - 0.20 eV before (dashed) and after (solid) addition of analytes IgG (a) and CBP (b).

IV Conclusion

In combination with graphene's infrared enhanced absorption biosensor, we use protein IgG and organic semiconductor CBP as the analytes to sense their molecular fingerprints. Due to the modulation ability of graphene, we can have a high amount of infrared enhancement when detecting both analytes. It is expected that this research will be beneficial to graphene application and near-mid infrared biosensors.

References

- Li, Ming, Scott K. Cushing, and Nianqiang Wu. 2015. Plasmon-enhanced optical sensors: a review, *Analyst* 140.2, 386-406, October
- Qilin Hong, Jie Luo, Chunchao Wen, Jianfa Zhang, Zhihong Zhu, Shiqiao Qin, and Xiaodong Yuan. 2019. Hybrid metal-graphene plasmonic sensor for multi-spectral sensing in both near-and mid-infrared ranges. *Optics express*, 27.24, 35914-35924, November.
- Rodrigo, D., Limaj, O., Janner, D., Etezadi, D., García de Abajo, F. J., Pruneri, V., & Altug, H. (2015). Mid-infrared plasmonic biosensing with graphene. *Science*, 165-168. July.
- Kavitha K. Gopalan, Bruno Paulillo, David M.A. Mackenzie, Daniel Rodrigo, Nestor Bareza, Patrick R. Whelan, Abhay Shivayogimath, and Valerio Pruneri. (2018) Scalable and Tunable Periodic Graphene Nanohole Arrays for Mid-Infrared Plasmonics. *Nano letters*, 5913-5918. August